Development and Application of a Multiscale Model for the Magnetic Fusion Edge Plasma Region

Felix Martin Michael Hasenbeck

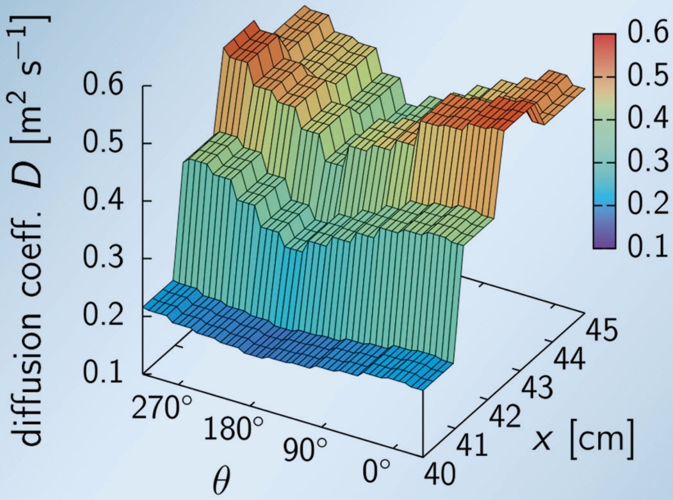

$$\frac{\partial n_0}{\partial t} + \boldsymbol{\nabla}\cdot\left[n_0\boldsymbol{u}_{\parallel 0} - D(\langle\tilde{n}\boldsymbol{v}_{\mathrm{E}}\rangle)\boldsymbol{\nabla}_\perp n_0\right] = S_{0in}^{ic}$$

$$\begin{aligned}\left(\frac{\partial}{\partial t} + \boldsymbol{v}_{\mathrm{E}}\cdot\boldsymbol{\nabla}_\perp\right)\tilde{n} &= -\boldsymbol{v}_{\mathrm{E}}\cdot\boldsymbol{\nabla}_\perp n_0 + \frac{T_{0e}}{e}\mathcal{K}(\tilde{n}) \\ &\quad - n_0\mathcal{K}(\phi) - n_0 B_0\left(\nabla_{\parallel 0} + \tilde{\nabla}_\parallel\right)\left(\frac{u_\parallel}{B_0} - \frac{j_\parallel}{e n_0 B_0}\right) + \gamma(\tilde{n})\end{aligned}$$

Member of the Helmholtz Association

Energie & Umwelt / Energy & Environment
Band / Volume 307
ISBN 978-3-95806-120-0

JÜLICH
FORSCHUNGSZENTRUM

Schriften des Forschungszentrums Jülich
Reihe Energie & Umwelt / Energy & Environment Band / Volume 307

Forschungszentrum Jülich GmbH
Institute of Energy and Climate Research
Plasma Physics IEK-4

Development and Application of a Multiscale Model for the Magnetic Fusion Edge Plasma Region

Felix Martin Michael Hasenbeck

Schriften des Forschungszentrums Jülich
Reihe Energie & Umwelt / Energy & Environment Band / Volume 307

ISSN 1866-1793 ISBN 978-3-95806-120-0

Bibliographic information published by the Deutsche Nationalbibliothek.
The Deutsche Nationalbibliothek lists this publication in the Deutsche
Nationalbibliografie; detailed bibliographic data are available in the
Internet at http://dnb.d-nb.de.

Publisher and Distributor: Forschungszentrum Jülich GmbH
Zentralbibliothek
52425 Jülich
Tel: +49 2461 61-5368
Fax: +49 2461 61-6103
Email: zb-publikation@fz-juelich.de
www.fz-juelich.de/zb

Cover Design: Grafische Medien, Forschungszentrum Jülich GmbH

Printer: Grafische Medien, Forschungszentrum Jülich GmbH

Schriften des Forschungszentrums Jülich
Reihe Energie & Umwelt / Energy & Environment, Band / Volume 307

D 82 (Diss. RWTH Aachen University, 2015)

ISSN 1866-1793
ISBN 978-3-95806-120-0

Für Midori

Abstract

Plasma edge particle and energy transport perpendicular to the magnetic field plays a decisive role for the performance and lifetime of a magnetic fusion reactor. For the particles, classical and neoclassical theories underestimate the associated radial transport by at least an order of magnitude. Drift fluid models, including mesoscale processes on scales down to tenths of millimeters and microseconds, account for the experimentally found level of radial transport; however, numerical simulations for typical reactor scales (of the order of seconds and centimeters) are computationally very expensive. Large scale code simulations are less costly but usually lack an adequate model for the radial transport.

The multiscale model presented in this work aims at improving the description of radial particle transport in large scale codes by including the effects of averaged local drift fluid dynamics on the macroscale profiles. The multiscale balances are derived from a generic multiscale model for a fluid, using the Braginskii closure for a collisional, magnetized plasma, and the assumptions of the B2 code model (macroscale balances) and the model of the local version of the drift fluid code ATTEMPT (mesoscale balances). A combined concurrent–sequential coupling procedure is developed for the implementation of the multiscale model within a coupled code system. An algorithm for the determination of statistically stationary states and adequate averaging intervals for the mesoscale data is outlined and tested, proving that it works consistently and efficiently.

The general relation between mesoscale and macroscale dynamics is investigated exemplarily by means of a passive scalar system. While mesoscale processes are convective in this system, earlier studies for small Kubo numbers $K \ll 1$ have shown that the macroscale behavior is diffusive. In this work it is demonstrated by numerical experiments that also in the regime of large Kubo numbers $K \gg 1$ the macroscale transport remains diffusive. An analytic expression for the diffusion coefficient D is found, being consistent with results from percolation theory.

The multiscale model and the coupling procedure are benchmarked with a one-dimensional test problem which consists of coupling the local version of the drift fluid code ATTEMPT to a 1D macroscale code to determine the time-dependent evolution of the flux surface averaged density in radial direction in the tokamak edge region. The reference simulation is given by a simulation of the non-local version

of ATTEMPT, accounting for both the mesoscale and the macroscale evolution. Results of the coupled code simulations show that the macroscale evolution of the density and the radial particle flux can be reproduced with typical uncertainties of 6 and 22%, respectively. Time savings with respect to the non-local simulations are of a factor of ten for a typical macroscale evolution time of 10 milliseconds while a speedup factor of the order of 50 is achievable for an edge region with a radial extent of ~ 30 cm and typical radial profile lengths of ~ 5 cm.

The multiscale model for two-dimensional, stationary problems is realized by coupling of the B2 code and the local version of the ATTEMPT code. The results of the corresponding coupled code simulations for experiments at the tokamak TEXTOR provide plasma profiles in agreement with experimental measurements with uncertainties regarding the electron density and electron temperature measured at the outer midplane around 10 to 25%. Poloidally and radially dependent profiles of the radial particle diffusion coefficients D, self-consistently determined by B2-ATTEMPT, have typical values of 0.3 to 0.9 $\mathrm{m}^2\ \mathrm{s}^{-1}$ and are within a 10 to 30% range of effective diffusion coefficients employed in B2-EIRENE simulations to fit simulation results to measured density profiles. The poloidal dependence of D as given by the B2-ATTEMPT simulations accounts for the experimentally confirmed ballooning character of radial transport with D at the low field side, being up to a factor two larger than on the high field side.

Contents

1. Introduction

The aim of a scientist is, generally speaking, to formulate descriptions of nature which are as universal as possible and therefore valid on all temporal and spatial scales. It quickly becomes obvious that by using the finest, most detailed models for an arbitrary system of interest, the effort that has to be invested into a solution may become enormous – imagine, for example, the attempt to describe the motion of billiard balls using quantum mechanics. Often, the next logical step is therefore to move to a coarser model, i.e. to neglect processes which take place on scales smaller or larger than the scales of interest. In the example of billiard balls this coarse graining could be the step from quantum mechanics to Newtonian mechanics. However, one might find that in some cases the simplifications lead to erroneous results, meaning that the interplay of the processes taking place on disparate scales cannot be neglected.

The objective of multiscale models is to include the most important aspects of the interdependency between the dynamics of different scales and to provide solutions which are both accurate and can be obtained efficiently. Multiscale models play a crucial role in many fields of physics and range from the Born-Oppenheimer approximation [1], where the electron motion is separated from motion of the (much heavier) nucleus, to the Reynolds decomposition and large-eddy simulations [2] to describe turbulent fluid dynamics. These approaches are usually based on separate models for the dynamics on the disparate scales whose interplay is then described by a number of coupling mechanisms responsible for interchanging information. In this work a multiscale model for the plasma in the edge region of a tokamak device is presented and evaluated.

Tokamaks represent a concept of a fusion reactor, aiming at the production of electrical energy, which is based on the fusion of the hydrogen isotopes deuterium and tritium within a plasma confined by a magnetic field. The edge region of these devices next to the vessel wall is of special importance for the tokamak's design since it is the region where the power exhaust of the plasma takes place. The interaction of the plasma with the vessel wall greatly influences the tokamak's performance and its lifetime. For more than 30 years, plasma models and the computer codes used to solve the corresponding equations have played a crucial role in complementing experimental investigations, in improving the design of new devices and components, and in increasing the physical understanding of the plasma dynamics. Depending on the topic of interest, these codes focus on the description of neutrals [3, 4], the small scale, turbulent plasma dynamics, using either gyrokinetic approaches [5, 6, 7]

or drift fluid approaches [8, 9, 10, 11, 12], on the two-dimensional plasma profiles on the reactor scale [13, 14, 15] or on three-dimensional configurations [16]. While turbulence models describe the complex transport processes of the plasma in detail on typical time scales on the order of microseconds and typical spatial scales on the order of millimeters, corresponding simulations on the characteristic tokamak scales of one meter and one second become computationally very expensive. Two-dimensional large scale codes have usually much shorter runtimes and the ability to include more complex geometrical aspects of the machine, while on the other hand partly employ reduced models for transport processes. One important example is the radial transport of particles, being crucial for the plasma confinement. In the large scale codes, it is usually modeled by an ad-hoc diffusion-convection model with transport coefficients prescribed by the modeler which are then used to fit the simulation results to experimentally determined profiles, see for example [17]. Classical and neoclassical transport theories based on a diffusion description underestimate it by at least one order of magnitude [18]. It is well accepted nowadays that for its correct description plasma turbulence models, such as drift fluid models, are required.
Combining models of microscale and mesoscale dynamics with macroscale models to account for the experimentally found level of radial transport has been a research topic for many years, with various theoretical studies [19, 20, 21] and numerical simulations [22, 23, 24, 25] having been performed in this context. The specific multiscale model for the plasma edge and its realization in form of coupled code system developed in this thesis complement and extend the previous analyses by investigating several aspects of this research field in detail: the concrete requirements for the implementation of an efficient multiscale system and its technical challenges, including the development of an adapted procedure to determine the statistically stationary state of a given time series and the corresponding averaged mesoscale terms, the modeling of time-dependent problems and the comparison of two-dimensional multiscale simulation results to experimentally found profiles.

The chapters of this thesis are structured as follows:

- The basis for the specific multiscale model for the plasma edge is given by a generic multiscale model for a fluid, which is derived in chapter 2 from the famous Boltzmann equation [26]. Since the fluid characteristics are being kept as general as possible, the structure of the particle, momentum and energy balances illustrates the general mechanisms governing the interplay between mesoscale and macroscale dynamics. With the objective of performing multiscale simulations to numerically calculate the evolution of the fluid, such as a fusion plasma, in mind, a possible realization of a corresponding coupled code system is described and the required nomenclature and input parameters are introduced.

- In chapter 3, the tokamak device and the concept of magnetic confinement is presented. Subsequently, the Braginskii closure of the fluid equations for a collisional, magnetized plasma [27] is outlined to specify the fluid considered here, a plasma. With this information at hand, the physical system of interest is defined. Next, the large scale model equations are derived from the macroscale part of the generic multiscale model. The derivation is based on the assumptions of the model of the large scale code B2 [28, 29]. Two versions of these equations are presented: one which still contains averaged mesoscale terms and which will be related to the macroscale part of the specific multiscale model for the plasma edge, and one which uses a macroscale transport model to replace the averaged mesoscale terms and is therefore self-contained.

- To complete the specific multiscale model for the plasma edge, a model for the mesoscale processes is needed. For this purpose, a drift fluid model is derived in chapter 4 along the lines of the work of B. Scott [30]. Its global version can be seen as an extension of the self-contained large scale model, additionally including the fluctuations of the magnetic field, the electric potential, and the detailed plasma dynamics perpendicular to the magnetic field. It evolves the plasma both on the mesoscale and macroscale. The respective local version only accounts for the fast, small-scale mesoscale dynamics, assuming constant macroscale profiles. It is related to the mesoscale part of the specific multiscale model presented in chapter 5.

- The large scale model for the macroscale and the local drift fluid model for the mesoscale are merged in chapter 5 to yield the specific multiscale model for the plasma edge. A survey on comparable projects that have been realized in the past is given to identify open questions and challenges.

- The self-contained large scale model uses a diffusion-convection macroscale transport model to represent averaged mesoscale terms which are, in the specific multiscale model, determined by mesoscale simulations. In chapter 6, the relation between mesoscale dynamics and the macroscale evolution of profiles is analyzed by means of a passive scalar system [31, 32, 33], serving as a model for synthetic turbulence. This passive scalar system is also used for an example of a coupled code system as a realization of a multiscale model for a first assessment of the influence of the coupling input parameters on the coupled code results.

- In chapter 7, the specific multiscale model is implemented into an one-dimensional coupled code system to reproduce the evolution of the flux surface averaged density profiles in radial direction in the edge of a tokamak device. It consists of a one-dimensional code to solve the density continuity equation on the macroscale and the local version of the drift fluid code ATTEMPT [11] to determine the mesoscale dynamics, corresponding to the model derived in chapter 4. On the basis of this reduced system, the technical details of the coupling procedure can be assessed and its performance can be evaluated by comparing the coupled code results to a sophisticated mesoscale simulation with the non-local version of ATTEMPT.

- With the results of chapter 7, the two-dimensional coupled code system, based on the full specific multiscale model, is set up in chapter 8. While the macroscale evolution is determined by the two-dimensional large scale code B2 [28], the drift fluid code ATTEMPT code is employed for the mesoscale simulations. Simulations of the plasma edge of the TEXTOR tokamak [34] are investigated and compared to previously obtained modeling results where the radial transport coefficients were fitted to reproduce experimentally observed profiles of the density [17].
- A summary of the results and an outlook is given in chapter 9.

2. Generic multiscale model for a fluid

In this chapter, a generic multiscale model to describe the temporal and spatial evolution of a fluid is derived. Basis for this derivation are the well-known fluid balance equations for the particle density, the momentum, and the energy, see for instance [35]. A fluid is, referring to the definition of the New Encyclopædia Britannica [36],

> [...] any liquid or gas or generally any material that cannot sustain a tangential, or shearing, force when at rest and that undergoes a continuous change in shape when subjected to such a stress. [...]

The term multiscale relates to the fact that the model comprises dynamical processes on disparate scales: the physical quantity α (α being for example the particle density or temperature) can then be decomposed into two parts:

$$\alpha = \alpha_0 + \widetilde{\alpha} \ . \tag{2.1}$$

The macroscale part α_0 of α evolves on characteristic spatial and temporal scales large compared to those of the mesoscale part $\widetilde{\alpha}$, while $\widetilde{\alpha}$ accounts for the comparably fast evolution on small spatial scales. On the characteristic scales of the mesoscale system the macroscale quantities can then assumed to be constant. Processes on both the mesoscale and macroscale interact with each other by a number of mechanisms which will be specified below. The adjective generic refers to the fact that the specifications of the model regarding the characteristics of the fluid, the forces acting on the fluid, and the sources of particles, momentum, and energy, are kept at a minimum. Thus, the resulting multiscale equations can be applied to describe a stream of water in a river bed or the dynamics of a magnetized, collisional plasma as it is found in a tokamak device. The applications regarding the latter, resulting in the multiscale simulations for the plasma edge, will be the focus of the following chapters. However, the generic form of the multiscale equations outlined here provides a fundamental picture of the interactions of mesoscale and macroscale dynamics.

The structure of this chapter is as follows. The well-known transition from the kinetic Boltzmann equation to a fluid model[1] (e.g. see [35]) is presented in paragraph 2.1 for

---

[1] In this context, the term fluid is not used to describe the character of the material as above, but the mathematical approach to obtain the evolution equations of the system.

completeness. On its basis, the new generic multiscale model is derived in paragraph 2.2. In paragraph 2.3, the implementation of the multiscale model into a coupled code system (which aims at solving the equations numerically) is outlined. It serves as a blueprint for the concrete design of the coupled code systems in chapters 7 and 8. The basic concepts and nomenclature for the coupling of codes are presented and related to common multiscale approaches [37]. Also, the benefits of a multiscale system compared to solving the full system on the mesoscale are discussed.
Note that above it is spoken of the interaction between mesoscale and macroscale processes while one would probably think of a microscale and a macroscale as the 'natural' scales of a multiscale model. However, in this work, the term microscale is reserved for a kinetic description of processes on the atomic level which happen on scales below the mesoscale fluid model considered here for the small scale dynamics.

2.1. From a kinetic to a fluid description

A fundamental way to describe a physical system consisting of many particles is to use the single particle probability distribution function $f_a(\boldsymbol{r}, \boldsymbol{V}, t)$. The probability $P_a(\boldsymbol{r}, \boldsymbol{V}, t)$ to find a particle of species a with velocity $\boldsymbol{V}$ at position $\boldsymbol{r}$ at time t is given by

$$P_a(\boldsymbol{r}, \boldsymbol{V}, t) \;=\; f_a(\boldsymbol{r}, \boldsymbol{V}, t)\; d^3r\, d^3V \;. \tag{2.2}$$

The evolution equation of f_a is the **Boltzmann equation** [38]:

$$\boxed{\frac{\partial f_a}{\partial t} \;+\; \boldsymbol{V}\cdot\boldsymbol{\nabla} f_a \;+\; \frac{\boldsymbol{F}_a}{m_a}\cdot\boldsymbol{\nabla}_V f_a \;=\; C_a \;, \qquad (2.3)}$$

where $\boldsymbol{\nabla}_V$ is the nabla operator with respect to the particle velocities, $\boldsymbol{F}_a$ the force acting on the particles, m_a the particle mass, and C_a the so-called collision term. Note that the lhs of eq. (2.3) is the total time derivative df/dt of the probability distribution function. The characteristic physics of the system due to collisions are described by C_a.

For many particle systems it can be advantageous to move from a kinetic to a fluid description to simplify the corresponding evolution equations. Instead of a particle distribution function f_a one considers quantities like the density n_a, the fluid velocity $\boldsymbol{v}_a$, and the temperature T_a, which are defined as moments of f_a. Thus, the transition from a kinetic to a fluid model involves an averaging (or coarse graining) procedure.

The density n (zeroth moment) is given by

$$n_a \;=\; \int f_a(\boldsymbol{r}, \boldsymbol{V}, t)\; d^3V \;, \tag{2.4}$$

the fluid velocity $\boldsymbol{v}_a$ (first moment) by

$$n_a \boldsymbol{v}_a \;=\; \int \boldsymbol{V}\, f_a(\boldsymbol{r}, \boldsymbol{V}, t)\; d^3V \;, \tag{2.5}$$

and the temperature T_a (second moment) by

$$3 n_a T_a \;=\; m_a \int (\boldsymbol{V} - \boldsymbol{v}_a)^2\, f_a(\boldsymbol{r}, \boldsymbol{V}, t)\; d^3V \;. \tag{2.6}$$

The integrals are carried out over the whole velocity space. By defining the random velocity $\boldsymbol{V}_{ar}$,

$$\boldsymbol{V}_{ar} \;\equiv\; \boldsymbol{V} \;-\; \boldsymbol{v}_a \;, \tag{2.7}$$

the particle velocity $\boldsymbol{V}$ can be understood as sum of the fluid velocity $\boldsymbol{v}_a$ and the random velocity $\boldsymbol{V}_{ar}$. Therefore, the temperature T_a measures the energy contained in the random motion of the particles.

The balance equations for n_a, $\boldsymbol{v}_a$, and T_a are obtained by integrating the Boltzmann equation (2.3) over the particle velocity space with weighting factors m_a, $m_a\boldsymbol{V}$, and $m_a V^2/2$, respectively. Note that the coordinates $\boldsymbol{r}$, $\boldsymbol{V}$, and t are independent of each other so that $\partial r_i / \partial V_j = 0 \;\forall\; i, j$, and $\partial V_i / \partial V_j = \delta_{ij}$, δ_{ij} being the Kronecker Delta. It is additionally assumed that f_a vanishes at the boundaries of the integration domain ($V = -\infty$ and $V = +\infty$). The **particle balance** reads:

$$\frac{\partial n_a}{\partial t} \;+\; \boldsymbol{\nabla} \cdot \Big(n_a \boldsymbol{v}_a \Big) \;=\; \int C_a\; d^3V \;. \tag{2.8}$$

The **momentum balance** is given by

$$\begin{aligned} \frac{\partial}{\partial t}\Big(m_a n_a \boldsymbol{v}_{\boldsymbol{a}} \Big) \;+\; \boldsymbol{\nabla} \cdot \Big(m_a n_a \Big\langle \boldsymbol{V}\boldsymbol{V} \Big\rangle_V \Big) & \\ -\; \int \boldsymbol{V} \Big(\boldsymbol{F}_a \cdot \boldsymbol{\nabla}_V f \Big)\; d\boldsymbol{V} \;&=\; m_a \int \boldsymbol{V} C_a\; d^3V \;, \end{aligned} \tag{2.9}$$

where the averaging operator $\langle ... \rangle_V$ with respect to the particle velocity,

$$\Big\langle ... \Big\rangle_V \;\equiv\; \frac{1}{n_a} \int ...\; f_a(\boldsymbol{r}, \boldsymbol{V}, t)\; d^3V \;, \tag{2.10}$$

has been introduced. The product $\boldsymbol{V}\boldsymbol{V}$ is the dyadic product which is given for two arbitrary vectors $\boldsymbol{a}$ and $\boldsymbol{b}$ by

$$\boldsymbol{a}\boldsymbol{b} \;=\; a_i b_j \boldsymbol{e}^i \boldsymbol{e}^j \;=\; a^i b^j \boldsymbol{e}_i \boldsymbol{e}_j \;, \tag{2.11}$$

where $\boldsymbol{e}^i$ and $\boldsymbol{e}_i$ are the contravariant and covariant basis vectors, and a^i, a_i, b^i, and b_i are the respective components of the vectors $\boldsymbol{a}$ and $\boldsymbol{b}$ [39]. The evolution of the temperature T_a is determined by the **energy balance**:

$$\frac{\partial}{\partial t}\left(\frac{3}{2}n_a T_a + \frac{1}{2}m_a n_a \boldsymbol{v}_a^2\right) \;+\; \boldsymbol{\nabla}\cdot\left(\frac{m_a n_a}{2}\left\langle \boldsymbol{V} V^2\right\rangle_V\right)$$

$$-\;\frac{1}{2}\int V^2\Big(\boldsymbol{F}_a\cdot\boldsymbol{\nabla}_V f_a\Big)\,d^3V \;=\; \frac{m_a}{2}\int V^2 C_a\,d^3V\,. \tag{2.12}$$

Eqs. (2.8), (2.9) and (2.12) determine the dynamics of the fluid considered. Note that knowledge of f_a is still needed for calculating the terms $\langle \boldsymbol{V}\boldsymbol{V}\rangle_V$ and $\langle \boldsymbol{V}V^2\rangle_V$ in eqs. (2.9) and (2.12). This so-called closure problem can be solved by setting these higher order moments in relation with gradients of the lower order moments n_a, $\boldsymbol{v}_a$, and T_a, as it is outlined in paragraph 3.2. To simplify the notation, the quantities scalar pressure p_a, viscosity tensor $\boldsymbol{\Pi}_a$ and heat flux density $\boldsymbol{q}_a$ are introduced:

$$p_a \;\equiv\; \frac{m_a n_a}{3}\left\langle V_{ar}^2\right\rangle_V \;=\; n_a T_a\;, \tag{2.13}$$

$$\boldsymbol{\Pi}_a \;\equiv\; m_a n_a\left[\left\langle \boldsymbol{V}_{ar}\boldsymbol{V}_{ar}\right\rangle_V \;-\; \frac{1}{3}\left\langle V_{ar}^2\right\rangle_V \mathbf{I}\right]\;, \tag{2.14}$$

$$\boldsymbol{q}_a \;\equiv\; \frac{m_a n_a}{2}\left\langle \boldsymbol{V}_{ar} V_{ar}^2\right\rangle_V\;. \tag{2.15}$$

$\mathbf{I}$ is the unit tensor. The pressure tensor $\mathbf{P}_a$ is given by

$$\mathbf{P}_a \;\equiv\; p_a\mathbf{I} \;+\; \boldsymbol{\Pi}_a\;. \tag{2.16}$$

The higher order moments $\langle \boldsymbol{V}\boldsymbol{V}\rangle_V$ and $\langle \boldsymbol{V}V^2\rangle_V$ can now be written as

$$m_a n_a\left\langle \boldsymbol{V}\boldsymbol{V}\right\rangle_V \;=\; \mathbf{P}_a \;+\; m_a n_a \boldsymbol{v}_a\boldsymbol{v}_a\;, \tag{2.17}$$

$$\frac{m_a n_a}{2}\left\langle \boldsymbol{V}V^2\right\rangle_V \;=\; \boldsymbol{q}_a \;+\; \boldsymbol{v}_a\cdot\boldsymbol{\Pi}_a \;+\; \frac{5}{2}n_a T_a\boldsymbol{v}_a \;+\; \frac{m_a n_a}{2}v_a^2\boldsymbol{v}_a\;. \tag{2.18}$$

The source terms due to the forces $\boldsymbol{F}_a$ are defined as

$$\boldsymbol{S}_{amV}^F \;\equiv\; \int \boldsymbol{V}\Big(\boldsymbol{F}_a\cdot\boldsymbol{\nabla}_V f\Big)\,d^3V\;, \qquad S_{aE}^F \;\equiv\; \frac{1}{2}\int V^2\Big(\boldsymbol{F}_a\cdot\boldsymbol{\nabla}_V f_a\Big)\,d^3V\;. \tag{2.19}$$

The collision term C_a can be split into a part C_a^{ec}, including all processes due to elastic collisions of particles of the species a with particles of the same species, and a part C_a^{ic}, including all processes due to elastic collisions of particles of species a with particles of different species and due to inelastic collisions:

$$C_a \;=\; C_a^{ec} \;+\; C_a^{ic}\;. \tag{2.20}$$

One can define the source terms

$$\begin{aligned} & & S^{ic}_{an} &\equiv \int C^{ic}_a \; d^3V \; , && \qquad (2.21) \\ \boldsymbol{S}^{ec}_{amV} &\equiv m_a \int \boldsymbol{V} \, C^{ec}_a \; d^3V \; , & \boldsymbol{S}^{ic}_{amV} &\equiv m_a \int \boldsymbol{V} \, C^{ic}_a \; d^3V \; , && \qquad (2.22) \\ S^{ec}_{aE} &\equiv \frac{m_a}{2} \int V^2 C^{ec}_a \; d^3V \; , & S^{ic}_{aE} &\equiv \frac{m_a}{2} \int V^2 C^{ic}_a \; d^3V \; . && \qquad (2.23) \end{aligned}$$

With definitions (2.17) to (2.19b) and (2.21) to (2.23b), the evolution equations for n_a, $\boldsymbol{v}_a$, and T_a, eqs. (2.8), (2.9) and (2.12), can be rewritten in compact form. The **particle balance** reads

$$\boxed{\frac{\partial n_a}{\partial t} \; + \; \boldsymbol{\nabla} \cdot \Big(n_a \boldsymbol{v}_a \Big) \; = \; S^{ic}_{an} \; , \qquad (2.24)}$$

the **momentum balance** is given by

$$\boxed{\frac{\partial}{\partial t} \Big(m_a n_a \boldsymbol{v}_{\boldsymbol{a}} \Big) \; + \; \boldsymbol{\nabla} \cdot \Big(m_a n_a \boldsymbol{v}_a \boldsymbol{v}_a + \mathbf{P}_a \Big) \; = \; \boldsymbol{S}^F_{amV} \; + \; \boldsymbol{S}^{ec}_{amV} \; + \; \boldsymbol{S}^{ic}_{amV} \; , \quad (2.25)}$$

and for the **energy balance** one has

$$\boxed{\begin{aligned} \frac{\partial}{\partial t} \left(\frac{3}{2} n_a T_a + \frac{1}{2} m_a n_a v_a^2 \right) \; + \; \boldsymbol{\nabla} \cdot \left(\frac{5}{2} n_a T_a \boldsymbol{v}_a + \frac{1}{2} m_a n_a v_a^2 \boldsymbol{v}_a + \boldsymbol{q}_a + \boldsymbol{v}_a \cdot \boldsymbol{\Pi}_a \right) \\ = \; S^F_{aE} \; + \; S^{ec}_{aE} \; + \; S^{ic}_{aE} \; . \qquad (2.26) \end{aligned}}$$

Eqs. (2.24) to (2.26) are the evolution equations for n_a, $\boldsymbol{v}_a$, and T_a in conservative form. Their non-conservative form can be obtained by using the particle balance (2.24) in the momentum balance (2.25) and the particle and momentum balances (2.24) and (2.25) in the energy balance (2.26). For the particle balance this yields

$$\boxed{\frac{dn_a}{dt} \; = \; S^{ic}_{an} \; - \; n_a \boldsymbol{\nabla} \cdot \boldsymbol{v}_a \; , \qquad (2.27)}$$

for the momentum balance one has

$$\boxed{m_a n_a \frac{d\boldsymbol{v}_a}{dt} \;=\; \boldsymbol{S}^F_{amV} \;+\; \boldsymbol{S}^{ec}_{amV} \;+\; \boldsymbol{S}^{ic}_{amV} \;-\; m_a \boldsymbol{v}_a S^{ic}_{an} \;-\; \boldsymbol{\nabla}\cdot\mathbf{P}_a \;, \qquad (2.28)}$$

and for the energy balance

$$\boxed{\begin{aligned} \frac{3}{2} n_a \frac{dT_a}{dt} \;=\;& S^F_{aE} \;+\; S^{ec}_{aE} \;+\; S^{ic}_{aE} \;-\; \boldsymbol{v}_a \cdot \left(\boldsymbol{S}^F_{amV} + \boldsymbol{S}^{ec}_{amV} + \boldsymbol{S}^{ic}_{amV}\right) \\ &+\; \left(\frac{m_a v_a^2}{2} - \frac{3}{2} T_a\right) S^{ic}_{an} - p_a \boldsymbol{\nabla}\cdot\boldsymbol{v}_a - \boldsymbol{\Pi}_a : \boldsymbol{\nabla}\boldsymbol{v}_a - \boldsymbol{\nabla}\cdot\boldsymbol{q}_a \;. \qquad (2.29) \end{aligned}}$$

The total time derivative is to be understood as the so-called advective or convective derivative [2]:

$$\frac{d}{dt} \;\equiv\; \frac{\partial}{\partial t} \;+\; \boldsymbol{v}\cdot\boldsymbol{\nabla} \;. \tag{2.30}$$

The double dot product $\mathbf{A} : \mathbf{B}$ appearing in the energy balance (2.29) for two arbitrary tensors $\mathbf{A}$ and $\mathbf{B}$ is defined as

$$\mathbf{A} : \mathbf{B} \;\equiv\; A^{ij} B_{ij} \;=\; A_{ij} B^{ij} \;=\; A^j_i B^i_j \;, \tag{2.31}$$

where Einstein's summation convention is used.

Eqs. (2.24) to (2.26) or eqs. (2.27) to (2.28) constitute a generic model for a fluid. Which form of the equations is preferred (conservative or non-conservative) can depend, for instance, on the method employed for solving them numerically. Finding expressions for the viscosity tensor $\boldsymbol{\Pi}_a$, the heat flux density $\boldsymbol{q}_a$, and the source terms S_a is required for the closure of the system of equations and further specifies the physical system under consideration. An example for a collisional, magnetized plasma, the Braginskii closure [27], is presented in paragraph 3.2.

2.2. Generic multiscale model equations

With the fluid balances at hand, one might question the necessity to derive a multiscale model since a comprehensive description of the system of interest is already available. To motivate the use of a multiscale model, it is helpful to consider a computer code which solves eqs. (2.24) to (2.26) numerically, since analytical solutions for n_a, $\boldsymbol{v}_a$, and T_a are available only for selected cases. Fast processes on small spatial scales (the mesoscale) typically will require time steps so small and a spatial grid so fine that simulations to capture also the macroscale evolution are very costly regarding the computational resources. In contrast, the use of a multiscale model enables one to analyze the macroscale evolution with reasonable computational times while still taking into account effects of the mesoscale dynamics. Like it was stated in the introduction of this thesis, multiscale models play an important role in many fields of science, see for instance [1, 2, 23, 24, 37, 40, 41] for examples from the fields of solid matter physics, atomic physics, fluid turbulence, and plasma physics. The generic multiscale model for a fluid derived below serves as the theoretical basis for the specific multiscale model for the plasma edge which is then outlined in chapter 5. In paragraph 2.2.1, the assumption of a scale separation and the method of a Reynolds decomposition is presented. The multiscale equations for the density, momentum and energy are derived in paragraphs 2.2.2 to 2.2.4, followed by a discussion of the generic multiscale model in paragraph 2.2.5.

2.2.1. Scale separation assumption and Reynolds decomposition

As stated in the introduction of this chapter, in the multiscale model the fluid quantities α are split into a macroscale part α_0 and a mesoscale part $\widetilde{\alpha}$. This procedure is analogous to the so-called Reynolds decomposition where the fluid quantities α are decomposed into their mean and their fluctuating part [2]. The averaging operator $\langle ... \rangle$ is

$$\langle \alpha \rangle (\boldsymbol{r}, t) \;\equiv\; \frac{1}{\delta t_{\mathrm{av}}} \frac{1}{\delta V_{\mathrm{av}}} \int\limits_{t-\delta t_{\mathrm{av}}}^{t} \int\limits_{\delta V_{\mathrm{av}}(\boldsymbol{r})} \alpha(\boldsymbol{r}', t')\; d^3r'\, dt' \;. \tag{2.32}$$

The time interval for averaging is given by δt_{av}. The integration limit $\delta V_{\mathrm{av}}(\boldsymbol{r})$ expresses that the spatial average is taken over a volume δV_{av} around the point $\boldsymbol{r}$. One can now define the macroscale and mesoscale part of α by

$$\alpha_0 \;\equiv\; \langle \alpha \rangle \,, \tag{2.33}$$

$$\widetilde{\alpha} \;\equiv\; \alpha - \langle \alpha \rangle \,, \tag{2.34}$$

so that any fluid quantity can be written as

$$\alpha \;=\; \alpha_0 \;+\; \widetilde{\alpha} \;. \tag{2.35}$$

The decisive point which gives this decomposition a deeper purpose is the assumption of a scale separation: the characteristic dynamics of α_0 and $\widetilde{\alpha}$ are assumed to take place on disparate temporal and spatial scales. This should be further specified here. For this purpose, the characteristic time $\tau_{\mathrm{D}}(\alpha)$ and length $\lambda_{\mathrm{D}}(\alpha)$ of the dynamics of a quantity α are introduced. There are different ways to determine $\tau_{\mathrm{D}}(\alpha)$ and length $\lambda_{\mathrm{D}}(\alpha)$. One possibility is to use the limit parameters d_x and d_t which denote a $100 \cdot d_x$, $100 \cdot d_t$ percentage change of α. With $\langle ... \rangle_{\mathrm{ev}}$ being the average over the simulation domain and evolution time for which $\lambda_{\mathrm{D}}(\alpha)$ and $\tau_{\mathrm{D}}(\alpha)$ should be valid, they can be defined by

$$\lambda_{\mathrm{D}}(\alpha) \;\equiv\; \Big\langle \min(\Delta r) \Big\rangle_{\mathrm{ev}} \qquad \text{with} \qquad \frac{|\alpha(r+\Delta r, t) - \alpha(r,t)|}{\max\Big\{|\alpha(r,t)|, \alpha_{\mathrm{R}}\Big\}} \;=\; d_x \;, \tag{2.36}$$

$$\tau_{\mathrm{D}}(\alpha) \;\equiv\; \Big\langle \min(\Delta t) \Big\rangle_{\mathrm{ev}} \qquad \text{with} \qquad \frac{|\alpha(r, t+\Delta t) - \alpha(r,t)|}{\max\Big\{|\alpha(r,t)|, \alpha_{\mathrm{R}}\Big\}} \;=\; d_t \;. \tag{2.37}$$

Here, only one spatial coordinate r is considered, but the estimate of $\lambda_{\mathrm{D}}(\alpha)$ can easily be generalized to the three-dimensional case. The max functions in eqs. (2.36) and (2.37), employing a reference value α_{R} characteristic for the evolution of α (e.g. $\alpha_{\mathrm{R}} = \langle \alpha \rangle_{\mathrm{ev}}$), are used to prevent division by zero[2]. The scale separation can now be expressed by

$$\lambda_{\mathrm{D}}(\tilde{\alpha}) \;\ll\; \lambda_{\mathrm{D}}(\alpha_0) \;, \qquad \tau_{\mathrm{D}}(\tilde{\alpha}) \;\ll\; \tau_{\mathrm{D}}(\alpha_0) \;. \tag{2.38}$$

With these relations, the averaging intervals δr_{av} and δt_{av} can be estimated by

$$\lambda_{\mathrm{D}}(\tilde{\alpha}) \;\ll\; \delta r_{\mathrm{av}} \;\ll \lambda_{\mathrm{D}}(\alpha_0) \;, \qquad \tau_{\mathrm{D}}(\tilde{\alpha}) \;\ll\; \delta t_{\mathrm{av}} \;\ll \tau_{\mathrm{D}}(\alpha_0) \;. \tag{2.39}$$

The choice of δr_{av} and δt_{av} is a very important point for setting up the multiscale model: if δr_{av} and δt_{av} are chosen too large, the characteristic dynamics of the macroscale are averaged out and therefore lost. On the other hand, if the intervals are chosen too small, the characteristic scales of α_0 and $\tilde{\alpha}$ might coincide and one can no longer speak of a scale separation. As explained in the next paragraph 2.2.2, this leads to a problem of causality regarding the coupled macroscale and mesoscale systems. A scale separation also means that the profile of $\alpha_0(r,t)$ can be sufficiently well approximated by a Taylor expansion up to first order on temporal and spatial scales on the order of δt_{av} and δr_{av}. This leads to the conclusion that $\langle \alpha_0 \rangle = \alpha_0$ and that $\langle \tilde{\alpha} \rangle = 0$ which is crucial for the derivation of the multiscale equations. The justification is as follows: focusing on the time dependency of α_0, a Taylor expansion of α_0 around the time t_0 is considered:

$$\alpha_0(t_0 + \Delta t) \;=\; \alpha_0(t_0) \;+\; \frac{\partial \alpha_0}{\partial t}\bigg|_{t_0} \Delta t \;+\; \frac{1}{2}\frac{\partial^2 \alpha_0}{\partial t^2}\bigg|_{t_0} (\Delta t)^2 \;+\; \mathcal{O}\Big[(\Delta t)^3\Big] \;. \tag{2.40}$$

---

[2] In some cases, the correlation length $\lambda_c(\alpha)$ and time $\tau_c(\alpha)$ (see [42] for the definition of correlation quantities of times series) might be good estimates for the characteristic scales of the dynamics of α. However, for an approximately linear decay, $\lambda_c(\alpha)$ and time $\tau_c(\alpha)$ can be significantly larger than $\lambda_{\mathrm{D}}(\alpha)$ and $\tau_{\mathrm{D}}(\alpha)$ and it is then more useful to employ a definition as given by eqs. (2.36) and (2.37) for an estimate of $\lambda_{\mathrm{D}}(\alpha)$ and $\tau_{\mathrm{D}}(\alpha)$.

It is now assumed that Δt is of the order of δt_{av}. The characteristic evolution time of α_0 is $\tau_{\mathrm{D}}(\alpha_0)$ so that $\partial\alpha_0/\partial t$ is of the order $\alpha_0/\tau_{\mathrm{D}}(\alpha_0)$ and $\partial^2\alpha_0/\partial t^2$ is of the order $\alpha_0/[\tau_{\mathrm{D}}(\alpha_0)]^2$. Thus

$$\left.\frac{\partial\alpha_0}{\partial t}\right|_{t_0}\Delta t \;\sim\; \alpha_0\varepsilon \;, \quad \left.\frac{\partial^2\alpha_0}{\partial t^2}\right|_{t_0}(\Delta t)^2 \;\sim\; \alpha_0\varepsilon^2 \;, \quad \varepsilon \;=\; \frac{\delta t_{\mathrm{av}}}{\tau_{\mathrm{D}}(\alpha_0)} \;. \tag{2.41}$$

Since the scale hierarchy according to eq. (2.39b) holds, ε can be considered as a small parameter, $\varepsilon \ll 1$. This justifies truncation of the expansion (2.40) after the first order term in ε. By then applying the averaging operator $\langle ... \rangle$ to $\alpha_0(t_0 + \Delta t)$ one gets:

$$\begin{aligned}\Big\langle \alpha_0(t_0+\Delta t)\Big\rangle \;&=\; \Big\langle \alpha_0(t_0)\Big\rangle \;+\; \left\langle \left.\frac{\partial\alpha_0}{\partial t}\right|_{t_0}\Delta t\right\rangle \\ &=\; \alpha_0(t_0) \;+\; \left.\frac{\partial\alpha_0}{\partial t}\right|_{t_0}\Delta t \;=\; \alpha_0(t_0+\Delta t) \;. \end{aligned} \tag{2.42}$$

Generalizing eq. (2.42) means that for $\Delta t \lesssim \delta t_{\mathrm{av}}$ one has $\langle\alpha_0(t)\rangle = \alpha_0(t)$. The same reasoning can be applied regarding the spatial dimensions and the averaging interval δr_{av}. Therefore

$$\langle\alpha_0\rangle \;\approx\; \alpha_0 \qquad \text{and} \qquad \langle\tilde{\alpha}\rangle \;\approx\; 0 \;. \tag{2.43}$$

For some systems also the amplitudes of the macroscale and mesoscale part are characterized by a scale separation, where it can then be assumed that $|\tilde{\alpha}| \ll |\alpha_0|$. Even though this relation of magnitudes will play an important role for the drift fluid model presented in chapter 4, it is not important for the generic multiscale model.

2.2.2. Particle balance

The derivation of the macroscale and mesoscale particle balances starts with the particle balance given by eq. (2.27):

$$\frac{dn}{dt} \;=\; S_n^{ic} \;-\; n\boldsymbol{\nabla}\cdot\boldsymbol{v} \;. \tag{2.44}$$

The subscripts a to denote the particle species are omitted in the following derivations for clarity. The density n and velocity $\boldsymbol{v}$ are split into their macroscale and mesoscale part:

$$n \;=\; n_0 \;+\; \tilde{n} \;, \qquad \boldsymbol{v} \;=\; \boldsymbol{v}_0 \;+\; \tilde{\boldsymbol{v}} \;. \tag{2.45}$$

Eq. (2.44) can then be transformed into

$$\begin{aligned}\frac{\partial n_0}{\partial t} + \frac{\partial \tilde{n}}{\partial t} + \boldsymbol{v}_0 \cdot \boldsymbol{\nabla} n_0 + \tilde{\boldsymbol{v}} \cdot \boldsymbol{\nabla} n_0 + \boldsymbol{v}_0 \cdot \boldsymbol{\nabla} \tilde{n} + \tilde{\boldsymbol{v}} \cdot \boldsymbol{\nabla} \tilde{n} \\ = S_n^{ic} - n_0 \boldsymbol{\nabla} \cdot \boldsymbol{v}_0 - \tilde{n} \boldsymbol{\nabla} \cdot \boldsymbol{v}_0 - n_0 \boldsymbol{\nabla} \cdot \tilde{\boldsymbol{v}} - \tilde{n} \boldsymbol{\nabla} \cdot \tilde{\boldsymbol{v}} \; . \end{aligned} \tag{2.46}$$

Now the averaging operator $\langle ... \rangle$ given by eq. (2.32) is applied to eq. (2.46) to obtain the macroscale particle balance. All terms which are first order in the mesoscale quantities become zero due to eq. (2.43). The evaluation of $\langle \partial \tilde{n} / \partial t \rangle$ yields:

$$\left\langle \frac{\partial \tilde{n}}{\partial t} \right\rangle = 0 \; . \tag{2.47}$$

This result, which is true for the time derivative of any mesoscale variable, is explained in detail in paragraph 2.3.2. The **macroscale particle balance** is given by

$$\boxed{\frac{\partial n_0}{\partial t} + \boldsymbol{v}_0 \cdot \boldsymbol{\nabla} n_0 = - n_0 \boldsymbol{\nabla} \cdot \boldsymbol{v}_0 + \left\langle S_n^{ic} \right\rangle - \left\langle \boldsymbol{\nabla} \cdot (\tilde{n} \tilde{\boldsymbol{v}}) \right\rangle \; .} \tag{2.48}$$

The evolution equation for the mesoscale density $\tilde{n}$ is obtained by taking the full particle balance (2.46) ('full' in the sense that it describes the evolution of n and therefore both n_0 and $\tilde{n}$) and subtracting the macroscale equation (2.48). This yields the **mesoscale particle balance**:

$$\boxed{\begin{aligned}\frac{\partial \tilde{n}}{\partial t} + \Big(\boldsymbol{v}_0 + \tilde{\boldsymbol{v}}\Big) \cdot \boldsymbol{\nabla} \tilde{n} + \tilde{\boldsymbol{v}} \cdot \boldsymbol{\nabla} n_0 \\ = - \tilde{n} \boldsymbol{\nabla} \cdot \Big(\boldsymbol{v}_0 + \tilde{\boldsymbol{v}}\Big) - n_0 \boldsymbol{\nabla} \cdot \tilde{\boldsymbol{v}} + S_n^{ic} - \left\langle S_n^{ic} \right\rangle + \left\langle \boldsymbol{\nabla} \cdot (\tilde{n} \tilde{\boldsymbol{v}}) \right\rangle \; .\end{aligned}} \tag{2.49}$$

Alternatively, the multiscale balances can also be written in conservative form which is presented here for the macroscale balances only, being used for the derivation of the large scale model in chapter 3. For the macroscale particle balance it yields

$$\frac{\partial n_0}{\partial t} + \boldsymbol{\nabla} \cdot \Big(n_0 \boldsymbol{v}_0\Big) = \left\langle S_n^{ic} \right\rangle - \left\langle \boldsymbol{\nabla} \cdot (\tilde{n} \tilde{\boldsymbol{v}}) \right\rangle \; . \tag{2.50}$$

The coupled macroscale and mesoscale particle balances (2.48) and (2.49) are now used to discuss causality in the context of the multiscale system. For this purpose, it is helpful to depart from the viewpoint where n_0 and $\tilde{n}$ can both be obtained from the profile of n and consider the macroscale and mesoscale balances, eqs. (2.48) and (2.49), as descriptions of two different systems which interact with each other. The evolution

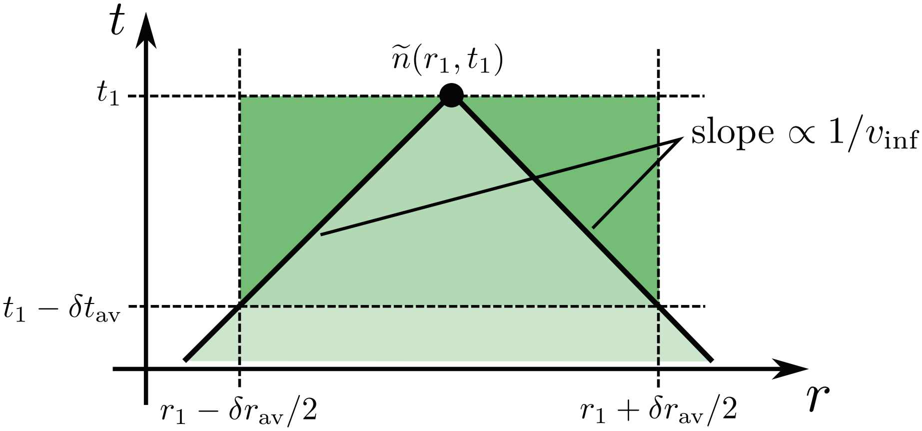

Figure 2.1.: Determining the averaged term $\langle \boldsymbol{\nabla} \cdot (\widetilde{n}\widetilde{\boldsymbol{v}}) \rangle$ for the the calculation of $\widetilde{n}(r_1, t_1)$. The dotted lines denote the limits of the averaging intervals for the operator $\langle ... \rangle$, the typical velocity of the transport of information in the system is given by v_{inf}.

of the mesoscale density $\widetilde{n}$ depends also on the term $\langle \boldsymbol{\nabla} \cdot (\widetilde{n}\widetilde{\boldsymbol{v}}) \rangle$, where the averaging area in time and space for $\widetilde{n}(r_1, t_1)$ for a one-dimensional case is limited by the dotted lines in fig. 2.1. This means that $\widetilde{n}(r_1, t_1)$ is also a function of $\widetilde{n}(t_1, r_1 - \delta r_{\text{av}}/2)$ and $\widetilde{n}(t_1, r_1 + \delta r_{\text{av}}/2)$ which are included in the average $\langle \boldsymbol{\nabla} \cdot (\widetilde{n}\widetilde{\boldsymbol{v}}) \rangle$. If information within the system is transported with a finite velocity v_{inf}, this dependency is unphysical: a quantity cannot depend on something of which it does not 'know'. The data points which actually could influence $\widetilde{n}(r_1, t_1)$ are within the light green triangle, limited by the continuous black lines whose inclination is given by $1/v_{\text{inf}}$.
However, including the dark green areas in the average for the determination of $\widetilde{n}(r_1, t_1)$ does not lead to spurious results due to the assumption of a scale separation, see eq. (2.38): as expressed by eqs. (2.39a) and (2.39b), the macroscale density n_0 varies little on lengths and times on the order of δr_{av} and δt_{av}, respectively, since they are below the typical lengths and times of the macroscale dynamics, $\lambda_{\text{D}}(n_0)$ and $\tau_{\text{D}}(n_0)$. If the source term $\langle S_n^{ic} \rangle$ also varies slowly on lengths δr_{av} and times δt_{av} (which is assumed here), this applies equally to the averaged mesoscale terms like $\langle \boldsymbol{\nabla} \cdot (\widetilde{n}\widetilde{\boldsymbol{v}}) \rangle$. Therefore it holds:

$$\Big\langle \boldsymbol{\nabla} \cdot (\widetilde{n}\widetilde{\boldsymbol{v}}) \Big\rangle (r_a, t_a) \;\approx\; \Big\langle \boldsymbol{\nabla} \cdot (\widetilde{n}\widetilde{\boldsymbol{v}}) \Big\rangle (r_b, t_b) \tag{2.51}$$

with

$$|r_a - r_b| \;\leq\; \delta r_{\text{av}} \;, \qquad |t_a - t_b| \;\leq\; \delta t_{\text{av}} \;. \tag{2.52}$$

Otherwise, if $\langle \boldsymbol{\nabla} \cdot (\widetilde{n}\widetilde{\boldsymbol{v}}) \rangle$ varied significantly on the mesoscale, this would have a similar effect on n_0 and there would no longer be a scale separation. Eq. (2.51) expresses that the relevant statistics of points in the domain limited by the dotted lines are similar. Because of this similarity including points outside of the light green triangle in the average $\langle \boldsymbol{\nabla} \cdot (\widetilde{n}\widetilde{\boldsymbol{v}}) \rangle$ does not lead to a false evolution of $\widetilde{n}(r_1, t_1)$.

2.2.3. Momentum balance

The derivation of the macroscale and mesoscale momentum balances is done analogously to the derivation of the particle balances. Starting point is the momentum balance (2.28). By defining the momentum density source $\boldsymbol{M}$,

$$\boldsymbol{M} \;\equiv\; \boldsymbol{S}^{F}_{mV} \;+\; \boldsymbol{S}^{ec}_{mV} \;+\; \boldsymbol{S}^{ic}_{mV} \;-\; m\boldsymbol{v}S^{ic}_{n} \;-\; \boldsymbol{\nabla}\cdot\mathbf{P}\;, \tag{2.53}$$

the momentum balance can be written as

$$\frac{\partial \boldsymbol{v}}{\partial t} \;+\; \boldsymbol{v}\cdot\boldsymbol{\nabla}\boldsymbol{v} \;=\; \frac{\boldsymbol{M}}{mn}\;. \tag{2.54}$$

By decomposing the velocity into its macroscale and mesoscale part and applying the averaging operator one obtains the **macroscale momentum balance:**

$$\boxed{\frac{\partial \boldsymbol{v}_0}{\partial t} \;+\; \boldsymbol{v}_0\cdot\boldsymbol{\nabla}\boldsymbol{v}_0 \;=\; \left\langle \frac{\boldsymbol{M}}{mn}\right\rangle \;-\; \left\langle \widetilde{\boldsymbol{v}}\cdot\boldsymbol{\nabla}\widetilde{\boldsymbol{v}}\right\rangle\;. \qquad (2.55)}$$

The **mesoscale momentum balance** is obtained by subtracting the macroscale balance from the full equation (2.28):

$$\boxed{\frac{\partial \widetilde{\boldsymbol{v}}}{\partial t} \;+\; \left(\boldsymbol{v}_0+\widetilde{\boldsymbol{v}}\right)\cdot\boldsymbol{\nabla}\widetilde{\boldsymbol{v}} \;+\; \widetilde{\boldsymbol{v}}\cdot\boldsymbol{\nabla}\boldsymbol{v}_0 \;=\; \frac{\boldsymbol{M}}{mn} \;-\; \left\langle \frac{\boldsymbol{M}}{mn}\right\rangle \;+\; \left\langle \widetilde{\boldsymbol{v}}\cdot\boldsymbol{\nabla}\widetilde{\boldsymbol{v}}\right\rangle\;. \qquad (2.56)}$$

The equivalent conservative form of the macroscale momentum balance is given by

$$\begin{aligned}\frac{\partial}{\partial t}\Big(mn_0\boldsymbol{v}_0\Big) \;+\; \boldsymbol{\nabla}\cdot\Big(mn_0\boldsymbol{v}_0\boldsymbol{v}_0\Big) \;=\; n_0\left\langle\frac{\boldsymbol{M}}{n}\right\rangle \;-\; mn_0\left\langle \widetilde{\boldsymbol{v}}\cdot\boldsymbol{\nabla}\widetilde{\boldsymbol{v}}\right\rangle& \\ +\; m\boldsymbol{v}_0\left\langle S^{ic}_{n}\right\rangle \;-\; m\boldsymbol{v}_0\left\langle \boldsymbol{\nabla}\cdot(\widetilde{n}\widetilde{\boldsymbol{v}})\right\rangle\;,&\end{aligned} \tag{2.57}$$

which is obtained by using the macroscale particle balance (2.48) for transformation of the macroscale momentum balance (2.55).

2.2.4. Energy balance

With the definition of the energy density source W,

$$\begin{aligned} W \;\equiv\; & S_E^F \;+\; S_E^{ec} \;+\; S_E^{ic} \;-\; \boldsymbol{v}\cdot\Big(\boldsymbol{S}_{mV}^F + \boldsymbol{S}_{mV}^{ec} + \boldsymbol{S}_{mV}^{ic}\Big) \\ & + \;\left(\frac{mv^2}{2} - \frac{3}{2}T\right) S_n^{ic} \;-\; p\boldsymbol{\nabla}\cdot\boldsymbol{v} \;-\; \boldsymbol{\Pi} : \boldsymbol{\nabla}\boldsymbol{v} \;-\; \boldsymbol{\nabla}\cdot\boldsymbol{q}\;, \end{aligned} \tag{2.58}$$

the energy balance (2.29) can be rewritten as

$$\frac{3}{2}\left(\frac{\partial T}{\partial t} + \boldsymbol{v}\cdot\boldsymbol{\nabla}T\right) \;=\; \frac{W}{n}\;. \tag{2.59}$$

Splitting velocity and temperature into their macroscale and mesoscale parts and applying the averaging operator yields the **macroscale energy balance:**

$$\frac{3}{2}\left(\frac{\partial T_0}{\partial t} + \boldsymbol{v}_0\cdot\boldsymbol{\nabla}T_0\right) \;=\; \left\langle\frac{W}{n}\right\rangle \;-\; \frac{3}{2}\Big\langle\tilde{\boldsymbol{v}}\cdot\boldsymbol{\nabla}\widetilde{T}\Big\rangle\;. \tag{2.60}$$

The **mesoscale energy balance** is obtained in the same way as the mesoscale balances for particles and momentum and is given by

$$\frac{3}{2}\left[\frac{\partial\widetilde{T}}{\partial t} + \Big(\boldsymbol{v}_0 + \tilde{\boldsymbol{v}}\Big)\cdot\boldsymbol{\nabla}\widetilde{T} + \tilde{\boldsymbol{v}}\cdot\boldsymbol{\nabla}T_0\right] \;=\; \frac{W}{n} \;-\; \left\langle\frac{W}{n}\right\rangle \;+\; \frac{3}{2}\Big\langle\tilde{\boldsymbol{v}}\cdot\boldsymbol{\nabla}\widetilde{T}\Big\rangle\;. \tag{2.61}$$

For the conservative form of the macroscale energy balance one has:

$$\begin{aligned} & \frac{\partial}{\partial t}\left(\frac{3}{2}n_0T_0 + \frac{1}{2}mn_0v_0^2\right) \;+\; \boldsymbol{\nabla}\cdot\left(\frac{3}{2}n_0T_0\boldsymbol{v}_0 + \frac{1}{2}mn_0v_0^2\boldsymbol{v}_0\right) \\ & \quad = \; n_0\left\langle\frac{W}{n}\right\rangle \;+\; n_0\boldsymbol{v}_0\left\langle\frac{\boldsymbol{M}}{n}\right\rangle \;-\; \frac{3}{2}n_0\Big\langle\tilde{\boldsymbol{v}}\cdot\boldsymbol{\nabla}\widetilde{T}\Big\rangle \;-\; mn_0\boldsymbol{v}_0\cdot\Big\langle\tilde{\boldsymbol{v}}\cdot\boldsymbol{\nabla}\tilde{\boldsymbol{v}}\Big\rangle \\ & \quad + \;\left(\frac{3}{2}T_0 + \frac{1}{2}mv_0^2\right)\Big\langle S_n^{ic}\Big\rangle \;-\; \left(\frac{3}{2}T_0 + \frac{1}{2}mv_0^2\right)\Big\langle\boldsymbol{\nabla}\cdot(\tilde{n}\tilde{\boldsymbol{v}})\Big\rangle\;. \end{aligned} \tag{2.62}$$

For the transition from eq. (2.60) to eq. (2.62) the macroscale particle and momentum balances (2.48) and (2.55) were used. It holds:

$$\frac{1}{2}mn\frac{\partial v^2}{\partial t} \;=\; mn\boldsymbol{v}\cdot\frac{\partial\boldsymbol{v}}{\partial t}\;, \qquad \frac{1}{2}mn\boldsymbol{v}\cdot\boldsymbol{\nabla}v^2 \;=\; mn\Big(\boldsymbol{v}\cdot\boldsymbol{\nabla}\boldsymbol{v}\Big)\cdot\boldsymbol{v}\;. \tag{2.63}$$

2.2.5. Discussion of the generic multiscale model

The particle balances (2.48) and (2.49), the momentum balances (2.55) and (2.56), and the energy balances (2.60) and (2.61) constitute the generic multiscale model for a fluid whose dynamics exhibit a scale separation. The evolution equations hold for all particle species a separately. The general structure of all balances is similar: in the macroscale balances (2.48), (2.55), and (2.60) the macroscale part of the considered quantity (n_0, $\boldsymbol{v}_0$ or T_0) is advected only by the macroscale velocity $\boldsymbol{v}_0$. The effect of the averaged mesoscale dynamics is represented by a term of the form $\langle\widetilde{\boldsymbol{v}} \cdot \boldsymbol{\nabla}\widetilde{\alpha}\rangle$, where $\widetilde{\alpha}$ is the mesoscale part of the considered macroscale variable ($\widetilde{n}$, $\widetilde{\boldsymbol{v}}$, or $\widetilde{T}$). In the mesoscale balances (2.49), (2.56) and (2.61), the mesoscale quantities are advected by the full velocity $\boldsymbol{v} = \boldsymbol{v}_0 + \widetilde{\boldsymbol{v}}$. Additionally, the advection of the macroscale quantity by $\widetilde{\boldsymbol{v}}$ is taken into account. The averaged terms like $\langle\boldsymbol{\nabla} \cdot (\widetilde{n}\widetilde{\boldsymbol{v}})\rangle$, present in the mesoscale balances, guarantee that any macroscale evolution of the mesoscale quantity is canceled out, thus ensure that $\langle\widetilde{\alpha}\rangle = 0$ and therefore an enduring scale separation. Note that the full balance equations (2.27), (2.28), and (2.29) can be recovered by adding the associated macroscale and mesoscale balances, illustrating the completeness of the multiscale model.

The term $\langle\widetilde{\boldsymbol{v}} \cdot \boldsymbol{\nabla}\widetilde{\boldsymbol{v}}\rangle$, appearing in the momentum balance (2.55), and the conservative form of the energy balance (2.62) can be rewritten as

$$\left\langle\widetilde{\boldsymbol{v}} \cdot \boldsymbol{\nabla}\widetilde{\boldsymbol{v}}\right\rangle \;=\; \boldsymbol{\nabla} \cdot \langle\widetilde{\boldsymbol{v}}\widetilde{\boldsymbol{v}}\rangle \;-\; \left\langle(\boldsymbol{\nabla} \cdot \widetilde{\boldsymbol{v}})\widetilde{\boldsymbol{v}}\right\rangle , \tag{2.64}$$

where it has been assumed that the averaging operator and spatial derivative are commutable (see paragraph 2.3.2 for a detailed investigation of this property on a discretized grid). The tensor $\langle\widetilde{\boldsymbol{v}}\widetilde{\boldsymbol{v}}\rangle$ is the so-called Reynolds stress, commonly used in fluid mechanics. It is usually introduced in the context of the Reynolds-averaged Navier-Stokes equations (or short RANS equations) whose derivation bears a strong resemblance to the procedure used here to deduce the multiscale model [2]. By defining the Reynolds decomposition of fluid quantities into a macroscale and mesoscale part according to eq. (2.35), the Reynolds stress appears in the momentum balance of the RANS equations. To close the equation, an expression for $\langle\widetilde{\boldsymbol{v}}\widetilde{\boldsymbol{v}}\rangle$ is needed. Different approaches to determine $\langle\widetilde{\boldsymbol{v}}\widetilde{\boldsymbol{v}}\rangle$ in fluid mechanics via reduced mesoscale models are for example presented in chapters 10 and 11 of [2].

2.3. Outline of a coupled code system

Analytical solutions for the coupled partial differential equations that constitute the generic multiscale model, i.e. eqs. (2.48), (2.49), (2.55), (2.56), (2.60), and (2.61), are difficult to find. Hence, these equations are typically solved numerically

by specialized computer codes. In this paragraph, the generic multiscale model is analyzed with the objective of setting up a coupled code system where the macroscale and mesoscale balances are solved by two independent codes which are linked together. Via a coupling procedure these codes exchange the necessary information so that the dynamics of the complete system can be determined, the focus lying on its macroscale evolution. Outlining the coupling procedure also serves for further elucidating the advantage of the coupled code system compared to solving the full fluid balances numerically: a significantly diminished need for computational resources.
This section is subdivided as follows. The structure of a coupling procedure that was developed for this thesis is described in paragraph 2.3.1 and related to the so-called heterogeneous multiscale method [37, 43, 44]. The question in how far the averaging operator (2.32) and the temporal and spatial derivatives are commutable is investigated in paragraph 2.3.2. The concept of macroscale transport models to describe averaged mesoscale terms like $\langle \boldsymbol{\nabla} \cdot (\tilde{n}\tilde{\boldsymbol{v}}) \rangle$ in the macroscale balances is introduced in paragraph 2.3.3. Finally, the challenge to find (statistically) stationary solutions of the system is discussed in paragraph 2.3.4.

2.3.1. Structure of the coupling procedure

The setup of the coupled code system to solve the multiscale model equations should be illustrated with the help of the macroscale and mesoscale particle balances (2.48) and (2.49) which are given by

$$\frac{\partial n_0}{\partial t} + \boldsymbol{v}_0 \cdot \boldsymbol{\nabla} n_0 = - n_0 \boldsymbol{\nabla} \cdot \boldsymbol{v}_0 + \left\langle S_n^{ic} \right\rangle - \left\langle \boldsymbol{\nabla} \cdot (\tilde{n}\tilde{\boldsymbol{v}}) \right\rangle ,$$

and

$$\begin{aligned} &\frac{\partial \tilde{n}}{\partial t} + \Big(\boldsymbol{v}_0 + \tilde{\boldsymbol{v}}\Big) \cdot \boldsymbol{\nabla} \tilde{n} + \tilde{\boldsymbol{v}} \cdot \boldsymbol{\nabla} n_0 \\ &\quad = -\tilde{n} \boldsymbol{\nabla} \cdot \Big(\boldsymbol{v}_0 + \tilde{\boldsymbol{v}}\Big) - n_0 \boldsymbol{\nabla} \cdot \tilde{\boldsymbol{v}} + S_n^{ic} - \left\langle S_n^{ic} \right\rangle + \left\langle \boldsymbol{\nabla} \cdot (\tilde{n}\tilde{\boldsymbol{v}}) \right\rangle . \end{aligned}$$

It is assumed that both a macroscale and mesoscale code are at hand for solving these equations numerically on their characteristic temporal and spatial scales. For illustrative purposes, a one-dimensional problem in space is considered here but the relations and concepts obtained below are easily generalizable to the three-dimensional case.

A sketch of the general structure of the coupled code system is given in fig. 2.2, with a summary of the employed quantities and parameters shown in table 2.1. The green grid of continuous lines represents the macroscale grid on which the discretized macroscale particle balance (2.48) is solved, the total simulated time being t_{sim}. The spatial distance between two grid points, the cell length, is given by Δr_s, while the time step size of the macroscale code is Δt_s. The points marked with a green dot are the points for which a mesoscale simulation is carried out to determine the averaged mesoscale terms $\langle \boldsymbol{\nabla} \cdot (\tilde{n}\tilde{\boldsymbol{v}}) \rangle$, i.e. for which these terms are 'updated' during the course of the simulation. The updating points have a distance of Δr_{up} in space and Δt_{up} in time.

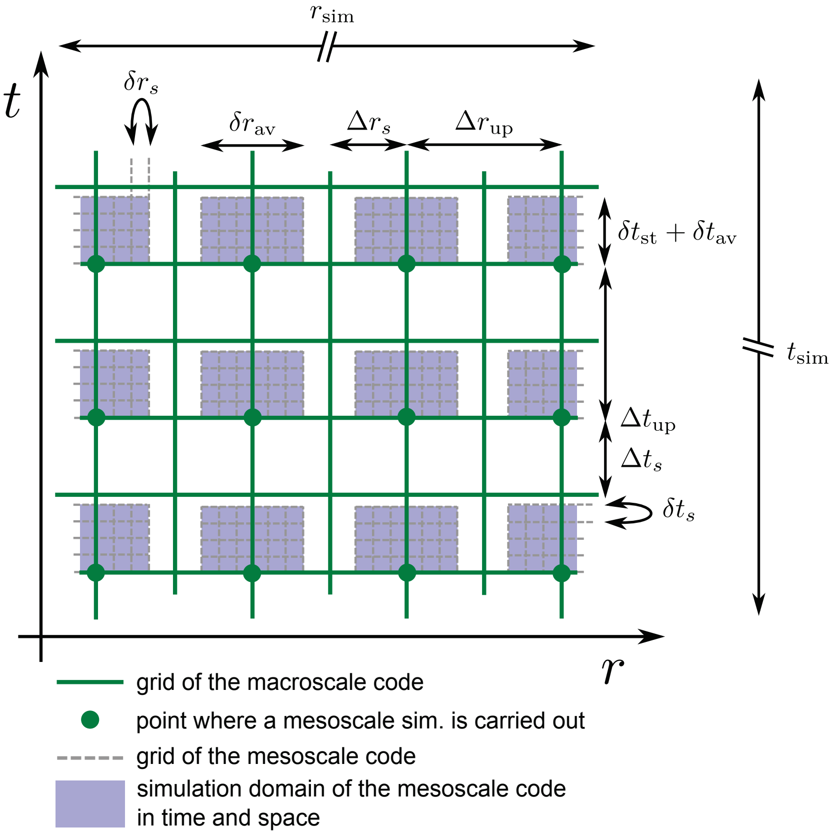

Figure 2.2.: Sketch of the spatial and temporal structure of the coupling procedure.

The mesoscale simulation domains in time and space are highlighted in violet. Each mesoscale simulation has a spatial extent δr_{av} and simulates a total time $\delta t_{\mathrm{st}} + \delta t_{\mathrm{av}}$, where δt_{st} is the time needed for the mesoscale system to reach a statistically stationary state. Statistical stationarity of a quantity $\alpha(\boldsymbol{r}, t)$ means that its expectation value and its autocovariance (and therefore also its variance) are constant in time and space:

$$E\Big[\alpha(\boldsymbol{r}, t)\Big] \;=\; \mu \;, \tag{2.65}$$

$$\mathrm{Var}\Big[\alpha(\boldsymbol{r},t)\Big] \;=\; \sigma^2 \;, \tag{2.66}$$

$$\mathrm{Cov}\Big[\alpha(\boldsymbol{r}_1,t_1),\alpha(\boldsymbol{r}_2,t_2)\Big] \;=\; \mathrm{Cov}\Big[\alpha(\boldsymbol{r}_1+\Delta r,t_1+\Delta t),\alpha(\boldsymbol{r}_2+\Delta r,t_2+\Delta t)\Big] \;. \tag{2.67}$$

If $\alpha(\boldsymbol{r},t)$ is a stochastic processes, eqs. (2.65) to (2.67) correspond to the definition of so-called weak stationarity [45]. Note that statistical stationarity does not mean that $\partial\alpha/\partial t$. The mesoscale grid, given by the dotted gray lines, has a cell length of δr, the time step is denoted δt. Note that the mesoscale grid is usually much finer compared to the macroscale grid than it is shown in fig. 2.2. This fact is ignored here for a better illustration of the coupled code system. Important for its proper working is that the following relations regarding the spatial and temporal parameters and quantities are fulfilled:

$$\delta t_s \;\ll\; \tau_{\mathrm{D}}(\tilde{\alpha}) \;\ll\; \delta t_{\mathrm{av}} \tag{2.68}$$

and

$$\Delta t_s \;\ll\; \tau_{\mathrm{D}}(\alpha_0)\;, \qquad \tau_{\mathrm{D}}(\tilde{\alpha}) \;\ll\; \Delta t_{\mathrm{up}} \;\sim\; \tau_{\mathrm{D}}(\alpha_0)\;, \qquad \delta t_{\mathrm{st}} \;\ll \tau_{\mathrm{D}}(\alpha_0)\;. \tag{2.69}$$

For the spatial quantities one has analogously:

$$\delta r_s \;\ll\; \lambda_{\mathrm{D}}(\tilde{\alpha}) \;\ll\; \delta r_{\mathrm{av}} \tag{2.70}$$

and

$$\Delta r_s \;\ll\; \lambda_{\mathrm{D}}(\alpha_0)\;, \qquad \lambda_{\mathrm{D}}(\tilde{\alpha}) \;\ll\; \delta r_{\mathrm{av}} \;\sim\; \lambda_{\mathrm{D}}(\alpha_0)\;. \tag{2.71}$$

These relations should be elucidated for the temporal quantities, with similar considerations holding also for the spatial quantities:

- eq. (2.68): the time step δt_s of the mesoscale code has to be significantly smaller than the characteristic time $\tau_{\mathrm{D}}(\tilde{\alpha})$ of the mesoscale dynamics to ensure that the mesoscale dynamics are captured by the numerical scheme. The averaging time δt_{av} has to be chosen larger than $\tau_{\mathrm{D}}(\tilde{\alpha})$ to ensure that the averages are statistically meaningful, i.e. do not change significantly for variations of the averaging intervals' position and extent once the statistically stationary state has been reached. This ensures that the averaged terms are representative for the set of macroscale variables used in the mesoscale simulation.

- eq. (2.69a): the time step Δt_s of the macroscale code has to be chosen much smaller than $\tau_{\mathrm{D}}(\alpha_0)$ to capture the macroscale dynamics.

- eq. (2.69b): a reasonable estimate for the time Δt_{up} to update the mesoscale information in the macroscale code is given by the characteristic time $\tau_{\mathrm{D}}(\alpha_0)$ of the macroscale profile change. In the sense of the scale separation $\tau_{\mathrm{D}}(\tilde{\alpha})$ then has to be much smaller than Δt_{up}. If Δt_{up} is much shorter than $\tau_{\mathrm{D}}(\alpha_0)$, the set of macroscale variables used in the mesoscale simulation will not differ significantly from the set used for the previous mesoscale simulation. The resulting averaged mesoscale terms $\langle \boldsymbol{\nabla} \cdot (\tilde{n}\tilde{\boldsymbol{v}}) \rangle$ can be expected to be rather similar to that of the previous iteration. This does not lead to erroneous results – it will rather improve the accuracy of the macroscale evolution – but will increase the need for computational resources since more mesoscale simulations have to be carried out. If, on the other hand, Δt_{up} is much longer than $\tau_{\mathrm{D}}(\alpha_0)$ the macroscale quantities used to determine $\langle \boldsymbol{\nabla} \cdot (\tilde{n}\tilde{\boldsymbol{v}}) \rangle$ might differ significantly from the macroscale profiles which are calculated using $\langle \boldsymbol{\nabla} \cdot (\tilde{n}\tilde{\boldsymbol{v}}) \rangle$. This means an inconsistency in the model and leads to incorrect results. The choice of Δt_{up} therefore is crucial regarding the outcome of the coupled code system, accuracy-wise as well as computational time savings-wise.

- eq. (2.69c): the time δt_{st} for the mesoscale system to reach a statistically stationary state has to be much smaller than $\tau_{\mathrm{D}}(\alpha_0)$ to ensure that the scale separation hypothesis is fulfilled, expressing that the mesoscale system adjusts quickly from its previous state to the new macroscale variables.

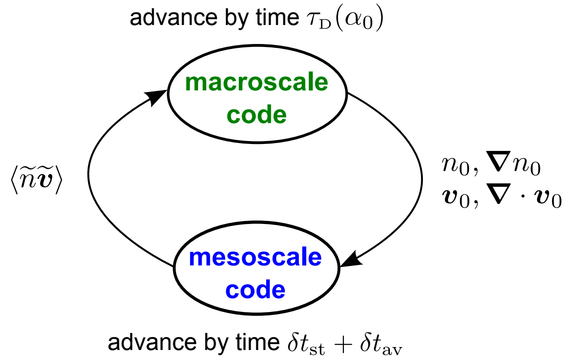

Figure 2.3.: Coupling procedure for one updating point of the macroscale grid for which the averaged mesoscale fluxes are updated after a time interval Δt_{up}.

The coupling procedure that is carried out at each of the green updating points in fig. 2.2 (after a time Δt_{up} and for macroscale cells separated by a length Δr_{up}) is sketched in fig. 2.3. It is assumed here that for the averaged term $\langle \boldsymbol{\nabla} \cdot (\tilde{n}\tilde{\boldsymbol{v}}) \rangle$ it holds:

$$\Big\langle \boldsymbol{\nabla} \cdot (\tilde{n}\tilde{\boldsymbol{v}}) \Big\rangle \approx \boldsymbol{\nabla} \cdot \langle \tilde{n}\tilde{\boldsymbol{v}} \rangle \; . \tag{2.72}$$

This relation is justified and explained in detail in the next paragraph 2.3.2. At time t, a mesoscale simulation is started for all updating points in the spatial simulation

variable	**description**
δt_s	time step of the mesoscale code
δt_{st}	simulated time of the mesoscale code to reach statistical stationarity
δt_{av}	averaging time for mesoscale quantities
Δt_s	time step of the macroscale code
Δt_{up}	updating time/time between two mesoscale simulations
$\tau_{\mathrm{D}}(\alpha)$	characteristic time of the dynamics of α
$\tau_c(\alpha)$	correlation time of α
$t_c(\alpha)$	computing time needed to determine the evolution of α
t_{sim}	total simulated time
a_t	desired ratio of $\delta t_{\mathrm{av}}/\tau_{\mathrm{D}}(\widetilde{\alpha})$, used for choosing δt_{av}
δr_s	cell length of the mesoscale code
δr_{av}	spatial averaging interval for mesoscale quantities
Δr_s	cell length of the macroscale code
Δr_{up}	spatial updating interval/‘distance’ between two mesoscale simulations
$\lambda_{\mathrm{D}}(\alpha)$	characteristic length of the dynamics of α
$\lambda_c(\alpha)$	correlation length of α
r_{sim}	extent of the simulation domain
a_r	desired ratio $\delta r_{\mathrm{av}}/\lambda_{\mathrm{D}}(\widetilde{\alpha})$, used for choosing δr_{av}

Table 2.1.: Variables used for the description of the coupling process and the mesoscale and macroscale codes.

domain, using the respective set of macroscale quantities $(n_0, \boldsymbol{\nabla} n_0, \boldsymbol{v}_0, \boldsymbol{\nabla}\cdot\boldsymbol{v}_0)$. Once the statistically stationary state is reached after a time δt_{st}, the mesoscale simulation is continued for a time δt_{av} after which the average $\langle\widetilde{n}\widetilde{\boldsymbol{v}}\rangle$ is calculated and handed to the macroscale code. Values of $\langle\widetilde{n}\widetilde{\boldsymbol{v}}\rangle$ for points of the macroscale grid for which no mesoscale simulation is carried out can be calculated via interpolation, for instance. The divergence of the averaged particle flux, $\boldsymbol{\nabla}\cdot\langle\widetilde{n}\widetilde{\boldsymbol{v}}\rangle$, needed to advance the macroscale system, is determined by the difference quotient

$$\boldsymbol{\nabla}\cdot\langle\widetilde{n}\widetilde{\boldsymbol{v}}\rangle(r,t) \;=\; \frac{1}{2\Delta r_{\mathrm{up}}}\Bigg[\langle\widetilde{n}\widetilde{\boldsymbol{v}}\rangle(r-\Delta r_{\mathrm{up}},t)-\langle\widetilde{n}\widetilde{\boldsymbol{v}}\rangle(r+\Delta r_{\mathrm{up}},t)\Bigg]\,. \tag{2.73}$$

The macroscale code then advances the macroscale system by a time Δt_{up} after which the procedure is repeated.

As already mentioned, the generic multiscale system is, under the assumption of a scale separation, equivalent to the full system, given by the fluid balances (2.24) to (2.26). The advantage of a coupled code system,, solving the multiscale equations as compared to a code determining the evolution of the full quantities α directly are the possibilities for saving computational resources or computing time. This should be explained here. Consider the speedup factor $\varepsilon(t_c)$,

$$\varepsilon(t_c) \;\equiv\; \frac{t_c(\alpha)}{t_c(\alpha_0) + t_c(\widetilde{\alpha})} \;, \tag{2.74}$$

which is given by the computing time $t_c(\alpha)$ to determine the evolution for a given time t_{sim} and a simulation domain $\boldsymbol{r}_{\text{sim}}$ by using the full balances, divided by the sum of the computational times $t_c(\alpha_0)$ and $t_c(\widetilde{\alpha})$ that are needed by a coupled code system for the same task. The cell length and time step length of the code solving the full balances are about the same as those of the mesoscale code to be able to resolve the fast and small scale dynamics. With the computational time taken to be proportional to the number of grid points in time and space, one can state that (referring to fig. 2.2):

$$\varepsilon(t_c) \;\propto\; \frac{\begin{array}{c}\text{number of gray grid points needed to fill the}\\ \text{total simulation area in time and space}\end{array}}{\begin{array}{c}\text{number of gray grid}\\ \text{points of violet areas}\end{array} + \begin{array}{c}\text{number of green}\\ \text{grid points}\end{array}} \;. \tag{2.75}$$

If it is assumed that the computing time of the macroscale code is negligible compared to that of the mesoscale code, $t_c(\alpha_0) \ll t_c(\widetilde{\alpha})$ (i.e. the green grid points do not count in eq. (2.75)), it holds:

$$\varepsilon(t_c) \;\propto\; \frac{\Delta r_{\text{up}}}{\delta r_{\text{av}}}\,\frac{\Delta t_{\text{up}}}{\delta t_{\text{av}}} \;. \tag{2.76}$$

Having relations (2.68) and (2.70) to be fulfilled, the averaging intervals are set to

$$\delta r_{\text{av}} \;\approx\; a_r \lambda_{\text{D}}(\widetilde{\alpha}) \;, \qquad \delta t_{\text{av}} \;\approx\; a_t \tau_{\text{D}}(\widetilde{\alpha}) \;, \tag{2.77}$$

with a_r and a_t being at least on the order of ten. By setting $\Delta r_{\text{up}} = \lambda_{\text{D}}(\alpha_0)$ and $\Delta t_{\text{up}} = \tau_{\text{D}}(\alpha_0)$ one finds that

$$\boxed{\varepsilon(t_c) \;\propto\; \frac{\tau_{\text{D}}(\alpha_0)}{\tau_{\text{D}}(\widetilde{\alpha})}\,\frac{\lambda_{\text{D}}(\alpha_0)}{\lambda_{\text{D}}(\widetilde{\alpha})} \;. \qquad (2.78)}$$

This means that the more disparate the mesoscale and the macroscale are, i.e. the larger the ratios $\tau_{\text{D}}(\alpha_0)/\tau_{\text{D}}(\widetilde{\alpha})$ and $\lambda_{\text{D}}(\alpha_0)/\lambda_{\text{D}}(\widetilde{\alpha})$ are, the larger the possible benefits of the coupled code system.

The mesoscale code of the coupled code system in the above example is called a *local* mesoscale code if the set of macroscale quantities $(n_0, \boldsymbol{\nabla} n_0, \boldsymbol{u}_0, \boldsymbol{\nabla}\cdot\boldsymbol{u}_0)$ is taken to be constant for the mesoscale simulation of extent $\delta t_{\mathrm{st}} + \delta t_{\mathrm{av}}$ and δr_{av}. Due to the scale separation, the variation of the macroscale quantities on the averaging intervals is small so that the errors introduced by neglecting it are assumed to be small, too. A code which takes these variations (partly) into account and solves the full balances for the variables n, $\boldsymbol{v}$ and T is called a *global* (*non-local*) mesoscale code. Usually, the cell length and the time step length are of the same order for all three types of codes (local, non-local and global) since the mesoscale processes to be captured, denoting the smallest scale to be resolved, are basically the same. In this context it should be highlighted that, even though the macroscale quantities like n_0 and $\boldsymbol{v}_0$ are assumed to be constant, their gradients and divergences are kept, like $\boldsymbol{\nabla} n_0$ in the local mesoscale model for the mesoscale particle balance (2.49). The differences between a local and a non-local model are further investigated in chapter 7.

Before elucidating further details of the multiscale approach presented here, it should be classified regarding the different types of multiscale problems and models that are discussed in the literature. For this purpose it is referred to the comprehensive overview given in [37].

The coupled code system to solve the generic multiscale model as outlined in this paragraph makes use of heterogeneous multiscale method (HMM) [43, 44, 37] which belongs to the class of multigrid methods to tackle a type B multiscale problem. Multigrid simply refers to the fact that both the mesoscale and macroscale system are using grids of different dimensions and resolutions (see fig. 2.2). Type A multiscale problems rely on a microscale or mesoscale model only for a number of selected spatial positions and/or instances, e.g. near defects or heterogeneities, while the major part of the evolution of the system is captured by the macroscale model. Type B multiscale problems resort on the microscale/mesoscale model basically at all positions of the computational domain.

The HMM has the following defining elements, as given in [37], pages 249 to 250, with the counterpart of the coupled code system presented here highlighted in blue:

- ***'A macroscopic solver:*** *on the basis of whatever knowledge is available about the macroscale behavior of the system, we make an assumption about the form of the macroscale model from which we select a suitable macroscale solver.'*

  Solve

  $$\frac{\partial \alpha_0}{\partial t} = L(\alpha_0; C) \ , \tag{2.79}$$

  where C denotes the data needed for the macroscale model to be complete.

  Eq. (2.79) corresponds to the macroscale particle balance (2.48) with $\alpha_0 = n_0$ The data C to complete the macroscale model is contained in the terms $\langle S_n^{ic} \rangle$ and $\langle \boldsymbol{\nabla} \cdot (\tilde{n}\tilde{\boldsymbol{v}}) \rangle$.

- ***'A procedure for estimating the missing macroscale data C using the microscale model.***

  1. ***Constrained microscale simulation:*** *at each point where some macroscale data is needed, perform a series of microscopic simulations which are constrained to be consistent with the local value of the macro variable.'*

     Solve

     $$\frac{\partial\tilde{\alpha}}{\partial t} = \mathcal{L}(\tilde{\alpha};\alpha_0) \; . \tag{2.80}$$

     Eq. (2.80) corresponds to the mesoscale particle balance (2.49) with $\tilde{\alpha} = \tilde{n}$. The identification as 'constrained simulation' refers to the fact that the macroscale quantities α_0 appearing in $\mathcal{L}$ are taken to be constant during the mesoscale simulation.

  2. ***'Data processing:*** *use the results from the microscopic simulations to extract the macroscale data needed in the macroscale solver.'*

     The extraction of the data needed for our model is carried out by applying the averaging operator $\langle ... \rangle$ as given by eq. (2.32) on the mesoscale terms.

The HMM has a similar structure as the extended multigrid method [46] and the equation-free approach [47]. All three models have in common that their focus lies on the reproduction of the macroscale evolution and that they use a concurrent coupling procedure, i.e. obtain the microscale/mesoscale information 'on the fly'. In contrast, sequential coupling procedures first create a database containing the required microscale/mesoscale data and then carry out the macroscale simulation. An example for a multiscale model using this approach is given in the survey of comparable projects in paragraph 5.3.

The considerations following in paragraphs 2.3.2, 2.3.3 and 2.3.4 are oriented towards the generic multiscale model and do not longer refer explicitly to the simplified multiscale model of the balance equations.

2.3.2. Averages of temporal and spatial derivatives

For the derivation of the generic multiscale model it was used that

$$\left\langle \frac{\partial\tilde{\alpha}}{\partial t} \right\rangle = 0 \; . \tag{2.81}$$

This can be justified by considering a discretized mesoscale grid. For an arbitrary mesoscale variable $\widetilde{\alpha}$ one has:

$$\begin{aligned}\left\langle\frac{\partial\widetilde{\alpha}}{\partial t}\right\rangle(t) &= \frac{1}{N_t}\sum_{i=0}^{N_t}\frac{1}{2\delta t_s}\left[\Big\langle\widetilde{\alpha}(t-\delta t_{\mathrm{av}}+[i+1]\delta t_s)\Big\rangle_r - \Big\langle\widetilde{\alpha}(t-\delta t_{\mathrm{av}}+[i-1]\delta t_s)\Big\rangle_r\right] \\ &= \frac{1}{2\delta t_s}\left[\Big\langle\widetilde{\alpha}(t+\delta t_s)\Big\rangle - \Big\langle\widetilde{\alpha}(t-\delta t_s)\Big\rangle\right] , \qquad (2.82)\end{aligned}$$

where N_t is the number of time steps used for the temporal averaging (so that $(N_t-1)\delta t_s = \delta t_{\mathrm{av}}$), and $\langle ... \rangle_r$ is the averaging operator regarding only the spatial coordinate. Note the transition from the average in space only in the first line of eq. (2.82) to the average in space *and* time in the second line. Since the average of the mesoscale variables is zero, $\langle\widetilde{\alpha}\rangle = 0$, both $\langle\widetilde{\alpha}(t+\delta t_s)\rangle$ and $\langle\widetilde{\alpha}(t-\delta t_s)\rangle$ are zero. Thus, eq. (2.81) holds.

For the averaged spatial derivatives of second order in the mesoscale quantities of the form $\langle\boldsymbol{\nabla}\cdot(\widetilde{\alpha}\widetilde{\boldsymbol{v}})\rangle$ one obtains a different result. Analogously to eq. (2.82), they are given by

$$\Big\langle\boldsymbol{\nabla}\cdot(\widetilde{\alpha}\widetilde{\boldsymbol{v}})\Big\rangle(r) = \frac{1}{2\delta r_s}\left[\langle\widetilde{\alpha}\widetilde{\boldsymbol{v}}\rangle(r+\delta r_s) - \langle\widetilde{\alpha}\widetilde{\boldsymbol{v}}\rangle(r-\delta r_s)\right] , \qquad (2.83)$$

It is important to recall that terms of the form $\langle\widetilde{\alpha}\widetilde{\boldsymbol{v}}\rangle(r)$ are not necessarily zero – this only holds for terms first order in the mesoscale quantities. Therefore, due to the (small) variation of $\langle\widetilde{\alpha}\widetilde{\boldsymbol{v}}\rangle(r)$ on the mesoscale, $\langle\boldsymbol{\nabla}\cdot(\widetilde{\alpha}\widetilde{\boldsymbol{v}})\rangle(r)$ does not equal zero neither.

A problem arises if $\langle\widetilde{\alpha}\widetilde{\boldsymbol{v}}\rangle(r+\delta r)$ and $\langle\widetilde{\alpha}\widetilde{\boldsymbol{v}}\rangle(r-\delta r)$ are determined by the local mesoscale simulation carried out at point r. For a local mesoscale code, the macroscale values will be constant over its entire simulation domain, meaning that also the statistics of the mesoscale dynamics are homogeneous, too. This results in that the averaged divergence $\langle\boldsymbol{\nabla}\cdot(\widetilde{\alpha}\widetilde{\boldsymbol{v}})\rangle(r)$ becomes zero. If not, this is due to an insufficient amount of data available for evaluating the averages $\langle\widetilde{\alpha}\widetilde{\boldsymbol{v}}\rangle(r+\delta r_s)$ and $\langle\widetilde{\alpha}\widetilde{\boldsymbol{v}}\rangle(r-\delta r_s)$ and does not reflect any physical effect. A constant divergence of zero for all times is in contradiction to the reasoning presented above and therefore an erroneous result.

This issue can be overcome by assuming that for spatial distances Δr up to the order of Δr_{up} the macroscale quantities α_0 and the mesoscale averages of the type $\langle\widetilde{\alpha}\widetilde{\boldsymbol{v}}\rangle$ can be sufficiently approximated by a Taylor expansion up to first order:

$$\alpha_0(r_1+\Delta r) \approx \alpha_0(r_1) + \left.\frac{\partial\alpha_0}{\partial r}\right|_{r_1}\Delta r , \qquad (2.84)$$

$$\langle\widetilde{\alpha}\widetilde{\boldsymbol{v}}\rangle(r_1+\Delta r) \approx \langle\widetilde{\alpha}\widetilde{\boldsymbol{v}}\rangle(r_1) + \left.\frac{\partial\langle\widetilde{\alpha}\widetilde{\boldsymbol{v}}\rangle}{\partial r}\right|_{r_1}\Delta r , \qquad (2.85)$$

with $0 < \Delta r \lesssim \Delta r_{\text{up}}$. Eq. (2.83) can be transformed to yield

$$\Big\langle \boldsymbol{\nabla} \cdot (\widetilde{\alpha}\widetilde{\boldsymbol{v}}) \Big\rangle (r) \;\approx\; \frac{1}{2\Delta r_{\text{up}}} \left[\langle \widetilde{\alpha}\widetilde{\boldsymbol{v}} \rangle (r + \Delta r_{\text{up}}) - \langle \widetilde{\alpha}\widetilde{\boldsymbol{v}} \rangle (r - \Delta r_{\text{up}}) \right] , \tag{2.86}$$

which can be written as

$$\Big\langle \boldsymbol{\nabla} \cdot (\widetilde{\alpha}\widetilde{\boldsymbol{v}}) \Big\rangle (r) \;\approx\; \boldsymbol{\nabla} \cdot \langle \widetilde{\alpha}\widetilde{\boldsymbol{v}} \rangle (r) \; . \tag{2.87}$$

Eq. (2.87) is the generalization of eq. (2.72) for any given mesoscale quantity $\widetilde{\alpha}$. Note that the rhs of eq. (2.87) has to be understood in such a way that the divergence is evaluated on the macroscale grid.

2.3.3. Macroscale transport models for averaged mesoscale terms

One way of transferring mesoscale information to the macroscale code is the evaluation of the terms $\langle \widetilde{\alpha}\widetilde{\boldsymbol{v}} \rangle$ and $\langle \widetilde{\boldsymbol{v}} \cdot \boldsymbol{\nabla}\widetilde{\alpha} \rangle$ for each time step and spatial grid point of the macroscale code by separate local mesoscale simulations. With such a procedure even the mesoscale evolution of the averaged mesoscale terms can be captured. The drawback of this approach is that the computational cost increases and the speedup factor $\varepsilon(t_c)$ decreases (due to small Δt_{up} and Δr_{up} are, see eq. (2.76)). On the other hand, by updating the averaged mesoscale terms using larger temporal and spatial intervals $\Delta t_{\text{up}} > \tau_{\text{D}}(\alpha_0)$ and $\Delta r_{\text{up}} > \lambda_{\text{D}}(\alpha_0)$, the need for computational resources is decreased and $\varepsilon(t_c)$ therefore increased. However, this usually means that the accuracy regarding the reproduction of the macroscale dynamics worsens since $\langle \widetilde{\alpha}\widetilde{\boldsymbol{v}} \rangle$ and $\langle \widetilde{\boldsymbol{v}} \cdot \boldsymbol{\nabla}\widetilde{\alpha} \rangle$, determined with a certain set of macroscale quantities $\boldsymbol{\alpha}_0(r', t')$, are used at points where $\boldsymbol{\alpha}_0(r, t)$ deviates significantly from $\boldsymbol{\alpha}_0(r', t')$. It can be assumed that also the associated averaged mesoscale terms vary significantly. The two 'antagonistic' factors – accuracy and saving of computational resources – have to be balanced when setting up a coupled code system.

Using a macroscale transport model aims at increasing the savings of computational time of the coupled code system (which is used synonymously with savings in computational resources) while at the same time ensuring a high accuracy of its results. For a basic example one can look at the gradient-diffusion hypothesis [2] for modeling averaged mesoscale fluxes of the form $\langle \widetilde{\alpha}_l \widetilde{\boldsymbol{v}} \rangle$. For a three-dimensional problem with isotropic transport, one has

$$\langle \widetilde{\alpha}_l \widetilde{\boldsymbol{v}} \rangle (\boldsymbol{r}, t) \;=\; -D(\boldsymbol{r}', t')\, \boldsymbol{\nabla} \alpha_{l0}(\boldsymbol{r}, t) \tag{2.88}$$

for the intervals

$$t' \;\leq\; t \;\leq\; t' + \Delta t_{\text{up}} \; , \qquad \boldsymbol{r}' - \Delta \boldsymbol{r}_{\text{up}} \;\leq\; \boldsymbol{r} \;\leq\; \boldsymbol{r}' + \Delta \boldsymbol{r}_{\text{up}} \; . \tag{2.89}$$

$D(\boldsymbol{r}', t')$ is given by

$$D(\boldsymbol{r}', t') \;=\; -\frac{\langle \tilde{\alpha}_l \tilde{\boldsymbol{v}} \rangle (\boldsymbol{\alpha}_0(\boldsymbol{r}', t'))}{|\boldsymbol{\nabla} \alpha_{l0}(\boldsymbol{r}', t')|} \; . \tag{2.90}$$

The vector $\boldsymbol{\alpha}_0$ refers to all macroscale quantities relevant for the local mesoscale simulations, while α_{l0} is the specific macroscale quantity considered here. Eqs. (2.88) and (2.90) are to be read in the following manner. The averaged mesoscale flux $\langle \tilde{\alpha} \tilde{\boldsymbol{v}} \rangle (\boldsymbol{r}, t)$ (as used in the macroscale code) is given by a diffusive model. The diffusion coefficient $D(\boldsymbol{r}', t)$ used at position $\boldsymbol{r}$ and time t on the macroscale is determined with the averaged mesoscale flux obtained with the macroscale input parameters $\boldsymbol{\alpha}_0$ of position $\boldsymbol{r}'$ and at time t'.

In general, the generalized macroscale transport model $\mathcal{M}$ and its transport coefficients like D, used on the macroscale to represent the averaged mesoscale term $\langle f(\tilde{\boldsymbol{\alpha}}) \rangle$, have to fulfill at spatial position $\boldsymbol{r}'$ and time t:

$$\mathcal{M}\Big(\Big\langle f(\tilde{\boldsymbol{\alpha}}) \Big\rangle ; \boldsymbol{r}', t'\Big) \;=\; \Big\langle f(\tilde{\boldsymbol{\alpha}}) \Big\rangle (\boldsymbol{r}', t') \; . \tag{2.91}$$

Also, employing $\mathcal{M}$ should lead to more accurate results than using constant averaged mesoscale terms for the intervals given by eqs. (2.89a) and (2.89b)):

$$\boxed{\left| \mathcal{M}_0\Big(\Big\langle f(\tilde{\boldsymbol{\alpha}}) \Big\rangle ; \boldsymbol{r}', t'\Big) - \Big\langle f(\tilde{\boldsymbol{\alpha}}) \Big\rangle (\boldsymbol{r}, t) \right| \;\overset{!}{<}\; \left| \Big\langle f(\tilde{\boldsymbol{\alpha}}) \Big\rangle (\boldsymbol{r}', t') - \Big\langle f(\tilde{\boldsymbol{\alpha}}) \Big\rangle (\boldsymbol{r}, t) \right| \, , \quad (2.92)}$$

where it is assumed that the exact value of $\langle f(\tilde{\boldsymbol{\alpha}}) \rangle$ is known for all spatial positions and times. For the diffusive transport model eq. (2.92) reads:

$$\left| D(\boldsymbol{r}', t') \boldsymbol{\nabla} \alpha_0(\boldsymbol{r}, t) \; + \; \langle \tilde{\alpha} \tilde{\boldsymbol{v}} \rangle (\boldsymbol{r}, t) \right| \;\overset{!}{<}\; \left| \langle \tilde{\alpha} \tilde{\boldsymbol{v}} \rangle (\boldsymbol{r}', t') - \langle \tilde{\alpha} \tilde{\boldsymbol{v}} \rangle (\boldsymbol{r}, t) \right| \, . \tag{2.93}$$

In some cases, relation (2.92) might hold for temporal and spatial intervals much larger than $\tau_{\mathrm{D}}(\alpha_0)$ and $\lambda_{\mathrm{D}}(\alpha_0)$. A classical example are the diffusive dynamics of a system whose microscale dynamics are governed by Brownian motion [48]. In chapter 6, a passive scalar model with similar properties is presented and analyzed in detail. Such phenomena - microscale and mesoscale processes which can be described accurately by macroscale laws – are embraced by the term *emergence* and play important roles in different branches of the natural sciences [49].

2.3.4. Stationary states in the generic multiscale model

The evolution equations of the generic multiscale model are time-dependent. Here, it is outlined what considerations have to be made if one is interested only in (statistically) stationary solutions of these equations. Two cases are distinguished: case one, where both the macroscale and mesoscale system have reached a stationary state,

$$\frac{\partial \alpha_0}{\partial t} + \frac{\partial \widetilde{\alpha}}{\partial t} = \frac{\partial \alpha}{\partial t} = 0 \; , \tag{2.94}$$

and case two, where the macroscale system is in a stationary state and the mesoscale system is in a statistically stationary state:

$$\frac{\partial \alpha_0}{\partial t} = 0 \; , \qquad \frac{\partial \widetilde{\alpha}}{\partial t} \neq 0 \; . \tag{2.95}$$

Consider the case one. Eq. (2.94) is fulfilled for

$$\frac{\partial \alpha_0}{\partial t} = -\frac{\partial \widetilde{\alpha}}{\partial t} \; . \tag{2.96}$$

If

$$\frac{\partial \alpha_0}{\partial t} \neq 0 \; , \qquad \frac{\partial \widetilde{\alpha}}{\partial t} \neq 0 \; , \tag{2.97}$$

the derivatives can be estimated using the characteristic times $\tau_{\mathrm{D}}(\alpha_0)$ and $\tau_{\mathrm{D}}(\widetilde{\alpha})$ of the macroscale and mesoscale processes, assuming that the characteristic changes of α_0 are on the order of α_0 and that the characteristic changes of $\widetilde{\alpha}$ are on the order of $\widetilde{\alpha}$:

$$\frac{\partial \alpha_0}{\partial t} \sim \frac{\alpha_0}{\tau_{\mathrm{D}}(\alpha_0)} \; , \qquad \frac{\partial \widetilde{\alpha}}{\partial t} \sim \frac{\widetilde{\alpha}}{\tau_{\mathrm{D}}(\widetilde{\alpha})} \; . \tag{2.98}$$

Using the estimates (2.98) in eq. (2.96) leads to the approximation

$$\frac{\tau_{\mathrm{D}}(\widetilde{\alpha})}{\tau_{\mathrm{D}}(\alpha_0)} \sim \frac{\widetilde{\alpha}}{\alpha_0} \; . \tag{2.99}$$

Since a scale separation regarding the macroscale and mesoscale dynamics with $\tau_{\mathrm{D}}(\widetilde{\alpha}) \ll \tau_{\mathrm{D}}(\alpha_0)$ is assumed, eq. (2.99) can only hold for $\widetilde{\alpha} \ll \alpha_0$, i.e. if the magnitude of the mesoscale variable is significantly smaller than its macroscale counterpart. This assumption has not been made yet for the generic multiscale model. Even if it were included in its requisites and eq. (2.96) were fulfilled, this would correspond to a somewhat particular situation for a multiscale system: at all points in space and time the time derivative of $\widetilde{\alpha}$ would have to balance exactly the time derivative of α_0 so that $\partial \alpha / \partial t = 0$. In how far such a system can be modeled efficiently by a multiscale approach will not be investigated here. Therefore, stationarity of α as expressed by eq. (2.94) can only be reached if

$$\frac{\partial \alpha_0}{\partial t} = \frac{\partial \widetilde{\alpha}}{\partial t} = 0 \; . \tag{2.100}$$

Eq. (2.100) means that both the macroscale and mesoscale dynamics are stationary. The associated multiscale model is obtained by setting the time derivatives in the balance equations (2.48), (2.49), (2.55), (2.56), (2.60), and (2.61) to zero and adapt the averaging operator $\langle ... \rangle$ to include only the spatial average.
However, it is unclear in how far stationary solutions for α exist. For the following coupled code studies the focus is therefore on case two, meaning that the macroscale system reaches a state of stationarity while the mesoscale system is in a statistically stationary state, i.e. still exhibits temporal fluctuations of its quantities $\widetilde{\alpha}$. For the macroscale particle balance this means for instance

$$\boldsymbol{\nabla} \cdot (n_0 \boldsymbol{v}_0) \overset{!}{=} -\boldsymbol{\nabla} \cdot \langle \widetilde{n} \widetilde{\boldsymbol{v}} \rangle \;, \tag{2.101}$$

assuming that the source term $\langle S_n^{ic} \rangle$ is negligible. Eq. (2.101) expresses that the divergence of the macroscale particle flux is balanced by the averaged divergence of the mesoscale particle flux. Note that relation (2.101) is less restrictive regarding the mesoscale dynamics than eq. (2.96) since it only affects the average of mesoscale quantities. The complete macroscale model is given by eqs. (2.48), (2.55), and (2.60) with the time derivatives $\partial \alpha_0 / \partial t$ set to zero. The mesoscale model is described by eqs. (2.49), (2.56), and (2.61) where the time derivatives of the mesoscale quantities are kept. A self-consistent solution for the considered system is found by iterating both the macroscale and mesoscale part until the macroscale quantities and the averaged mesoscale terms like $\langle \widetilde{n} \widetilde{\boldsymbol{v}} \rangle$ stay constant. This approach is used for the two-dimensional coupled code system presented in chapter 8.

3. Large scale model for the plasma edge

The main objectives of this thesis is to develop a specific multiscale model for describing the plasma in the edge region of a tokamak device, i.e. a future fusion reactor. In the former chapter 2, a generic multiscale model for a fluid has been presented and a coupled code system to solve the set of partial differential equations has been outlined. With this model as a basis, the next logical step towards a specific multiscale model is to characterize the fluid as a plasma (which is the state of matter present within a tokamak) and to apply the corresponding specifications to the mesoscale and macroscale parts of the generic multiscale model. Additional assumptions regarding the mesoscale and macroscale systems, e.g. regarding the geometry of the magnetic field and the relevant forces and sources, adapt the models to the dynamics they should capture: either the fast dynamics on comparably small spatial scales with times down to $\tau_{\mathrm{D}}(\widetilde{\alpha}) \sim 10^{-7}$ s and lengths down to $\lambda_{\mathrm{D}}(\widetilde{\alpha}) \sim 10^{-4}$ m or the transport on the large scales of the tokamak device with $\tau_{\mathrm{D}}(\alpha_0) \sim 1$ s and $\lambda_{\mathrm{D}}(\alpha_0) \sim 1$ m.

In this chapter, the focus lies on the derivation of a macroscale model which will form the macroscale part of the specific multiscale model in chapter 5, and an corresponding self-contained large scale model for the plasma edge. Self-contained refers to the fact that for solving the model equations, a mesoscale model is no longer needed – the averaged mesoscale terms, present in the macroscale model, are replaced by an ad-hoc macroscale transport model with transport coefficients prescribed by the modeler. The assumptions of both models are basically those of the B2 model used for description of the plasma edge in a tokamak device [28, 14, 29] to which also the self-contained large scale model bears a strong resemblance. The aspect that should be highlighted here is the macroscale models' relation to the macroscale part of a multiscale model, its equations depending explicitly on the averaged mesoscale terms.

The chapter is structured as follows. The tokamak device and the basics of its design, defining the area of application for the models, are outlined in paragraph 3.1. In paragraph 3.2, a summary of the widely used Braginskii closure [27] to specify the fluid as a magnetized, collisional plasma is given. It provides explicit expressions for the viscosity tensor $\mathbf{\Pi}$, the heat flux density $\boldsymbol{q}$, the force $\boldsymbol{F}$, and the source terms S^{ec}, appearing in the fluid balances of chapter 2. With this closure and the outline

of the tokamak, the fundamental columns of the physical system that is investigated in the following chapters are established.
The Braginskii closure is applied to the macroscale balances (2.48), (2.55), and (2.60) of the generic multiscale model. In paragraph 3.3, the resulting equations are further specified by a number of additional assumptions regarding the large scale transport which coincide with those of the B2 model outlined in [29], leading to the macroscale part of the specific multiscale model. To make the macroscale model self-contained, the averaged mesoscale terms are replaced by the widely used diffusive macroscale transport model for the perpendicular transport [15, 16, 29]. The large scale model is discussed in paragraph 3.4.

3.1. The tokamak device

The tokamak is a device to achieve nuclear fusion reactions by magnetic confinement of an extremely hot plasma. Extensive literature is available on this topic [50, 51, 52] so that here only the basic principles needed for the further understanding of the modeling challenges and the model assumptions should be given.

Fusion reactions, like the Deuterium-Tritium reaction

$$^{2}\mathrm{H} + {}^{3}\mathrm{H} \rightarrow {}^{4}\mathrm{He} + \mathrm{n} + 17.6\ \mathrm{MeV} \tag{3.1}$$

can only take place if the reactants have a high enough energy so that the repulsive Coulomb force between the ions is overcome and the strong interaction triggers the fusion between the nuclei. One concept is to heat the hydrogen isotopes and thereby increase their kinetic energy. For the required energies, the resulting state of matter is a plasma, i.e. a state where the electrons can no longer be assigned to specific atomic nuclei. Ions and electrons interact with each other mainly via the electromagnetic force and collisions. With plasma temperatures reaching up to 100 million Kelvin for the ITER tokamak currently built as in international undertaking in the South of France [53], one can easily imagine that the extremely hot plasma is to be prevented to be in contact with the vessel's wall.
The concept of magnetic confinement has been developed for this purpose since the 1950s. It is based on the use of magnetic fields to confine the plasma within a certain volume. The Lorentz force forces charged particles to gyrate around the magnetic field lines; the particles therefore have limited mobility in direction perpendicular to the field lines. With an adequate configuration of the magnetic field, a high rate of fusion reactions should be achievable while the plasma-wall interaction is kept at a minimum.

A sketch of a tokamak device is shown in fig. 3.1. The underlying shape of the plasma vessel is a torus, the plasma within being depicted in light pink. The magnetic field

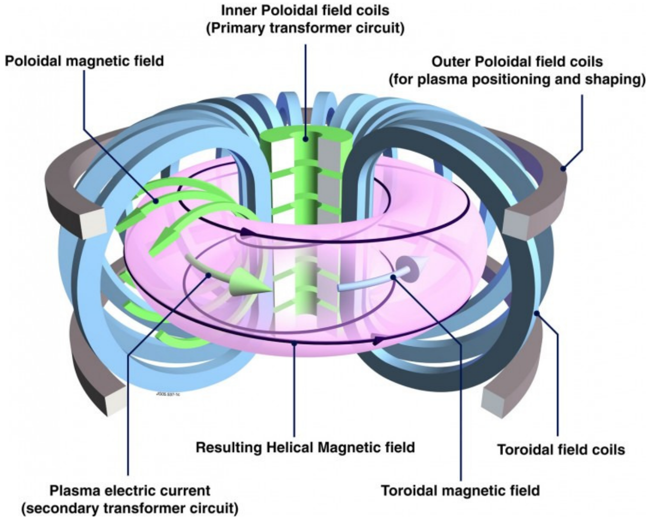

Figure 3.1.: Sketch of a tokamak device [54].

$\boldsymbol{B}$ used for confinement consists of two main components: a toroidal one, $\boldsymbol{B}_\varphi$, whose orientation is given by the thick blue arrow, generated by a set of toroidal field coils depicted in blue, and a poloidal one, $\boldsymbol{B}_\theta$, whose orientation is indicated by the flat green arrows. $\boldsymbol{B}_\theta$ is generated by a toroidal plasma current I_p whose direction is denoted by the thick green arrow. I_p is induced into the plasma by a changing magnetic field created by a set of inner poloidal field coils which are depicted in green. These coils can be understood as a primary transformer circuit while the plasma is the secondary transformer circuit. An additional set of outer poloidal field coils, depicted in gray, is used for plasma positioning and shaping. The field lines of the resulting magnetic field $\boldsymbol{B} = \boldsymbol{B}_\varphi + \boldsymbol{B}_\theta$ wind themselves helically around the torus (black line). These field lines represent the trajectories of charged particles in first order when gyration is neglected. The safety factor q is the number of toroidal turns a field line has to make to complete one poloidal turn. It can be defined as the poloidal angel $\Delta\phi$ covered by the field line per toroidal turn:

$$q \;\equiv\; \frac{\Delta\varphi}{2\pi}\;. \tag{3.2}$$

The direction of $\boldsymbol{B}$ and the field lines, respectively, provides the so-called parallel direction. Together with two vectors perpendicular to $\boldsymbol{B}$, an orthogonal trihedron can be constructed within the vessel. Transport of particles, energy, etc. in parallel direction is typically assumed to be much faster than in the perpendicular directions.

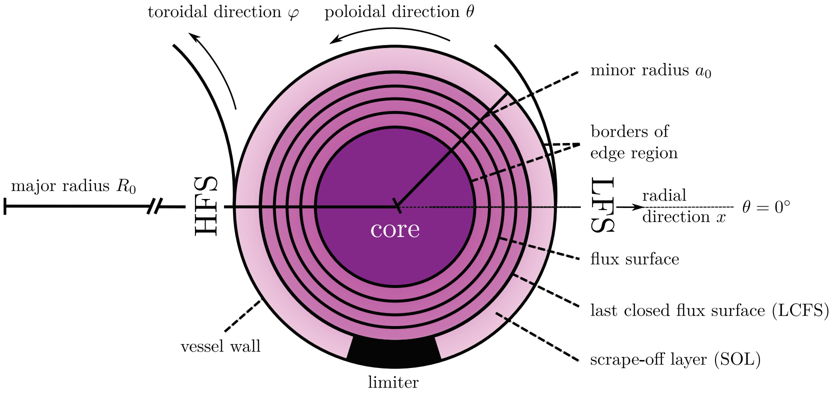

Figure 3.2.: Sketch of a poloidal cut of a tokamak device.

A poloidal cut through the toroidal vessel of a tokamak with a limiter is sketched in fig. 3.2. Here, the toroidal coordinate system, consisting of the radial coordinate x, the poloidal angle φ, and the toroidal angle θ, is presented. Details regarding this toroidal coordinate system can be found in [39]. For the further discussions it is convenient to introduce the poloidal magnetic flux function Ψ [50] which satisfies

$$\boldsymbol{B} \cdot \boldsymbol{\nabla} \Psi \;=\; 0\;. \tag{3.3}$$

A flux surface is given by the three-dimensional shape on which Ψ takes a constant value. The contours of the nested flux surfaces are given by the concentric circles in fig. 3.2. In the case of concentric flux surfaces centered within the vessel the radial direction and the direction normal to the flux surfaces coincide.

The volume in the plasma vessel is radially divided into two regions: the core region with the highest occurring temperatures and densities (typically $T \sim 10^8$ K and $n \sim 10^{20}$ m^{-3} for ITER) and the edge region where $T \lesssim 10^6$ K and $n \lesssim 10^{20}$ m^{-3}. The latter can be subdivided into a region of closed flux surfaces (which are not 'broken' by solid obstacles) and a region of open flux surfaces, the scrape-off layer (SOL). Responsible for the SOL is a solid structure protruding from the wall into the vessel, a so-called limiter, which typically exhibits toroidal symmetry. The density and temperature profiles typically decay exponentially in radial direction in the SOL. The major radius R_0, measuring the distance between the symmetry axis going through the torus' center and the center of the vessel, and the minor radius a_0 are important design parameters of the tokamak.

The configuration shown in fig. 3.2 is an idealization: in most modern day tokamaks the poloidal cut of the vessel usually has the shape of a D, with the contours of the flux surfaces being adapted to this profile. Also, the flux surfaces are typically

shifted against each other by the Grad-Shafranov shift [50]. However, the geometry assumed here allows for a significantly simplified numerically treatment of the models presented in chapters 3, 4, and 5. It still captures the strong anisotropy regarding the direction parallel and perpendicular to the field lines which is exploited in most of the existent models for the edge plasma in a tokamak [8, 11, 15, 16, 29].
Describing transport in direction normal to the flux surfaces (here coinciding with the radial direction) is crucial since this is the only way that particles, energy, etc. will reach the SOL and the vessel wall and thus the only way that the confinement of the plasma is lost. During the course of fusion research it was quickly found out that the reduction of mobility of the charged particles perpendicular to the field lines due to the Lorentz force is far from perfect: turbulent processes emerge which increase transport from the core outwards. These dynamics will strongly influence the characteristics of the plasma core where most of the fusion reactions take place. They also determine the heat and particle loads reaching the materials present in the outer region of the vessel and therefore set the requirements for their properties and design. For these reasons, one of the focus of the multiscale model derived here lies on a sophisticated description of this transport component, as it will be further elucidated below.

3.2. Braginskii closure for a collisional, magnetized plasma

For the transition from a generic fluid model to a specific model for the plasma dynamics the decisive step is to characterize the fluid as a plasma. This is done mainly through the choice of transport models and coefficients used for the viscosity tensor $\mathbf{\Pi}_a$ and the heat flux density $\boldsymbol{q}_a$, to name two examples. The approach employed here was first derived by Braginskii [27]. The presentation of its basic results is kept close to the discussion in [35].

A plasma consists of ions (subscript i) and electrons (subscript e). Typical quantities used for its characterization are the collision times τ_e and τ_i, which are

$$\tau_e \;=\; \frac{3^{1/2} 6\pi\, \varepsilon_0^2\, m_e^{1/2}\, T_e^{3/2}}{e^4 n_e \ln\Lambda} \,, \qquad \tau_i \;=\; \frac{3^{1/2} 6\pi\, \varepsilon_0^2\, m_i^{1/2}\, T_i^{3/2}}{Z_i^4 e^4 n_i \ln\Lambda} \,, \tag{3.4}$$

with ε_0 being the vacuum permittivity and Z_i the ion atomic number. For the Coulomb logarithm $\ln\Lambda$ [35] one has

$$\ln\Lambda \;\approx\; \ln\left(\frac{12\pi\varepsilon_0^{3/2}}{e^3}\frac{T_e^{3/2}}{n_e^{1/2}}\right) \,. \tag{3.5}$$

The gyration frequencies of ions and electrons, Ω_i and Ω_e, denoting the frequency with which particles gyrate around the magnetic field lines, are given by

$$\Omega_i \;=\; \frac{Z_i e B}{m_i}\;, \qquad \Omega_e \;=\; \frac{eB}{m_e}\;. \tag{3.6}$$

The plasma of interest, i.e. in the edge region of the tokamak, is considered to be strongly magnetized and collisional so that

$$\tau_a\,\Omega_a \;\gg\; 1\;, \tag{3.7}$$

where a again denotes the particle species.

If the plasma is in a state close to an equilibrium as it is assumed in the following models, the distribution function f_a, solving the Boltzmann equation (2.3), can be decomposed into an equilibrium part f_{0a} which is given by a Maxwellian distribution, and a small perturbation $\widetilde{f}_a$ so that $f_a = f_{0a} + \widetilde{f}_a$ with $\widetilde{f}_a \ll f_{0a}$. This allows to express the viscosity tensor $\mathbf{\Pi}_a$, the heat flux density $\boldsymbol{q}_a$, and the source terms S_a^{ec} appearing in the momentum and energy balance equations, such as eqs. (2.55), (2.56), (2.60), and (2.61) (where they are contained in the generalized sources $\boldsymbol{M}_a$ and W_a), as a linear combination of gradients of the moments n_a, $\boldsymbol{v}_a$, and T_a, and transport coefficients.

First, $\mathbf{\Pi}_a$ is specified by using the rate of strain tensor $\mathbf{W}_a$,

$$\mathbf{W}_a \;\equiv\; \frac{1}{2}\boldsymbol{\nabla}\boldsymbol{v}_a \;+\; \frac{1}{2}\Big(\boldsymbol{\nabla}\boldsymbol{v}_a\Big)^T \;-\; \frac{1}{3}\Big(\boldsymbol{\nabla}\cdot\boldsymbol{v}_a\Big)\mathbf{I}\;. \tag{3.8}$$

The components of $\Pi_{aij} = \hat{\boldsymbol{e}}_i \cdot \mathbf{\Pi}_a \cdot \hat{\boldsymbol{e}}_j$ are given for an orthogonal coordinate system where $\hat{\boldsymbol{e}}_\parallel$ is the unit vector pointing in direction parallel to the magnetic field ($\hat{\boldsymbol{e}}_\parallel \equiv \boldsymbol{B}/B$) and $\hat{\boldsymbol{e}}_{\perp_1}$ and $\hat{\boldsymbol{e}}_{\perp_2}$ are two unit vectors determining the two perpendicular directions:

$$\begin{aligned}
\Pi_{a\perp_1\perp_1} \;&=\; -\frac{\eta_{a0}}{2}\Big(W_{a\perp_1\perp_1} + W_{a\perp_2\perp_2}\Big) \;-\; \frac{\eta_{a1}}{2}\Big(W_{a\perp_1\perp_1} - W_{a\perp_2\perp_2}\Big) \;-\; \eta_{a3}W_{a\perp_1\perp_2}\;,\\
\Pi_{a\perp_2\perp_2} \;&=\; -\frac{\eta_{a0}}{2}\Big(W_{a\perp_1\perp_1} + W_{a\perp_2\perp_2}\Big) \;+\; \frac{\eta_{a1}}{2}\Big(W_{a\perp_1\perp_1} - W_{a\perp_2\perp_2}\Big) \;+\; \eta_{a3}W_{a\perp_1\perp_2}\;,\\
\Pi_{a\parallel\parallel} \;&=\; -\eta_{a0}W_{a\parallel\parallel}\;,\\
\Pi_{a\perp_1\perp_2} \;&=\; \Pi_{a\perp_2\perp_1} \;=\; -\eta_{a1}W_{a\perp_1\perp_2} \;+\; \frac{\eta_{a3}}{2}\Big(W_{a\perp_1\perp_1} - W_{a\perp_2\perp_2}\Big)\;,\\
\Pi_{a\perp_1\parallel} \;&=\; \Pi_{a\parallel\perp_1} \;=\; -\eta_{a2}W_{a\perp_1\parallel} \;-\; \eta_{a4}W_{a\perp_2\parallel}\;,\\
\Pi_{a\perp_2\parallel} \;&=\; \Pi_{a\parallel\perp_2} \;=\; -\eta_{a2}W_{a\perp_2\parallel} \;+\; \eta_{a3}W_{a\perp_1\parallel}\;.
\end{aligned} \tag{3.9}$$

The ion viscosity coefficients η_i are given by

$$\begin{aligned}\eta_{i0} &= 0.96\, n_i T_i \tau_i \ , \qquad \eta_{i1} = 0.3\, \frac{n_i T_i}{\Omega_i^2 \tau_i} \ , \qquad \eta_{i2} = 4\, \eta_{i1} \ , \\ \eta_{i3} &= 0.5\, \frac{n_i T_i}{\Omega_i} \ , \qquad \eta_{i4} = 2\, \eta_{i3} \ , \end{aligned} \tag{3.10}$$

the electron viscosity coefficients η_e by

$$\begin{aligned}\eta_{e0} &= 0.73\, n_e T_e \tau_e \ , \qquad \eta_{e1} = 0.51\, \frac{n_e T_e}{\Omega_e^2 \tau_e} \ , \qquad \eta_{e2} = 4\eta_{e1} \ , \\ \eta_{e3} &= -0.5\, \frac{n_e T_e}{\Omega_e} \ , \qquad \eta_{e4} = 2\, \eta_{e3} \ . \end{aligned} \tag{3.11}$$

For the ion and electron heat flux densities $\boldsymbol{q}_i$ and $\boldsymbol{q}_e$, the following expressions are derived:

$$\boldsymbol{q}_i = -\kappa_{\parallel i} \boldsymbol{\nabla}_\parallel T_i - \kappa_{\perp i} \boldsymbol{\nabla}_\perp T_i - \kappa_{\wedge i}\, \hat{\boldsymbol{e}}_\parallel \times \boldsymbol{\nabla}_\perp T_i \ , \tag{3.12}$$

$$\boldsymbol{q}_e = -\kappa_{\parallel e} \boldsymbol{\nabla}_\parallel T_e - \kappa_{\perp e} \boldsymbol{\nabla}_\perp T_e - \kappa_{\wedge e}\, \hat{\boldsymbol{e}}_\parallel \times \boldsymbol{\nabla}_\perp T_e - \zeta_{\parallel e} \boldsymbol{j}_\parallel - \zeta_{\wedge e} \hat{\boldsymbol{e}}_\parallel \times \boldsymbol{j} \ . \tag{3.13}$$

The subscript $\wedge$ denotes the so-called diamagnetic components. Here, $\boldsymbol{j}$ is the electric current density:

$$\boldsymbol{j} = Z_i e n_i \boldsymbol{u} - e n_e \boldsymbol{v} \ . \tag{3.14}$$

The vector $\boldsymbol{u} \equiv \boldsymbol{v}_i$ denotes the ion velocity and $\boldsymbol{v} \equiv \boldsymbol{v}_e$ is the electron velocity. The parallel gradient $\boldsymbol{\nabla}_\parallel$ and its perpendicular counterpart $\boldsymbol{\nabla}_\perp$ are defined as

$$\boldsymbol{\nabla}_\parallel \equiv \hat{\boldsymbol{e}}_\parallel \hat{\boldsymbol{e}}_\parallel \cdot \boldsymbol{\nabla} \ , \qquad \boldsymbol{\nabla}_\perp \equiv \boldsymbol{\nabla} - \boldsymbol{\nabla}_\parallel \ . \tag{3.15}$$

Both $\boldsymbol{q}_i$ and $\boldsymbol{q}_e$ describe heat conduction due to temperature gradients. The electron heat flux density $\boldsymbol{q}_e$ additionally includes heat transport due to particle flow, being determined by the terms proportional to $\boldsymbol{j}$ in eq. (3.13). The transport coefficients are given by

$$\begin{aligned}\kappa_{\parallel i} &= 3.9\, \frac{n_i T_i \tau_i}{m_i} \ , & \kappa_{\parallel e} &= 3.2\, \frac{n_e T_e \tau_e}{m_e} \ , \\ \kappa_{\perp i} &= 2.0\, \frac{n_i T_i}{m_i \Omega_i^2 \tau_i} \ , & \kappa_{\perp e} &= 4.7\, \frac{n_e m_e T_e}{e^2 B^2 \tau_e} \ , \\ \kappa_{\wedge i} &= -\frac{5}{2}\, \frac{n_i T_i}{m_i \Omega_i} \ , & \kappa_{\wedge e} &= \frac{5}{2}\, \frac{n_e T_e}{e B} \ , \end{aligned}$$

$$\zeta_{\parallel e} \;=\; 0.71\,\frac{T_e}{e}\;, \qquad\qquad \zeta_{\wedge e} \;=\; \frac{3}{2}\,\frac{T_e}{e\,\Omega_e\tau_e}\;. \tag{3.16}$$

Next, the force $\boldsymbol{F}_a$ and the source term S_a^F are evaluated. For charged particles moving in an electric and magnetic field $\boldsymbol{F}_a$ is determined by the Lorentz force:

$$\boldsymbol{F}_a \;=\; q_a\Big[\boldsymbol{E} \;+\; \Big(\boldsymbol{V}\times\boldsymbol{B}\Big)\Big]\;. \tag{3.17}$$

The gravitational force is neglected since it is small compared to the electromagnetic forces. The source terms $\boldsymbol{S}_{amV}^F$ and S_{aE}^F, defined by eqs. (2.19a) and (2.19b), yield:

$$\boldsymbol{S}_{amV}^F \;=\; q_a n_a\Big[\boldsymbol{E} \;+\; \Big(\boldsymbol{v}_a\times\boldsymbol{B}\Big)\Big]\;, \tag{3.18}$$

$$S_{aE}^F \;=\; q_a n_a \boldsymbol{E}\cdot\boldsymbol{v}_a\;. \tag{3.19}$$

As described in paragraph 2.1, the collision term C_a (which is needed for the evaluation of the source terms S^{ic} and S^{ec}) can be divided into two parts, $C_a = C_a^{ec} + C_a^{ic}$. While the terms S_a^{ic} which are related to C_a^{ic} by eqs. (2.21), (2.22b) and (2.23b) are kept here as unknowns (for a comprehensive investigation see [55]), the terms S_a^{ec}, defined by eqs. (2.22a) and (2.23a), are further evaluated. $\boldsymbol{S}_{amV}^{ec}$ from the rhs of the fluid momentum balance (2.25) consists of two parts: a friction force $\boldsymbol{R}_a^f$ due to differences in the fluid velocities of ions and electrons, and a thermal force $\boldsymbol{R}_a^T$ due to temperature gradients. One can define:

$$\boldsymbol{S}_{amV}^{ec} \;\equiv\; \boldsymbol{R}_a \;=\; \boldsymbol{R}_a^f \;+\; \boldsymbol{R}_a^T\;. \tag{3.20}$$

For electrons it holds

$$\boldsymbol{R}_e^f \;=\; en_e\left(\frac{\boldsymbol{j}_\parallel}{\sigma_\parallel} \;+\; \frac{\boldsymbol{j}_\perp}{\sigma_\perp}\right)\;, \tag{3.21}$$

$$\boldsymbol{R}_e^T \;=\; -\frac{en_e}{T_e}\Big(\zeta_{\parallel e}\boldsymbol{\nabla}_\parallel T_e \;+\; \zeta_{\wedge e}\,\hat{\boldsymbol{e}}_\parallel\times\boldsymbol{\nabla}_\perp T_e\Big)\;. \tag{3.22}$$

The specific conductivities $\sigma_\parallel$ and $\sigma_\perp$ in parallel and perpendicular direction, respectively, are

$$\sigma_\parallel \;=\; \frac{2n_e e^2\tau_e}{m_e}\;, \qquad \sigma_\perp \;=\; \frac{n_e e^2\tau_e}{m_e}\;. \tag{3.23}$$

For a hydrogen plasma one has:

$$\boldsymbol{R}_i \;=\; -\,\boldsymbol{R}_e\;. \tag{3.24}$$

The source term S_{aE}^{ec} of the energy balance (2.26) is defined as

$$S_{aE}^{ec} \;\equiv\; Q_a \;+\; \boldsymbol{v}_a\cdot\boldsymbol{R}_a \tag{3.25}$$

with

$$Q_i \;=\; \frac{3}{2}\frac{T_e - T_i}{\tau^{\epsilon}_{ei}} \;, \qquad Q_e \;=\; -Q_i \;-\; \boldsymbol{R}_e(\boldsymbol{v}-\boldsymbol{u}) \;. \tag{3.26}$$

The form of Q_i and Q_e corresponds to the fact that a temperature difference between ions and electrons will lead to an equilibration process between both species, with the characteristic time scale determined by the electron-ion temperature relaxation time τ^{ϵ}_{ei}:

$$\tau^{\epsilon}_{ei} \;\approx\; \frac{(2\pi)^{1/2}\, 3\pi m_i m_e^{-1/2} T_e^{3/2}}{Z_i^2 e^4 n_i \ln\Lambda} \;. \tag{3.27}$$

With eqs. (3.18) and (3.20) the generalized momentum density source $\boldsymbol{M}_a$, given by eq. (2.53), becomes

$$\begin{aligned}\boldsymbol{M}_a \;=\;& q_a n_a\Big[\boldsymbol{E} + \Big(\boldsymbol{v}_a \times \boldsymbol{B}\Big)\Big] \;+\; \boldsymbol{R}_a \;-\; \boldsymbol{\nabla}\cdot\boldsymbol{\Pi}_a \\ &-\; \boldsymbol{\nabla} p_a \;+\; \boldsymbol{S}^{ic}_{amV} \;-\; m_a \boldsymbol{v}_a S^{ic}_{an} \;,\end{aligned} \tag{3.28}$$

and the generalized energy density source W_a, see eq. (2.58), yields with eqs. (3.12), (3.13), and (3.25):

$$\begin{aligned}W_a \;=\;& Q_a \;-\; p_a \boldsymbol{\nabla}\cdot\boldsymbol{v}_a \;-\; \boldsymbol{\Pi}_a : \boldsymbol{\nabla}\boldsymbol{v}_a \;-\; \boldsymbol{\nabla}\cdot\boldsymbol{q}_a \\ &+\; \left(\frac{m_a v_a^2}{2} - \frac{3}{2}T_a\right) S^{ic}_{an} \;-\; \boldsymbol{v}_a\cdot\boldsymbol{S}^{ic}_{amV} \;+\; S^{ic}_{aE} \;.\end{aligned} \tag{3.29}$$

Expressions (3.28) and (3.29) are now used for the macroscale part of the generic multiscale model, represented in its conservative form by the balance eqs. (2.50), (2.57) and (2.62). The averaged terms $\langle \boldsymbol{M}_a/n_a\rangle$ and $\langle W_a/n_a\rangle$ are evaluated using the macroscale quantities only ($\alpha \approx \alpha_0$), the species index a is omitted for clarity. The resulting macroscale model for a collisional, strongly magnetized plasma consists of a **particle balance**,

$$\frac{\partial n_0}{\partial t} \;+\; \boldsymbol{\nabla}\cdot\Big(n_0\boldsymbol{v}_0\Big) \;=\; S^{ic}_{0n} \;-\; \boldsymbol{\nabla}\cdot\langle\tilde{n}\tilde{\boldsymbol{v}}\rangle \;, \tag{3.30}$$

a **momentum balance**,

$$\begin{aligned}\frac{\partial}{\partial t}\Big(m n_0 \boldsymbol{v}_0\Big) \;+\; \boldsymbol{\nabla}\cdot\Big(m n_0 \boldsymbol{v}_0\boldsymbol{v}_0\Big) \;=\;& q n_0\left[\boldsymbol{E}_0 + (\boldsymbol{v}_0\times\boldsymbol{B}_0)\right] \;+\; \boldsymbol{R}_0 \\ -\; \boldsymbol{\nabla}\cdot\boldsymbol{\Pi}_0 \;-\; \boldsymbol{\nabla}p_0 \;+\; \boldsymbol{S}^{ic}_{0mV} \;-\; m n_0\Big\langle\tilde{\boldsymbol{v}}\cdot\boldsymbol{\nabla}\tilde{\boldsymbol{v}}\Big\rangle \;-\;& m\boldsymbol{v}_0\,\boldsymbol{\nabla}\cdot\langle\tilde{n}\tilde{\boldsymbol{v}}\rangle \;,\end{aligned} \tag{3.31}$$

and an **energy balance**,

$$
\boxed{
\begin{aligned}
&\frac{\partial}{\partial t}\left(\frac{3}{2}n_0T_0 + \frac{1}{2}mn_0v_0^2\right) + \boldsymbol{\nabla}\cdot\left(\frac{5}{2}n_0T_0\boldsymbol{v}_0 + \frac{1}{2}mn_0v_0^2\boldsymbol{v}_0\right)\\
&\qquad = qn_0\boldsymbol{v}_0\cdot\boldsymbol{E}_0 + \boldsymbol{v}_0\cdot\boldsymbol{R}_0 - \boldsymbol{\nabla}\cdot\Big(\boldsymbol{v}_0\cdot\boldsymbol{\Pi}\Big) + Q_0 - \boldsymbol{\nabla}\cdot\boldsymbol{q}_0 + S_{0E}^{ic}\\
&\qquad - \frac{3}{2}n_0\left\langle\tilde{\boldsymbol{v}}\cdot\boldsymbol{\nabla}\tilde{T}\right\rangle - mn_0\boldsymbol{v}_0\cdot\left\langle\tilde{\boldsymbol{v}}\cdot\boldsymbol{\nabla}\tilde{\boldsymbol{v}}\right\rangle - \left(\frac{3}{2}T_0 + \frac{1}{2}mv_0^2\right)\boldsymbol{\nabla}\cdot\langle\tilde{n}\tilde{\boldsymbol{v}}\rangle\,. \qquad (3.32)
\end{aligned}
}
$$

Note that eqs. (3.30) to (3.32) still contain averaged mesoscale terms for whose evaluation a local mesoscale system is needed.

3.3. The large scale model

In this paragraph, the large scale model for the plasma edge is outlined. It differs from eqs. (3.30) to (3.32) on the one hand by a number of additional assumptions regarding the geometry and the magnetic field which are introduced in paragraph 3.3.1 and are based on those of the B2 model [29]. On the other hand, it employs a macroscale transport model, presented in paragraph 3.3.2, to represent the averaged mesoscale terms. The large scale model equations are outlined in paragraph 3.3.3 and discussed in paragraph 3.4. An intermediate form of them, still including the averaged mesoscale terms in their original form, is given in paragraph 3.3.1. These equations will be related to the macroscale part of the specific multiscale model in chapter 5.

3.3.1. Assumptions of the large scale edge model

The main assumptions included in the large scale edge model comprise the following points:

- The plasma is taken to be quasineutral: a plasma volume of dimensions above the Debye length λ_D [35], i.e. the length above which an electrostatic perturbation is effectively shielded, is assumed to have only small net charge. Therefore $q_in_i \approx -q_en_e$. For a hydrogen plasma this yields:

  $$n_i \approx n_e\,. \qquad (3.33)$$

  The assumption of quasineutrality reduces the number of model equations by one because it is not necessary to consider separate ion and electron particle balances anymore. In the following derivations, both densities are denoted by n_0.

- The ambipolarity condition implies that no currents are present in the edge plasma:

  $$\boldsymbol{j} \;=\; 0 \qquad \rightarrow \qquad \boldsymbol{v} \;=\; \boldsymbol{u} \;. \tag{3.34}$$

  This assumption also means that the induced plasma current I_p becomes zero in the edge region. The ambipolarity condition reduces the set of equations by one since one of the momentum balances becomes redundant. For the large scale edge model the ion momentum balance for $\boldsymbol{u}$ will be used.

- The macroscale velocity is assumed to have only a parallel part:

  $$\boldsymbol{u}_0 \;=\; \boldsymbol{u}_{\|0} \;, \tag{3.35}$$

  so that $\boldsymbol{u}_{\perp 0} = 0$. It is based on the idea that the mobility of charged particles in directions perpendicular to the magnetic field lines is efficiently reduced due to the Lorentz force.

- The tokamak vessel, the magnetic field $\boldsymbol{B}$, and the profiles of the macroscale plasma quantities α_0 are assumed to be toroidally symmetric. Even though this symmetry can, for example, be broken by block limiters [56], resonant magnetic perturbation fields [57], or plasma turbulence [11], it serves as a first order approximation regarding the macroscale dynamics. The plasma quantities then no longer depend on the toroidal angle φ:

  $$\frac{\partial \alpha_0}{\partial \varphi} \;=\; 0 \;. \tag{3.36}$$

  The problem of describing the plasma in the edge region is therefore reduced from three to two dimensions.

- The magnetic field $\boldsymbol{B}$ does not depend explicitly on time:

  $$\frac{\partial \boldsymbol{B}}{\partial t} \;=\; 0 \;. \tag{3.37}$$

  Spatial derivatives of $\boldsymbol{B}$ are only partly evaluated.

The above assumptions are used to further transform the macroscale balances (3.30) to (3.32) to yield equations for the density n_0, the ion parallel velocity $\boldsymbol{u}_{\|0}$, and the ion and electron temperature T_{0i} and T_{0e}. To determine n_0 the ion particle balance

(3.30) is employed:

$$\boxed{\frac{\partial n_0}{\partial t} \;+\; \boldsymbol{\nabla}\cdot\left(n_0\boldsymbol{u}_{\|0}\right) \;=\; S^{ic}_{0in} \;-\; \boldsymbol{\nabla}\cdot\left\langle\tilde{n}\tilde{\boldsymbol{u}}\right\rangle \;. \qquad (3.38)}$$

The macroscale parallel ion velocity $\boldsymbol{u}_{\|0}$ is determined by the total parallel momentum balance. The latter is obtained by taking a reduced electron momentum balance, consisting of the electron version of eq. (3.31), and neglecting all terms proportional to m_e due to its smallness:

$$\boldsymbol{\nabla} p_{0e} \;=\; -en_0\boldsymbol{E}_0 \;-\; \boldsymbol{R}_{0i} \;. \qquad (3.39)$$

Adding the corresponding ion version of eq. (3.31) yields:

$$\begin{aligned}\frac{\partial}{\partial t}\Big(m_i n_0\boldsymbol{u}_0\Big) + \boldsymbol{\nabla}\cdot\Big(m_i n_0\boldsymbol{u}_0\boldsymbol{u}_0\Big) \;&=\; -\boldsymbol{\nabla}\cdot\boldsymbol{\Pi}_{0i} - \boldsymbol{\nabla}(p_{0i}+p_{0e}) + \boldsymbol{S}^{ic}_{0imV} \\ &\quad - m_i n_0\left\langle\tilde{\boldsymbol{u}}\cdot\boldsymbol{\nabla}\tilde{\boldsymbol{u}}\right\rangle - m_i\boldsymbol{u}_0\,\boldsymbol{\nabla}\cdot\left\langle\tilde{n}\tilde{\boldsymbol{u}}\right\rangle \;. \qquad (3.40)\end{aligned}$$

The parallel component of eq. (3.40) is given by

$$\begin{aligned}\frac{\partial}{\partial t}\Big(m_i n_0 u_{\|0}\Big) + \Big[\boldsymbol{\nabla}\cdot\Big(m_i n_0\boldsymbol{u}_0\boldsymbol{u}_0\Big)\Big]_{\|} &= -\Big[\boldsymbol{\nabla}\cdot\boldsymbol{\Pi}_{0i}\Big]_{\|} - \nabla_{\|}(p_{0i}+p_{0e}) + S^{ic}_{\|0imV} \\ &\quad - m_i n_0\left\langle\tilde{\boldsymbol{u}}\cdot\boldsymbol{\nabla}\tilde{\boldsymbol{u}}\right\rangle_{\|} - m_i u_{\|0}\,\boldsymbol{\nabla}\cdot\left\langle\tilde{n}\tilde{\boldsymbol{u}}\right\rangle . \qquad (3.41)\end{aligned}$$

With the tensor and vector identities

$$\boldsymbol{\nabla}\cdot(\boldsymbol{a}\boldsymbol{b}) \;=\; \boldsymbol{a}\cdot\boldsymbol{\nabla}\boldsymbol{b} \;+\; (\boldsymbol{\nabla}\cdot\boldsymbol{a})\boldsymbol{b} \;, \qquad (3.42)$$

$$\boldsymbol{\nabla}(\boldsymbol{a}\cdot\boldsymbol{b}) \;=\; (\boldsymbol{\nabla}\boldsymbol{a})\cdot\boldsymbol{b} \;+\; (\boldsymbol{\nabla}\boldsymbol{b})\cdot\boldsymbol{a} \;, \qquad (3.43)$$

the terms $[\boldsymbol{\nabla}\cdot(m_i n_0\boldsymbol{u}_0\boldsymbol{u}_0)]_{\|}$ and $m_i n_0\langle\tilde{\boldsymbol{u}}\cdot\boldsymbol{\nabla}\tilde{\boldsymbol{u}}\rangle_{\|}$ are evaluated:

$$\begin{aligned}\Big[\boldsymbol{\nabla}\cdot\Big(m_i n_0\boldsymbol{u}_0\boldsymbol{u}_0\Big)\Big]_{\|} \;&=\; \Big[m_i n_0\boldsymbol{u}_0\cdot\boldsymbol{\nabla}\boldsymbol{u}_0\Big]_{\|} \;+\; m_i u_{\|0}\boldsymbol{\nabla}\cdot\left(n_0\boldsymbol{u}_0\right) \\ &=\; \boldsymbol{\nabla}\cdot\Big(m_i n_0 u_{\|0}\boldsymbol{u}_0\Big) \;, \qquad (3.44) \\ m_i n_0\left\langle\tilde{\boldsymbol{u}}\cdot\boldsymbol{\nabla}\tilde{\boldsymbol{u}}\right\rangle_{\|} \;&=\; m_i n_0\left\langle\tilde{\boldsymbol{u}}\cdot\boldsymbol{\nabla}\tilde{u}_{\|}\right\rangle \;. \qquad (3.45)\end{aligned}$$

The total parallel momentum balance becomes

$$\boxed{\begin{aligned}\frac{\partial}{\partial t}\Big(m_i n_0 u_{\|0}\Big) + \boldsymbol{\nabla}\cdot\Big(m_i n_0 u_{\|0}\boldsymbol{u}_{\|0}\Big) \;&=\; -\Big[\boldsymbol{\nabla}\cdot\boldsymbol{\Pi}_{0i}\Big]_{\|} - \nabla_{\|}(p_{0i}+p_{0e}) + S^{ic}_{\|0imV} \\ &\quad - m_i n_0\left\langle\tilde{\boldsymbol{u}}\cdot\boldsymbol{\nabla}\tilde{u}_{\|}\right\rangle - m_i u_{\|0}\,\boldsymbol{\nabla}\cdot\left\langle\tilde{n}\tilde{\boldsymbol{u}}\right\rangle . \qquad (3.46)\end{aligned}}$$

The energy balance (3.32) for the ions with the assumptions listed above is

$$\boxed{\begin{aligned} \frac{\partial}{\partial t}\left(\frac{3}{2}n_0T_{0i}+\frac{1}{2}\,m_in_0u_{\|0}^2\right) \;+\; \boldsymbol{\nabla}\cdot\left(\frac{5}{2}n_0T_{0i}\boldsymbol{u}_{\|0}+\frac{1}{2}m_in_0u_{\|0}^2\boldsymbol{u}_{\|0}\right)& \\ = \;-u_{\|0}\nabla_{\|}p_{0e} - \;\boldsymbol{\nabla}\cdot\Big(\boldsymbol{u}_{\|0}\cdot\boldsymbol{\Pi}_{0i}\Big) \;+\; Q_{0i} \;-\; \boldsymbol{\nabla}\cdot\boldsymbol{q}_{0i}& \\ +\; S^{ic}_{0Ei} \;-\; m_in_0u_{\|0}\Big\langle\widetilde{\boldsymbol{u}}\cdot\boldsymbol{\nabla}\widetilde{u}_{\|}\Big\rangle \;-\; \frac{3}{2}n_0\Big\langle\widetilde{\boldsymbol{u}}\cdot\boldsymbol{\nabla}\widetilde{T}_i\Big\rangle& \\ -\;\left(\frac{3}{2}T_{0i}+\frac{1}{2}m_iu_{\|0}^2\right)\boldsymbol{\nabla}\cdot\langle\widetilde{n}\widetilde{\boldsymbol{u}}\rangle\;,& \qquad (3.47) \end{aligned}}$$

where the reduced electron momentum balance (3.39) was used. For the electron energy balance one has analogously

$$\boxed{\begin{aligned} \frac{\partial}{\partial t}\left(\frac{3}{2}n_0T_{0e}\right) \;+\; \boldsymbol{\nabla}\cdot\left(\frac{5}{2}n_0T_{0e}\boldsymbol{u}_{\|0}\right) \;=\; u_{\|0}\nabla_{\|}p_{0e} \;+\; Q_{0e} \;-\; \boldsymbol{\nabla}\cdot\boldsymbol{q}_{0e} \;+\; S^{ic}_{0Ee}& \\ -\;\frac{3}{2}n_0\Big\langle\widetilde{\boldsymbol{u}}\cdot\boldsymbol{\nabla}T_e\Big\rangle \;-\; \frac{3}{2}T_{0e}\,\boldsymbol{\nabla}\cdot\langle\widetilde{n}\widetilde{\boldsymbol{u}}\rangle\,.& \qquad (3.48) \end{aligned}}$$

3.3.2. Specification of the macroscale transport model

To solve the macroscale balance equations (3.38), (3.46), (3.47) and (3.48) without having a mesoscale model at hand to evaluate the averaged mesoscale terms like $\langle\widetilde{n}\widetilde{\boldsymbol{u}}\rangle$ a macroscale transport model is required. Here, it is resorted to the diffusion hypothesis introduced in paragraph 2.3.3, see eq. (2.88), to find expressions for the terms of the form $\langle\widetilde{\alpha}\widetilde{\boldsymbol{u}}\rangle$ and $\langle\widetilde{\boldsymbol{u}}\cdot\boldsymbol{\nabla}\widetilde{\alpha}\rangle$. $\mathcal{M}$ is given by

$$\mathcal{M}\Big(\langle\widetilde{\boldsymbol{u}}\cdot\boldsymbol{\nabla}\widetilde{\alpha}\rangle;\alpha_0\Big) \;=\; \mathcal{M}\Big(\Big\langle\boldsymbol{\nabla}\cdot(\widetilde{\alpha}\widetilde{\boldsymbol{u}})\Big\rangle;\alpha_0\Big) \;\equiv\; -\boldsymbol{\nabla}\cdot\Big(D_\perp\boldsymbol{\nabla}_\perp\,\alpha_0\Big)\;, \qquad (3.49)$$

with $D_\perp$ being an arbitrary diffusion coefficient which can be chosen by the modeler according to experimental measurements or theoretical considerations, for example. In chapter 6 it is shown that for certain properties of the velocity field $\widetilde{\boldsymbol{u}}$ and the quantity $\widetilde{\alpha}$ being a passive scalar regarding the advection by $\widetilde{\boldsymbol{u}}$, eq. (3.49) becomes exact, with $D_\perp$ depending only on the statistical properties of $\widetilde{\boldsymbol{u}}$[1]. ‘Passive’ refers to the fact that the dynamics of the mesoscale quantities $\widetilde{\alpha}$ have no influence on $\widetilde{\boldsymbol{u}}$. For

---

[1] The requirements are that the velocity field $\widetilde{\boldsymbol{u}}(\boldsymbol{r},t)$ is isotropic, divergence-free, has a Gaussian PDF, a correlation length $\lambda_c(\widetilde{\boldsymbol{u}})$, a correlation time $\tau_c(\widetilde{\boldsymbol{u}})$ and a root mean square velocity $\widetilde{u}_{\mathrm{RMS}}$ with $\widetilde{u}_{\mathrm{RMS}}\tau_c(\widetilde{\boldsymbol{u}})/\lambda_c(\widetilde{\boldsymbol{u}}) \ll 1$.

the macroscale transport model here it is additionally assumed that

$$\left\langle \widetilde{\boldsymbol{u}}_{\|} \cdot \boldsymbol{\nabla} \widetilde{\alpha} \right\rangle \ll \left\langle \widetilde{\boldsymbol{u}}_{\perp} \cdot \boldsymbol{\nabla} \widetilde{\alpha} \right\rangle , \tag{3.50}$$

so that only the *perpendicular* transport is considered in the evaluation of the averaged mesoscale terms. Also,

$$\left\langle \widetilde{\boldsymbol{u}} \cdot \boldsymbol{\nabla} \widetilde{u}_{\|} \right\rangle = -\boldsymbol{\nabla} \cdot \left(D_{\perp} \boldsymbol{\nabla}_{\perp} u_{\|0} \right) , \tag{3.51}$$

which, in the picture of the passive scalar model of chapter 6, means that $\widetilde{u}_{\|}$ is taken to act like a passive scalar regarding the advection via $\widetilde{\boldsymbol{u}}_{\perp}$.

Together with the diffusion hypothesis, a perpendicular viscosity coefficient $\eta_{\perp}$ and a thermal conductivity $\kappa_{\perp}$ can be introduced to describe averaged mesoscale momentum and energy transport in perpendicular direction:

$$\eta_{\perp} = m_i n_0 D_{\perp} , \qquad \kappa_{\perp} = n_0 D_{\perp} . \tag{3.52}$$

3.3.3. Model equations of the self-contained large scale edge model

The large scale model for the plasma edge is obtained by applying the diffusion hypothesis, represented by eqs. (3.49) to (3.52), to the macroscale balances (3.38), (3.46), (3.47) and (3.48). The **ion particle balance** becomes:

$$\frac{\partial n_0}{\partial t} + \boldsymbol{\nabla} \cdot \left(n_0 \boldsymbol{u}_{\perp}^{*} + n_0 \boldsymbol{u}_{\|0} \right) = S_{0in}^{ic} , \tag{3.53}$$

where an effective perpendicular velocity $\boldsymbol{u}_{\perp}^{*}$ has been introduced:

$$\boldsymbol{u}_{\perp}^{*} \equiv -\frac{D_{\perp}}{n_0} \boldsymbol{\nabla}_{\perp} n_0 . \tag{3.54}$$

For the **total momentum balance** one has

$$\begin{aligned} \frac{\partial}{\partial t}\left(m_i n_0 u_{\|0} \right) &+ \boldsymbol{\nabla} \cdot \left(m_i n_0 u_{\|0} \boldsymbol{u}_{\perp}^{*} + m_i n_0 u_{\|0} \boldsymbol{u}_{\|0} \right) \\ &= -\left[\boldsymbol{\nabla} \cdot \boldsymbol{\Pi}_{0i} \right]_{\|} + \boldsymbol{\nabla} \cdot \left(\eta_{\perp} \boldsymbol{\nabla}_{\perp} u_{\|0} \right) - \nabla_{\|} \left(p_{0i} + p_{0e} \right) \\ &+ S_{\|0imV}^{ic} + 2 m_i n_0 \boldsymbol{u}_{\perp}^{*} \cdot \boldsymbol{\nabla}_{\perp} u_{\|0} . \end{aligned} \tag{3.55}$$

The **ion energy balance** yields

$$\begin{aligned}
&\frac{\partial}{\partial t}\left(\frac{3}{2}n_0T_{0i}+\frac{1}{2}m_in_0u_{\|0}^2\right) + \boldsymbol{\nabla}\cdot\left(\frac{3}{2}n_0T_{0i}\boldsymbol{u}_\perp^* + \frac{5}{2}n_0T_{0i}\boldsymbol{u}_{\|0}\right)\\
&\quad + \boldsymbol{\nabla}\cdot\left(\frac{1}{2}m_in_0u_{\|0}^2\boldsymbol{u}_\perp^* + \frac{1}{2}m_in_0u_{\|0}^2\boldsymbol{u}_{\|0}\right) - \boldsymbol{\nabla}\cdot\left(\frac{3}{2}\kappa_\perp\boldsymbol{\nabla}_\perp T_{0i} + \frac{1}{2}\eta_\perp\boldsymbol{\nabla}_\perp u_{\|0}^2\right)\\
&\quad = -u_{\|0}\nabla_\| p_{0e} - \boldsymbol{\nabla}\cdot\left(\boldsymbol{u}_{\|0}\cdot\boldsymbol{\Pi}_{0i}\right) + Q_{0i} - \boldsymbol{\nabla}\cdot\boldsymbol{q}_{0i} + S_{0iE}^{ic} + \eta_\perp\left(\boldsymbol{\nabla}_\perp u_{\|0}\right)^2\\
&\quad + 3n_0\boldsymbol{u}_\perp^*\cdot\boldsymbol{\nabla}_\perp T_{0i} + m_in_0\boldsymbol{u}_\perp^*\cdot\boldsymbol{\nabla}_\perp u_{\|0}^2\ , \qquad (3.56)
\end{aligned}$$

and the **electron energy balance** gives

$$\begin{aligned}
&\frac{\partial}{\partial t}\left(\frac{3}{2}n_0T_{0e}\right) + \boldsymbol{\nabla}\cdot\left(\frac{3}{2}n_0T_{0e}\boldsymbol{u}_\perp^* + \frac{5}{2}n_0T_{0e}\boldsymbol{u}_{\|0}\right) - \boldsymbol{\nabla}\cdot\left(\frac{3}{2}\kappa_\perp\boldsymbol{\nabla}_\perp T_{0e}\right)\\
&\qquad = u_{\|0}\nabla_\| p_{0e} + Q_{0e} - \boldsymbol{\nabla}\cdot\boldsymbol{q}_{0e} + S_{0Ee}^{ic} + 3n_0\boldsymbol{u}_\perp^*\cdot\boldsymbol{\nabla}_\perp T_{0e}\,. \qquad (3.57)
\end{aligned}$$

3.4. Discussion of the large scale model

The particle balance (3.53), the total parallel momentum balance (3.55) and the ion and electron energy balances, eqs. (3.56) and (3.57), are the evolution equations for the variables n_0, $\boldsymbol{u}_{\|0}$, T_{0i} and T_{0e} of the large scale model for the plasma edge. Due to the quasineutrality and ambipolarity condition, the original number of ten equations of the fluid model with the Braginskii closure, given by eqs. (3.30), (3.31), and (3.32), is reduced to four. The assumption of toroidal symmetry allows for a reduction of the problem from three to two spatial dimensions. Using the diffusion hypothesis of paragraph 3.3.2, the averaged mesoscale terms of the form $\langle\widetilde{n}\widetilde{\boldsymbol{u}}\rangle$ and $\langle\widetilde{\boldsymbol{u}}\cdot\boldsymbol{\nabla}\widetilde{\alpha}\rangle$ are described by a linear combination of the transport coefficients $D_\perp$, $\eta_\perp$, $\kappa_\perp$, and macroscale radial gradients of the related macroscale quantities. Transport in radial direction in this model is purely due to averaged mesoscale processes modeled by a diffusion. The final large scale model equations bear a strong resemblance to the model of the B2 simulation code [28, 29] which is presented in chapter 8, the main difference being that in the B2 model, the perpendicular transport is restricted to its radial component.

The terms missing to solve the large scale model equations are the source terms S^{ic}_{0in}, $S^{ic}_{\|0imV}$, S^{ic}_{0iE}, and S^{ic}_{0eE}, which also include effects due to interactions between charged particles and neutrals. The description of the latter is not included in the model presented here. The respective processes and their effects on the charged particles can be evaluated by resorting to the linear transport solver EIRENE [3, 4], for instance. The intermediate form of the model equations, given by eqs. (3.38), (3.46), (3.47), and (3.48), which still contain the averaged mesoscale terms in their original form, is related to the macroscale part of the specific multiscale model in chapter 5.

4. Drift fluid models for the plasma edge

In the previous chapter 3, the macroscale part of a multiscale model for the plasma edge in a tokamak device has been derived, given by eqs. (3.38), (3.46), (3.47), and (3.48). It determines the evolution of the macroscale quantities α_0. To complete the multiscale model, a local mesoscale model for the quantities $\widetilde{\alpha}$ is needed which can be used to calculate the averaged mesoscale terms of the form $\langle \widetilde{u} \cdot \boldsymbol{\nabla} \widetilde{\alpha} \rangle$ and $\langle \widetilde{\alpha} \widetilde{\boldsymbol{u}} \rangle$, appearing in the macroscale balances. One option for such a model, a so-called local drift fluid model, is presented in this chapter, which can be understood as an extension of the Hasegawa-Wakatani model [58] and is based the work of B. Scott [59, 30]. The new feature of the equations shown here is that they contain averaged mesoscale terms, which effectively 'filter out' any macroscale evolution of the quantities so that the scale separation between mesoscale and macroscale dynamics is ensured. The local drift fluid model will be related to the mesoscale part of the specific multiscale model in chapter 5. The latter provides the basis for the coupled code simulations of chapters 7 and 8, with the local drift fluid model accounting for the determination of the perpendicular transport coefficients.

The main differences between the local drift fluid model outlined in this chapter and the large scale model presented in chapter 3 lie in the fact that the former includes detailed treatment of the perpendicular velocity components, also called perpendicular fluid drifts, and the dynamics of the electric potential ϕ and the perturbations of the magnetic field. For the local drift fluid model, the assumption of a scale separation not only regarding the temporal and spatial scales of the dynamics, but also regarding the amplitudes is made: the mesoscale quantities $\widetilde{\alpha}$ are considered to be small compared to macroscale quantities α_0, $\widetilde{\alpha} \ll \alpha_0$. If no scale separation neither for the scales of the typical dynamics nor for the amplitudes is assumed, one obtains a self-contained global drift fluid model which accounts for both the evolution on the mesoscale and on the macroscale. It can be understood as an extended version of the self-contained large scale model of the former chapter 3 and can be used to benchmark the specific multiscale model since it evolves the full quantities $\alpha = \widetilde{\alpha} + \alpha_0$ on the mesoscale and macroscale.

As the first point in this chapter, the perpendicular fluid drifts are introduced in paragraph 4.1, with detailed descriptions of their derivation and physical effect being given in [35, 60], for instance. In paragraph 4.2, the global drift fluid model is derived from the general fluid balances (2.27), (2.28) and (2.29) of paragraph 2.1 with the Braginskii closure outlined in paragraph 3.2 and the assumptions given in [30]. The local drift fluid model is introduced and discussed in paragraph 4.3.

4.1. Perpendicular fluid drifts

In contrast to the large scale models of chapter 3, where the macroscale ion velocity $\boldsymbol{u}_0$ was assumed to have only a parallel component, $\boldsymbol{u}_0 = \boldsymbol{u}_{\|0}$, the perpendicular components of the velocities are explicitly taken into account in the drift fluid models. The equation for both the ion and electron perpendicular velocity $\boldsymbol{v}_{\perp a}$ is obtained by using the so-called drift operator $(\boldsymbol{B}/B^2\times)$ in the momentum balance (2.28) under the Braginskii closure and division by $m_a n_a$. This yields:

$$\boldsymbol{v}_{\perp a} = \frac{\boldsymbol{B}\times\boldsymbol{\nabla}_\perp\phi}{B^2} + \frac{\boldsymbol{B}\times\boldsymbol{\nabla}_\perp p_a}{q_a n_a B^2} + \frac{m_a\boldsymbol{B}}{q_a B^2}\times\frac{d\boldsymbol{v}_{\perp a}}{dt} + \frac{\boldsymbol{B}\times\boldsymbol{\nabla}\cdot\boldsymbol{\Pi_a}}{q_a n_a B^2} - \frac{\boldsymbol{B}\times\boldsymbol{R}_a}{q_a n_a B^2}\ , \tag{4.1}$$

where ϕ is the electric potential. Eq. (4.1) is only a formal solution for $\boldsymbol{v}_{\perp a}$ and can be understood as an iteration equation for the perpendicular velocity $\boldsymbol{v}_{\perp a}$.

The acceleration of charged particles by an electric field leads to a varying gyroradius and a motion perpendicular to both the electric field and the magnetic field (see fig. 4.1, left). The **E×B drift** $\boldsymbol{v}_{\mathrm{E}}$,

$$\boldsymbol{v}_{\mathrm{E}} = \frac{\boldsymbol{B}\times\boldsymbol{\nabla}_\perp\phi}{B^2}\ , \tag{4.2}$$

does not depend on the particle charge and is therefore denoted by $\boldsymbol{v}_{\mathrm{E}}$ for both electrons and ions.

The **diamagnetic drifts** $\boldsymbol{u}_*$ and $\boldsymbol{v}_*$ for ions and electrons, respectively, are given by

$$\boldsymbol{u}_* = \frac{\boldsymbol{B}\times\boldsymbol{\nabla}_\perp p_i}{Z_i e n_i B^2}\ , \qquad \boldsymbol{v}_* = -\frac{\boldsymbol{B}\times\boldsymbol{\nabla}_\perp p_e}{e n_e B^2}\ . \tag{4.3}$$

A pressure gradient $\boldsymbol{\nabla}p$ corresponds to a variation of the gyroradius and/or the particle density which, in the fluid picture, leads to a drift perpendicular to both $\boldsymbol{\nabla}p$ and $\boldsymbol{B}$. This effect is visualized in fig. 4.1, right.

The **polarization drifts** $\boldsymbol{u}_p$ and $\boldsymbol{v}_p$ are

$$\boldsymbol{u}_p = \frac{m_i\boldsymbol{B}}{Z_i e B^2}\times\frac{d\boldsymbol{u}_\perp}{dt}\ , \qquad \boldsymbol{v}_p = -\frac{m_e\boldsymbol{B}}{e B^2}\times\frac{d\boldsymbol{v}_\perp}{dt}\ . \tag{4.4}$$

They are responsible for the nonlinear character of eq. (4.1).

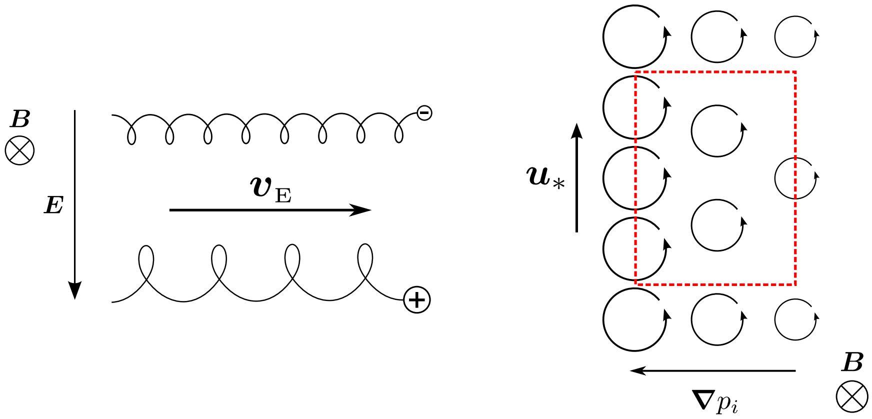

Figure 4.1.: Left: The E×B drift $\boldsymbol{v}_{\mathrm{E}}$. **Right:** The diamagnetic drift $\boldsymbol{u}_*$ for the ions. Integration over the fluid parcel given by the dotted red line yields a net flow velocity perpendicular to $\boldsymbol{\nabla} p_i$ and $\boldsymbol{B}$. For electrons which are rotating in opposite direction the drift is also in opposite direction. Note that the diamagnetic drift only exists in the fluid picture; the gyrocenters themselves are not moving.

The **viscosity drifts** $\boldsymbol{u}_\Pi$ and $\boldsymbol{v}_\Pi$ are given by

$$\boldsymbol{u}_\Pi = \frac{\boldsymbol{B} \times \boldsymbol{\nabla} \cdot \boldsymbol{\Pi}_i}{Z_i e n_i B^2} , \qquad \boldsymbol{v}_\Pi = - \frac{\boldsymbol{B} \times \boldsymbol{\nabla} \cdot \boldsymbol{\Pi}_e}{e n_e B^2} , \tag{4.5}$$

and for the **friction drifts** $\boldsymbol{u}_{\mathrm{R}}$ and $\boldsymbol{v}_{\mathrm{R}}$ one has

$$\boldsymbol{u}_{\mathrm{R}} = - \frac{\boldsymbol{B} \times \boldsymbol{R}_i}{Z_i e n_i B^2} , \qquad \boldsymbol{v}_{\mathrm{R}} = \frac{\boldsymbol{B} \times \boldsymbol{R}_e}{e n_e B^2} . \tag{4.6}$$

4.2. Global drift fluid model

In this paragraph, the global drift fluid model is presented. Before coming to an outline of the model assumptions in paragraph 4.2.1 and the derivation of the balance equations in paragraphs 4.2.2 to 4.2.6 the development of a drift fluid model is motivated.

In the classical picture with a homogeneous B-field, mobility in direction perpendicular to the field lines is assumed to be strongly suppressed due to the Lorentz force and the subsequent gyration of charged particles around the magnetic field lines. Referring to paragraph 3.1, where the tokamak device was presented, this is one of the main objectives of the magnetic configuration employed: to limit the transport of particles and energy from the core region to the vessel wall. From the classical point of view the existing perpendicular transport is mainly collisional. The assumption that the perpendicular velocity components can be neglected compared to the parallel component (see the assumptions of the large scale model in paragraph 3.3.1) is based on this reasoning. Neoclassical theories also account for the inhomogeneities in the magnetic field of a tokamak, e.g. due to its toroidal shape and thus a non-uniform magnetic field. This leads to additional fluid drifts, longer mean free paths of particles, and an increased cross-field transport as in the classical picture. Neither classical nor neoclassical theories succeed in fully describing the experimentally observed processes and the magnitude of perpendicular transport, being significantly higher than predicted by those theories. To understand the perpendicular dynamics it is necessary to investigate the complex interactions of magnetic and electric fields and charged particles which requires inclusion of the perpendicular drifts of paragraph 4.1 in the model equations. Transport due to the mesoscale dynamics, as it is described by the drift fluid models of this chapter, is usually referred to as *anomalous* in contrast to *classical* and *neoclassical* transport [18]. A number of fluid models exists to capture the respective processes in the plasma edge, see for example [59, 30, 11, 10, 8, 12] to name only a few. They are, for instance, discussed under the name of drift-Alfvén turbulence, shear-Alfvén turbulence, or reduced magnetohydrodynamics (MHD). Here, they are more generally called drift fluid models.

4.2.1. Model assumptions

Starting point for the global drift fluid model are the full fluid balances of paragraph 2.1, eqs. (2.27) to (2.29), which are applied to a hydrogen plasma ($Z_i = 1$) under the Braginskii closure introduced in paragraph 3.2. The additional assumptions comprise the following points:

- As for the large scale model the quasineutrality condition is used. For a hydrogen plasma this means

  $$n_e \;=\; n_i \;. \tag{4.7}$$

  Hence, n refers both to the ion and electron density. From condition (4.7) and the condition of continuity in charge it follows that the current density is divergence-free:

  $$\boldsymbol{\nabla} \cdot \boldsymbol{j} \;=\; 0 \;. \tag{4.8}$$

- The total time derivative d/dt is given by the advective derivative as defined in eq. (2.30). Advection in parallel direction is neglected, advection in perpendicular direction is governed by the E×B velocity $\boldsymbol{v}_{\mathrm{E}}$ and the diamagnetic velocity $\boldsymbol{v}_{a*}$ of the corresponding species a:

$$\frac{d\alpha}{dt} \;=\; \left(\frac{\partial}{\partial t} + \boldsymbol{v}_{\mathrm{E}} \cdot \boldsymbol{\nabla}_{\perp}\right)\alpha \;+\; \boldsymbol{v}_{a*} \cdot \boldsymbol{\nabla}_{\perp}\alpha \;. \tag{4.9}$$

The first term on the rhs of eq. (4.9) is also called the E×B advective derivative.

- Perturbations of the equilibrium magnetic field $\boldsymbol{B}_0$ (referring to the magnetic field created only by the tokamak coils and the induced plasma current I_p) are only allowed for its perpendicular component $B_{\perp}$. Hence, it can be concluded that

  $$\frac{\partial B_{\parallel}}{\partial t} \;=\; 0 \quad\rightarrow\quad \frac{\partial \boldsymbol{A}_{\perp}}{\partial t} \;=\; 0 \;, \tag{4.10}$$

  where $\boldsymbol{A}$ is the vector potential with $\boldsymbol{B} = \boldsymbol{\nabla} \times \boldsymbol{A}$. Therefore, $\boldsymbol{E}_{\perp}$ is electrostatic and $E_{\parallel}$ is electrodynamic:

  $$\boldsymbol{E}_{\perp} \;=\; -\boldsymbol{\nabla}\phi \;, \qquad E_{\parallel} \;=\; -\,\frac{\partial A_{\parallel}}{\partial t} \;-\; \nabla_{\parallel}\phi \;. \tag{4.11}$$

  For the vector potential, the Lorentz gauge is used [61]:

  $$\boldsymbol{\nabla} \cdot \boldsymbol{A} \;+\; \frac{\partial \phi}{\partial t} \;=\; 0 \;. \tag{4.12}$$

- The source terms S^{ic} due to inelastic Coulomb collisions and reactions with neutrals are neglected.

In comparison with the large scale model and its assumptions (see paragraph 3.3.1) the drift fluid model includes electrical currents in the plasma and thereby can account for a complex interaction between the charged particles, constituting the plasma, and the extrinsic and intrinsic magnetic and electric fields.

Next, the global drift fluid balances for the density n, the ion parallel velocity $u_{\parallel}$, the ion and electron temperatures T_i and T_e, the vector potential $A_{\parallel}$, and the electric potential ϕ are derived.

4.2.2. Particle balance

The particle balance of the global drift fluid model is based on the fluid particle balance (2.27) for the electrons. Applying the Braginskii closure and the assumptions listed above yields:

$$\left(\frac{\partial}{\partial t} + \boldsymbol{v}_{\mathrm{E}} \cdot \boldsymbol{\nabla}_{\perp} + \boldsymbol{v}_{*} \cdot \boldsymbol{\nabla}_{\perp}\right)n \;=\; -\,n\boldsymbol{\nabla} \cdot \left(v_{\parallel}\frac{\boldsymbol{B}}{B} + \boldsymbol{v}_{\mathrm{E}} + \boldsymbol{v}_{*}\right) \;, \tag{4.13}$$

neglecting the divergence of the electron polarization drift $\boldsymbol{v}_p$ due to its proportionality to m_e. One can use that

$$\boldsymbol{\nabla} \cdot \left(\frac{\boldsymbol{B}}{B}\,\alpha\right) \;=\; B\nabla_{\|}\frac{\alpha}{B} \tag{4.14}$$

and express the terms $\boldsymbol{\nabla} \cdot \boldsymbol{v}_{\mathrm{E}}$ and $\boldsymbol{\nabla} \cdot (n\boldsymbol{v}_*)$ via the curvature operator $\mathcal{K}(\alpha)$:

$$\mathcal{K}(\alpha) \;\equiv\; \boldsymbol{\nabla} \cdot \frac{\boldsymbol{B} \times \boldsymbol{\nabla}\alpha}{B^2} \;=\; \left(\boldsymbol{\nabla} \times \frac{\boldsymbol{B}}{B^2}\right) \cdot \boldsymbol{\nabla}\alpha\ . \tag{4.15}$$

The parallel electron velocity $v_{\|}$ can be rewritten using the parallel current density $j_{\|}$ and the parallel ion velocity $u_{\|}$:

$$j_{\|} \;=\; en(u_{\|} - v_{\|}) \qquad \Leftrightarrow \qquad v_{\|} \;=\; u_{\|} - \frac{j_{\|}}{en}\ . \tag{4.16}$$

The **electron particle balance** of the model then reads:

$$\left(\frac{\partial}{\partial t} + \boldsymbol{v}_{\mathrm{E}} \cdot \boldsymbol{\nabla}_{\perp}\right)n \;=\; nB\nabla_{\|}\left(\frac{j_{\|}}{enB} - \frac{u_{\|}}{B}\right) \;-\; n\mathcal{K}(\phi) \;+\; \frac{1}{e}\mathcal{K}(p_e)\ . \tag{4.17}$$

4.2.3. Total parallel momentum balance

With the Braginskii closure and the above assumptions the fluid momentum balance (2.28) yields the ion and electron momentum balances

$$m_i n\frac{d\boldsymbol{u}}{dt} \;=\; en\Big(\boldsymbol{E} + \boldsymbol{u} \times \boldsymbol{B}\Big) \;-\; \boldsymbol{R}_e \;-\; \boldsymbol{\nabla} \cdot \mathbf{P}_i\ , \tag{4.18}$$

$$m_e n\frac{d\boldsymbol{v}}{dt} \;=\; -\,en\Big(\boldsymbol{E} + \boldsymbol{v} \times \boldsymbol{B}\Big) \;+\; \boldsymbol{R}_e \;-\; \boldsymbol{\nabla} \cdot \mathbf{P}_e\ . \tag{4.19}$$

By summation of the parallel part of eqs. (4.18) and (4.19) and neglect of all terms proportional to m_e and the total time derivative $d\boldsymbol{B}/dt$ one gets the **total parallel momentum balance**:

$$m_i n\left(\frac{\partial}{\partial t} + \boldsymbol{v}_{\mathrm{E}} \cdot \boldsymbol{\nabla}_{\perp}\right)u_{\|} \;=\; -\nabla_{\|}\Big(p_e + p_i\Big) -\; \mu_{\|i}\nabla_{\|}^2 u_{\|}\ , \tag{4.20}$$

with the approximation

$$\left[\boldsymbol{\nabla}\cdot\boldsymbol{\Pi}_i\right]_{\parallel} \;=\; \mu_{\parallel i}\nabla_{\parallel}^2 u_{\parallel}\ . \tag{4.21}$$

The parallel ion viscosity is denoted by $\mu_{\parallel i}$, the parallel Laplace operator $\nabla_{\parallel}^2$ is defined as $\nabla_{\parallel}^2 \equiv \boldsymbol{\nabla}\cdot\boldsymbol{\nabla}_{\parallel}$. The so-called gyroviscous cancellation prevents the velocities from being directly advected by the diamagnetic velocities $\boldsymbol{u}_*$ and $\boldsymbol{v}_*$ [62].

4.2.4. Ion and electron energy balance

The fluid energy balance (2.29) with the Braginskii closure and the drift fluid model assumptions becomes

$$\frac{3}{2}n\frac{dT_a}{dt} \;=\; Q_a \;-\; p_a\boldsymbol{\nabla}\cdot\boldsymbol{v}_a \;-\; \boldsymbol{\Pi}_a : \boldsymbol{\nabla}\boldsymbol{v}_a \;-\; \boldsymbol{\nabla}\cdot\boldsymbol{q}_a\ . \tag{4.22}$$

The terms Q_a and $\boldsymbol{\Pi}_a : \boldsymbol{\nabla}\boldsymbol{v}_a$ are neglected compared to the divergence of the heat flux $\boldsymbol{q}_a$. For the ions eq. (4.22) is transformed into

$$\frac{3}{2}n\left(\frac{\partial}{\partial t} + \left[\boldsymbol{v}_{\mathrm{E}} + \boldsymbol{v}_*\right]\cdot\boldsymbol{\nabla}_{\perp}\right)T_i \;=\; -\,p_i\boldsymbol{\nabla}\cdot\left(\boldsymbol{u}_{\parallel} + \boldsymbol{v}_{\mathrm{E}} + \boldsymbol{u}_* + \boldsymbol{u}_p\right) \;-\boldsymbol{\nabla}\cdot\boldsymbol{q}_i\ . \tag{4.23}$$

Due to the strong magnetization of the plasma the perpendicular heat flux $\boldsymbol{q}_{\perp i}$ can be neglected compared to its diamagnetic component $\boldsymbol{q}_{\wedge i}$. The so-called diamagnetic cancellation prevents the temperatures from being advected by the diamagnetic velocities. One finds that

$$\frac{3}{2}n\boldsymbol{u}_*\cdot\boldsymbol{\nabla}_{\perp}T_i \;+\; p_i\boldsymbol{\nabla}\cdot\boldsymbol{u}_* \;+\; \boldsymbol{\nabla}\cdot\boldsymbol{q}_{\wedge i} \;=\; \frac{T_i}{e}\mathcal{K}(p_i) \;+\; \frac{5}{2}\frac{p_i}{e}\mathcal{K}(T_i)\ , \tag{4.24}$$

where for the diamagnetic heat fluxes $\boldsymbol{q}_{\wedge i}$ and $\boldsymbol{q}_{\wedge e}$ the expressions

$$\boldsymbol{q}_{\wedge i} \;=\; \frac{5}{2}\frac{p_i}{e}\frac{\boldsymbol{B}\times\boldsymbol{\nabla}_{\perp}T_i}{B^2}\ , \qquad \boldsymbol{q}_{\wedge e} \;=\; -\frac{5}{2}\frac{p_e}{e}\frac{\boldsymbol{B}\times\boldsymbol{\nabla}_{\perp}T_e}{B^2}\ , \tag{4.25}$$

have been used. Note that the curvature terms $\mathcal{K}(\alpha)$ on the rhs of eq. (4.24) vanish for a homogeneous magnetic field. One can then recover the result given in [63].
To obtain an expression for the divergence of the polarization drift $\boldsymbol{u}_p$ of the ions condition (4.8) of a divergence-free current density is employed:

$$\boldsymbol{\nabla}\cdot\boldsymbol{j}_p \;=\; \frac{ep_i}{T_i}\boldsymbol{\nabla}\cdot\boldsymbol{u}_p \;=\; -\boldsymbol{\nabla}\cdot\boldsymbol{j}_{\parallel} - \boldsymbol{\nabla}\cdot\boldsymbol{j}_* \;=\; -B\nabla_{\parallel}\frac{j_{\parallel}}{B} - \mathcal{K}(p_i) - \mathcal{K}(p_e)\ . \tag{4.26}$$

The **ion energy balance** becomes:

$$\boxed{\begin{aligned}\frac{3}{2}n\left(\frac{\partial}{\partial t}+\boldsymbol{v}_{\mathrm{E}}\cdot\boldsymbol{\nabla}_{\perp}\right)T_i \;&=\; -B\nabla_{\|}\frac{q_{\|i}}{B} \;-\; p_iB\nabla_{\|}\frac{u_{\|}}{B} \;+\; \frac{T_iB}{e}\nabla_{\|}\frac{j_{\|}}{B}\\ &\quad-\; p_i\mathcal{K}(\phi) \;+\; \frac{T_i}{e}\mathcal{K}(p_e) \;-\; \frac{5}{2}\frac{p_i}{e}\mathcal{K}(T_i)\;. \qquad (4.27)\end{aligned}}$$

The derivation of the electron energy balance is carried out in an analogous way. The diamagnetic cancellation for the electrons is expressed via

$$\frac{3}{2}n\boldsymbol{v}_*\cdot\boldsymbol{\nabla}_{\perp}T_e \;+\; p_e\boldsymbol{\nabla}\cdot\boldsymbol{v}_* \;+\; \boldsymbol{\nabla}\cdot\boldsymbol{q}_{\wedge e} \;=\; -\frac{T_e}{e}\mathcal{K}(p_e) \;-\frac{5}{2}\frac{p_e}{e}\mathcal{K}(T_e)\;\;. \qquad (4.28)$$

The **electron energy balance** has the form:

$$\boxed{\begin{aligned}\frac{3}{2}n\left(\frac{\partial}{\partial t}+\boldsymbol{v}_{\mathrm{E}}\cdot\boldsymbol{\nabla}_{\perp}\right)T_e \;&=\; -B\nabla_{\|}\frac{q_{\|e}}{B} \;-\; p_eB\nabla_{\|}\frac{u_{\|}}{B} \;+\; \frac{p_e}{e}B\nabla_{\|}\frac{j_{\|}}{nB}\\ &\quad-\; p_e\mathcal{K}(\phi) \;+\; \frac{T_e}{e}\mathcal{K}(p_e) \;+\; \frac{5}{2}\frac{p_e}{e}\mathcal{K}(T_e)\;. \qquad (4.29)\end{aligned}}$$

4.2.5. Ohm's law

The derivation of Ohm's law is based on the parallel momentum balances (4.18) and (4.19). By multiplication with $\hat{\boldsymbol{e}}_{\|}/(m_en)$ and $\hat{\boldsymbol{e}}_{\|}/(m_in)$, respectively, subtracting eq. (4.19) from eq. (4.18), and neglecting the term including the parallel electron viscosity $\mu_{\|e}$ and all terms proportional to $1/m_i$ one obtains:

$$\frac{du_{\|}}{dt} \;-\; \frac{dv_{\|}}{dt} \;=\; \frac{e}{m_e}E_{\|} \;-\; \frac{1}{m_en}R_{\|e} \;-\; \frac{1}{m_en}\nabla_{\|}p_e\;. \qquad (4.30)$$

The terms on the lhs of eq. (4.30) can be expressed via the parallel current density $j_{\|}$, see eq. (4.16). Eq. (4.11b) is used to replace the parallel electric field $E_{\|}$ by the electric potential ϕ and the parallel vector potential $A_{\|}$. Due to the gyroviscous cancellation, $j_{\|}$ is only advected by $\boldsymbol{v}_{\mathrm{E}}$. It is also assumed that $d(u_{\|}-v_{\|})/dt \approx 1/(en)dj_{\|}/dt$. Multiplication of eq. (4.30) with m_en leads to **Ohm's law**:

$$\boxed{\frac{m_e}{e}\left(\frac{\partial}{\partial t}+\boldsymbol{v}_{\mathrm{E}}\cdot\boldsymbol{\nabla}_{\perp}\right)j_{\|} \;=\; -\,en\frac{\partial A_{\|}}{\partial t} \;-\; en\nabla_{\|}\phi \;-\; R_{\|e} \;+\; \nabla_{\|}p_e\;. \qquad (4.31)}$$

4.2.6. Vorticity equation

The vorticity equation is obtained from condition (4.8) of a divergence-free current density. The vorticity is given by $\nabla_\perp^2\phi$, where the perpendicular Laplace operator $\nabla_\perp^2$ is defined as $\nabla_\perp^2 \;\equiv\; \boldsymbol{\nabla}\cdot\boldsymbol{\nabla}_\perp$. For the diamagnetic current density $\boldsymbol{j}_*$ one has

$$\boldsymbol{j}_* \;=\; en\Big(\boldsymbol{u}_* - \boldsymbol{v}_*\Big) \;=\; \frac{\boldsymbol{B}\times\boldsymbol{\nabla}_\perp(p_i + p_e)}{B^2}\;, \tag{4.32}$$

while the polarization current density $\boldsymbol{j}_p$ is given by

$$\boldsymbol{j}_p \;=\; \frac{m_i n}{B}\boldsymbol{B}\times\frac{d\boldsymbol{u}_\perp}{dt}\;. \tag{4.33}$$

The electron polarization velocity $\boldsymbol{v}_p$ is neglected in eq. (4.33) since $m_e \ll m_i$. With eqs. (4.32) and (4.33), eq. (4.8), stating that $\boldsymbol{\nabla}\cdot\boldsymbol{j} = 0$, can be transformed into

$$\boldsymbol{\nabla}\cdot\left(\frac{m_i n}{B^2}\boldsymbol{B}\times\frac{d\boldsymbol{u}_\perp}{dt}\right) \;+\; B\nabla_\parallel\frac{j_\parallel}{B} \;+\; \mathcal{K}(p_i) \;+\; \mathcal{K}(p_e) \;=\; 0\;. \tag{4.34}$$

By neglecting spatial and temporal dependencies of n and B and using that in lowest order $\boldsymbol{u}_\perp = \boldsymbol{v}_{\mathrm{E}} + \boldsymbol{u}_*$ one gets the **vorticity equation**:

$$\boxed{\frac{m_i n}{B^2}\left(\frac{\partial}{\partial t} + \boldsymbol{v}_{\mathrm{E}}\cdot\boldsymbol{\nabla}_\perp\right)\left(\nabla_\perp^2\phi + \frac{\nabla_\perp^2 p_i}{en}\right) \;=\; B\nabla_\parallel\frac{j_\parallel}{B} \;+\; \mathcal{K}(p_i) \;+\; \mathcal{K}(p_e)\;. \quad (4.35)}$$

The gyroviscous cancellation prevents any advection by the diamagnetic velocity.

4.2.7. Discussion of the global drift fluid model

The particle balance (4.17), the total parallel momentum balance (4.20), the ion and electron energy balances (4.27) and (4.29), Ohm's law (4.31), and the vorticity equation (4.35) form a closed system of partial differential equations for the scalar fields $n, u_\parallel, T_i, T_e, \phi$ and $A_\parallel$. The Maxwell equation

$$\boldsymbol{\nabla}\times\boldsymbol{B} \;=\; \mu_0\boldsymbol{j} \;+\; \mu_0\varepsilon_0\frac{\partial\boldsymbol{E}}{\partial t} \tag{4.36}$$

is used to relate the parallel current density to the parallel vector potential,

$$j_\parallel \;=\; -\frac{1}{\mu_0}\hat{\boldsymbol{e}}_\parallel\cdot\Big(\boldsymbol{\nabla}^2\boldsymbol{A}\Big) \;\approx\; -\frac{1}{\mu_0}\nabla_\perp^2 A_\parallel\;, \tag{4.37}$$

with the vector Laplace operator $\boldsymbol{\nabla}^2$ being defined as $\boldsymbol{\nabla}^2\boldsymbol{a} \equiv \boldsymbol{\nabla}(\boldsymbol{\nabla}\cdot\boldsymbol{a}) - \boldsymbol{\nabla}\times(\boldsymbol{\nabla}\times\boldsymbol{a})$.

To investigate the relation between the global drift fluid model and the large scale model presented in paragraph 3.3.3, the balance equations of the former can be rewritten into conservative form. Also, the current density $\boldsymbol{j}$ is set to zero (as in the large scale model). The ion counterpart to the electron particle balance, the total parallel momentum balance, and the energy balances of the modified global drift fluid model are then given by:

$$\frac{\partial n}{\partial t} \;+\; \boldsymbol{\nabla} \cdot \Big(n[\boldsymbol{u}_\parallel + \boldsymbol{v}_{\mathrm{E}} + \boldsymbol{u}_*] \Big) \;=\; \boldsymbol{u}_\parallel \cdot \boldsymbol{\nabla}_\parallel n \;, \tag{4.38}$$

$$\begin{aligned} &\frac{\partial}{\partial t}\Big(m_i n u_\parallel \Big) \;+\; \boldsymbol{\nabla} \cdot \Big(m_i n u_\parallel [\boldsymbol{u}_\parallel + \boldsymbol{v}_{\mathrm{E}} + \boldsymbol{u}_*] \Big) \\ &\qquad = \; -\mu_{\parallel i} \nabla_\parallel^2 u_\parallel \;-\; \nabla_\parallel (p_i + p_e) \;+\; \Big(\boldsymbol{u}_\parallel + \boldsymbol{u}_* \Big) \cdot \boldsymbol{\nabla} \Big(m_i n u_\parallel \Big) \;, \end{aligned} \tag{4.39}$$

$$\begin{aligned} &\frac{\partial}{\partial t}\left(\frac{3}{2} n T_i + \frac{1}{2} m_i n u_\parallel^2 \right) \;+\; \boldsymbol{\nabla} \cdot \left(\frac{5}{2} n T_i [\boldsymbol{u}_\parallel + \boldsymbol{v}_{\mathrm{E}} + \boldsymbol{u}_*] + \frac{1}{2} m_i n u_\parallel^2 [\boldsymbol{u}_\parallel + \boldsymbol{v}_{\mathrm{E}} + \boldsymbol{u}_*] \right) \\ &\qquad = \; -u_\parallel \nabla_\parallel p_e \;-\; \mu_{\parallel i} u_\parallel \nabla_\parallel^2 u_\parallel \;-\; \boldsymbol{\nabla} \cdot (\boldsymbol{q}_{\parallel i} + \boldsymbol{q}_{\wedge i}) \;+\; (\boldsymbol{v}_{\mathrm{E}} + \boldsymbol{u}_*) \cdot \boldsymbol{\nabla}_\perp p_i \\ &\qquad + \; \frac{3}{2} \boldsymbol{u}_\parallel \cdot \boldsymbol{\nabla} p_i \;+\; u_\parallel (\boldsymbol{u}_\parallel + \boldsymbol{u}_*) \cdot \boldsymbol{\nabla} (m_i n u_\parallel) \;+\; \frac{1}{2} m_i u_\parallel \boldsymbol{u}_\parallel \cdot \boldsymbol{\nabla} n \;, \end{aligned} \tag{4.40}$$

$$\begin{aligned} &\frac{\partial}{\partial t}\left(\frac{3}{2} n T_e \right) \;+\; \boldsymbol{\nabla} \cdot \left(\frac{5}{2} n T_e [\boldsymbol{u}_\parallel + \boldsymbol{v}_{\mathrm{E}} + \boldsymbol{v}_*] \right) \\ &\qquad = \; -u_\parallel \nabla_\parallel p_e \;-\; \boldsymbol{\nabla} \cdot (\boldsymbol{q}_{\parallel e} + \boldsymbol{q}_{\wedge e}) \;+\; (\boldsymbol{v}_{\mathrm{E}} + \boldsymbol{v}_*) \cdot \boldsymbol{\nabla}_\perp p_i \;+\; \frac{3}{2} \boldsymbol{u}_\parallel \cdot \boldsymbol{\nabla}_\parallel p_i \,. \end{aligned} \tag{4.41}$$

Terms like $\boldsymbol{u}_\parallel \cdot \boldsymbol{\nabla}_\parallel n$ on the rhs of eq. (4.38) cancel out the parallel advection which is here included in the divergence $\boldsymbol{\nabla} \cdot (n\boldsymbol{u}_\parallel)$ for better comparability with the large scale model equation, but is neglected in the drift fluid model.
Comparing eqs. (4.38) to (4.41) with the large scale model equations (3.53), (3.55), (3.56), and (3.57) shows that the global drift fluid model includes the advection by the perpendicular velocities and their divergences due to the compressible velocity fields $\boldsymbol{v}_{\mathrm{E}}$, $\boldsymbol{u}_*$, and $\boldsymbol{v}_*$: instead of using a macroscale transport model to account for the effect of mesoscale processes on the macroscale, it includes the evolution of the plasma on both the mesoscale and macroscale.

4.3. Local drift fluid model

The equations (4.17), (4.20), (4.27), (4.29), (4.31), and (4.35) of the global drift fluid model account for the evolution of the full plasma quantities α on the mesoscale and macroscale. Within the specific multiscale model for the plasma edge the macroscale evolution on the largest occurring scales of today's tokamak experiments (with $\tau_{\text{D}}(\alpha_0) \sim 1$ s and $\lambda_{\text{D}}(\alpha_0) \sim 1$ m) is accounted for by the macroscale model presented in paragraph 3.3.1. For the completion of the specific multiscale model a *local* mesoscale model is needed to determine the averaged mesoscale terms of the macroscale equations in agreement with the large scale plasma profiles.

The local drift fluid model which is derived in this paragraph fulfills this purpose. It is derived from the mesoscale balances (2.49), (2.56), and (2.61) of the generic multiscale model with the Braginskii closure of paragraph 3.2 and uses information of the macroscale profiles such as the perpendicular density gradient as input parameters. The model assumptions are given by those of the global drift fluid model (paragraph 4.2.1) and a number of additional assumptions outlined in paragraph 4.3.1 which are based on [30]. The model equations are presented and discussed in paragraph 4.3.2.

4.3.1. Assumptions of the local drift fluid model

The following assumptions, adding to those of the global drift fluid model outlined in paragraph 4.2.1, are made for the local drift fluid model:

- The characteristic macroscale gradient length $L_\perp$ of the dynamics in perpendicular direction is estimated by the typical macroscale perpendicular density gradient:

  $$L_\perp \sim \frac{n_0}{\nabla_\perp n_0} \; . \qquad (4.42)$$

  With $L_\perp$ being usually of the order of centimeters and the ion Larmor radius ρ_s of the order of tenths of millimeters in the edge region of a tokamak, the small quantity δ can be introduced:

  $$\delta \sim \frac{\rho_s}{L_\perp} \ll 1 \; . \qquad (4.43)$$

  Additionally, a small plasma beta β_p is required:

  $$\beta_p = \frac{2\mu_0 p}{B^2} = \frac{c_s^2}{v_{\text{A}}^2} \overset{!}{\ll} 1 \; . \qquad (4.44)$$

  The plasma beta β_p is the ratio of the plasma pressure p to the magnetic pressure $B^2/(2\mu_0)$, where μ_0 is the electromagnetic permeability of free space. A small β_p means in this context that perturbations of the plasma pressure result only in minimal deformation of the magnetic field lines.

  The so-called drift ordering is carried out for the local drift fluid model with the small parameters β_p and δ (for details see [30]). It results in a scale separation regarding the amplitudes of α_0 and $\widetilde{\alpha}$ with $\widetilde{\alpha} \ll \alpha_0$. The scale separation is expressed using the small parameter δ:

$$\frac{\widetilde{n}}{n_0} \sim \frac{\widetilde{B}_\perp}{B_0} \sim \frac{u_\|}{c_s} \sim \frac{e\widetilde{\phi}}{T_{0e}} \sim \delta \ . \tag{4.45}$$

Additionally, the perpendicular dynamics of $\widetilde{\alpha}$ are assumed to take place on temporal and spatial scales much smaller than those associated to the changes of α_0. This is expressed by

$$\lambda_{\mathrm{D}\perp}(\widetilde{\alpha}) \ll \lambda_{\mathrm{D}\perp}(\alpha_0) \ , \qquad \tau_{\mathrm{D}\perp}(\widetilde{\alpha}) \ll \tau_{\mathrm{D}\perp}(\alpha_0) \ . \tag{4.46}$$

Thus, the local drift fluid model assumes a scale separation regarding the temporal and spatial scales, expressed by eqs. (4.46a) and (4.46b), and regarding the amplitudes of plasma quantities, expressed by eq. (4.45).

- The parallel gradient $\nabla_\|$ is split into a macroscale part and a mesoscale part (sometimes also called perturbed or fluctuating part), $\nabla_\| = \nabla_{\|0} + \widetilde{\nabla}_\|$, with

$$\nabla_{\|0} = \frac{\boldsymbol{B}_0}{B} \cdot \boldsymbol{\nabla} \tag{4.47}$$

and

$$\begin{aligned} \widetilde{\nabla}_\| &= \frac{\widetilde{\boldsymbol{B}}_\perp}{B} \cdot \boldsymbol{\nabla} = \frac{1}{B}\Big(\boldsymbol{\nabla} \times \widetilde{\boldsymbol{A}}_\perp + \boldsymbol{\nabla} \times \widetilde{\boldsymbol{A}}_\|\Big) \cdot \boldsymbol{\nabla} \\ &\approx \left(\widetilde{A}_\| \boldsymbol{\nabla} \times \frac{\boldsymbol{B}_0}{B} + \frac{\boldsymbol{B}_0}{B} \times \boldsymbol{\nabla}\widetilde{A}_\|\right) \cdot \boldsymbol{\nabla} \approx \frac{\boldsymbol{B}_0}{B} \times \boldsymbol{\nabla}\widetilde{A}_\| \cdot \boldsymbol{\nabla} \ . \end{aligned} \tag{4.48}$$

The term $\boldsymbol{\nabla} \times \widetilde{\boldsymbol{A}}_\perp$ appearing in the first line of eq. (4.48) is neglected since it corresponds to a perturbation of the magnetic field in parallel direction which is not taken into account here. Also, the rotation of the equilibrium magnetic field $\boldsymbol{B}_0$ is assumed to be small compared to $\boldsymbol{B}_0/B \times \boldsymbol{\nabla}\widetilde{A}_\|$.

- The only gradients of macroscale quantities taken into account are the perpendicular and perturbed parallel gradients of n_0, $u_{\|0}$, T_{0i} and T_{0e}. The equilibrium parallel gradients of these quantities are set to zero as well as their curvature terms:

$$\mathcal{K}(\alpha_0) = \nabla_{\|0}\alpha_0 = 0 \ . \tag{4.49}$$

- The macroscale electric potential and the parallel current density are set to zero:

$$\phi_0 = j_{\|0} = 0 \ . \tag{4.50}$$

4.3.2. Local drift fluid model equations

The balances of the local drift fluid model are obtained by taking the mesoscale balances for the particle density (2.49), momentum (2.56), and energy (2.61) of the generic multiscale model and apply the Braginskii closure and the assumptions of the global and local drift fluid model, outlined in paragraphs 4.2.1 and 4.3.1. The generalized sources $\boldsymbol{M}_a$ and W_a, see eqs. (2.53) and (2.58), are evaluated here with both the macroscale and mesoscale quantities. As the global drift fluid model, the local drift fluid model consists of an **electron particle balance**,

$$\begin{aligned}\frac{\partial \widetilde{n}}{\partial t} + \widetilde{\boldsymbol{v}}_{\mathrm{E}} \cdot \boldsymbol{\nabla} \widetilde{n} + \widetilde{\boldsymbol{v}}_{\mathrm{E}} \cdot \boldsymbol{\nabla} n_0 \;&=\; \frac{T_{0e}}{e}\mathcal{K}(\widetilde{n}) + \frac{n_0}{e}\mathcal{K}(\widetilde{T}_e) - n_0\mathcal{K}(\widetilde{\phi}) \\ &- n_0 B\Big(\nabla_{\|0} + \widetilde{\nabla}_{\|}\Big)\left(\frac{\widetilde{u}_{\|}}{B} - \frac{\widetilde{j}_{\|}}{e n_0 B}\right) + n_0 B \widetilde{\nabla}_{\|}\frac{u_{\|0}}{B} + \Big\langle \widetilde{\boldsymbol{v}}_{\mathrm{E}} \cdot \boldsymbol{\nabla}\widetilde{n}\Big\rangle + \Big\langle \widetilde{n}\mathcal{K}(\widetilde{\phi})\Big\rangle\,, \end{aligned} \tag{4.51}$$

a **total parallel momentum balance**,

$$\begin{aligned} m_i n_0 \frac{\partial \widetilde{u}_{\|}}{\partial t} + m_i n_0 \widetilde{\boldsymbol{v}}_{\mathrm{E}} \cdot \boldsymbol{\nabla}\widetilde{u}_{\|} \;&=\; -\widetilde{\nabla}_{\|}\Big[n_0(T_{0i} + T_{0e})\Big] - (T_{0i} + T_{0e})\Big(\nabla_{\|0} + \widetilde{\nabla}_{\|}\Big)\widetilde{n} \\ &- n_0\Big(\nabla_{\|0} + \widetilde{\nabla}_{\|}\Big)\Big(\widetilde{T}_i + \widetilde{T}_e\Big) - \mu_{i\|}\nabla_{\|}^2\widetilde{u}_{\|} + \Big\langle \widetilde{\nabla}_{\|}\Big[(n_0 + \widetilde{n})(\widetilde{T}_i + \widetilde{T}_e)\Big]\Big\rangle \\ &+ \Big\langle \widetilde{\nabla}_{\|}\Big[\widetilde{n}(T_{0i} + T_{0e})\Big]\Big\rangle + \Big\langle \nabla_{\|0}\Big[\widetilde{n}(\widetilde{T}_i + \widetilde{T}_e)\Big]\Big\rangle + m_i n_0 \Big\langle \widetilde{\boldsymbol{v}}_{\mathrm{E}} \cdot \boldsymbol{\nabla}\widetilde{u}_{\|}\Big\rangle\,, \end{aligned} \tag{4.52}$$

an **ion energy balance**,

$$\begin{aligned} \frac{3}{2}n_0\left(\frac{\partial \widetilde{T}_i}{\partial t} + \widetilde{\boldsymbol{v}}_{\mathrm{E}} \cdot \boldsymbol{\nabla}\widetilde{T}_i + \widetilde{\boldsymbol{v}}_{\mathrm{E}} \cdot \boldsymbol{\nabla} T_{0i}\right) \;&=\; -B\Big(\nabla_{\|0} + \widetilde{\nabla}_{\|}\Big)\frac{\widetilde{q}_{\|i}}{B} \\ &- n_0 T_{0i} B\left[\Big(\nabla_{\|0} + \widetilde{\nabla}_{\|}\Big)\frac{\widetilde{u}_{\|}}{B} + \widetilde{\nabla}_{\|}\frac{u_{\|0}}{B}\right] + \frac{T_{0i}B}{e}\Big(\nabla_{\|0} + \widetilde{\nabla}_{\|}\Big)\frac{\widetilde{j}_{\|}}{B} - n_0 T_{0i}\mathcal{K}(\widetilde{\phi}) \\ &+ \frac{T_{0i}T_{0e}}{e}\mathcal{K}(\widetilde{n}) - \frac{n_0 T_{0i}}{e}\left[\frac{5}{2}\mathcal{K}(\widetilde{T}_i) - \mathcal{K}(\widetilde{T}_e)\right] + B\left\langle \widetilde{\nabla}_{\|}\frac{\widetilde{q}_{\|i}}{B}\right\rangle \\ &+ n_0 T_{0i} B\left\langle \widetilde{\nabla}_{\|}\frac{\widetilde{u}_{\|}}{B}\right\rangle - \frac{T_{0i}}{e}\left\langle \widetilde{\nabla}_{\|}\frac{\widetilde{j}_{\|}}{B}\right\rangle + \frac{3}{2}n_0\Big\langle \widetilde{\boldsymbol{v}}_{\mathrm{E}} \cdot \boldsymbol{\nabla}\widetilde{T}_i\Big\rangle\,, \end{aligned} \tag{4.53}$$

an **electron energy balance**,

$$\begin{aligned}
&\frac{3}{2} n_0 \left(\frac{\partial \widetilde{T}_e}{\partial t} +, \; \widetilde{\boldsymbol{v}}_{\mathrm{E}} \cdot \boldsymbol{\nabla} \widetilde{T}_e \, + \, \widetilde{\boldsymbol{v}}_{\mathrm{E}} \cdot \boldsymbol{\nabla} T_{0e} \right) \\
&\quad = \; \frac{T_{0e}^2}{e} \mathcal{K}(\widetilde{n}) \, + \, \frac{7}{2} \frac{n_0 T_{0e}}{e} \mathcal{K}(\widetilde{T}_e) \, - \, n_0 T_{0e} \mathcal{K}(\widetilde{\phi}) \, - \, B \Big(\nabla_{\|0} + \widetilde{\nabla}_{\|} \Big) \frac{\widetilde{q}_{\|e}}{B} \\
&\quad - n_0 T_{0e} B \left[\Big(\nabla_{\|0} + \widetilde{\nabla}_{\|} \Big) \frac{\widetilde{u}_{\|}}{B} + \widetilde{\nabla}_{\|} \frac{u_{\|0}}{B} \right] + \frac{T_{0e} B}{e} \Big(\nabla_{\|0} + \widetilde{\nabla}_{\|} \Big) \frac{\widetilde{j}_{\|}}{B} \\
&\quad + \, B \left\langle \widetilde{\nabla}_{\|} \frac{\widetilde{q}_{\|e}}{B} \right\rangle \, + \, n_0 T_{0e} B \left\langle \widetilde{\nabla}_{\|} \frac{\widetilde{u}_{\|}}{B} \right\rangle \, - \, \frac{T_0}{e} \left\langle \widetilde{\nabla}_{\|} \frac{\widetilde{j}_{\|}}{B} \right\rangle \, + \, \frac{3}{2} n_0 \left\langle \widetilde{\boldsymbol{v}}_{\mathrm{E}} \cdot \boldsymbol{\nabla} \widetilde{T}_e \right\rangle , \qquad (4.54)
\end{aligned}$$

Ohm's law,

$$\begin{aligned}
\frac{m_e}{e} \left(\frac{\partial}{\partial t} + \widetilde{\boldsymbol{v}}_{\mathrm{E}} \cdot \boldsymbol{\nabla}_{\perp} \right) \widetilde{j}_{\|} \; &= \; - \, e n_0 \frac{\partial \widetilde{A}_{\|}}{\partial t} \; - \; e n_0 \Big(\nabla_{\|0} + \widetilde{\nabla}_{\|} \Big) \widetilde{\phi} \; - \; R_{\|e} \\
&\quad + \; n_0 \Big(\nabla_{\|0} + \widetilde{\nabla}_{\|} \Big) \widetilde{T}_e \; + \; T_{0e} \Big(\nabla_{\|0} + \widetilde{\nabla}_{\|} \Big) \widetilde{n} \; , \qquad (4.55)
\end{aligned}$$

and the **vorticity equation**:

$$\begin{aligned}
&\frac{m_i n_0}{B^2} \left(\frac{\partial}{\partial t} + \widetilde{\boldsymbol{v}}_{\mathrm{E}} \cdot \boldsymbol{\nabla}_{\perp} \right) \left(\nabla_{\perp}^2 \widetilde{\phi} + \frac{1}{e n_0} \Big[n_0 \nabla_{\perp}^2 \widetilde{T}_i + T_{0i} \nabla_{\perp}^2 \widetilde{n} \Big] \right) \\
&\qquad = \; B \nabla_{\|} \frac{\widetilde{j}_{\|}}{B} \; + \; n_0 \mathcal{K}(\widetilde{T}_i + \widetilde{T}_e) \; + \; \Big(T_{0i} + T_{0e} \Big) \mathcal{K}(\widetilde{n}) \; . \qquad (4.56)
\end{aligned}$$

Eqs. (4.51) to (4.56) of the local drift fluid model correspond to eqs. (4.17), (4.20), (4.27), (4.29), (4.31), and (4.35) of the global drift fluid model. They do not longer account for the evolution of the full quantities n, $u_{\|}$, T_e, T_i, $A_{\|}$, and ϕ, but only determine the mesoscale dynamics of $\widetilde{n}$, $\widetilde{u}_{\|}$, $\widetilde{T}_e$, $\widetilde{T}_i$, $\widetilde{A}_{\|}$, and $\widetilde{\phi}$ 'on top' of a macroscale background which is assumed to be constant. The nonlinearities in the local model are restricted to the advection by the E×B velocity $\widetilde{\boldsymbol{v}}_{\mathrm{E}}$ and the perturbed parallel gradient $\widetilde{\nabla}_{\|}$. Averaged mesoscale terms like $\langle \widetilde{\boldsymbol{v}}_{\mathrm{E}} \cdot \boldsymbol{\nabla} \widetilde{n} \rangle$, appearing in the particle, momentum and energy balances (4.51) to (4.54), ensure an enduring scale separation between the mesoscale and macroscale evolution. The perpendicular macroscale gradients $\boldsymbol{\nabla}_{\perp} n_0$, $\boldsymbol{\nabla}_{\perp} T_{0i}$, and $\boldsymbol{\nabla}_{\perp} T_{0e}$ are important driving terms for the fast, small scale dynamics captured by the local model. They are input parameters for the local simulations and, within a multiscale model, determined by the macroscale simulations. In the next chapter, the relation between the local drift fluid model presented here and the mesoscale part of the specific multiscale model for the plasma edge is established.

Both the local and the global model comprise a large number of different phenomena, such as shear-Alfvén waves and sound waves affecting the parallel dynamics, and resistive drift waves and instabilities due to the curvature of the magnetic field affecting transport perpendicular to the flux surfaces. These processes are analyzed in detail for comparable models in [64], [9], and [10] and references therein. Further work regarding the characteristics of drift fluid models can for example be found in [8], [65], [12], and [66]. In the following, the focus is on high-m dynamics, where m refers to the Fourier mode number in poloidal direction, and on the particle transport due to advection by the E×B velocity $\boldsymbol{v}_{\mathrm{E}}$.

5. Specific multiscale model for the plasma edge

The macroscale model from chapter 3 and the local drift fluid model from chapter 4 are brought together in this chapter to form a specific multiscale model for the edge region of a tokamak. It represents the basis of the coupled code systems investigated in chapters 7 and 8. Its aim is to efficiently compute the dynamics of a tokamak plasma on scales several orders of magnitudes larger than the smallest scales of the drift fluid processes. At the same time it includes the effects that these small scale dynamics have on the large scale dynamics. The mesoscale and macroscale balances are presented in a consistent form, allowing for a clear identification of the terms through which the processes on both scales interact.

The equations of the specific multiscale model are outlined in paragraph 5.1 and discussed in paragraph 5.2. In paragraph 5.3, a short survey on comparable multiscale models for the tokamak plasma edge is given and open questions and challenges are identified.

5.1. Model equations

A general multiscale model for the plasma edge can be directly obtained by taking eqs. (3.38), (3.46), (3.47), and (3.48) of chapter 3 for the macroscale part and the local drift fluid equations (4.51) to (4.56) for the microscale part. The specific multiscale model presented in this thesis is further specified by neglecting the mesoscale temperature dynamics ($\widetilde{T}_i = \widetilde{T}_e = 0$), assuming that the ion temperature T_{0i} is zero and that the macroscale electron temperature T_{0e} is constant. This means that the model is isothermal for the mesoscale dynamics like those presented in [9] and [10] while the temperature evolution is fully kept on the macroscale.

5.1.1. Macroscale part

For the macroscale part the above assumptions mean the omission of the terms $\langle \widetilde{\boldsymbol{u}} \cdot \boldsymbol{\nabla} \widetilde{T}_i \rangle$ and $\langle \widetilde{\boldsymbol{u}} \cdot \boldsymbol{\nabla} \widetilde{T}_e \rangle$ in the macroscale energy balances (3.47) and (3.48) while the ion particle balance (3.38) and the total parallel momentum balance (3.46) remain unchanged. For completeness they are presented here again together with the modified energy balances, the averaged mesoscale terms being highlighted in blue. The **particle balance** is given by

$$\frac{\partial n_0}{\partial t} + \boldsymbol{\nabla}\cdot\left(n_0 \boldsymbol{u}_{\parallel 0}\right) = S^{ic}_{0in} - \boldsymbol{\nabla}\cdot\langle \tilde{n}\tilde{\boldsymbol{u}}\rangle , \tag{5.1}$$

the **total parallel momentum balance** by

$$\begin{aligned} \frac{\partial}{\partial t}\left(m_i n_0 u_{\parallel 0}\right) + \boldsymbol{\nabla}\cdot\left(m_i n_0 u_{\parallel 0}\boldsymbol{u}_{\parallel 0}\right) &= -\left[\boldsymbol{\nabla}\cdot\boldsymbol{\Pi}_{0i}\right]_{\parallel} - \nabla_{\parallel}\left[n_0(T_{0i}+T_{0e})\right] + S^{ic}_{\parallel 0imV} \\ &\quad - m_i n_0 \left\langle \tilde{\boldsymbol{u}}\cdot\boldsymbol{\nabla}\tilde{u}_{\parallel}\right\rangle - m_i u_{\parallel 0}\,\boldsymbol{\nabla}\cdot\langle \tilde{n}\tilde{\boldsymbol{u}}\rangle . \end{aligned} \tag{5.2}$$

For the **ion energy balance** one has

$$\begin{aligned} &\frac{\partial}{\partial t}\left(\frac{3}{2}n_0T_{0i} + \frac{1}{2}m_i n_0 u_{\parallel 0}^2\right) + \boldsymbol{\nabla}\cdot\left(\frac{5}{2}n_0T_{0i}\boldsymbol{u}_{\parallel 0} + \frac{1}{2}m_i n_0 u_{\parallel 0}^2\boldsymbol{u}_{\parallel 0}\right) \\ &\qquad = -u_{\parallel 0}\nabla_{\parallel}(n_0T_{0e}) - \boldsymbol{\nabla}\cdot\left(\boldsymbol{u}_{\parallel 0}\cdot\boldsymbol{\Pi}_{0i}\right) + Q_{0i} - \boldsymbol{\nabla}\cdot\boldsymbol{q}_{0i} \\ &\qquad + S^{ic}_{0Ei} - m_i n_0 u_{\parallel 0}\left\langle \tilde{\boldsymbol{u}}\cdot\boldsymbol{\nabla}\tilde{u}_{\parallel}\right\rangle - \left(\frac{3}{2}T_{0i} + \frac{1}{2}m_i u_{\parallel 0}^2\right)\boldsymbol{\nabla}\cdot\langle \tilde{n}\tilde{\boldsymbol{u}}\rangle , \end{aligned} \tag{5.3}$$

and for **electron energy balance**

$$\begin{aligned} \frac{\partial}{\partial t}\left(\frac{3}{2}n_0T_{0e}\right) + \boldsymbol{\nabla}\cdot\left(\frac{5}{2}n_0T_{0e}\boldsymbol{u}_{\parallel 0}\right) &= u_{\parallel 0}\nabla_{\parallel}(n_0T_{0e}) + Q_{0e} - \boldsymbol{\nabla}\cdot\boldsymbol{q}_{0e} + S^{ic}_{0Ee} \\ &\quad - \frac{3}{2}T_{0e}\,\boldsymbol{\nabla}\cdot\langle \tilde{n}\tilde{\boldsymbol{u}}\rangle . \end{aligned} \tag{5.4}$$

5.1.2. Mesoscale part

Neglecting the dynamics of $\widetilde{T}_i$ and $\widetilde{T}_e$ on the mesoscale reduces the number of local drift fluid equations, given by eqs. (4.51) to (4.56), from six to four since the temperature balances (4.53) and (4.54) can be neglected. With the macroscale quantities highlighted in green the mesoscale part of the specific multiscale model then comprises the **particle balance**,

$$\begin{aligned} \frac{\partial \tilde{n}}{\partial t} + \tilde{\boldsymbol{v}}_{\mathrm{E}} \cdot \boldsymbol{\nabla} \tilde{n} + \tilde{\boldsymbol{v}}_{\mathrm{E}} \cdot \boldsymbol{\nabla} n_0 &= \frac{T_{0e}}{e} \mathcal{K}(\tilde{n}) - n_0 \mathcal{K}(\widetilde{\phi}) \\ &\quad - n_0 B \Big(\nabla_{\|0} + \widetilde{\nabla}_{\|} \Big) \left(\frac{\tilde{u}_{\|}}{B} - \frac{\widetilde{j}_{\|}}{e n_0 B} \right) + \gamma(\tilde{n}) \, , \qquad (5.5) \end{aligned}$$

the **total parallel momentum balance**,

$$m_i n_0 \frac{\partial \tilde{u}_{\|}}{\partial t} + m_i n_0 \tilde{\boldsymbol{v}}_{\mathrm{E}} \cdot \boldsymbol{\nabla} \tilde{u}_{\|} = -T_{0e} \widetilde{\nabla}_{\|} n_0 - T_{0e} \Big(\nabla_{\|0} + \widetilde{\nabla}_{\|} \Big) \tilde{n} + \gamma(\tilde{u}_{\|}) \, , \qquad (5.6)$$

Ohm's law,

$$\begin{aligned} \frac{m_e}{e} \left(\frac{\partial}{\partial t} + \tilde{\boldsymbol{v}}_{\mathrm{E}} \cdot \boldsymbol{\nabla} \right) \widetilde{j}_{\|} &= -e n_0 \frac{\partial \widetilde{A}_{\|}}{\partial t} - e n_0 \Big(\nabla_{\|0} + \widetilde{\nabla}_{\|} \Big) \widetilde{\phi} - R_{\|e} \\ &\quad + T_{0e} \Big(\nabla_{\|0} + \widetilde{\nabla}_{\|} \Big) \tilde{n} \, , \qquad (5.7) \end{aligned}$$

and the **vorticity equation**:

$$\frac{m_i n_0}{B^2} \left(\frac{\partial}{\partial t} + \boldsymbol{v}_{\mathrm{E}} \cdot \boldsymbol{\nabla} \right) \nabla_{\perp}^2 \widetilde{\phi} = B \Big(\nabla_{\|0} + \widetilde{\nabla}_{\|} \Big) \frac{\widetilde{j}_{\|}}{B} + T_{0e} \, \mathcal{K}(\tilde{n}) \, . \qquad (5.8)$$

The damping terms $\gamma(\tilde{n})$ and $\gamma(\tilde{u}_{\|})$ are given by

$$\gamma(\tilde{n}) = \Big\langle \tilde{\boldsymbol{v}}_{\mathrm{E}} \cdot \boldsymbol{\nabla} \tilde{n} \Big\rangle + \Big\langle \tilde{n} \, \mathcal{K}(\widetilde{\phi}) \Big\rangle \, , \qquad (5.9)$$

$$\gamma(\tilde{u}_{\|}) = T_{0e} \Big\langle \widetilde{\nabla}_{\|} \tilde{n} \Big\rangle + m_i n_0 \Big\langle \tilde{\boldsymbol{v}}_{\mathrm{E}} \cdot \boldsymbol{\nabla} \tilde{u}_{\|} \Big\rangle \, . \qquad (5.10)$$

5.2. Discussion of the multiscale model

The specific multiscale model for the plasma edge consists of eqs. (5.1) to (5.4) to describe the macroscale evolution via the quantities n_0, $u_{\|0}$, T_{0i}, and T_{0e}. The mesoscale part, given by eqs. (5.5) to (5.8) for $\widetilde{n}$, $\widetilde{u}_\|$, $\widetilde{A}_\|$, and $\widetilde{\phi}$, provides the averaged terms $\langle \widetilde{n}\widetilde{\boldsymbol{u}} \rangle$, corresponding to a particle flux, and $\langle \widetilde{\boldsymbol{u}} \cdot \boldsymbol{\nabla} \widetilde{u}_\| \rangle$, a part of the divergence of a momentum flux, for the macroscale evolution. The terms of the form $3/2\, T_0 \boldsymbol{\nabla} \cdot \langle \widetilde{n}\widetilde{\boldsymbol{u}} \rangle$ present in the macroscale temperature balances (5.3) and (5.4) illustrate the fact that the mesoscale dynamics still influence the energy balances on the macroscale, even though the dynamics of $\widetilde{T}_i$ and $\widetilde{T}_e$ are neglected in the model. The large scale profile provides a driving term of the local mesoscale dynamics in form of the perpendicular density gradient $\boldsymbol{\nabla}_\perp n_0$ as well as the parameters n_0 and T_{0e} which influence the ion Larmor radius ρ_s, the plasma beta β_p, and the collisionality ν_e of the plasma. While the interaction of the plasma with neutrals is not directly considered on the mesoscale level corresponding effects can be partly incorporated due to their impact on the large scale profiles via the source terms S^{ic}. Numerically solving the mesoscale system with the damping terms $\gamma(\widetilde{n})$ and $\gamma(\widetilde{u}_\|)$ as given by eqs. (5.9) and (5.10) is complicated and time consuming due to the involved averaging procedure. Therefore, one might choose another form of $\gamma(\widetilde{n})$ and $\gamma(\widetilde{u}_\|)$ to ensure that $\langle \widetilde{\alpha} \rangle = 0$, for which an example is given in chapter 7.

5.3. Survey on comparable models

A number of coupled code systems, combining microscale and mesoscale plasma turbulence/drift fluid codes with large scale codes, has been set up to study the plasma profiles of a tokamak device for stationary cases. A survey is given in table 5.1, including information about the codes that have been used, the tokamak region for which the coupled code system applies, and the basic characteristics of the investigated cases. They are presented here to classify the multiscale model and coupled code system developed in this thesis and identify unsolved questions. The list in table 5.1 is incomplete – other examples of how to incorporate the effects of the microscale and mesoscale dynamics into large scale models are for example given in [67], [68], and [69], with a mean field model for transport dominated by the E×B turbulence described in [70]. The choice of systems summarized here was made with regard to their relative similarity to the multiscale approach outlined here.

All coupled code systems are based on the scale separation hypothesis regarding disparate temporal and spatial scales and the amplitudes of the respective dynamics. They use multigrid methods for a type B multiscale problem, determining the microscale/mesoscale quantities for the whole simulation domain, and belong, as the specific multiscale model derived here, to the class of heterogeneous multiscale methods [37] (see the classification of multiscale methods in paragraph 2.3.1). Regarding these aspects they are similar to the multiscale model and the coupled code system presented here.

For the gyrokinetic approaches, the TGYRO and TRINITY code systems, the scale separation applies to the probability distribution function $f = f_0 + \widetilde{f}$; for the fluid approaches B2-DALF/B2-DW2D and UEDGE-BOUT it affects the plasma quantities $\alpha = \alpha_0 + \widetilde{\alpha}$. The TRINITY and TGYRO systems, which both use local gyrokinetic simulations to determine the averaged fluxes, consider the core region. Neither of them uses a macroscale transport model but finds the macroscale state associated to the microscale fluxes via application of the Newton-Raphson method [71].

The B2-DALF/B2-DW2D and UEDGE-BOUT systems are utilized to examine the plasma edge and SOL region. In both cases, the large scale code assumes toroidal symmetry, with the focus being on radial plasma profiles and studying only statistically stationary cases. The B2-DALF/B2-DW2D system does not employ a direct coupling procedure but relies on a matrix of pre-calculated transport coefficients for particle and energy transport. From this database the large scale code B2 obtains the required transport coefficients via an interpolation procedure. The coupling method is therefore a sequential one while the other systems use a concurrent procedure. Because the used averaged mesoscale fluxes are volume averaged, their poloidal variation, e.g. due to the curvature of the magnetic field, is neglected.

Various open questions and challenges regarding a multiscale modeling approach for the plasma edge are investigated in the following chapters 6, 7 and 8. The reproduction of time-dependent profiles is investigated with a simplified coupled code system in chapter 7. The poloidal dependence of mesoscale transport and its effect on the large scale profiles is assessed in form of an outlook in chapter 8. Besides these physical questions also technical issues are to be discussed, e.g. regarding the detection of a statistically stationary state of the local drift fluid simulation and the influence of the chosen macroscale transport model on the results. The latter topic is also discussed on the basis of a passive scalar model in the following chapter.

code system	**large-scale**	**microscale/mesoscale**	**region**	**cases**
TRINITY [72, 23]	TRINITY [72, 23] 4D phase space gyrokinetic (averaged)	GENE [5]/GS2 [73] 5D phase space gyrokinetic flux tube approximation	core	radial dep. of transport coeff. stationary cases on large scale coupling: particle, mom., energy no $\mathcal{M}$ used
TGYRO [22]	NEO[74] 1D kinetic	GYRO [6] 5D phase space gyrokinetic flux tube approximation	core	radial dep. of transport coeff. stationary cases on large scale coupling: energy no $\mathcal{M}$ used
B2-DALF [75] B2-DW2D [41, 25]	B2 [76, 77] 2D fluid $n_{0i},\ u_{\parallel 0},\ \phi_0,\ T_{0i},\ T_{0e}$	DALF [78, 79]/DW2D [78] 2D fluid $\widetilde{n}_i,\ \widetilde{\phi},\ \widetilde{T}_i,\ \widetilde{T}_e$	edge SOL	radial dep. of transport coeff. stationary cases on large scale coupling: particle, energy $\mathcal{M}$: diffusion
UEDGE-BOUT [80, 24, 81]	UEDGE [13] 2D fluid $n_{0i},\ u_{\parallel 0},\ T_{0i},\ T_{0e}$	BOUT [82] 3D fluid $\widetilde{n}_i,\ \widetilde{u}_{\parallel},\ \widetilde{\boldsymbol{v}}_{\parallel},\ \widetilde{T}_i,\ \widetilde{T}_e,\ \widetilde{\phi}$	edge SOL	radial and poloidal dep. of transport coeff. stationary cases on large scale coupling: particle, energy $\mathcal{M}$: diffusion + convection

Table 5.1.: Survey of coupled code systems to simulate a tokamak plasma. $\mathcal{M}$ denotes the macroscale transport model used.

6. Macroscale transport models for averaged mesoscale dynamics

The specific multiscale model of the previous chapter 5 describes the dynamics of the plasma in the edge region of a tokamak device. Both its mesoscale and macroscale part contain averaged mesoscale terms of the form $\langle \tilde{\alpha} \tilde{\boldsymbol{v}} \rangle$ and $\langle \tilde{\boldsymbol{v}} \cdot \boldsymbol{\nabla} \tilde{\alpha} \rangle$ which represent the effect of the mesoscale processes on the macroscale evolution of profiles. As it was outlined in chapter 2, paragraph 2.3.3, macroscale transport models can be used to represent these terms in the macroscale equations and thereby increase the time savings of the coupled code system. As an example, a diffusive macroscale transport model has been used in the derivation of the self-contained large scale model of chapter 3.

The present chapter focuses on these macroscale transport models. It is divided into two parts. In paragraph 6.1, a short overview on the widely used diffusion-convection scheme is given. The main objective is to provide information about the statistical elements governing transport which, on the macroscale, can be described by a diffusive scheme. This includes the important relation $\langle \Delta r^2 \rangle = D \Delta t$ which relates the mean squared displacement $\langle \Delta r^2 \rangle$ and the diffusion coefficient and is used for the analysis of the passive scalar model in paragraph 6.2. Also, a method to decompose a given (averaged microscale/mesoscale) flux into a diffusive and a convective part is presented in paragraph 6.1.2 which can be applied to formulate macroscale transport models for coupled code systems.

In paragraph 6.2, a passive scalar model is presented in which a scalar quantity is advected by a given velocity field. It serves as a more realistic extension of the basic examples of diffusive transport outlined in paragraph 6.1 and motivates the choice of the diffusive macroscale transport model of the large scale transport model (chapter 3). Additionally, it provides an exemplary insight into the interaction between averaged mesoscale dynamics and macroscale processes as it is analyzed in detail for a magnetized, collisional plasma in the following chapters. The existing studies [31, 32, 33], which were carried out for small Kubo number regimes (see paragraph 6.2.1) are extended to dynamical regimes with large Kubo numbers. An analytical description for the macroscale transport behavior of these regimes is determined and related to percolation theory [83]. In paragraph 6.2.3, a first test with a simplified coupled code system, using the passive scalar model, is carried out to study the interplay between the macroscale transport model and the accuracy of the macroscale results with respect to a benchmark case.

6.1. Representation of transport via a diffusion-convection scheme

Diffusion is a well-known phenomenon in physics [84, 85], chemistry [84, 86], and biology [87] to describe transport on a macroscale due to a specific statistical character of motion of particles or fluid parcels on the microscale/mesoscale. To provide a basic understanding of diffusive processes, a straightforward derivation of Fick's first and second law using a simple random walk is given in paragraph 6.1.1.

6.1.1. Fick's laws and drift-diffusion equations

Fick's first law [88] states that a particle flux $\mathbf{\Gamma}$ is proportional to the density gradient $\boldsymbol{\nabla} n$ and directed in opposite direction:

$$\mathbf{\Gamma} \;=\; -D\boldsymbol{\nabla} n \; . \tag{6.1}$$

D is the diffusion coefficient. Eq. (6.1) can for instance be applied to an ensemble of particles, performing a discrete random walk. The example presented here is taken from [89].

Consider an one-dimensional system with a large number N of particles and an inhomogeneous initial distribution. After a time interval Δt, each particle makes a step of length Δx either to the left (-) or to the right (+), the probabilities p_- and p_+ for both directions being equal, $p_- = p_+ = 0.5$. The point x_0 is crossed by N^- particles from the left and N^+ particles from the right during the time interval Δt:

$$N^-(x_0) \;=\; \frac{1}{2}\int\limits_{x_0-\Delta x}^{x_0} n(x)\; dx \; , \qquad N^+(x_0) \;=\; \frac{1}{2}\int\limits_{x_0}^{x_0+\Delta x} n(x)\; dx \; . \tag{6.2}$$

Approximating the density $n(x)$ by a Taylor expansion up to first order yields

$$n(x) \;=\; n(x_0) \;+\; (x-x_0)\,\frac{\partial n}{\partial x}(x_0) \;+\; \mathcal{O}\Big([x-x_0]^2\Big) \; . \tag{6.3}$$

Eq. (6.3) can be used for the determination of N^- and N^+:

$$N^-(x_0) \;=\; \frac{1}{2}n_0\Delta x \;-\; \frac{\Delta x^2}{4}\frac{\partial n}{\partial x}\bigg|_{x_0} \; , \quad N^+(x_0) \;=\; \frac{1}{2}n_0\Delta x \;+\; \frac{\Delta x^2}{4}\frac{\partial n}{\partial x}\bigg|_{x_0} \; . \tag{6.4}$$

The particle flux $\Gamma(x_0)$ at position x_0 is then determined by

$$\Gamma(x_0) \;=\; \frac{1}{\Delta t}\Big[N^-(x_0) - N^+(x_0)\Big] \;=\; -D\,\frac{\partial n}{\partial x}(x_0) \; , \tag{6.5}$$

where for D one has

$$\boxed{D = \frac{(\Delta x)^2}{2\Delta t} \ . \qquad (6.6)}$$

The relation (6.6), connecting D to the squared displacement $(\Delta x)^2$ and the respective time Δt, can be interpreted as the signature of a diffusive process. With the generalized mean squared displacement $\langle \Delta r^2 \rangle$ for a continuous, three-dimensional case,

$$\langle \Delta r^2 \rangle \ \propto \ \Delta t^a \qquad \text{with} \qquad \langle \Delta r^2 \rangle \ \equiv \ \left\langle \left| \boldsymbol{r}_p(t_0 + \Delta t) - \boldsymbol{r}_p(t_0) \right|^2 \right\rangle \ , \qquad (6.7)$$

$\boldsymbol{r}_p$ denoting the position of a given particle and $\langle ... \rangle$ being the ensemble average, the following regimes are defined:

$$\begin{aligned} a \ &= \ 2 : \quad &&\text{convection,} \\ 2 > \ a \ &> \ 1 : \quad &&\text{superdiffusion,} \\ a \ &= \ 1 : \quad &&\text{diffusion,} \\ 1 > a \ &> \ 0 : \quad &&\text{subdiffusion.} \end{aligned} \qquad (6.8)$$

The statistical character of transport mentioned above refers to the fact that eq. (6.7) only holds for the ensemble average, but may differ for individual particles.
Eq. (6.5) can be easily generalized for three dimensions to yield Fick's first law (6.1). Fick's second law is the obtained by using Fick's first law in the particle balance equation (2.27) with $S = 0$ and assuming a constant diffusion coefficient, which gives:

$$\frac{\partial n}{\partial t} \ = \ D \nabla^2 n \ . \qquad (6.9)$$

The operator ∇^2 is the Laplace operator, $\nabla^2 \equiv \boldsymbol{\nabla} \cdot \boldsymbol{\nabla}$.

The characteristics of this simple many-particle system can be generalized further to arrive at a transport description including diffusion and convection. For this purpose consider that the probability for a particle to make a jump of length $\beta_+ \Delta x$ after a time interval Δt to the right is now given by p_+, while the probability of making a jump of length $\beta_- \Delta x$ to the left is given by $p_- = 1 - p_+$. For the number of particles N^- and N^+, crossing the point $x = x_0$ from the left and right, respectively, one gets:

$$N^-(x_0) \ = \ p_+ \int\limits_{x_0 - \beta_+ \Delta x}^{x_0} n(x) \ dx \ , \quad N^+(x_0) \ = \ (1 - p_+) \int\limits_{x_0}^{x_0 + \beta_- \Delta x} n(x) \ dx \ . \qquad (6.10)$$

The corresponding density continuity equation is given by

$$\frac{\partial n}{\partial t} \;=\; -v_c \frac{\partial n}{\partial x} \;+\; D\,\frac{\partial^2 n}{\partial x^2}\;, \tag{6.11}$$

with

$$v_c \;=\; \Big(p_+\beta_+ - [1-p_+]\beta_-\Big)\frac{\Delta x}{\Delta t}\;, \qquad D \;=\; \Big(p_+\beta_+^2 + [1-p_+]\beta_-^2\Big)\frac{(\Delta x)^2}{2\Delta t}\;. \tag{6.12}$$

For the symmetric case $p_+ = p_- = 0.5$ and an equal step length for both directions ($\beta_+ = \beta_- = \beta$) Fick's first law (6.1) is recovered and D is given by eq. (6.6), multiplied by β^2. In general, the flux Γ is purely diffusive if $p_+\beta_+ - (1-p_+)\beta_- = 0$, i.e. if the averaged displacement $\langle \Delta x\rangle$ becomes zero.

Similar examples for higher dimensional problems and a detailed discussion of diffusion-convection processes in the context of stochastic processes can for instance be found in [84, 85].

6.1.2. Splitting flux into a diffusive and a convective part

In the multiscale systems discussed in chapters 7 and 8, convective-diffusive macroscale transport models $\mathcal{M}$ are used to represent the averaged mesoscale terms. The ansatz for the flux $\langle\widetilde{\alpha}\widetilde{\boldsymbol{v}}\rangle$ is given by

$$\langle\widetilde{\alpha}\widetilde{\boldsymbol{v}}\rangle \;=\; -\mathbf{D}\cdot\boldsymbol{\nabla}\alpha_0 + \alpha_0\boldsymbol{v}_c\;. \tag{6.13}$$

There is now *a priori* rule how to divide a given flux appropriately into a convective and a diffusive part. One approach for such a division based on the characteristics of the diffusion tensor $\mathbf{D}$ is presented below.

The diffusion tensor $\mathbf{D}$ has to be symmetric and positive semi-definite by definition [2]. This information is used for constructing $\mathbf{D}$. With the vectors $\boldsymbol{a}$ and $\boldsymbol{b}$,

$$\boldsymbol{a} \;\equiv\; \frac{\langle\widetilde{\alpha}\widetilde{\boldsymbol{v}}\rangle}{|\langle\widetilde{\alpha}\widetilde{\boldsymbol{v}}\rangle|}\;, \qquad \boldsymbol{b} \;\equiv\; \frac{\boldsymbol{\nabla}\alpha_0}{|\boldsymbol{\nabla}\alpha_0|}\;, \tag{6.14}$$

the tensor $\mathbf{F}$ can be defined:

$$\mathbf{F} \;\equiv\; \frac{|\langle\widetilde{\alpha}\widetilde{\boldsymbol{v}}\rangle|}{|\boldsymbol{\nabla}\alpha_0|}\,\boldsymbol{ab}\;. \tag{6.15}$$

$\mathbf{F}$ has the property that, when multiplied with $\boldsymbol{\nabla}\alpha_0$, it yields the averaged mesoscale flux, $\mathbf{F}\cdot\boldsymbol{\nabla}\alpha_0 = \langle\widetilde{\alpha}\widetilde{\boldsymbol{v}}\rangle$.
Next, $\mathbf{F}$ is used to calculate $\mathbf{D}$. For this purpose, $\mathbf{F}$ is split into a symmetric part $\mathbf{S}$ and an antisymmetric part $\mathbf{A}$:

$$\mathbf{F} \;=\; \mathbf{S}+\mathbf{A}\;, \quad \mathbf{S} \;=\; \frac{|\langle\widetilde{\alpha}\widetilde{\boldsymbol{v}}\rangle|}{2|\boldsymbol{\nabla}\alpha_0|}(\boldsymbol{ab}+\boldsymbol{ba})\;, \quad \mathbf{A} \;=\; \frac{|\langle\widetilde{\alpha}\widetilde{\boldsymbol{v}}\rangle|}{2|\boldsymbol{\nabla}\alpha_0|}(\boldsymbol{ab}-\boldsymbol{ba})\;. \tag{6.16}$$

Since $\mathbf{D}$ has to be symmetric continue with $\mathbf{S}$ for its construction. The positive semi-definiteness of $\mathbf{D}$ is ensured by finding the eigenvalues $\lambda_i \geq 0$ and the eigenvectors $\boldsymbol{s}_i(\lambda_i \geq 0)$ of $\mathbf{S}$. Then $\mathbf{D}$ can be constructed by:

$$\mathbf{D} \; = \; \sum_i \lambda_i \boldsymbol{s}_i(\lambda_i) \boldsymbol{s}_i(\lambda_i) \; , \quad \lambda_i \; \geq \; 0 \; . \tag{6.17}$$

The eigenvalues λ_i and eigenvectors $\boldsymbol{s}_i(\lambda_i)$ of $\mathbf{S}$ are given by

$$\lambda_1 \; = \; \frac{|\langle \tilde{\alpha} \tilde{\boldsymbol{v}} \rangle|}{2|\boldsymbol{\nabla} \alpha_0|}(1 + \boldsymbol{a} \cdot \boldsymbol{b}) \; , \qquad \boldsymbol{s}_1(\lambda_1) \; = \; \frac{1}{\sqrt{2}} \frac{\boldsymbol{a} + \boldsymbol{b}}{\sqrt{1 + \boldsymbol{a} \cdot \boldsymbol{b}}} \; , \tag{6.18}$$

$$\lambda_2 \; = \; -\frac{|\langle \tilde{\alpha} \tilde{\boldsymbol{v}} \rangle|}{2|\boldsymbol{\nabla} \alpha_0|}(1 - \boldsymbol{a} \cdot \boldsymbol{b}) \; , \qquad \boldsymbol{s}_2(\lambda_2) \; = \; \frac{1}{\sqrt{2}} \frac{\boldsymbol{a} - \boldsymbol{b}}{\sqrt{1 - \boldsymbol{a} \cdot \boldsymbol{b}}} \; , \tag{6.19}$$

$$\lambda_3 \; = \; 0 \; , \qquad \boldsymbol{s}_3(\lambda_3) \; = \; \frac{\boldsymbol{b} \times \boldsymbol{a}}{\sqrt{1 - (\boldsymbol{a} \cdot \boldsymbol{b})^2}} \; . \tag{6.20}$$

It holds that $\lambda_1 \geq 0$ and $\lambda_2 \leq 0$. In the case where the flux $\langle \tilde{\alpha} \tilde{\boldsymbol{v}} \rangle$ and the gradient $\boldsymbol{\nabla} \alpha_0$ are antiparallel, $\lambda_1 = 0$ and thus $\mathbf{D} = 0$. For all other cases $\lambda_1 > 0$. Hence, the diffusion tensor $\mathbf{D}$ determined via eq. (6.17) is

$$\boxed{\mathbf{D} \; = \; \frac{|\langle \tilde{\alpha} \tilde{\boldsymbol{v}} \rangle|}{4|\boldsymbol{\nabla} \alpha_0|}(\boldsymbol{aa} + \boldsymbol{ab} + \boldsymbol{ba} + \boldsymbol{bb}) \; .} \tag{6.21}$$

The diffusive flux $\langle \tilde{\alpha} \tilde{\boldsymbol{v}} \rangle_{\text{diff}}$ is then given by

$$\langle \tilde{\alpha} \tilde{\boldsymbol{v}} \rangle_{\text{diff}} \; = \; \mathbf{D} \cdot \boldsymbol{\nabla} \alpha_0 \; = \; \frac{|\langle \tilde{\alpha} \tilde{\boldsymbol{v}} \rangle|}{4|\boldsymbol{\nabla} \alpha_0|}(1 + \boldsymbol{a} \cdot \boldsymbol{b})(\boldsymbol{a} + \boldsymbol{b}) \; . \tag{6.22}$$

Note that $\langle \tilde{\alpha} \tilde{\boldsymbol{v}} \rangle_{\text{diff}}$ points into a direction between $\langle \tilde{\alpha} \tilde{\boldsymbol{v}} \rangle$ and $\boldsymbol{\nabla} \alpha_0$, given by the vector $\boldsymbol{a} + \boldsymbol{b}$.
In the above derivation, the part of the flux $\langle \tilde{\alpha} \tilde{\boldsymbol{v}} \rangle$ contained in $\mathbf{A} \cdot \boldsymbol{\nabla} \alpha_0$ has been neglected. This part cannot be modeled by a diffusive model. Here, a convective velocity $\boldsymbol{v}_c$ can be used to account for this component of the flux:

$$\boxed{\boldsymbol{v}_c = \; \frac{1}{\alpha_0} \Big[\langle \tilde{\alpha} \tilde{\boldsymbol{v}} \rangle - \mathbf{D} \cdot \boldsymbol{\nabla} \alpha_0 \Big] \; ,} \tag{6.23}$$

so that $\langle \tilde{\alpha} \tilde{\boldsymbol{v}} \rangle = \langle \tilde{\alpha} \tilde{\boldsymbol{v}} \rangle_{\text{diff}} + \langle \tilde{\alpha} \tilde{\boldsymbol{v}} \rangle_{\text{conv}}$ with $\langle \tilde{\alpha} \tilde{\boldsymbol{v}} \rangle_{\text{conv}} = \alpha_0 \boldsymbol{v}_c$.

With eqs. (6.21) and (6.23) one has a macroscale transport model for representing

$\langle\widetilde{\alpha}\widetilde{\boldsymbol{v}}\rangle$ at hand. For the scalar terms of the form $\langle\widetilde{\boldsymbol{u}}\cdot\boldsymbol{\nabla}\widetilde{\alpha}\rangle$ that correspond to a divergence of a flux and that also appear in the macroscale particle, parallel momentum, and ion energy balances (5.1), (5.2) and (5.3) of the specific multiscale model one could, for example, choose the approach

$$\langle\widetilde{\boldsymbol{u}}\cdot\boldsymbol{\nabla}\widetilde{\alpha}\rangle \;=\; \boldsymbol{v}_c^*\cdot\boldsymbol{\nabla}\alpha_0 \;+\; G\nabla^2\alpha_0 \tag{6.24}$$

with

$$\boldsymbol{v}_c^* \;=\; \beta\,\frac{\langle\widetilde{\boldsymbol{u}}\cdot\boldsymbol{\nabla}\widetilde{\alpha}\rangle}{|\boldsymbol{\nabla}\alpha_0|^2}\,\boldsymbol{\nabla}\alpha_0\;, \qquad G \;=\; (1-\beta)\,\frac{\langle\widetilde{\boldsymbol{u}}\cdot\boldsymbol{\nabla}\widetilde{\alpha}\rangle}{\nabla^2\alpha_0}\;. \tag{6.25}$$

The parameter β with $0\leq\beta\leq 1$ determines the fraction of $\langle\widetilde{\boldsymbol{u}}\cdot\boldsymbol{\nabla}\widetilde{\alpha}\rangle$ which is modeled by the first and the second term, respectively, of the rhs of eq. (6.24).

In how far macroscale plasma transport due to averaged microscale and mesoscale dynamics can be represented by a diffusion-convection scheme is subject of ongoing discussions [90, 91, 92]. Note that in the macroscale transport models outlined here the idea is that the transport coefficients are updated after time intervals Δt_{up} and spatial intervals $\Delta\boldsymbol{r}_{\mathrm{up}}$ with the current values of the averaged mesoscale terms and are therefore functions of space and time. Therefore, using a macroscale model with a temporally and spatially dependent diffusion tensor $\mathbf{D}=\mathbf{D}(\boldsymbol{r},t)$ does not necessarily mean that the associated averaged mesoscale transport is diffusive, i.e. that the mean squared displacement $\langle\Delta r^2\rangle$ is proportional to the corresponding time interval Δt, compare eq. (6.7) with $a=1$. In that case the choice to model an averaged mesoscale flux using a diffusive model becomes rather arbitrary and one should reflect upon employing more suiting approaches. Nonetheless, diffusive models have a widespread popularity in fluid modeling [2] due to their relatively easy implementation and their numerically benevolent behavior. An example where an averaged mesoscale flux can be modeled exactly by a diffusive model is given in the next paragraph 6.2.

6.2. Passive scalar system

In this paragraph, a passive scalar system based on the work presented in [31, 32, 33] is investigated to study the relation between mesoscale and macroscale transport behavior. It serves to motivate the diffusive macroscale transport model used here for the self-contained large scale model of chapter 3 which is often employed in large scale plasma edge codes, e.g. see [14, 16, 15]. The passive scalar system is an extension of the simple random walk examples given in paragraph 6.1.1. Here, instead of a discrete step process the continuous advection of a scalar α by a velocity field $\boldsymbol{v}(\boldsymbol{r}, t)$ is considered, the characterizing quantities of the latter being its correlation time $\tau_c(\boldsymbol{v})$, its correlation length $\lambda_c(\boldsymbol{v})$, and its root mean square velocity v_{RMS}. The dynamics of α have no influence on $\boldsymbol{v}(\boldsymbol{r}, t)$; thus the characterization of the system as 'passive'.
After an outline of the passive scalar system in paragraph 6.2.1, the numerical simulations are studied in detail in paragraph 6.2.2. A simple coupled code system is presented and used for a first assessment of the influence of the input parameters like Δt_{up} and different macroscale transport models on the correct reproduction of the macroscale evolution of the system.

6.2.1. Outline of the passive scalar system

The underlying equation to be considered for the passive scalar system is the continuity equation for an arbitrary fluid quantity α and a divergence-free velocity field $\boldsymbol{v}$:

$$\frac{\partial \alpha}{\partial t} + \boldsymbol{v} \cdot \boldsymbol{\nabla} \alpha = 0 . \tag{6.26}$$

The velocity field considered here is isotropic and has a Gaussian PDF $p(v)$ with zero mean:

$$\langle \boldsymbol{v} \rangle = 0 , \qquad p(v) = \frac{1}{\sqrt{2\pi}\sigma} \exp\left(- \frac{v^2}{2\sigma^2} \right) \tag{6.27}$$

Here, the operator $\langle ... \rangle$ denotes the ensemble average, i.e. is given by $\langle ... \rangle \equiv \int ... \, p(v) \, d^3v$. The velocity field is further characterized by its root mean square velocity $v_{\mathrm{RMS}} \equiv \sqrt{\langle \boldsymbol{v}^2 \rangle}$, its correlation time $\tau_c(\boldsymbol{v})$, and its correlation length $\lambda_c(\boldsymbol{v})$. Analogously to the scale separation introduced for the generic multiscale model in chapter 2, paragraph 2.2.1, the ensemble average $\alpha_0 = \langle \alpha \rangle$, and the fluctuation $\widetilde{\alpha} \equiv \alpha - \alpha_0$ are introduced. By applying $\langle ... \rangle$ to eq. (6.26) one obtains the evolution equation for the macroscale part α_0,

$$\frac{\partial \alpha_0}{\partial t} + \Big\langle \boldsymbol{v} \cdot \boldsymbol{\nabla} \alpha \Big\rangle = 0 . \tag{6.28}$$

As outlined in [31] eq. (6.28) can be transformed to yield

$$\boxed{\frac{\partial \alpha_0}{\partial t} \;=\; D\nabla^2\alpha_0 \qquad \text{with} \qquad D \;=\; v_{\text{RMS}}^2\tau_c(\boldsymbol{v}) \; . \tag{6.29}}$$

This means that while the evolution of α is determined by advection via the velocity field $\boldsymbol{v}$, the evolution of its ensemble average given by eq. (6.29) is given by Fick's second law, with D depending only on the characteristic velocity v_{RMS} and correlation time $\tau_c(\boldsymbol{v})$ of the velocity field $\boldsymbol{v}$. The macroscale transport model related to eq. (6.29) is

$$\langle \boldsymbol{v} \cdot \boldsymbol{\nabla}\tilde{\alpha} \rangle \;=\; -D\nabla^2\alpha_0 \; . \tag{6.30}$$

Considering the large scale model of chapter 3, eqs. (3.53), (3.55), (3.56), and (3.57) one therefore finds that the diffusion hypothesis used to represent the terms of the form $\langle \boldsymbol{v} \cdot \boldsymbol{\nabla}\alpha \rangle$ and $\langle \alpha\boldsymbol{v} \rangle$ by a diffusive macroscale transport model becomes well-founded if α is a passive scalar and $\boldsymbol{v}$ is an incompressible Gaussian velocity field with zero mean.

As explained in [31], eq. (6.29) only holds if

$$K \;\equiv\; \frac{\tau_c(\boldsymbol{v})\, v_{\text{RMS}}}{\lambda_c(\boldsymbol{v})} \;\ll 1 \; . \tag{6.31}$$

The ratio $\tau_c(\boldsymbol{v})\, v_{\text{RMS}}/\lambda_c(\boldsymbol{v})$ is identified here with the Kubo number K which was introduced in [93] and is commonly used to characterize different regimes of turbulent dynamics, e.g. see. [94], and also applied in the analysis of plasma turbulence, e.g. see [95, 96]. Typically, the regime with $K \ll 1$ is characterized as 'weak turbulence' while $K \gg 1$ corresponds to the 'strong turbulence' regime: eq. (6.31) expresses that the typical displacement of a fluid parcel during the time $\tau_c(\boldsymbol{v})$ has to be much smaller than the correlation length $\lambda_c(\boldsymbol{v})$ of the velocity field. If eq. (6.31) holds, the fluid parcel cannot explore different regions of the velocity field (which have a characteristic extent on the order of $\lambda_c(\boldsymbol{v})$) before its convective velocity changes due to the temporal variation of $\boldsymbol{v}$. This is called 'weak turbulence'. If the opposite is true with $K \gg 1$, i.e. the particle *is* able to explore the velocity field during a time $\tau_c(\boldsymbol{v})$, this corresponds to 'strong turbulence'.

In the following paragraph it is investigated what are the macroscale transport characteristics for cases where $K \gg 1$. This is done by carrying out numerical simulations of eq. (6.26) and systematically varying $\tau_c(\boldsymbol{v})$ (series one), v_{RMS} (series two), and $\lambda_c(\boldsymbol{v})$ (series three). The work complements the results presented in [33] and [32] where the passive scalar system has been studied for low Kubo numbers $K \ll 1$.

6.2.2. Diffusion in passive scalar simulations for high and low Kubo numbers

To solve eq. (6.26) numerically it is discretized in time and space for a two-dimensional domain with Cartesian coordinates x and y. Advection is modeled by a total variation diminishing (TVD) MUSCL-Hancock scheme [97]. For the sampling of the velocity field $\boldsymbol{v}$ a procedure similar to that outlined in [32] and[98] is used. The velocity components are defined via a potential ϕ to ensure that $\boldsymbol{v}$ is divergence-free:

$$v_x \equiv -\frac{\partial \phi}{\partial y} , \qquad v_y \equiv \frac{\partial \phi}{\partial x} . \tag{6.32}$$

Due to the determination of $\boldsymbol{v}$ via a potential ϕ it bears a certain resemblance to the E×B velocity (compare eq. (4.2)), even though the latter is usually not divergence-free. The potential ϕ itself is determined by a stochastic Langevin equation:

$$\tau \frac{\partial \phi}{\partial t} = -\phi + \varepsilon Q[-\lambda^2 \nabla^2] \zeta , \tag{6.33}$$

where τ is a characteristic time, ε an additional parameter to define the velocity field, and ζ is a Gaussian white noise with

$$\Big\langle \zeta(\boldsymbol{r}_1, t_1) \zeta(\boldsymbol{r}_2, t_2) \Big\rangle = \delta(\boldsymbol{r}_1 - \boldsymbol{r}_2)\, \delta(t_1 - t_2) . \tag{6.34}$$

$Q[-\lambda^2 \nabla^2]$ represents an operator responsible for a spatial filtering so that ϕ will have a predefined correlation length $\lambda_c(\phi)$. The details how to solve eq. (6.33) and sample $\phi(\boldsymbol{r}, t)$ are given in appendix A. One finds that the parameters τ, λ, and ε are closely related to the correlation time $\tau_c(\phi)$ and correlation length $\lambda_c(\phi)$ of the potential field ϕ and therefore also to the correlation time $\tau_c(\boldsymbol{v})$, correlation length $\lambda_c(\boldsymbol{v})$, and root mean square velocity v_{RMS} of the velocity field $\boldsymbol{v}$:

$$\tau_c(\boldsymbol{v}) = \tau = \tau_c(\phi) , \tag{6.35}$$

$$\lambda_c(\boldsymbol{v}) = \sqrt{\frac{\pi}{2}}\, \lambda = \frac{\lambda_c(\phi)}{2} , \tag{6.36}$$

$$v_{\mathrm{RMS}} = \sqrt{\langle \boldsymbol{v}^2 \rangle} = \sqrt{\Big\langle v_x^2 + v_y^2 \Big\rangle} = \frac{\sqrt{x_{\mathrm{sim}} y_{\mathrm{sim}}}\, \varepsilon}{\sqrt{32 \pi \tau \lambda^2}} , \tag{6.37}$$

where x_{sim} is the extent of the simulation domain in x direction and y_{sim} is its extent in y direction. For the two-dimensional problem, D is determined by

$$D = \frac{1}{2} v_{\mathrm{RMS}}^2 \tau_c(\boldsymbol{v}) = \frac{\pi \varepsilon^2 x_{\mathrm{sim}} y_{\mathrm{sim}}}{256 \lambda_c^4(\boldsymbol{v})} . \tag{6.38}$$

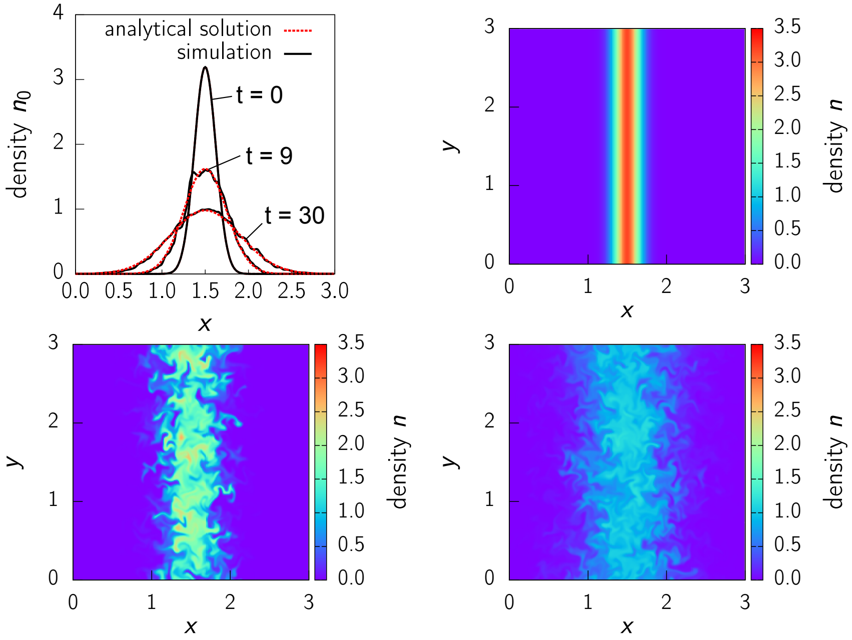

Figure 6.1.: Example of a passive scalar simulation for the parameters given in table 6.1. **Top, left:** Analytical solution of eq. (6.40) and the simulation results for $n_0 = \langle n \rangle_y$ for times $t = 0$, $t = 9$ and $t = 30$. **Top, right:** Snapshot of n at $t = 0$. **Bottom, left:** snapshot of n at $t = 9$. **Bottom, right:** Snapshot of n at $t = 30$.

The passive scalar simulations are set up as follows. All quantities are chosen to have dimension one and α is identified with the particle density n. Neumann boundary conditions are used in x direction with $\partial n / \partial x = 0$, in y direction periodical boundary conditions are employed. The initial profile of n is given by a Gaussian bell curve,

$$n(\boldsymbol{x}, t) = \frac{1}{\sqrt{2\pi\sigma^2}} \exp\left[-\frac{1}{2} \frac{(x-\mu)^2}{\sigma^2} \right] , \tag{6.39}$$

with $\mu = 1.5$ and $\sigma = 0.125$. The ensemble average $\langle ... \rangle$ is approximated by the average in y direction, $\langle ... \rangle_y$. Both averages coincide for $\lambda / L_y \to 0$ if the chosen initial distribution is symmetric in y direction. The analytical solution of the macroscale continuity equation for n_0,

$$\frac{\partial n_0}{\partial t} = D \nabla^2 n_0 , \tag{6.40}$$

par.	value	par.	value	par.	value	par.	value
t_{sim}	60	N_t	60 000	Δt_p	0.001	$\lambda_c(\boldsymbol{v})$	0.1
x_{sim}	3	N_x	256	Δx_p	0.012	v_{RMS}	0.14
y_{sim}	3	N_y	256	$\tau_c(\boldsymbol{v})$	0.125	K	0.3536

Table 6.1.: Parameters used for the passive scalar simulation shown in fig. 6.1. The total simulation duration is given by t_{sim}, N_t is the number of time steps, N_x and N_y are the numbers of grid points in x and y direction, respectively, Δt_p is the duration of one time step, and Δx_p the cell width in x and y direction. $D = 0.0013$.

with D given by eq. (6.38) is

$$n_0(x,t) \;=\; \frac{1}{\sqrt{2\pi\sigma^2 + 4\pi Dt}} \exp\left[-\frac{1}{2}\frac{(x-\mu)^2}{\sigma^2 + 2Dt}\right] . \tag{6.41}$$

An example for a simulation with $K = 0.35 \ll 1$ is shown in fig. 6.1, the simulation parameters being outlined in table 6.1. The analytical solution for n_0 with D determined by eq. (6.38) and the associated y-averaged values of n coincide and show the diffusive divergency of the density peak on the macroscale. The snapshots of the two-dimensional density map illustrate the complex structure of n on the mesoscale and thus the disparate character of dynamics on the mesoscale and macroscale.

First results for the dynamical regime with $K \gg 1$ which has not been studied previously are shown in fig. 6.2, left. K is increased successively from $K = 0.71$ (black) to $K = 5.66$ (violet) only by the variation of the correlation length $\lambda_c(\boldsymbol{v})$ of the velocity field, leaving the analytically determined $D = 5 \cdot 10^{-3}$ (see eq. (6.38)) constant. The higher K the slower the divergency of the density peak. The rather smooth, Gaussian-like shapes of the graphs of n_0 seem to suggest that macroscale transport is diffusive also for $K \gg 1$, even though with a smaller D than predicted by eq. (6.38).

The character of the macroscale transport for $K \gg 1$ can be classified by resorting to the displacement-time relation $\langle \Delta x^2 \rangle \propto \Delta t^a$, see eqs. (6.7) and (6.8). For this purpose, the exponent a is determined from the simulation data by plotting $\langle \Delta x^2 \rangle$ against Δt and a subsequent linear fit. The mean squared displacement $\langle \Delta x^2 \rangle$ is approximated by

$$\langle \Delta x^2 \rangle(t) \;\approx\; \frac{\int x^2 \, \langle n \rangle(x,t) \; dx}{\int \langle n \rangle_y(x,t) \; dx} . \tag{6.42}$$

This is a reasonable estimate for $\langle \Delta x^2 \rangle$ for a Gaussian initial distribution sharply located around its mean and symmetric in y direction, as it was used here.

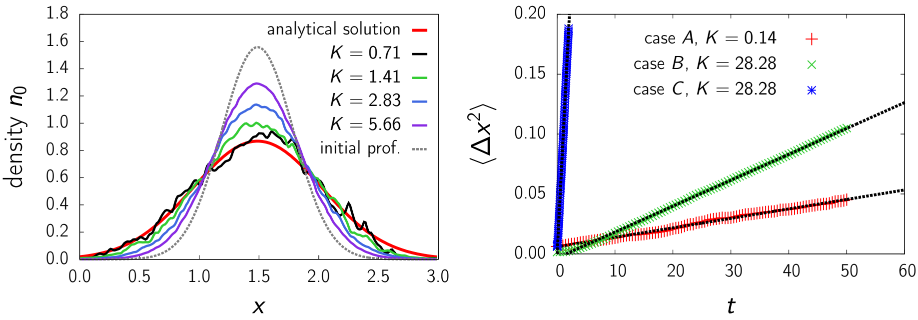

Figure 6.2.: Left: Divergency of a Gaussian density peak for different K at $t = 20$ with $t_{\text{sim}} = 20$, $\tau_c(\boldsymbol{v}) = 0.5$, $v_{\text{RMS}} = 0.14$ and $\lambda_c(\boldsymbol{v})$, starting at 0.1 for $K = 0.71$ and successively divided by two until $1.25 \cdot 10^{-2}$ for $K = 5.66$. For the spatial extent and time and spatial resolutions see table 6.1. **Right:** Dependency of the displacement $\langle \Delta x^2 \rangle$ on t for different simulation parameters given in table 6.2. The dotted black lines represent linear fits carried out with Gnuplot.

The results of the corresponding simulations are shown in fig. 6.2, right. Three different cases are investigated. The two cases with $K = 28.28$ have identical Kubo numbers but different values for $\tau_c(\boldsymbol{v})$, $\lambda_c(\boldsymbol{v})$, and v_{RMS} which are listed in table 6.2. In all three cases the linear dependence between $\langle \Delta x^2 \rangle(t)$ and t (i.e. $a = 1$) which is characteristic for a diffusive behavior is clearly visible.

To determine the diffusion coefficients from the given data – which is done for the study of the macroscale transport behavior for $K \gg 1$ below – there are basically two methods available: one can either calculate D by a linear fit of $\langle \Delta x^2 \rangle$ versus t or by a linear fit of $\langle n v_x \rangle$ versus the gradient $-\langle \partial n / \partial x \rangle$. In both cases, the slope of the fitted straight line can be identified with D. Both procedures have been carried out with the data shown in fig. 6.2, right, the results being given in table 6.2, D_{I} corresponding to the first procedure, D_{II} corresponding to the second one. The fitting for both cases was carried out with the program Gnuplot 4.4 [99] which uses the Levenberg-Marquardt algorithm [100] to solve the least squares problems of a linear fit. The small fitting errors of D_{I} and D_{II} (see table 6.2) confirm that the macroscale transport is diffusive. Both methods result in different diffusion coefficients, the maximum deviation of D_{II} from D_{I} being around 23% (case B). When comparing D_{I} and D_{II} for case A with the analytically determined $D = 5 \cdot 10^{-4}$, given by eq. (6.38), one finds that D_{I} and D_{II} are about 20% smaller than D. The origin of this deviation is currently unclear but might be explained by a re-investigation of the steps outlined in [31] that lead to eq. (6.38). Also, this result does not alter the

case	K	$\tau_c(\boldsymbol{v})$	$\lambda_c(\boldsymbol{v})$	v_{RMS}	D_{I} $[10^{-4}]$	D_{II} $[10^{-4}]$
A	0.14	0.05	0.025	0.14	3.96 ± 0.03	4.07 ± 0.11
B	28.28	0.25	0.025	2.83	10.81 ± 0.03	8.32 ± 0.10
C	28.28	10.00	0.05	0.07	472.03 ± 1.37	438.07 ± 5.99

Table 6.2.: Parameters of the passive scalar simulations corresponding to the results shown in fig. 6.2, right.

observation that the macroscale transport is diffusive. For the analysis below, the method using a linear fit of $\langle n v_x \rangle$ versus the gradient $-\langle \partial n / \partial x \rangle$ (as used for D_{II}) is employed to determine the diffusion coefficient.

While the above results suggest that the macroscale transport behavior is diffusive also for the cases with $K \gg 1$ there is not yet an equation available for this dynamical regime as one has with eq. (6.38) for $K \ll 1$. It should be established below and is especially for relevance for fusion plasmas since here, K can also be expected to be of the order of unity or above [95, 101]. For this purpose some general considerations regarding transport in the two dynamical regimes, $K \ll 1$ and $K \gg 1$, are discussed to elucidate the pattern governing the motion of the fluid parcels which eventually leads to a diffusive behavior on the macroscale.

For all cases, the density parcels are moving on equipotential lines of the potential ϕ, see fig. 6.3. Thus, the parcels are 'confined' to the corresponding structures for a time of the order of $\tau_c(\boldsymbol{v})$ after which the structure of ϕ changes significantly and a new map of potential 'hills' and 'valleys' has evolved. During this time $\tau_c(\boldsymbol{v})$ the distance a parcel can travel is determined by its velocity and the characteristic extent of such a 'hill' or 'valley'. Fig. 6.3 illustrates that the structures formed by the equipotential lines of ϕ have diameters of the order of $\lambda_c(\phi) = 2\lambda_c(\boldsymbol{v})$.
For $K \ll 1$ the fluid parcels do not have the possibility to explore areas of the velocity field with an extent larger than $\lambda_c(\boldsymbol{v})$ during the time $\tau_c(\boldsymbol{v})$ since $v_{\mathrm{RMS}}\tau_c(\boldsymbol{v}) \ll \lambda_c(\boldsymbol{v})$. Hence, a change in the parcel's velocity is usually due to the temporal variation of the potential (and therefore also velocity) field, the characteristic time of this variation being given by $\tau_c(\boldsymbol{v})$. The typical displacement $\langle \Delta r^2 \rangle = \langle \Delta x^2 + \Delta y^2 \rangle$ of a fluid parcel for a time interval of length $\tau_c(\boldsymbol{v})$ can then be estimated by $\langle \Delta r^2 \rangle \approx v_{\mathrm{RMS}}^2 \tau_c^2(\boldsymbol{v})$. To estimate the diffusion coefficient $D(K \ll 1)$, relation (6.6), stating that $D = \langle \Delta r^2 \rangle / \Delta t$, can be used, yielding

$$D(K \ll 1) \;\propto\; \frac{v_{\mathrm{RMS}}^2 \tau_c^2(\boldsymbol{v})}{\tau_c(\boldsymbol{v})} \;=\; v_{\mathrm{RMS}}^2\, \tau_c(\boldsymbol{v}) \; . \tag{6.43}$$

Despite of a factor two, this is identical with the analytical result for D given by eq. (6.38).
In cases where $K \gg 1$, the situation changes and fluid parcels are now able to explore the velocity field before it changes due to its temporal variation since

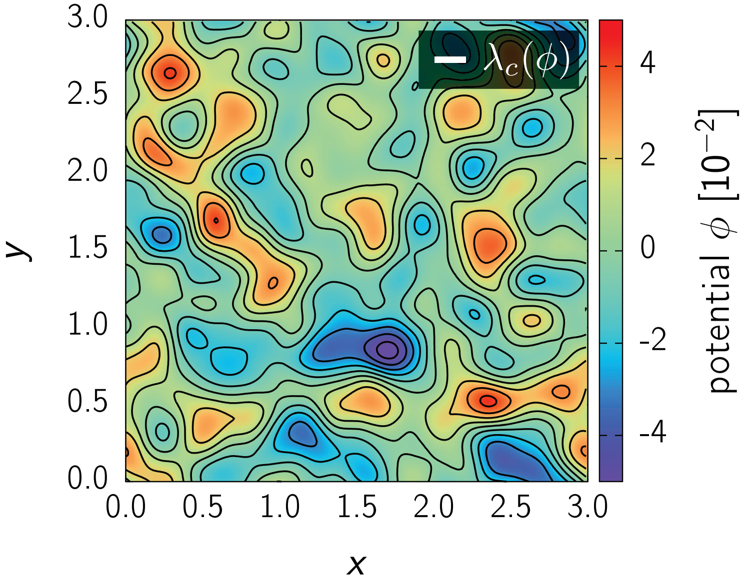

Figure 6.3.: Plot of the potential ϕ with equipotential lines and $\lambda_c(\phi) = 0.2$ which is illustrated by the thick white line.

$v_{\mathrm{RMS}}\tau_c(\boldsymbol{v}) \gg \lambda_c(\boldsymbol{v})$. The maximum distance a parcel can travel during time $\tau_c(\boldsymbol{v})$ is mainly limited by the extent of the related equipotential line, being of the order of $\lambda_c(\boldsymbol{v})$. An estimate of the respective diffusion coefficient D_1 yields

$$D_1(K \gg 1) \;\propto\; \frac{\lambda_c^2(\boldsymbol{v})}{\tau_c(\boldsymbol{v})} \; . \tag{6.44}$$

Eq. (6.44) holds if the potential structure does not change significantly during time $\tau_c(\boldsymbol{v})$, i.e. $\phi(\boldsymbol{r}, t)$ is basically frozen. Even small fluctuations of ϕ due to the underlying sampling procedure of $\phi(\boldsymbol{r}, t)$ might temporarily break the structures of $\phi(\boldsymbol{r}, t)$ open before a time interval of length $\tau_c(\boldsymbol{v})$ has passed. Parcels might then be able to change from one equipotential line to another. In the most extreme case parcels would move without any restrictions through the simulation domain due to this jumping from equipotential line to equipotential line. For this unrestricted motion one can estimate

$$D(K \gg 1) \;\propto\; \lambda_c^2(\boldsymbol{v}) \cdot \left[\frac{\lambda_c(\boldsymbol{v})}{v_{\mathrm{RMS}}}\right]^{-1} \;=\; v_{\mathrm{RMS}}\lambda_c(\boldsymbol{v}) \; , \tag{6.45}$$

where $\lambda_c(\boldsymbol{v})$ is the typical distance that a particle travels during time $\lambda_c(\boldsymbol{v})/v_{\mathrm{RMS}}$. Eqs. (6.44) and (6.45) represent two opposing estimates for $D(K \gg 1)$ which can be

	$\tau_c(\boldsymbol{v})$	$\lambda_c(\boldsymbol{v})$	v_{RMS}	exponent	y axis interc.
s. 1	0.01 - 1000	0.1	0.14	$\gamma\ = 0.261 \pm 0.011$	0.418 ± 0.014
s. 2	0.1	0.1	0.14 - 282.84	$\alpha\ = 0.739 \pm 0.005$	0.398 ± 0.010
s. 3	10	0.005 - 25	0.14	$\beta_1 = 1.204 \pm 0.048$	0.387 ± 0.046
				$\beta_2 = 1.205$	0.217

Table 6.3.: Simulation parameters of series one, two and three whose results are shown in figs. 6.4 and 6.5. The initial profile was given by $n(x) = a_0/(\sqrt{2\pi}\sigma) \cdot \exp(-0.5[x-\mu]^2/\sigma^2)$ with $a_0 = 1.17 \cdot 10^{-2}$, $\sigma = 3\lambda_c(\boldsymbol{v})$ and $\mu = x_{\text{sim}}/2$. The averaging parameters used were $\delta t_{\text{av}} = t_{\text{sim}}/20$ and $N_{x,\text{av}} = N_x/64$, where $/N_{x,\text{av}}$ is the number of cells in x direction used for averaging. The averaged y axis intercept is given by 0.355 ± 0.069.

associated either with total confinement or unrestricted motion. They are both of the form

$$D(K \gg 1) \ \propto \frac{v_{\text{RMS}}^{\alpha}\lambda_c^{\beta}(\boldsymbol{v})}{[\tau_c(\boldsymbol{v})]^{\gamma}} \ . \tag{6.46}$$

Coming from the picture of free parcel motion related to eq. (6.45), an exponent $\alpha < 1$ expresses that possible confinement of the fluid parcels within the potential structure results in a lower effective velocity than v_{RMS}. The case $\alpha = 1$ corresponds to free parcel motion with a velocity v_{RMS}. Obviously, the effective velocity will not decrease if the root mean square velocity v_{RMS} increases; thus $\alpha > 0$. The exponent β represents the fact that the typical extent of the potential structures might vary from $\lambda_c(\phi)$. The extent of the potential 'hills' and 'valleys' will not decrease with increasing $\lambda_c(\boldsymbol{v})$, yielding that $\beta > 0$. The exponent γ for $\tau_c(\boldsymbol{v})$ relativizes the idea used for the estimate (6.44) that the potential structure is completely frozen for a time $\tau_c(\boldsymbol{v})$, meaning that the particle is perfectly confined for a time $\tau_c(\boldsymbol{v})$. The effective confinement time will increase with increasing $\tau_c(\boldsymbol{v})$, thus $\gamma > 0$. To summarize one has

$$0 \ < \ \alpha \ < \ 1 \ , \qquad 0 \ < \ \beta \ , \qquad 0 \ < \ \gamma \ , \tag{6.47}$$

as initial assumptions for the parameters α, β and γ.

The parameters α, β, and γ are determined by a least square fit to a series of passive scalar simulations, systematically varying either $\tau_c(\boldsymbol{v})$, $\lambda_c(\boldsymbol{v})$, or v_{RMS}, respectively, while the other two quantities are held constant. The fitted D are plotted against the ratio R,

$$R \ \equiv \ \frac{v_{\text{RMS}}\lambda_c(\boldsymbol{v})}{\tau_c(\boldsymbol{v})} \ , \tag{6.48}$$

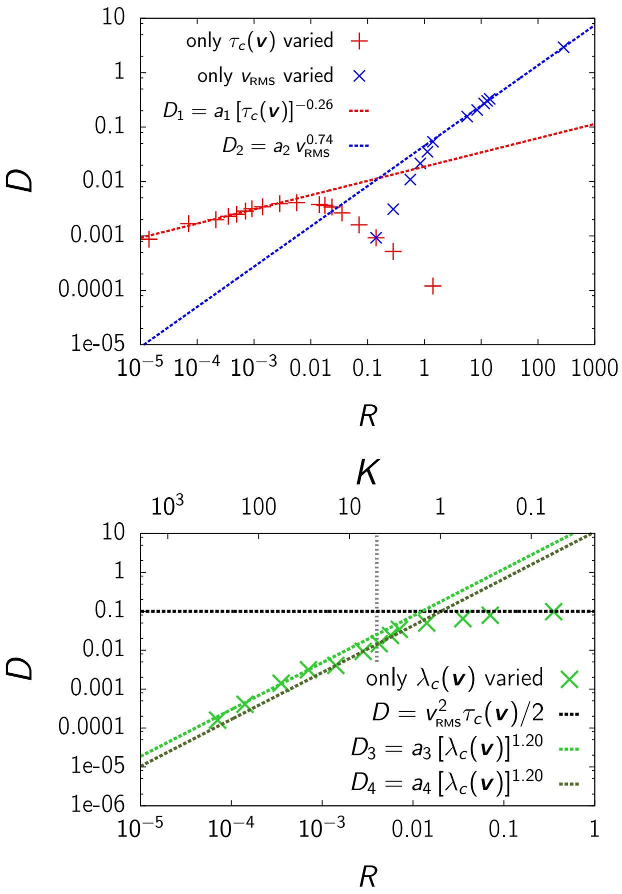

Figure 6.4.: Top: Results of simulation series one and two. For series one (red +) $R < 0.01$ corresponds to the case where $K \gg 1$ while $R > 0.01$ corresponds to the case where $K \ll 1$. Regarding series 2 (blue ×) $R > 1$ means that $K \gg 1$ while $K \ll 1$ for $R < 1$. **Bottom:** Results of simulation series three. The simulation parameters for all series are given in table 6.3. The position $K = 5$ is marked by the gray, dotted line, D determined by eq. (6.38 is given by the black dotted line.

and the exponents α, β and γ are obtained by a linear fit of D versus R.

The simulation parameters are given in table 6.3. The time step Δt_s and the grid resolution $\Delta x_s = \Delta y_s$ are chosen so that the Courant condition $v_{\text{RMS}}\Delta t_s/\Delta x_s \ll 1$

is fulfilled [71] and $\lambda_c(\boldsymbol{v})/\Delta x_s \geq 8$. The first 10% of the simulated time t_{sim} are neglected for the fitting procedure to let the velocity field 'mix up' the smooth initial profile which is given by a Gaussian bell curve. Also, the first and last 12.5 % of the cells in x direction are excluded to ensure that no effects due to the boundary condition are taken into account. In all series both regions with $K \ll 1$ and $K \gg 1$ are covered to evaluate the transition between the two different dynamical regimes.

The results are shown in in fig. 6.4 and confirm the power law expressed by eq. (6.46) with adjusted parameters α, β, and γ. For each simulation series, two different regions regarding the dependency of D on R can be identified: one referring to the case $K \ll 1$ with D analytically given by eq. (6.38), and one with $K \gg 1$ with D approximated by eq. (6.46). For series three (green ×, fig. 6.4, bottom), the changing dependency of D on R regarding the distinct K regions is well visible. For $K \lesssim 1$ the fitted diffusion coefficients stay basically constant and converge towards the analytically determined $D = 0.1$, given by the black dotted line. For series one (red +) and two (blue ×) the dependence of D on K is illustrated separately in fig. 6.5 since it cannot be displayed for both series within the same plot. As for series three, the fitted diffusion coefficients converge towards the analytical expression (6.38) for $K \ll 1$ while for $K \gg 1$ they follow the behavior given by eq. (6.46). Between these two regimes a region of transition can be identified ($K \approx 1$).

For the regions with $K \gg 1$ the exponents α, β, and γ have been determined by a linear fit of D versus R with Gnuplot, including all data points with $K > 5$. The results and the fits are shown in figs. 6.4 and 6.5 and in table 6.3. For series three, two fits have been made since the values of D 'sag' around $R \approx 10^{-3}$ but then seem to follow the same power law as before up to values of $R \approx 0.01$ (see fig. 6.4, bottom). One obtains for $D(K \gg 1)$:

$$D(K \gg 1) \;=\; 0.35 \cdot \frac{v_{\text{RMS}}^{0.74}\,[\lambda_c(\boldsymbol{v})]^{1.20}}{[\tau_c(\boldsymbol{v})]^{0.26}}\;. \tag{6.49}$$

The axis intercept of 0.35 ± 0.07 is the average from all four fits. The exponents α, β, and γ fulfill the assumptions expressed by eq. (6.47). Note that the increase of the diffusion coefficient for the $K \gg 1$ region no longer is quadratic with v_{RMS} as for $K \ll 1$, but only with an exponent of 0.74 (see fig. 6.5, bottom). Also, the exponent of $\tau_c(\boldsymbol{v})$ changes from $\gamma = -1$ to $\gamma = 0.26$. This means that where for $K \ll 1$ increasing $\tau_c(\boldsymbol{v})$ increased also the diffusivity, the opposite is true for $K \gg 1$. In the latter regime increasing $\tau_c(\boldsymbol{v})$ basically means to further limit the motion of the fluid parcel by confining it longer to the same equipotential line. Its characteristic extent shows a proportionality to $[\lambda_c(\boldsymbol{v})]^\beta$ with $\beta = 1.2$. Note also that for series one and two D is smaller than the analytical results for $K \ll 1$, which coincides with the former simulation result for $\log(u_0^2 t_0) \gtrsim 1$ of [33], shown in fig. 6.6 .

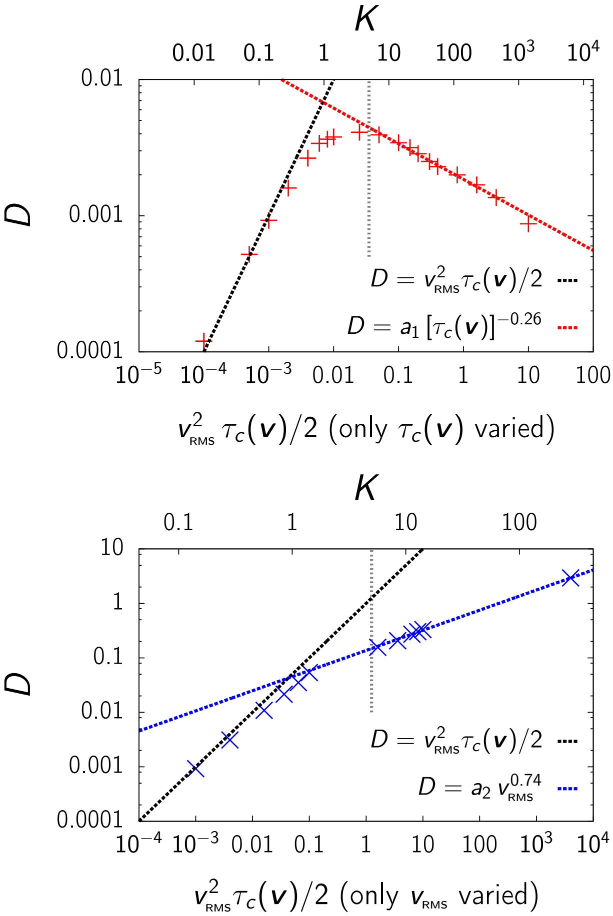

Figure 6.5.: Results of simulation series one (**top**) and two (**bottom**). The position $K = 5$ is marked by the gray dotted line.

The results obtained for the cases $K \gg 1$ can be related to theoretical considerations regarding the diffusion coefficient of a system governed by electrostatic turbulence and particle motion via a percolation scheme, i.e. the motion of fluids through porous materials (see [102, 83] and references therein). Here, the fluid is represented by the quantity α while the porous material can be identified with the potential hills and valleys. Motion is limited due to confinement to the equipotential lines which occasionally break open and form new structures. In [83], the diffusion coefficient for the low-frequency or high-amplitude regime, which corresponds to the case $K \gg 1$,

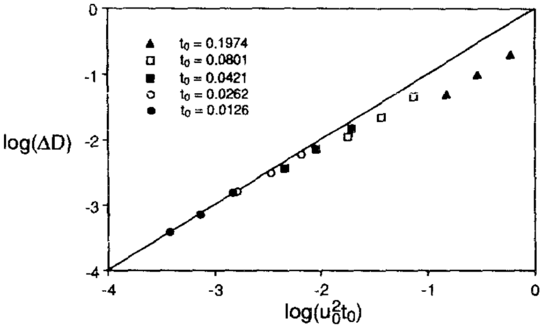

Figure 6.6.: Graph taken from [33]. The diffusion coefficient ΔD corresponds to D while $u_0^2 t_0$ can be associated with $v_{\mathrm{RMS}}^2 \tau_c(\boldsymbol{v})/2$. Moving towards larger values of $u_0^2 t$ means reaching the $K \gg 1$ domain.

is estimated by

$$D \approx \omega^{1-\nu}\left(\frac{E}{B}\right)^{\nu}, \tag{6.50}$$

where ω is the characteristic frequency and E/B is proportional to the magnitude of the E×B velocity field (compare eq. (4.2)). The percolation critical exponent ν for the low-frequency case is found to be 0.7. By estimating $\omega \sim 1/\tau_c(\boldsymbol{v})$ and $E/B \sim v_{\mathrm{RMS}}$ one finds that the theoretically predicted ν is 5.5 % off of the value of $\nu = \alpha = 0.74$ found here as exponent of v_{RMS}. The exponent $\gamma = 0.26$ of $\tau_c(\boldsymbol{v})$ is about 13 % off from the predicted value of 0.3, but the relation $\gamma = 1 - \alpha$ is exactly fulfilled. This correspondence leaves an interesting point to be investigated in further studies of the passive scalar model.

To summarize the above work it should be highlighted that the passive scalar studies carried out in this paragraph extend the previous work for dynamical regimes with $K \ll 1$ to regimes with $K \gg 1$, a region which is of relevance also for fusion plasmas. They show that the macroscale dynamics of the system can still be described by a diffusive model, even though the dependency of the diffusion coefficient D on the correlation time $\tau_c(\boldsymbol{v})$, the correlation length $\lambda_c(\boldsymbol{v})$, and the root mean square velocity v_{RMS} of the velocity field changes significantly. The general relation between the mesoscale convective dynamics and the macroscale diffusion can be visualized by the motion of fluid parcels on equipotential lines. The confirmation of the analytical formula for $D(K \gg 1)$ by results of studies on percolation dynamics proves the ideas leading to eq. (6.46) and the results represented by eq. (6.49) as correct.

6.2.3. Simple coupled code example for the diffusion of passive scalars

The passive scalar model can be used to set up a simple coupled code system to study the influence of the macroscale transport model and the coupling parameters Δt_{up} and δt_{av} on the macroscale simulation and its agreement with a benchmark run. The example presented here is used primarily to investigate two ideas introduced in paragraph 2.3: Firstly, that with an adequate macroscale transport model the updating intervals Δt_{up} for transport coefficients can be increased while the dynamics on the macroscale are still reproduced correctly. Secondly, that for some cases, even by resorting to an inadequate macroscale transport model, the macroscale evolution of the system can be approximately reproduced if Δt_{up} is chosen sufficiently short. The advantage of the passive scalar system for this study is that the correct macroscale transport model is known to be diffusive whereas for the multiscale problems presented in chapters 7 and 8 it is not known.

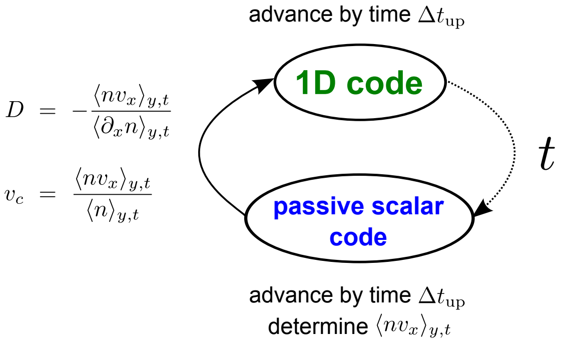

Figure 6.7.: Sketch of the spatial and temporal structure of the coupling procedure.

The coupling procedure is sketched in fig. 6.7. The coupled code system consists of a 1D code for solving the density continuity equation for n_0,

$$\frac{\partial n_0}{\partial t} + \frac{\partial}{\partial x} \langle n v_x \rangle_{y,t} = \frac{\partial n_0}{\partial t} + \frac{\partial \Gamma_0}{\partial x} = 0 \,, \tag{6.51}$$

and the two-dimensional passive scalar code as described in the previous paragraph 6.2.2. The objective is that by evolving n_0 with the averaged mesoscale flux $\Gamma_0 = \langle n v_x \rangle_{y,t}$ one is able to reproduce the macroscale evolution of $\langle n \rangle_y$ as given by a reference passive scalar simulation (thus, that n_0 can be identified with $\langle n \rangle_y$). For all cases $K \ll 1$ so that eq. (6.29) with D given by eq. (6.38) holds. The 1D code solves eq. (6.51) via a finite difference scheme. An explicit fourth-order Runge-Kutta method is used for time stepping [71]. To model convection a total variation diminishing (TVD) MUSCL-Hancock scheme is employed [97].

Both codes are started with identical initial profiles. At times $t = 0, \Delta t_{\mathrm{up}}, 2\Delta t_{\mathrm{up}}, ...$, the 1D code receives a new set of transport coefficients which depend on the averaged flux $\langle n v_x \rangle_{y,t}$ of the passive scalar code. The time interval for averaging the passive scalar data at instant t is given by $t - \delta t_{\mathrm{av}} \leq t' \leq t$ with $\delta t_{\mathrm{av}} = 10 \tau_c(\boldsymbol{v})$. The updating time Δt_{up} for the transport coefficients as well as the averaging interval δy_{av} in y direction are varied for the different runs. The averaging interval δy_{av} can be related to the averaging time δt_{av} of the coupled code system outlined in paragraph 2.3. The longer δy_{av}, the better the quality of statistics for determining the transport coefficients of the macroscale transport model.
The reference profile for comparison with the 1D results is given by $\langle n \rangle_y(x,t)$ with $\delta y_{\mathrm{av}} = y_{\mathrm{sim}} = 120\, \lambda_c(\boldsymbol{v})$. Note that in contrast to the coupled code example discussed in paragraph 2.3, the mesoscale part of the coupled code system does not depend on results of the macroscale part, given by the 1D code. The coupling procedure depicted in fig. 6.7 therefore is a one-way loop in the sense that information is only handed from the passive scalar code to the 1D code and not the other way around. However, this simplified example can be employed for a first assessment of the influence of Δt_{up}, δy_{av} (i.e. δt_{av}), and the macroscale transport model on the macroscale results.

Three different macroscale models for the flux Γ_0 are tested here – a diffusive and a convective model,

$$\Gamma_0^{\mathrm{A}} = -D \partial_x n_0 \ , \qquad D = -\frac{\langle n v_x \rangle_{y,t}}{\partial_x n_0} \ , \tag{6.52}$$

$$\Gamma_0^{\mathrm{B}} = n_0 v_c \ , \qquad v_c = \frac{\langle n v_x \rangle_{y,t}}{n_0} \ , \tag{6.53}$$

and a mix of both approaches,

$$\Gamma_0^{\mathrm{C}} = \begin{cases} \frac{1}{2}\Gamma_0^{\mathrm{A}} + \frac{1}{2}\Gamma_0^{\mathrm{B}} & \text{if} \quad D \geq 0 \ , \\ \Gamma_0^{\mathrm{B}} & \text{if} \quad D < 0 \ , \end{cases} \tag{6.54}$$

D and v_c being given by eqs. (6.52) and (6.53). The notation $\partial_x n_0$ is employed to abbreviate the derivative $\partial n_0 / \partial x$. Eq. (6.54) is to be understood as follows: for some points in space and time, the local value of D might become negative. In this case, a purely convective macroscale transport model is chosen for Γ_0^{C}. Otherwise, transport is split equally into a diffusive and a convective part. By determining the error $\eta_{\mathrm{ps}}(n)$,

$$\eta_{\mathrm{ps}}(n) = 100 \cdot \left\langle \frac{|n_0(x,t) - \langle n \rangle_y(x,t)|}{|\langle n \rangle_y(x,t)|} \right\rangle_{x,t} \ , \tag{6.55}$$

measured in percent, one can evaluate the quality of agreement of the coupled code system with the reference passive scalar simulation, depending on the chosen model for Γ_0 and the input parameters Δt_{up} and δy_{av}. The simulation parameters are given in table 6.4. As initial profile, a Gaussian bell curve as given by eq. (6.39) is used with $a_0 = 2.34 \cdot 10^{-2}$, $\mu = 3$, and $\sigma = 0.6$.

The results for the simulations are shown in fig. 6.8. The deviation $\eta_{\mathrm{ps}}(n)$ has been calculated for 100 profiles, always 300 time steps apart from each other. The first and last 25% of the simulation domain in x direction have been neglected to avoid division by zero in the summands of $\eta_{\mathrm{ps}}(n)$ due to very small values of $\langle n \rangle_y$.
Two general trends are found for all three macroscale transport models. Firstly, a large error $\eta_{\mathrm{ps}}(n)$ due to transport coefficients determined with insufficient statistics, meaning that $\delta y_{\mathrm{av}}/\lambda_c(\boldsymbol{v})$ is small, can partly be compensated by decreasing the updating time, i.e. reducing $\Delta t_{\mathrm{up}}/\tau_c(\boldsymbol{v})$. Secondly, even for good statistics ($\delta y_{\mathrm{av}}/\lambda_c(\boldsymbol{v}) = 96, 120$), the error $\eta_{\mathrm{ps}}(n)$ increases the larger $\Delta t_{\mathrm{up}}/\tau_c(\boldsymbol{v})$, i.e. the longer the updating time. These observations correspond to the theoretical reasoning of paragraph 2.3: the shorter Δt_{up}, the more often the macroscale transport coefficients are updated and the better is the agreement between the macroscale flux and the respective averaged mesoscale flux. However, the variation of $\eta_{\mathrm{ps}}(n)$ with $\Delta t_{\mathrm{up}}/\tau_c(\boldsymbol{v})$ differs significantly for the different macroscale transport models.
The results regarding the diffusive model Γ_0^{A} are presented in fig. 6.8, top left and right. They illustrate the already mentioned restrictions of a purely diffusive macroscale model: the diffusion coefficients are required to be positive. If the statistical data is insufficient, e.g. for the cases with $\delta y_{\mathrm{av}}/\lambda_c(\boldsymbol{v}) < 72$, the identification of $\langle ... \rangle_y$ with the ensemble average no longer holds and the diffusion coefficients occasionally become negative. Negative D occurred in all simulations: for $\delta y_{\mathrm{av}}/\lambda_c(\boldsymbol{v}) = 72$, the percentage of values of $D < 0$ was about 18%, for $\delta y_{\mathrm{av}}/\lambda_c(\boldsymbol{v}) = 96$ about 14% and for $\delta y_{\mathrm{av}}/\lambda_c(\boldsymbol{v}) = 120$ below 5%. In those cases $D(x_i)$ was set to the value of D of the closest cell k with $x_k < x_i$ and $D(x_k) \geq 0$. The diffusive model was only employed if the percentage of negative D was smaller than 20%. Therefore, no results are shown for Γ_0^{A} and $\delta y_{\mathrm{av}}/\lambda_c(\boldsymbol{v}) < 60$.
Γ_0^{A} leads to the best agreement of the 1D code results with the reference simulation. Even for the longest Δt_{up} and the shortest δt_{av} $\eta_{\mathrm{ps}}(n)$ is below 10%. This underlines that by using the adequate macroscale transport model the updating interval can be significantly reduced while the accuracy of the coupled code results stays high.
For the convective model Γ_0^{B} (fig. 6.8, bottom left) one only obtains values of $\eta_{\mathrm{ps}}(n)$ below 20% for updating times with $\Delta t_{\mathrm{up}}/\tau_c(\boldsymbol{v}) < 100$. Nevertheless, for the shortest Δt_{up} and the largest δt_{av}, $\eta_{\mathrm{ps}}(n)$ equals 2.7% and is of the same order as $\eta_{\mathrm{ps}}(n) = 1.5\%$ of the respective case using Γ_0^{A}. Hence, the inadequate macroscale transport model can be balanced by frequently updating the transport coefficients. The time savings of such a multiscale model compared to the full simulation are, of course, rather limited due to the need for frequent updates.
The mixed model Γ_0^{C} (fig. 6.8, bottom, right) shows a significantly better agreement with the reference case than Γ_0^{B}. Especially for $\delta y_{\mathrm{av}}/\lambda_c(\boldsymbol{v}) = 120$ the deviation is

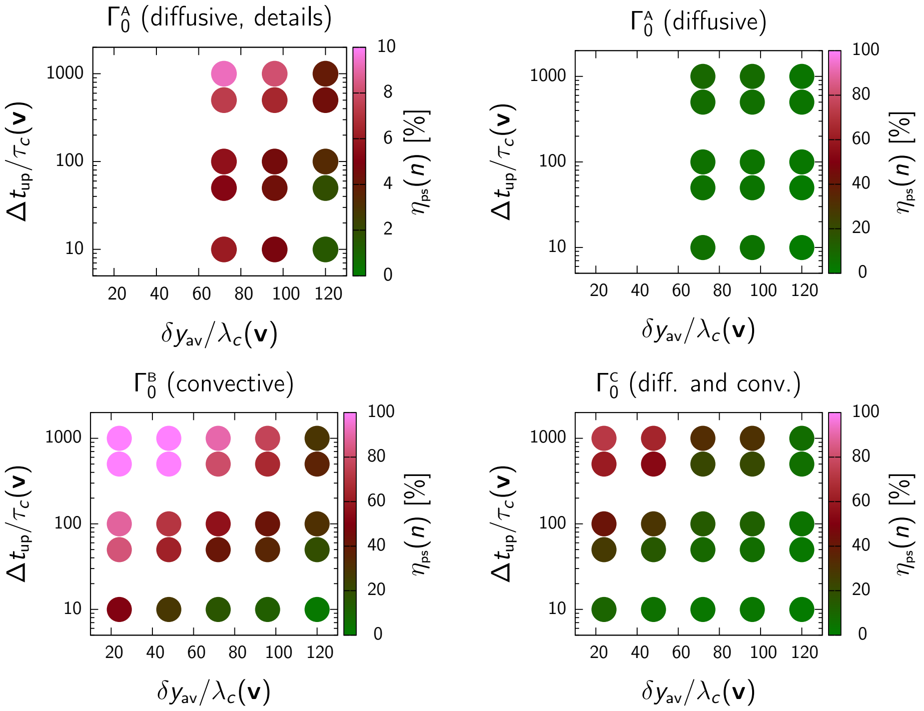

Figure 6.8.: Results for coupling the passive scalar code to the 1D code. The simulation parameters are given in table 6.1. **Top left:** Diffusive macroscale transport model Γ_0^A, see eq. (6.52). **Top right:** Same as top, left, but different scaling of $\eta_{ps}(n)$. **Bottom left:** Convective macroscale transport model Γ_0^B, see eq. (6.53). **Bottom right:** Mixed macroscale transport model Γ_0^C, see eq. (6.54).

par.	value	par.	value	par.	value	par.	value
t_{sim}	300	N_t	30 000	Δt_p	0.01	$\lambda_c(\boldsymbol{v})$	0.05
x_{sim}	6	N_x	256	Δx_p	0.023	v_{RMS}	0.14
y_{sim}	6	N_y	256	$\tau_c(\boldsymbol{v})$	0.1	K	0.28

Table 6.4.: Parameters used for coupling the passive scalar code to the 1D code whose results are shown in fig. 6.8.

below 10% for all updating intervals, with the minimal value of 1.6% being almost as good as for the associated Γ_0^A case with $\eta_{ps}(n) = 1.5\%$. Even for an average value of $\delta y_{av}/\lambda_c(\boldsymbol{v}) = 72$ and $\Delta t_{up}/\tau_c(\boldsymbol{v}) = 100$, $\eta_{ps}(n)$ is only 14.8% while for corresponding case of the purely convective model one has $\eta_{ps}(n) = 56.7\%$. Since for negative D

the transport is locally described by a purely convective model one circumvents the issues coming with a purely diffusive description.

In the next two chapters 7 and 8, the influence of Δt_{up}, δt_{av}, and the choice of the macroscale transport model will be assessed with more sophisticated coupled code systems to describe the evolution of the plasma in the tokamak edge region.

7. Example of a 1D coupled code system

In this chapter, the structure and results of a coupled code system based on a reduced version of the specific multiscale model for the plasma edge (see chapter 5) are presented. It combines the theory of the macroscale and mesoscale models (chapters 3 and 4) and the resulting specific multiscale model (chapter 5) with the considerations regarding the structure of a coupled code system (chapter 2) and the macroscale transport models (chapter 6).
The objective set for the coupled code system is to determine the macroscale time evolution of the flux surface averaged radial density profile in the edge region of a tokamak where flux surfaces are closed. Investigating this simplified problem case, being one-dimensional and focusing on the particle density and temporal scale separation only, instead of directly realizing a coupled code system based on the complete multiscale model of chapter 5 serves different purposes. By reducing the complexity of the problem and therefore also the runtime of the coupled code system the technical aspects can be tackled more efficiently, including the technical development of a coupling script needed for the communication between the macroscale and mesoscale code, and the design of the procedure to find the statistically stationary state and the corresponding averaged mesoscale terms of the local mesoscale simulations. Also, the results of the coupled code system can be easily compared to a benchmark simulation, realized by a non-local mesoscale code which captures both the mesoscale and macroscale evolution of the plasma. This allows for evaluating the general performance of the coupled code system regarding stability, time savings and different macroscale transport models. The results of these investigations can then be transferred to a coupled code system representing a more complete multiscale model.

The structure of this chapter is as follows. The coupled code system and the code used for the benchmark simulations are described in paragraph 7.1. The procedure to determine the statistically stationary state of a local mesoscale simulation and to extract the respective data for the macroscale transport model are outlined in paragraph 7.1.4. A comparison between local and non-local mesoscale simulations for statistically stationary cases is presented in paragraph 7.2, giving some qualitative guidelines for the benchmark of the coupled code simulations analyzed in detail in paragraph 7.3.

7.1. Setup of the coupled code system

The general structure of the coupled code system analyzed in this chapter is shown in fig. 7.1, right. The one dimensional code described in paragraph 6.2.3 for the coupling example with the passive scalar system solves the density continuity equation in radial direction x for the macroscale density $n_0(x,t)$. At the beginning of a coupled code simulation, at each of the $N_x^{1\mathrm{D}}$ cells of the 1D code (with cell indices $l \in [1, N_x^{1\mathrm{D}}]$), a local mesoscale simulation using the local version of the ATTEMPT code [11] is started. The local ATTEMPT code employs a local drift fluid model like that of the specific multiscale model (see paragraph 5.1.2). It uses the macroscale radial density gradient $\partial_x n_0$ as input parameter and determines the average of the radial mesoscale particle flux $\langle\widetilde{\Gamma}\rangle$ which is assumed to be dominated by the flux due to the E×B velocity $\boldsymbol{v}_{\mathrm{E}}$,

$$\langle\widetilde{\Gamma}\rangle \;\equiv\; \langle\tilde{n} v_{\mathrm{Ex}}\rangle \;, \tag{7.1}$$

where v_{Ex} is the radial part of $\boldsymbol{v}_{\mathrm{E}}$. Subsequently, $\langle\widetilde{\Gamma}\rangle$ is translated into the transport coefficients of the macroscale transport model, a convective velocity v_c and/or a diffusion coefficient D. They are used by the macroscale transport model of the 1D code to determine the macroscale radial particle flux $\Gamma_0(x,t)$. One execution of this coupling loop as illustrated in fig. 7.1 refers to one global iteration which are referred to using the index i. After the 1D code has simulated the evolution of the macroscale system for a time $\Delta t_{\mathrm{up}}(i)$ the coupling loop is repeated.

The benchmark simulation, shown in fig. 7.1, left, is carried out by the non-local version of the ATTEMPT code. It solves similar equations as the local ATTEMPT code, but accounts for the evolution of the full density $n = \tilde{n} + n_0$. To simplify the notation, the quantities $\langle n\rangle$ and $\langle\Gamma\rangle$ are defined:

$$\langle n\rangle(x,t) \;\equiv\; \langle n(\boldsymbol{r},t)\rangle_{\mathrm{fs},t}(x,t) \;, \qquad \langle\Gamma\rangle(x,t) \;\equiv\; \langle n(\boldsymbol{r},t)\, v_{\mathrm{Ex}}(\boldsymbol{r},t)\rangle_{\mathrm{fs},t}(x,t) \;, \tag{7.2}$$

with $\langle ...\rangle_{\mathrm{fs},t}$ being the average over the flux surface and the averaging time interval δt_{av}. Thus, within the framework of this chapter the quantities n_0 and Γ_0 refer to the density and flux as given by the 1D code of the coupled code system while the quantities $\langle n\rangle$ and $\langle\Gamma\rangle$ are determined by the non-local ATTEMPT simulations.

The 1D code used for the macroscale is described in paragraph 7.1.1, the ATTEMPT code used for the (local and non-local) drift fluid simulations is outlined in paragraph 7.1.2. In paragraph 7.1.3, the coupling procedure is explained in detail.

7.1.1. Macroscale part: 1D code

The 1D code that is employed to determine the evolution of n_0 is the same used for the passive scalar coupling example in paragraph 6.2.3. Here, it solves the density

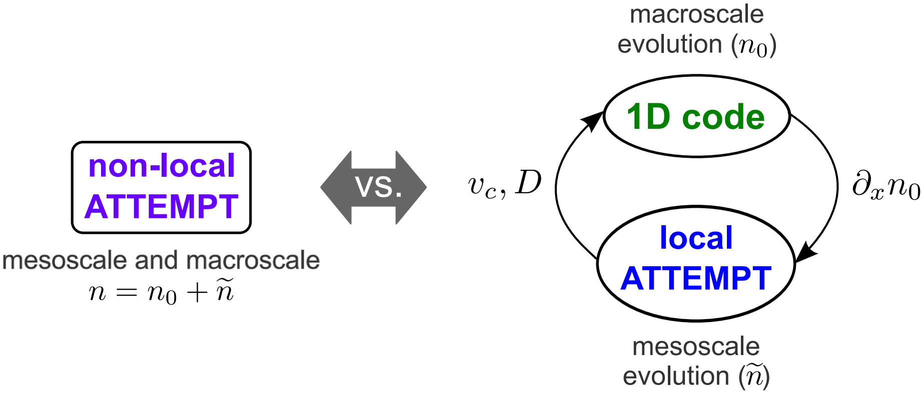

Figure 7.1.: Sketch of a coupled code simulation (right) and the benchmark case (left). A detailed chart of the coupling procedure is shown in fig. 7.2.

continuity equation in radial direction x with a source term S_0:

$$\frac{\partial n_0}{\partial t} + \frac{\partial \Gamma_0}{\partial x} = S_0 \ , \tag{7.3}$$

The macroscale transport model for the macroscale radial particle flux Γ_0 uses a convection-diffusion representation,

$$\Gamma_0 = n_0 v_c - D\,\partial_x n_0 \ , \tag{7.4}$$

with

$$v_c = v_c(x_l, t_i) = (1 - \beta_{\mathrm{D}}) \frac{\langle\widetilde{\Gamma}\rangle^{i,l}}{n_0^{i-1,l}} \ , \tag{7.5}$$

$$D = D(x_l, t_i) = -\beta_{\mathrm{D}} \frac{\langle\widetilde{\Gamma}\rangle^{i,l}}{\partial_x n_0^{i-1,l}} \ , \tag{7.6}$$

and

$$0 \le \beta_{\mathrm{D}} \le 1 \ . \tag{7.7}$$

The flux $\langle\widetilde{\Gamma}\rangle^{i,l}$ is to be understood as the averaged flux that was obtained by a local mesoscale simulation using the gradient $\partial_x n_0^{i-1,l}$ of macroscale cell l and global iteration $i-1$ as input parameters. The associated density is given by $n_0^{i-1,l}$. It is not used as an input parameter of the local ATTEMPT simulations but only to determine $v_c(x,t)$. The parameter β_{D} divides the flux into a convective and a diffusive part. Note that for a proper working of the splitting as given by eqs. (7.5) and (7.6) it is required that $\partial_x n_0^{i-1,l}$ and $\langle\widetilde{\Gamma}\rangle^{i,l}$ have opposite signs; otherwise $D(x,t)$ would become negative. Negative D are an exceptional case of diffusive transport, usually only appearing for multi-species systems, and are excluded from the analysis here.

7.1.2. Mesoscale part: drift fluid code ATTEMPT

The drift fluid code ATTEMPT, used for the local and non-local mesoscale simulations, is briefly described. Further details regarding the numerical algorithm, the discretization grid, and the boundary conditions can be found in [11].

The non-local version of ATTEMPT solves the following equations:

$$\left(\frac{\partial}{\partial t} + \boldsymbol{v}_{\mathrm{E}} \cdot \boldsymbol{\nabla}_\perp\right) n = \frac{T_{0e}}{e}\mathcal{K}(n) - n_0\mathcal{K}(\phi) - n_0 B_0\Big(\nabla_{\|0} + \widetilde{\nabla}_\|\Big)\left(\frac{u_\|}{B} - \frac{j_\|}{en_0B_0}\right) , \tag{7.8}$$

$$m_i n_0\left(\frac{\partial}{\partial t} + \boldsymbol{v}_{\mathrm{E}} \cdot \boldsymbol{\nabla}_\perp\right) u_\| = -T_{0e}\Big(\nabla_{\|0} + \widetilde{\nabla}_\|\Big) n , \tag{7.9}$$

$$\frac{m_e}{e}\left(\frac{\partial}{\partial t} + \boldsymbol{v}_{\mathrm{E}} \cdot \boldsymbol{\nabla}_\perp\right) j_\| = -en_0\frac{\partial A_\|}{\partial t} - en_0\Big(\nabla_{\|0} + \widetilde{\nabla}_\|\Big)\phi - R_{\|e} + T_{0e}\Big(\nabla_{\|0} + \widetilde{\nabla}_\|\Big) n , \tag{7.10}$$

$$\frac{m_i n_0}{B_0^2}\left(\frac{\partial}{\partial t} + \boldsymbol{v}_{\mathrm{E}} \cdot \boldsymbol{\nabla}_\perp\right)\nabla_\perp^2\phi = B_0\Big(\nabla_{\|0} + \widetilde{\nabla}_\|\Big)\frac{\widetilde{j}_\|}{B_0} + T_{0e}\,\mathcal{K}(n) . \tag{7.11}$$

Here, B_0 denotes the equilibrium magnetic field. Eqs. (7.8) to (7.11) correspond to the electron particle balance (4.17), the total parallel momentum balance (4.20), Ohm's law (4.31) and the vorticity equation (4.35) of the global drift fluid model outlined in paragraph 4.2. The only differences are that the magnetic field B is taken to be the equilibrium magnetic field B_0 except for the gradients $\widetilde{\nabla}_\|$, and that the density is at some points approximated by its macroscale part n_0. Sometimes, this non-local system is also called a *flux driven* system which means that the drift fluid dynamics are driven by a particle influx and not by an equilibrium perpendicular density gradient $\boldsymbol{\nabla}_\perp n_0$, as it is the case for a local or *gradient driven* system.

The local or gradient driven version of the ATTEMPT code solves

$$\begin{aligned}\left(\frac{\partial}{\partial t} + \boldsymbol{v}_{\mathrm{E}}\cdot\boldsymbol{\nabla}_\perp\right)\widetilde{n} &= -\boldsymbol{v}_{\mathrm{E}}\cdot\boldsymbol{\nabla}_\perp n_0 + \frac{T_{0e}}{e}\mathcal{K}(\widetilde{n}) - n_0\mathcal{K}(\phi)\\ &\quad - n_0B_0\left(\nabla_{\|0} + \widetilde{\nabla}_\|\right)\left(\frac{u_\|}{B_0} - \frac{j_\|}{en_0B_0}\right) + \gamma(\widetilde{n}) ,\end{aligned} \tag{7.12}$$

$$m_i n_0\left(\frac{\partial}{\partial t} + \boldsymbol{v}_{\mathrm{E}}\cdot\boldsymbol{\nabla}_\perp\right)u_\| = -T_{0e}\left(\nabla_{\|0} + \widetilde{\nabla}_\|\right)\widetilde{n} , \tag{7.13}$$

$$\begin{aligned}\frac{m_e}{e}\left(\frac{\partial}{\partial t} + \boldsymbol{v}_{\mathrm{E}}\cdot\boldsymbol{\nabla}_\perp\right)j_\| &= -\, en_0\frac{\partial A_\|}{\partial t} - en_0\left(\nabla_{\|0} + \widetilde{\nabla}_\|\right)\phi - R_{\|e}\\ &\quad + T_{0e}\left(\nabla_{\|0} + \widetilde{\nabla}_\|\right)\widetilde{n} ,\end{aligned} \tag{7.14}$$

$$\frac{m_i n_0}{B_0^2}\left(\frac{\partial}{\partial t} + \boldsymbol{v}_{\mathrm{E}}\cdot\boldsymbol{\nabla}_\perp\right)\nabla_\perp^2\phi = B_0\left(\nabla_{\|0} + \widetilde{\nabla}_\|\right)\frac{\widetilde{j}_\|}{B_0} + T_{0e}\,\mathcal{K}(\widetilde{n}) . \tag{7.15}$$

Eqs. (7.12) to (7.15) are similar to the flux driven model given by eqs. (7.8) to (7.11), except that only the mesoscale part $\widetilde{n}$ of the density is evolved. The damping term $\gamma(\widetilde{n})$ appearing in eq. (7.12) is explained further down.

The code details outlined below are valid for both ATTEMPT versions. The model equations are solved by a finite difference scheme on a semi-field aligned grid, using the set of coordinates (σ, χ, η), defined by

$$\sigma = \theta , \qquad \chi = x , \qquad \eta = \int \frac{B^\varphi_{a_0}}{B^\theta_{a_0}} d\theta - \varphi , \tag{7.16}$$

with basis vectors

$$\boldsymbol{e}_\sigma = \boldsymbol{e}_\theta + \frac{B^\varphi_{a_0}}{B^\theta_{a_0}}\boldsymbol{e}_\varphi , \qquad \boldsymbol{e}_\chi = \boldsymbol{e}_x , \qquad \boldsymbol{e}_\eta = -\boldsymbol{e}_\varphi . \tag{7.17}$$

$B^\varphi_{a_0}$ and $B^\theta_{a_0}$ denote the covariant components of the magnetic field at the reference flux surface with minor radius a_0, and $\boldsymbol{e}_x$, $\boldsymbol{e}_\theta$ and $\boldsymbol{e}_\varphi$ are the basis vectors of the toroidal coordinate system [39].
The simulation domain covers a radial region of length x_{sim} centered around a_0, and is composed out of N_{f} flux tubes, each of them performing one toroidal turn. The poloidal extent of one of these flux tubes at minor radius a in radians is $2\pi a/(q(a)N_{\mathrm{f}})$, where $q(a)$ is the safety factor related to the flux surface with radius a. Boundary conditions in σ and η direction have to be chosen so that periodicity of the simulation

domain in θ and φ direction is ensured.
The equilibrium magnetic field $\boldsymbol{B}_0$ is given by

$$\boldsymbol{B}_0 \;=\; \frac{B_{a_0}}{qR}\,\boldsymbol{e}_\theta \;+\; \frac{B_{a_0}R_0}{R^2}\,\boldsymbol{e}_\varphi \;, \tag{7.18}$$

where R_0 is the major radius of the tokamak device, and $R = R_0 + x\cos(\theta)$. The magnetic shear $\hat{s}$ is taken to be constant so that one obtains for the $q(\chi)$ profile

$$q(\chi) \;=\; q_0\left(1 + \hat{s}\,\frac{\chi - r_0}{r_0}\right) \;, \tag{7.19}$$

with $q_0 = q(a_0)$. Thus, the decisive input parameters for an ATTEMPT simulation are a_0, R_0, B_{a_0}, $q(a_0)$, $\hat{s}$, n_0, T_{0e}, and $L_\perp$ (the characteristic macroscale gradient length, see eq. (4.42)) plus the dissipation coefficients $s_\parallel(\alpha)$ and $s_\perp(\alpha)$. The ATTEMPT scaling (below referred to as AS) is guided by this parameters and given in [11]. Here, most quantities are given in SI units except for the density gradient $\partial_x n_0$,which is given in the ATTEMPT scaling if not mentioned otherwise: $\partial_x n_0$ [AS] $= L_\perp/n_0 \cdot \partial_x n_0$. To include dissipation on scales smaller than ρ_s (which is the lower limit regarding the spatial resolution of the drift fluid models) the rhs of eqs. (7.8) to (7.11) and eqs. (7.12) to (7.15), respectively, are complemented by a subscale dissipation term S_D, depending on the quantity α for which the equation is solved:

$$S_\mathrm{D} \;=\; s_\parallel(\alpha)\nabla_\parallel^2\alpha + s_\perp(\alpha)\nabla_\perp^2\alpha \;. \tag{7.20}$$

The coefficients $s_\parallel(\alpha)$ and $s_\perp(\alpha)$ have to be chosen in such a way that they provide sufficient dissipation but do not damp significantly the characteristic dynamics of the system. In the simulations discussed below values of $s_\parallel(n) = s_\parallel(u_\parallel) = s_\parallel(\nabla_\perp^2\phi) = 0.002$, $s_\parallel(j_\parallel) = 0$, and $s_\perp(n) = s_\perp(u_\parallel) = s_\perp(\nabla_\perp^2\phi) = 0.025$, $s_\perp(j_\parallel) = 0$ are used (all values in the AS).

The damping term $\gamma(\tilde{n})$ which eliminates any macroscale evolution of $\tilde{n}$ in eq. (7.12) is defined as

$$\gamma(\tilde{n}) \equiv \gamma_0 \cdot \left\{\exp\left(-\left[\frac{\chi - a_0 + x_\mathrm{sim}}{0.1\,x_\mathrm{sim}}\right]^2\right) + \exp\left(-\left[\frac{\chi - a_0}{0.1\,x_\mathrm{sim}}\right]^2\right)\right\} \cdot \mathfrak{R}\{\hat{n}(0,\chi,\sigma)\}\;, \tag{7.21}$$

where γ_0 is typically $= 0.1$ [AS] in the simulations below and $\mathfrak{R}\{\hat{n}(0,\chi,\sigma)\}$ is the real part of the Fourier coefficient $\hat{n}(0,\chi,\sigma)$, corresponding to the toroidally constant part of $\tilde{n}$.

7.1.3. Coupling procedure

The coupling procedure used for connecting the 1D code and the local ATTEMPT code is now explained in detail by means of the flow chart shown in fig 7.2. It can be understood as an in-depth version of the sketch shown in fig. 7.1. The uppercase

parameter	**description**
i	global iteration index
j	internal iteration index of 1D code
k	internal iteration index of local ATTEMPT code
l	cell index of 1D code
N_i	number of global iterations
$N_j(i)$	number of internal 1D code it. for global it. i
$N_k(i,l)$	number of internal local ATTEMPT it. for global it. i and 1D code cell l
$N_t^{\mathrm{1D,ii}}$	number of time steps of one internal 1D code it.
$N_t^{\mathrm{A,ii}}$	number of time steps of one internal local ATTEMPT it.
$N_k^{\max}$	maximum number of internal local ATTEMPT it.
N_x^{1D}	number of cells in 1D code
δt_{st}	simulated time of local ATTEMPT simulation until statistical stationarity is reached
δt_{run}	simulated time of local ATTEMPT simulation corresponding to one internal it.
Δt_{run}	simulated time of 1D code corresponding to one internal it.
t_{sim}	total simulated time of 1D code, $t_{\mathrm{sim}} = \sum_i N_j(i)\Delta t_{\mathrm{run}}$
$\partial_x n_0^{i,l}$	radial macroscale density gradient for global iteration i and cell l
$\langle\widetilde{\Gamma}\rangle^{i,l}$	statistically stationary flux obtained from ATTEMPT for global it. i and cell l

Table 7.1.: Parameters used for the coupled code system consisting of the 1D code and ATTEMPT.

letters in parenthesis (X) in the following text refer to the respective position in fig. 7.2. A summary of the coupling parameters is presented in table 7.1. While both the 1D code and ATTEMPT are written in Fortran [103] the coupling itself, i.e. the exchange of input parameters and transport coefficients, is managed via a Python script [104].

A coupled code simulation starts with an initial profile of the macroscale density $n_0(x, t = 0)$. The index i of the global iteration is set to one and the first cell of the 1D code with cell index $l = 1$ is considered (S). (Note that since the following procedure is carried out for all global iterations and 1D code cells, the indices i and l are kept undetermined here.)

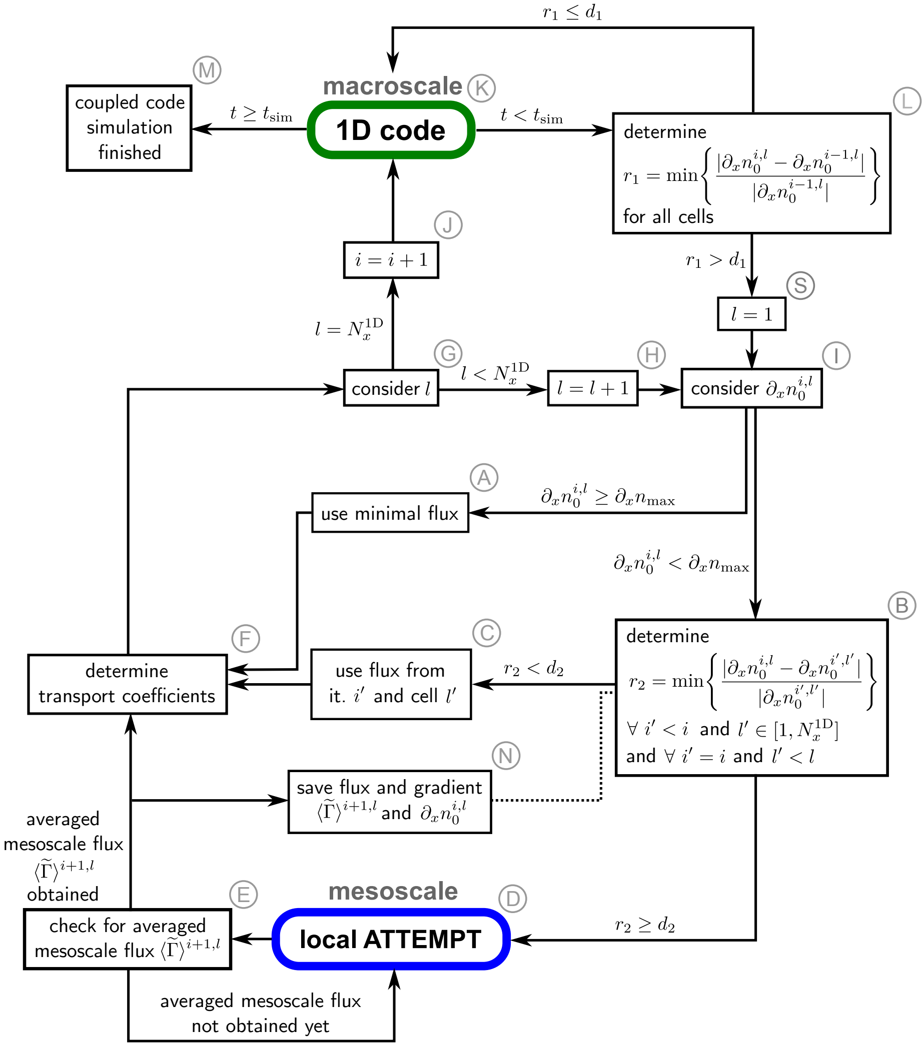

Figure 7.2.: Sketch of a coupled code simulation. The procedure used to check for the averaged mesoscale flux $\langle\widetilde{\Gamma}\rangle$ (E) is outlined in fig. 7.4.

A first check is carried out at (I) to determine if the macroscale density gradient $\partial_x n_0^{i,l}$ is smaller than an arbitrary maximum gradient $\partial_x n_{\max} < 0$. This comparison is done to ensure that, on the one hand, $\partial_x n_0^{i,l}$ is smaller than zero which is a prerequisite for running a local ATTEMPT simulation. On the other hand one finds that for local ATTEMPT simulations where $\partial_x n_0^{\max}$ is less than zero but has a relatively small absolute value, $\partial_x n_0^{\max}$ is not steep enough to drive local mesoscale dynamics which would result in a flux significantly larger than that represented by the artificial dissipation with coefficient $s_\perp(n)$, see eq. (7.20). It is then basically superfluous to carry out a local ATTEMPT simulation; instead, a minimal flux can be used (A). This minimal flux is also used if $\partial_x n_0^{i,l} \geq 0$ and is typically determined using a diffusion coefficient equal to $s_\perp(n)$.

In the case where $\partial_x n_0^{i,l} < \partial_x n_0^{\max}$ a second check is performed (B): that if a local ATTEMPT simulation with a similar density gradient $\partial_x n_0^{i',l'} \approx \partial_x n_0^{i,l}$ has already been carried out during this coupled code simulation. Every successfully determined flux $\langle\widetilde{\Gamma}\rangle^{i+1,l}$ and its input density gradient $\partial_x n_0^{i,l}$ are saved to a file (N). Similarity between the two gradients is determined by the deviation r_2: the two gradients are taken to be similar if d_2 is smaller than the limit parameter d_2 which is set by the modeler. If $r_2 < d_2$, the associated flux $\langle\widetilde{\Gamma}\rangle^{i',l'}$ of the previous local ATTEMPT simulation is used (C). If $r_2 \geq d_2$, no similar density gradient has been used before and a local ATTEMPT simulation with $\partial_x n_0^{i,l}$ as input parameter is started (D).

The local ATTEMPT simulations are run until a statistically stationary state has been reached and enough data for determining a statistically meaningful average $\langle\widetilde{\Gamma}\rangle^{i+1,l}$ has been obtained. This is checked after each internal iteration k of the local ATTEMPT simulation (E) which simulates a time interval $\delta t_{\text{run}} = N_t^{\text{A,ii}} \delta t_s$, $N_t^{\text{A,ii}}$ being the number of time steps used for one internal local ATTEMPT iteration. The checking procedure executed at (E) is rather complex and elucidated separately in the next paragraph 7.1.4. Here, it is simply assumed that after a number $N_k(i,l)$ of internal ATTEMPT iterations the averaged mesoscale flux $\langle\widetilde{\Gamma}\rangle^{i+1,l}$ can be calculated and is then translated at (F) into the transport coefficients used by the macroscale transport model $\mathcal{M}$ (e.g. see the eqs. (7.5) and (7.6) for a convection-diffusion scheme). Also, the flux and the gradient are saved to a separate file (N) for the comparison at (B).

The check for the macroscale cell index l at (G) determines if the macroscale transport coefficients have been updated for the whole macroscale simulation domain ($l = N_x^{\text{1D}}$) or if this is not yet the case ($l < N_x^{\text{1D}}$). In the latter case, the 1D code cell index l is increased by one (H) and the procedure explained above is repeated for the next 1D code cell $l = l + 1$, starting at (I). In the former case where $l = N_x^{\text{1D}}$ all local ATTEMPT simulations for this global iteration i have been finished. The global iteration index is increased by one (J) and the 1D code is started to determine the evolution of n_0 (K).

The execution of the 1D code is, like the execution of the local ATTEMPT code, divided into internal iterations with iteration index j. Each internal 1D code iteration simulates a time interval of length $\Delta t_{\text{run}} = N_t^{\text{1D,ii}} \Delta t_s$. The total simulated time after global iteration $i = m$ and internal 1D code iteration j is therefore given by $t = \sum_{i=1}^{m} N_j(i) \Delta t_{\text{run}} + j \Delta t_{\text{run}}$ where $N_j(i)$ is the total number of internal 1D code iterations carried out for global iteration i. As long as $t < t_{\text{sim}}$, with t_{sim} being the time the coupled code system should simulate, a check in how far the

density gradients have changed compared to those of the previous global iteration is carried out (L). This can be understood as an on-the-fly determination of $\tau_{\mathrm{D}}(\alpha_0)$, the characteristic time of the macroscale profile evolution, and therefore $\Delta t_{\mathrm{up}} \approx \tau_{\mathrm{D}}(\alpha_0)$. Here, the focus is on the macroscale density gradient $\partial_x n_0$ since this is the decisive input parameter for the local ATTEMPT simulations. As long as the deviation r_1 of the new gradient from the gradient of the previous global iteration of the respective cell is below the limit parameter r_2 for all macroscale cells, another internal 1D code iteration is carried out. If $r_1 > d_1$, it is decided that the macroscale profile has changed significantly. The 1D code cell index l is set to one (S) and the procedure is started from the beginning (I) for all 1D code cells. Thus, the updating time Δt_{up} can vary between global iterations and is given by $\Delta t_{\mathrm{up}}(i) = N_j(i)\Delta t_{\mathrm{run}}$.
The coupled code simulation is finished once the time t simulated in the 1D code is larger than the predetermined simulated time t_{sim} (M).

The new aspects of the above coupling procedure, compared to the coupling loop presented in fig. 7.1, right, can be summarized as follows. The limit parameter d_1 is used to determine the updating time $\Delta t_{\mathrm{up}}(i)$ which depends on the global iteration and the macroscale dynamics. The limit parameter d_2 determines in how far previously calculated values of $\langle\widetilde{\Gamma}\rangle^{i,l}$ may be reused. Due to the implemented procedure at (B), the coupling procedure is a mixture of a sequential and concurrent multiscale approach where the sequential part is introduced to increase the time savings and is not essential for the coupling (meaning that the steps (B), (C) and (N) could be eliminated without affecting the accuracy of the multiscale simulations). The updating time $\Delta t_{\mathrm{up}}(i)$ is adjusted to the current temporal scale of macroscale processes. The dynamic determination of δt_{st} and δt_{av} is explained in the next paragraph.

7.1.4. Determination of the averaged mesoscale terms

In the coupled code system outlined in the previous paragraph one is interested in finding the averaged mesoscale flux $\langle\widetilde{\Gamma}\rangle^{i+l}$ of a statistically stationary state which corresponds to a macroscale gradient $\partial_x n_0^{i,l}$. To determine $\langle\widetilde{\Gamma}\rangle^{i+l}$ knowledge of both δt_{st} (the time the local mesoscale code needs to reach the statistically stationary state from its initial profile) and $\tau_{\mathrm{D}}(\widetilde{\alpha})$ (the characteristic time of the local mesoscale dynamics from which the averaging interval δt_{av} is derived) is needed: δt_{st} and $\tau_{\mathrm{D}}(\widetilde{\alpha})$ determine the appropriate position and length of the temporal averaging interval employed to determine $\langle\widetilde{\Gamma}\rangle^{i+l}$. Even though a rough estimate for δt_{st} and $\tau_{\mathrm{D}}(\widetilde{\alpha})$ might be available beforehand, their exact values most likely vary for different local mesoscale simulations due to varying input gradients $\partial_x n_0^{i,l}$. Since the choice of δt_{st} and δt_{av} affects both the accuracy of the results of the coupled code system as well as its time savings, it is inevitable to determine these quantities appropriately. This is illustrated below.

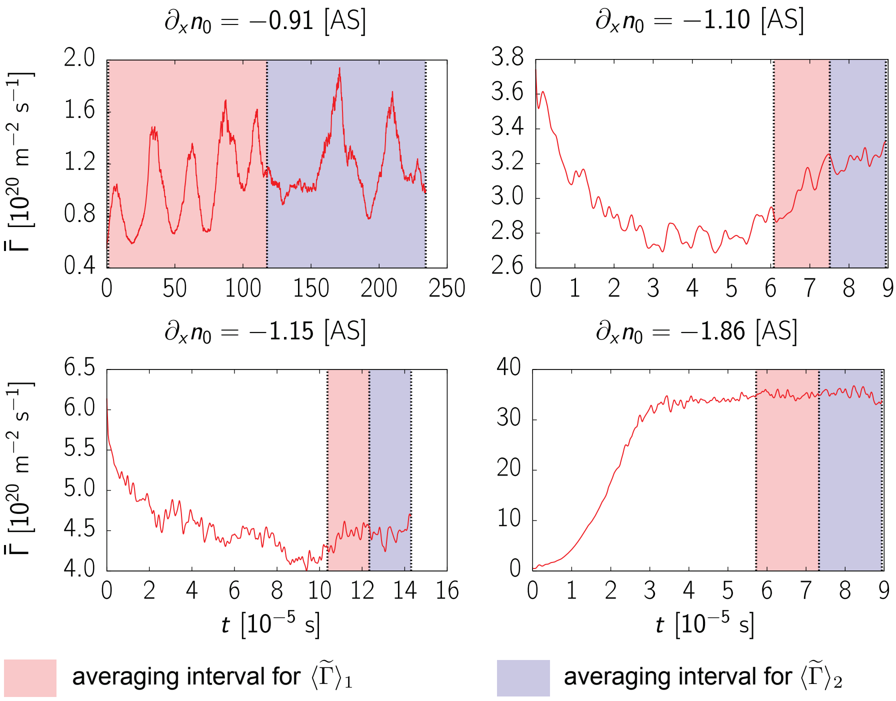

Figure 7.3.: Time traces of fluxes $\bar\Gamma$ and the averaging intervals for $\langle\widetilde\Gamma\rangle_1$ and $\langle\widetilde\Gamma\rangle_2$ that are determined automatically by the procedure illustrated in fig. 7.4 which is explained in paragraph 7.1.4.

In fig. 7.3, time traces of $\bar\Gamma(t)$ of local ATTEMPT simulations for different input gradients $\partial_x n_0$ are shown. The light red and blue intervals refer to the averaging intervals automatically determined by the procedure outlined below. The flux $\bar\Gamma$ is introduced to simplify the notation and is given by

$$\bar\Gamma(t) \;\equiv\; \langle \tilde n \tilde v_{\mathrm{E}x}\rangle_V(t) \;, \tag{7.22}$$

where the average $\langle \ldots \rangle_V$ corresponds to the entire simulation domain of the local mesoscale simulation (the averaged mesoscale flux $\langle\widetilde\Gamma\rangle$ therefore can be written as $\langle\widetilde\Gamma\rangle = \langle\bar\Gamma\rangle_t$). Obviously, both δt_{st} and $\tau_{\mathrm{D}}(\bar\Gamma)$ vary for the different input gradients: whereas for $\partial_x n_0 = -1.15$ (bottom, left) $\delta t_{\mathrm{st}} \approx 60$ μs, on has $\delta t_{\mathrm{st}} \approx 30$ μs for $\partial_x n_0 = -1.86$ (bottom, right). These 30 μs difference already correspond to roughly 3 000 time steps of a local ATTEMPT simulation, the time step size being $\delta t_s \approx 10^{-8}$ s. Significant differences regarding $\tau_{\mathrm{D}}(\bar\Gamma)$ and the consequential averaging time

$\delta t_{\rm av} \gg \tau_{\rm D}(\bar{\Gamma})$ can be found for $\partial_x n_0 = -0.91$ (top, left, $\delta t_{\rm av} \approx 2$ ms) and $\partial_x n_0 = -1.86$ (bottom, right, $\delta t_{\rm av} \approx 5$ μs).

Various tests that can be used to examine time series for statistical stationarity are available from the field of time series analysis [42, 105]. The procedure presented below is adapted to the specific needs of the coupling procedure used here, allowing for a quick assessment of both the equilibration time $\delta t_{\rm st}$ and the characteristic evolution time $\tau_{\rm D}(\alpha)$ of the quantity of interest, here $\bar{\Gamma}$. It also includes a decision-making process to determine if the time trace $\bar{\Gamma}(t)$ is sufficiently long to calculate a meaningful averaged mesoscale flux $\langle\widetilde{\Gamma}\rangle$ or if it has to be extended further. The procedure is sketched in fig. 7.4 and explained below, with Roman numbers referring to the related steps in fig. 7.4. Basically it can be applied to any system for which the statistically stationary state and the corresponding averaged quantities have to be determined automatically. This allows future use also in other coupled code systems with mesoscale models different from the local drift fluid model applied here.

Having completed the internal iteration k of the local ATTEMPT simulation to find the averaged mesoscale flux $\langle\widetilde{\Gamma}\rangle^{i+1,l}$ for global iteration i and 1D code cell l (position (E) in fig. 7.2), the so-called check for $\langle\widetilde{\Gamma}\rangle$ is started (0). It consists of three main procedures: firstly, determine the characteristic time scale on which the statistically stationary $\bar{\Gamma}$ evolves (I - VI). Secondly, check if enough data for calculating a meaningful value $\langle\widetilde{\Gamma}\rangle$ is available (VII). Thirdly, check if a statistically stationary state of $\bar{\Gamma}$ is reached. If yes, the averaged mesoscale flux $\langle\widetilde{\Gamma}\rangle^{i+1,l}$ is calculated and the local ATTEMPT simulation for this global iteration and 1D code cell is finished. If not, the next internal ATTEMPT iteration $k+1$ is started which basically extends the time trace of $\bar{\Gamma}(t)$ with the objective to fulfill the above criteria after the next internal iteration.

The characteristic time scale $\tau_{\rm D}(\bar{\Gamma})$ of the dynamics of $\bar{\Gamma}(t)$ in the statistically stationary state is approximated by the correlation time $\tau_c(\bar{\Gamma})$, $\tau_{\rm D}(\bar{\Gamma}) \approx \tau_c(\bar{\Gamma})$. To determine $\tau_c(\bar{\Gamma})$ the autocorrelation function $\rho(\bar{\Gamma}; t_l)$ is needed where t_l is the so-called lag. In general, the autocorrelation function $\rho(\alpha; l)$ of a discrete series for the quantity α with a total number N of data points is given by [42]

$$\rho(\alpha; l) \equiv \frac{\gamma(\alpha; l)}{\sigma_{\alpha,l}\sigma'_{\alpha,l}} \, . \tag{7.23}$$

It is to be understood as a function of l. The autocovariance function $\gamma(\alpha; l)$ is defined as

$$\gamma(\alpha; l) = \frac{1}{N-l} \sum_{j=1}^{N-l} \Big(\alpha_j - \langle\alpha_l\rangle\Big)\Big(\alpha_{l+j} - \langle\alpha'_l\rangle\Big) \, , \tag{7.24}$$

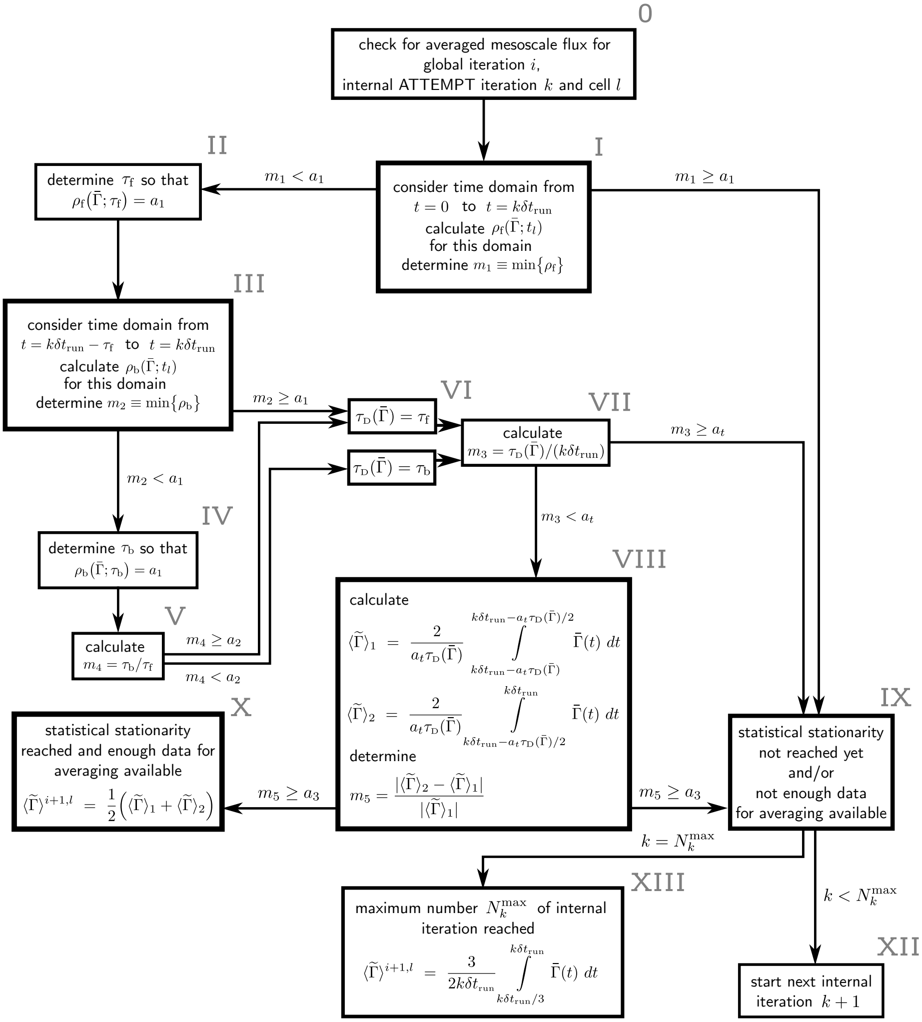

Figure 7.4.: Procedure to check for the averaged mesoscale flux $\langle\widetilde{\Gamma}\rangle$ of the local ATTEMPT simulation.

with the averages

$$\langle\alpha_l\rangle = \frac{1}{N-l}\sum_{j=1}^{N-l}\alpha_j\,, \qquad \langle\alpha_l'\rangle = \frac{1}{N-l}\sum_{j=1}^{N-l}\alpha_{j+l}\,. \tag{7.25}$$

The standard deviations are

$$\sigma_{\alpha,l} = \sqrt{\frac{1}{N-l}\sum_{j=1}^{N-l}\Big(\alpha_j - \langle\alpha_l\rangle\Big)^2}\;, \qquad \sigma'_{\alpha,l} = \sqrt{\frac{1}{N-l}\sum_{j=1}^{N-l}\Big(\alpha_{j+l} - \langle\alpha'_l\rangle\Big)^2}\;. \quad (7.26)$$

It holds that $\rho(\alpha;l) \in [-1,1]$. If $\rho(\alpha;l) = 1$ or $\rho(\alpha;l) = -1$ for a certain lag l, then the values α_j and α_{j+l} (at times t_j and t_{j+l}) depend linearly on each other (in the former case, the slopes for α_j and α_{j+l} coincide while in the latter case, they have opposite signs). For $l = 0$ the autocorrelation function always equals one, $\rho(\alpha;0) = 1$. Usually, the correlation time $\tau_c(\alpha)$ is defined as the e-folding length of the function $\rho(\alpha;t_l)$ with respect to the temporal lag t_l, assuming that $\rho(\alpha;t_l) \approx \exp(-t_l/\tau_c(\alpha))$, i.e. the time with $\rho(\alpha;\tau_c(\alpha)) = 1/e$ where e is Euler's number.

A first estimate for $\tau_c(\bar{\Gamma})$ (and therefore $\tau_{\rm D}(\bar{\Gamma})$) is determined as the correlation time $\tau_{\rm f}$ of the autocorrelation function $\rho_{\rm f}(\bar{\Gamma},t_l)$ of the complete time trace of $\bar{\Gamma}(t)$ from $t = 0$ to $t = k\delta t_{\rm run}$ (I). An example for $\rho_{\rm f}(\bar{\Gamma},t_l)$ is shown in fig. 7.5, red curve, for the time trace of $\bar{\Gamma}(t)$ shown in fig. 7.3, bottom, right. Obviously, $\rho_{\rm f}(\bar{\Gamma},t_l)$ does not decay exponentially yet so that an exponential fit to determine $\tau_{\rm f}$ is not reasonable. However, one would like to have a rough estimate for $\tau_{\rm f}$. It is calculated by setting $\tau_{\rm f}$ to $\min(t_l)$ with $\rho_{\rm f}(\bar{\Gamma};t_l) = a_1$ (II): $\tau_{\rm f}$ is simply estimated as the smallest lag t_l for which $\rho_{\rm f}(\bar{\Gamma},t_l)$ drops below a_1, with 1/e being a typical value for a_1. Beforehand, in the step from (I) to (II), it is simply checked if $\rho_{\rm f}$ drops to a_1 at all so that $\tau_{\rm f}$ can be determined.

In the example shown in fig. 7.5, $\tau_{\rm f} \approx 4.2 \cdot 10^{-5}$ s. By comparing it to the associated time trace in fig. 7.3, bottom, right, it becomes clear that $\tau_{\rm f}$ overestimates the correlation time of $\bar{\Gamma}(t)$ in the statistically stationary state, starting around $t \approx 3 \cdot 10^{-5}$ s, with $\tau_c(\bar{\Gamma})$ being of the order of 10^{-6} s. The overestimation of $\tau_c(\bar{\Gamma})$ is basically due to the first increase of $\bar{\Gamma}(t)$ until the statistically stationary state is reached, a phase which should be neglected for determining $\tau_c(\bar{\Gamma})$. This is realized automatically via steps (III) to (VI).

Once $\tau_{\rm f}$ is calculated, the time interval from $t = k\delta t_{\rm run} - \tau_{\rm f}$ to $t = k\delta t_{\rm run}$ is examined and the autocorrelation function $\rho_{\rm b}(\bar{\Gamma},t_l)$ using data of only this interval is determined at (III). If the system has already reached the statistically stationary state than this will be reflected by the data at the end of the simulated time interval. The corresponding graph is the green graph in fig. 7.5. The respective correlation time $\tau_{\rm b}$ is determined at (IV) by the same procedure that was used for $\tau_{\rm f}$. In the example case one finds that $\tau_{\rm b} = 7.21 \cdot 10^{-7}$. Next, a comparison of $\tau_{\rm b}$ with $\tau_{\rm f}$ is carried out at (V) to decide if the structure related to $\tau_{\rm b}$ is indeed significantly smaller than that given by $\tau_{\rm f}$. If yes, $\tau_{\rm f}$ can be assumed to correspond to the phase during which the system reaches the statistically stationary state, and $\tau_{\rm b}$ is the correlation time of $\bar{\Gamma}(t)$ of this statistically stationary state. If not, $\tau_{\rm f}$ is taken as an estimate for $\tau_{\rm D}(\bar{\Gamma})$. This decision is made at (VI).

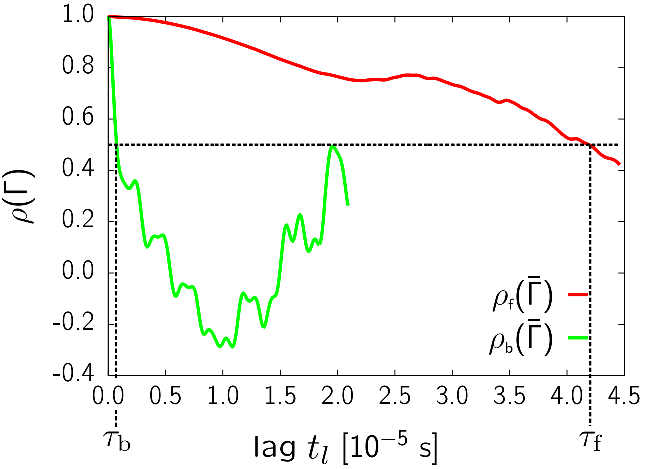

Figure 7.5.: Determination of the times τ_f and τ_b for the time trace shown in fig. 7.3, bottom right.

Having an estimate for the characteristic time scale $\tau_\mathrm{D}(\bar{\Gamma})$ of the dynamics of $\bar{\Gamma}(t)$ in the statistically stationary state, it has to be verified whether enough data for obtaining a statistically meaningful $\langle\widetilde{\Gamma}\rangle$ is available or not (VII). This means to check if the time trace of $\bar{\Gamma}(t)$ is long enough so that the averaging interval of length $\delta t_\mathrm{av} = a_t \tau_\mathrm{D}(\bar{\Gamma})$ 'fits' into it. Since $\tau_\mathrm{D}(\bar{\Gamma})$ may differ for different global iterations i and 1D code cells l, δt_av can now also be interpreted as function of i and l and is not constant for all local ATTEMPT simulations. With the same reasoning also the time δt_st depends on i and j.
A last check is performed at (VIII) which basically serves to assure that a statistically stationary state has been reached and also has the role of a control mechanism in case that one of the checks at steps (0) to (VII) failed, e.g. due to a very unusual form of the time series of $\bar{\Gamma}(t)$. It consists of calculating two averages $\langle\widetilde{\Gamma}\rangle_1$ and $\langle\widetilde{\Gamma}\rangle_2$ from the total averaging interval of length $a_t \tau_\mathrm{D}(\bar{\Gamma})$, and comparing their deviation m_5 from each other to a predefined limit parameter a_3. If $m_5 < a_3$, then $\langle\widetilde{\Gamma}\rangle^{i+1,l}$ is calculated as the average of $\langle\widetilde{\Gamma}\rangle_1$ and $\langle\widetilde{\Gamma}\rangle_2$ (X) and the local mesoscale simulation is finished.

At the three points (I), (VII), and (VIII), the check for the averaged mesoscale flux $\langle\widetilde{\Gamma}\rangle$ can be aborted: at (I) if ρ_f does not yet fall below the limit value a_1 and τ_f therefore cannot be determined, at (VII), if not enough data for averaging has been collected yet, and at (VIII), if by determination of the deviation of the two fluxes $\langle\widetilde{\Gamma}\rangle_1$ and $\langle\widetilde{\Gamma}\rangle_2$ it is decided that the statistically stationary state has not been reached yet. In all these cases the next internal ATTEMPT iteration $k+1$ is started (IX), (XII). Only exception is if the maximum number N_k^max of internal iterations is reached. In this case $\langle\widetilde{\Gamma}\rangle^{i+1,l}$ is determined by an average over the last two thirds of the time trace of $\bar{\Gamma}(t)$ (XIII). This step is introduced to prevent disproportionately long runtimes of local ATTEMPT simulations.

The proper working of the above procedure to determine the averaged flux $\langle\widetilde{\Gamma}\rangle$ is illustrated by fig. 7.3 for different density gradients $\partial_x n_0$. The light red and light blue intervals are the automatically determined averaging intervals for $\langle\widetilde{\Gamma}\rangle_1$ and $\langle\widetilde{\Gamma}\rangle_2$. Their length and position coincide roughly with the intervals' position and length one would choose with the naked eye, except for $\partial_x n_0 = -1.10$ (top, right) where a longer time trace of $\bar{\Gamma}(t)$ would be needed for a correct evaluation. How to develop this procedure and increase its reliability is one of the tasks for future work. For further evaluation of the performance of the procedure please refer to paragraph 7.3.3.

7.2. Comparison of local and non-local ATTEMPT simulations

The focus of the benchmark presented in this paragraph is the comparison of the non-local averaged radial particle flux $\langle\Gamma\rangle$ and the flux of the corresponding local system $\langle\widetilde{\Gamma}\rangle$. It will give an idea about the accessible minimum deviation of the coupled code results from the reference non-local ATTEMPT simulations for the benchmark cases presented in the next paragraph 7.3.

The setup of this comparison is as follows: a non-local ATTEMPT simulation is started for a plasma edge region with closed flux surfaces with a predefined density gradient $\partial_x n_{\text{in}}$ at the inner radial boundary. This boundary condition results in a particle flux in radial direction which, on average, points radially outwards. Once the statistically stationary state is reached the values of $\langle\Gamma\rangle$ and $\langle\partial_x n_0\rangle$ are determined, where the average is carried out over a time interval in the statistically stationary state and the whole simulation domain. Since the profile of $\langle n(\boldsymbol{r},t)\rangle_{\text{fs},t}(x,t)$ is basically linear in radial direction the gradient $\langle\partial_x n_0\rangle$ can be used as input parameter for a local ATTEMPT simulation. From its statistically stationary state the averaged radial local particle flux $\langle\widetilde{\Gamma}\rangle$ is calculated. Both flux values are compared with each other by determining the error $\eta_{\text{st}}(\Gamma)$,

$$\eta_{\text{st}}(\Gamma) \;\equiv\; 100 \cdot \frac{|\langle\Gamma\rangle - \langle\widetilde{\Gamma}\rangle|}{|\langle\Gamma\rangle|} \;. \tag{7.27}$$

The smaller η_{st}, the better is the agreement between the non-local and local ATTEMPT simulations. Additionally to η_{st}, also the one-point PDFs of v_{Ex}, n, $\widetilde{n}$, Γ, and $\widetilde{\Gamma}$ are compared.

The benchmark is carried out for two different tokamak devices: a rather small, TEXTOR-like device [34] with $a_0 = 0.4$ m, $R_0 = 1.75$ m, $T_{0e} = 50$ eV, $n_0 = 2{\cdot}10^{19}$ m^{-3}

case	$\partial_x n_{\text{in}}$ [AS]	$\partial_x n_0$ [AS]	non-local $\langle\Gamma\rangle$ [10^{19}m^{-2} s^{-1}]	local $\langle\widetilde{\Gamma}\rangle$ [10^{19}m^{-2} s^{-1}]	$\eta_{\text{st}}(\Gamma)$ [%]
A.1	-2.5	-0.61	0.87 ± 0.23	0.73 ± 0.19	16.10
A.2	-7.5	-1.17	4.52 ± 0.25	4.00 ± 0.22	11.50
A.3	-12.5	-1.49	10.61 ± 0.04	9.00 ± 0.30	15.18
B.1	-2.5	-0.61	4.52 ± 0.50	3.80 ± 0.48	15.86
B.2	-7.5	-1.11	24.07 ± 1.13	27.34 ± 1.20	13.74
B.3	-12.5	-1.51	57.05 ± 2.59	73.41 ± 1.13	28.68

Table 7.2.: Results of the ATTEMPT simulations to compare the non-local and corresponding local fluxes $\langle\Gamma\rangle$ and $\langle\widetilde{\Gamma}\rangle$.

	N_s^{A}	N_x^{A}	N_y^{A}	δx_s	δy_s	δt_s
cases A	16	64	128	$1\,\rho_s$	$1.01\,\rho_s$	$1.44 \cdot 10^{-8}$ s
cases B	16	64	256	$1\,\rho_s$	$1.33\,\rho_s$	$1.02 \cdot 10^{-8}$ s

Table 7.3.: Parameters for the comparison of local and non-local simulations.

(cases A), and a larger device with $a_0 = 1.5$ m, $R_0 = 3$ m, and a hotter and denser plasma with $n_0 = 4 \cdot 10^{19}$ m^{-3}, $T_{0e} = 100$ eV. The magnetic field $B_{a_0} = 2$ T, the safety factor $q_0 = 3$, and the shear $\hat{s} = 2$ are kept constant for both cases. Since the number of flux tubes needed to cover the full torus is chosen to be high, $N_{\text{f}} = 18$, only dynamics with high poloidal mode numbers $m \geq 54$ are considered here[1]. Further information on the simulation parameters is given in table 7.3.
Boundary conditions are as follows and apply for both the local and non-local ATTEMPT simulations if not mentioned otherwise. In σ and η direction boundary conditions are chosen so that periodicity in toroidal and poloidal direction is fulfilled. At both boundaries of the χ direction (corresponding to the radial direction), all quantities, i.e. n, $u_{\|}$, $A_{\|}$, ϕ, and $j_{\|}$, are set to zero. Only exception is the non-local ATTEMPT version, where at the inner boundary in χ direction the radial density gradient is set to $\partial_x n_{\text{in}}$.

For each device, three different cases with varying density gradients $\partial_x n_{\text{in}}$ at the inner boundary for the non-local simulations were carried out, representing varying particle influx from the core. The different cases are listed in table 7.2. Snapshots from the

---

[1] The minimum poloidal mode number that is resolved by the simulations, excluding the constant mode $m = 0$, is given by $m_{\text{min}} = N_{\text{f}} q_0$

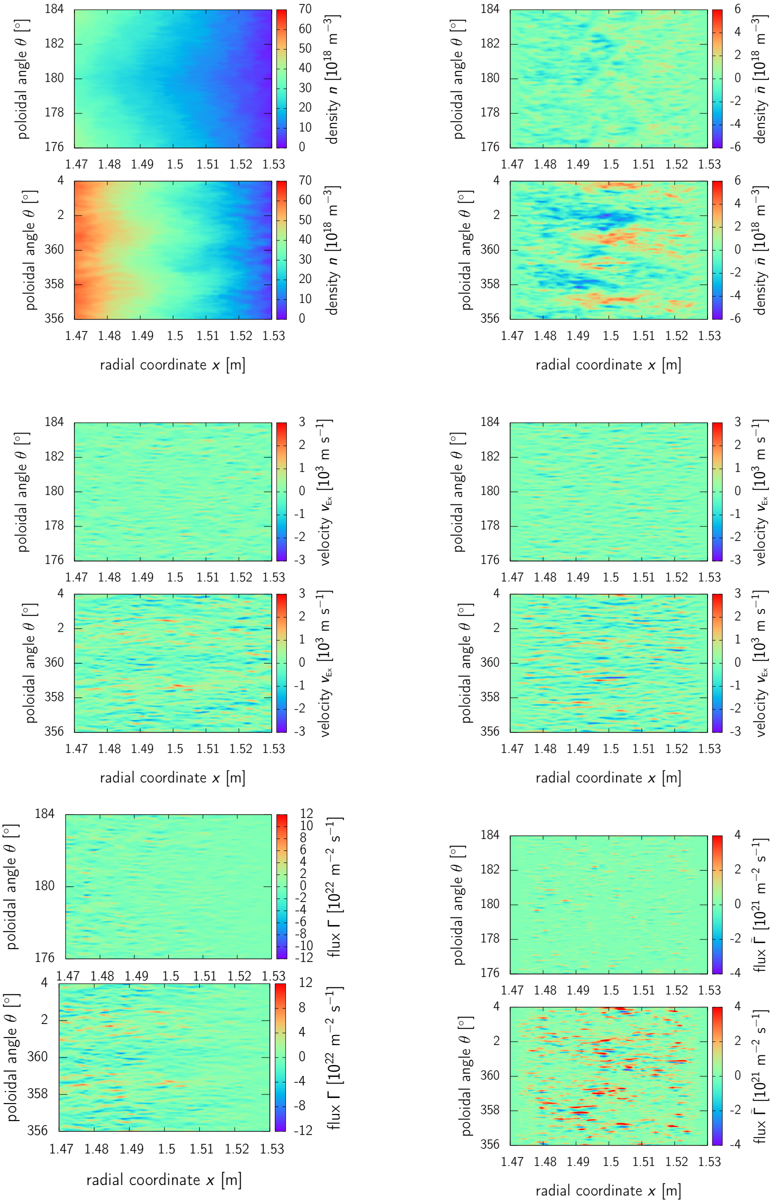

Figure 7.6.: Snapshots of non-local (**left column**) and corresponding local (**right column**) ATTEMPT simulations for a poloidal region of $\delta\theta = 8°$ at the HFS ($176° \leq \theta \leq 184°$) and the LFS ($356° \leq \theta \leq 4°$) for the density, the radial part v_{Ex} of the E×B velocity, and the radial flux.

simulations of the B.2 case from the statistically stationary state are shown in fig. 7.6 for the densities n and $\tilde{n}$, the velocities v_{Ex}, and the fluxes $\Gamma = nv_{\mathrm{Ex}}$ and $\widetilde{\Gamma} = \tilde{n}v_{\mathrm{Ex}}$. The plots in the left column correspond to the non-local ATTEMPT simulation while the plots in the right column belong to the local ATTEMPT simulation. The plots show the complete radial extent of the simulation domain for a toroidal angle of $\phi = 0°$ and refer to a poloidal region with an extent of $\Delta\theta = 8°$ at the HFS ($\theta = 176°$ to $\theta = 184°$) and at the LFS ($\theta = 356°$ to $\theta = 4°$), with $\theta = 0$ at the HFS (see also fig. 3.2).
The snapshots in fig. 7.6 illustrate different aspects of the local and non-local drift fluid dynamics. Firstly, they demonstrate the typical extent of structures for high-m dynamics in radial direction (down to lengths of one millimeter and below) and in poloidal direction (of the order of one tenth of degrees and below, corresponding to a length less or equal to two millimeters). Secondly, the plots of the fluxes Γ and $\widetilde{\Gamma}$ in the two bottom rows show that locally, particle transport is directed in both positive and negative radial direction. Only on average flux is directed radially outwards. Thirdly, the fluctuations of the densities, the velocities v_{Ex}, and the fluxes are more pronounced at the LFS, the region of ‘bad curvature’. This region shows increased radial transport due to the inertia of particles that counteracts the magnetic confinement within the torus, and instabilities such as the interchange instability. Fourthly, the general spatial structures of the velocity and flux are similar for both the non-local and local simulation, insofar as this can be evaluated by the naked eye. The velocities v_{Ex} are of the same order of magnitude in both cases.

Before having a closer look at the statistical properties of the non-local and local simulations by comparing the one-point PDFs, the results for $\langle\Gamma\rangle$, $\langle\widetilde{\Gamma}\rangle$ and $\eta_{\mathrm{st}}(\Gamma)$ which are shown in table 7.2 should be analyzed. For cases A the averages are carried out over 50 000 profiles, for cases B 30 000 profiles are averaged. In all cases the profiles used for averaging are taken from the statistically stationary state, with 10 time steps between each profile.
The error $\eta_{\mathrm{st}}(\Gamma)$ of the local simulations is between 11.5 and 16.1 for most cases. Only for B.3, the case with the highest averaged flux of $\langle\Gamma\rangle = 57.05 \cdot 10^{19}\ \mathrm{m}^{-2}\ \mathrm{s}^{-1}$, $\eta(\Gamma)$ increases up to 28.68. By doubling the damping term $\gamma(\tilde{n})$ of the local model, see eq. (7.21), $\eta_{\mathrm{st}}(\Gamma)$ can be reduced to 21.97. However, further increasing $\gamma(\tilde{n})$ might also damp the characteristic drift fluid dynamics. Therefore, an optimized choice of $\gamma(\tilde{n})$ and the corresponding coefficients by means of a benchmark of local simulation against experimental measurements can be an objective for future work.

The comparison of the non-local and local simulations is concluded by a look at the one-point PDFs of n, $\tilde{n}$, v_{Ex}, Γ, and $\widetilde{\Gamma}$ of case A.2 with the lowest error $\eta_{\mathrm{st}}(\Gamma) = 11.5$, and the case B.3 with the highest error $\eta_{\mathrm{st}}(\Gamma) = 28.68$. The PDFs for the densities and the velocities are shown in fig. 7.7 and are calculated for a point in the middle of the simulation domain at position $(N_s^{\mathrm{A}}/2, N_x^{\mathrm{A}}/2, N_y^{\mathrm{A}}/2)$. For case A.2 the PDFs are created using 50 000 data sets, for case B.3 30 000 data sets are analyzed. In

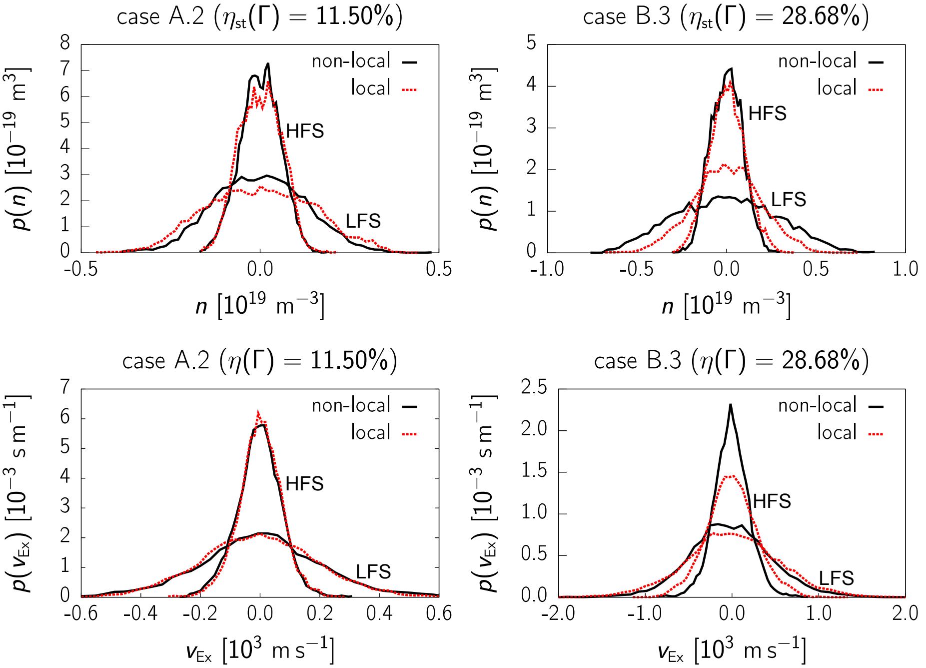

Figure 7.7.: PDFs of v_{Ex} for cases A.2 (**left**) and B.3 (**right**) for the LFS ($\theta = 0°$) and the HFS ($\theta = 180°$).

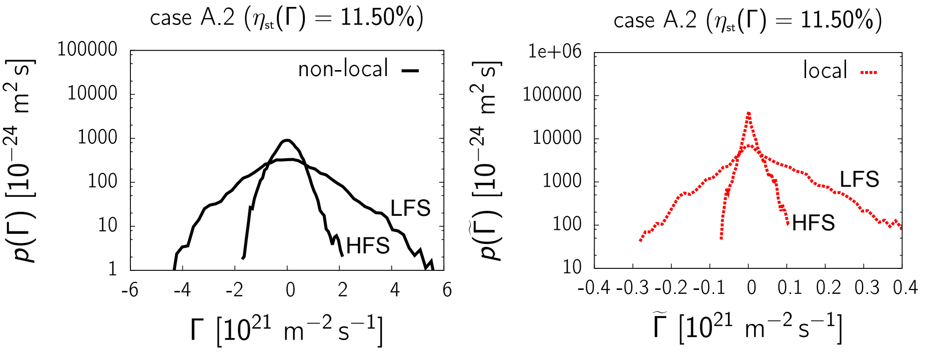

Figure 7.8.: PDFs of the flux nv_{Ex} and $\widetilde{n}v_{\mathrm{Ex}}$, respectively, of case A.2 for the non-local (**left**) and local (**right**) simulations. For both the LFS ($\theta = 0°$) and the HFS ($\theta = 180°$) the PDFs are shown.

both cases the data is taken from the statistically stationary case and the data sets are separated by 10 time steps. Note that for the non-local simulations the values of n have been normalized to $n - \langle n \rangle$, the average being carried out over all data sets included in the analysis, to allow for a better comparison with $\widetilde{n}$.
For A.2 (fig. 7.7, left column), the PDFs of the non-local and the local case almost perfectly coincide, especially for v_{Ex}. Also, they are almost perfectly symmetric with respect to $n = \widetilde{n} = v_{\text{Ex}} = 0$ and have Gaussian-like shapes. The effect of the 'bad curvature' on the LFS results in broader PDFs than on the HFS.
For the case B.3, in comparison, the PDFs of the local simulation deviate significantly from those of the non-local simulation except for the density at the HFS. The different magnitudes of transport at the HFS and LFS are again reflected by the different shapes of the PDFs, those at the LFS being significantly wider.

The PDFs of the fluxes Γ and $\widetilde{\Gamma}$ shown in fig. 7.8 are both tilted towards positive fluxes. However, to achieve a net positive radial flux time averaging is necessary. This is similar to the passive scalar simulations discussed in chapter 6 where on the mesoscale no preferential direction existed while on the macroscale transport was directed in opposite direction of the density gradient.

7.3. Results of the coupled code system

In this paragraph, the time-dependent evolution of the flux surface averaged density profile in radial direction is modeled with the coupled code system presented in paragraph 7.1 and benchmarked against non-local drift fluid simulation, carried out with the non-local ATTEMPT code (paragraph 7.1.2). This comparison for a transient process is done to evaluate the performance of the coupling procedure regarding accuracy and potential time savings, its sensitivity to the input parameters like the number of cells N_x^{1D} used on the macroscale, and the choice of the macroscale transport model.
The analysis starts with a detailed description of the simulation setup (paragraph 7.3.1) and then examines the agreement of the density n_0 and flux Γ_0 with the reference simulation (paragraph 7.3.2), the performance of the procedure to check for the averaged mesoscale flux $\langle \widetilde{\Gamma} \rangle$ (paragraph 7.3.3) and the time savings of the coupled code system (paragraph 7.3.4). A number of additional studies complementing the main series of simulations is presented in paragraph 7.3.5. In paragraph 7.3.6, the results are summarized and discussed.

7.3.1. Setup of the simulations

The general setup of the simulations is sketched in fig. 7.9, an overview of the simulation parameters is given in tables 7.4 and 7.5.

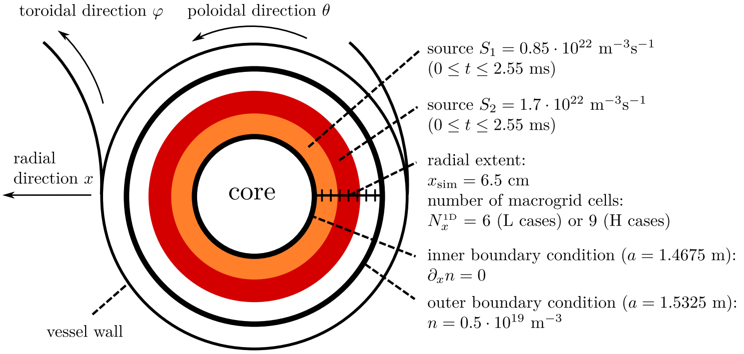

Figure 7.9.: Sketch of the simulation domain for the coupled code benchmark.

The tokamak configuration of the simulations is that of the B cases of paragraph 7.2 with a major radius $R_0 = 3$ m and a minor radius $a_0 = 1.5$ m. The simulation domain comprises the volume between the flux surfaces at $a_0 = 1.4675$ m (corresponding to the radial coordinate $x = 0$) and $a_0 = 1.5325$ m ($x = 6.5$ cm). A time interval of 7 ms is simulated. A particle source $S_0(x)$ for H^+ ions is switched on for the time interval $0 \leq t \leq 2.55$ ms and switched off from 2.55 ms $< t \leq t_{\mathrm{sim}} = 7$ ms, mimicking a gas puff in the plasma edge or a burst of particles coming from the core region. The profile of $S_0(x)$ is shown in fig. 7.9. Its stepwise form is chosen to obtain a resulting radial profile $\langle n \rangle(x)$ which deviates from a simple linear decay during the phase with the source switched on and therefore 'challenges' the coupled code system. In the following analysis the two time intervals 0 ms $\leq t \leq$ 2.55 ms and 2.55 ms $< t \leq t_{\mathrm{sim}} = 7$ ms are investigated separately since they exhibit different dynamical characteristics. The initial profiles of n_0 and $\langle n \rangle$ are given by a linear density decay from $n = 3.5 \cdot 10^{19}$ m^{-3} at the inner radial boundary to $n = 0.5 \cdot 10^{19}$ m^{-3} at the outer boundary.

Boundary conditions are as follows. In the 1D code simulations and the non-local ATTEMPT simulations, Neumann boundary conditions are used for the densities n_0 and $\langle n \rangle$ at the inner radial boundary ($\partial_x n_0 = \partial_x n = 0$) which means that there is no diffusive transport from the core into the edge region and vice versa. At the outer radial boundary the density is set to a typical value, $n_0 = \langle n \rangle = 0.5 \cdot 10^{19}$ m^{-3}. The remaining boundary conditions for both the local and non-local ATTEMPT simulations are those used for the statistically stationary benchmark cases (paragraph 7.2).

To test the multiscale system thoroughly its coupling input parameters N_x^{1D}, d_1, d_2, and β_{D} are varied systematically. By increasing the number N_x^{1D} of 1D code cells the updating length Δr_{up} is decreased. The limit parameter d_1 is used in the 1D code simulations to decide if a new set of local ATTEMPT simulations is started, see point

coupling parameters		**mesoscale local ATTEMPT**		**macroscale 1D code**	
R_0	3.0 m	N_s^{A}	16	N_x^{1D}	6 (L) or 9 (H)
a_0	1.5 m	N_x^{A}	64	Δx_s	1.10 (L) or 0.73 cm (H)
B_0	3 T	N_y^{A}	256	Δt_s	10^{-7} s
q_0	3	N_{f}	18	$N_t^{\mathrm{1D,ii}}$	100
$\hat{s}$	2	δt_s	$1.02 \cdot 10^{-8}$ s	Δt_{run}	10^{-5} s
T_{0e}	100 eV	δx_s	$1\,\rho_s$		
n_0	$4 \cdot 10^{19}$ m^{-3}	δy_s	$1.33\,\rho_s$		
ρ_s	0.51 mm	$L_\perp$	5 cm		
c_s	$9.79 \cdot 10^4$ m s^{-1}	$\partial_x n_{\mathrm{max}}$	-0.5		
x_{sim}	6.5 cm	N_k^{max}	15		
t_{sim}	7 ms	$N_t^{\mathrm{A,ii}}$	5 000		
		δt_{run}	$5.1 \cdot 10^{-5}$ s		
		a_1	0.5		
		a_2	1/7		
		a_3	0.15		
		a_t	1/40		

Table 7.4.: Parameters of the coupled code cases. A 1D code cell number N_x^{1D} of 6 refers to the L cases (low resolution), while $N_x^{\mathrm{1D}} = 9$ corresponds to the H cases (high resolution).

(L) in fig. 7.2. By decreasing it the updating time Δt_{up} is effectively decreased. The limit parameter d_2 determines whether a previously determined flux $\langle\widetilde{\Gamma}\rangle$ is re-used or not, see point (B) in fig. 7.2. In that way, the coupled code system's sequential part can be augmented or reduced. The parameter β_{D} denotes the part of the flux $\langle\widetilde{\Gamma}\rangle$ which is represented by a diffusive model while for the remaining part, a convective model is used, see the definition of the macroscale transport model in eq. (7.4). This means that by varying N_x^{1D}, d_1, d_2, and β_{D}, one can change Δr_{up}, Δt_{up}, the sequential part of the coupling procedure, and the macroscale transport model.

The case names and the parameter sets are given in table 7.5. The letters L and H refer to the resolution in x direction (low: $N_x^{\mathrm{1D}} = 6$, and high: $N_x^{\mathrm{1D}} = 9$), while the limit parameters d_1 and d_2 decrease from case 1 to case 3, the latter being the 'strictest' one with lowest d_1 and d_2.

As a measure for the accuracy of the multiscale simulations the errors $\eta(n)$ and $\eta(\Gamma)$ are introduced which are defined in the same manner as the error $\eta_{\mathrm{st}}(\Gamma)$, eq. (7.27), that was used for the statistically stationary cases in paragraph 7.2. The errors are measured in percent:

$$\eta(\Gamma) \;\equiv\; 100 \cdot \left\langle \frac{|\Gamma_0(t) - \langle\Gamma\rangle(t)|}{\max\left\{|\langle\Gamma\rangle(t)|, \langle\Gamma\rangle_{V,t_{\mathrm{sim}}}\right\}} \right\rangle_{t_{\mathrm{sim}}}, \tag{7.28}$$

case	**L.1**	**L.2**	**L.3**	**H.1**	**H.2**	**H.3**
$N_x^{1\text{D}}$ ($\sim 1/\Delta x_{\text{up}}$)	6	6	6	9	9	9
d_1 ($\sim \Delta t_{\text{up}}$)	0.25	0.10	0.05	0.25	0.10	0.05
d_2 ($\sim$ sequential part)	0.1	0.05	0.025	0.1	0.05	0.025

Table 7.5.: Parameters of the coupled code cases. For each of the shown cases, β_{D} takes the values of 0.25, 0.5, 0.75 and 1.

$$\eta(n) \equiv 100 \cdot \left\langle \frac{|n_0(t) - \langle n\rangle(t)|}{\max\left\{|\langle n\rangle(t)|, \langle n\rangle_{V,t_{\text{sim}}}\right\}} \right\rangle_{t_{\text{sim}}} . \qquad (7.29)$$

The maximum function in the denominator of the ratio in eq. (7.28), employing the flux average over the whole simulation domain and simulated time, is introduced to prevent that small deviations of Γ_0 from $\langle\Gamma\rangle$ at small values of $\langle\Gamma\rangle$ have a disproportionately strong influence on $\eta(\Gamma)$. The same is true for the maximum function used for $\eta(n)$, see eq. (7.29). The time interval used for calculating $\langle n\rangle$ and $\langle\Gamma\rangle$ is $\delta t^*_{\text{av}} = 10^{-4}$ s.

7.3.2. Agreement of the coupled code simulations with the reference simulation

In fig. 7.10, first and second row, radial profiles and time traces of n_0, Γ_0 (solid lines), and $\langle n\rangle$, $\langle\Gamma\rangle$ (dotted lines) are shown for the case L.1 with $\beta_{\text{D}} = 0.25$ and for case H.3 with $\beta_{\text{D}} = 1$ for times $t = 0.5$ ms (black), $t = 3.5$ ms (red), and $t = 6.5$ ms (green) to provide a first insight into the results of the coupled code system. First, consider the density profiles (fig. 7.10, left column). Despite the fact that for both cases significantly different parameters $N_x^{1\text{D}}$, d_1, d_2, and β_{D} were used, the agreement between the coupled code results and the non-local ATTEMPT simulation is satisfactory for the density, the general trend of the dynamics being reproduced in both cases. This is also underlined by the time traces of n_0 and $\langle n\rangle$ taken at the radial position $x = 4.4$ cm, shown in fig. 7.10, third row, left. Except for the offset of $\approx 15\%$ of n_0 from $\langle n\rangle$, starting from $t \approx 1$ ms, the time traces have a similar shape for both multiscale simulations and coincide qualitatively with the traces of the reference simulation.

Significantly different profiles between the coupled code simulations and the reference simulation can be detected for the fluxes Γ_0 and $\langle\Gamma\rangle$, which are shown fig. 7.10, right column. For the case L.1, $\beta_{\text{D}} = 0.25$, Γ_0 has a spatially strongly varying profile, partially deviating even more than 100% from the reference value $\langle\Gamma\rangle$. This error is much smaller for case H.3, $\beta_{\text{D}} = 1$, as it can be best seen for the profile for $t = 0.5$ ms. The disparate performance of the two cases is also reflected by the time traces

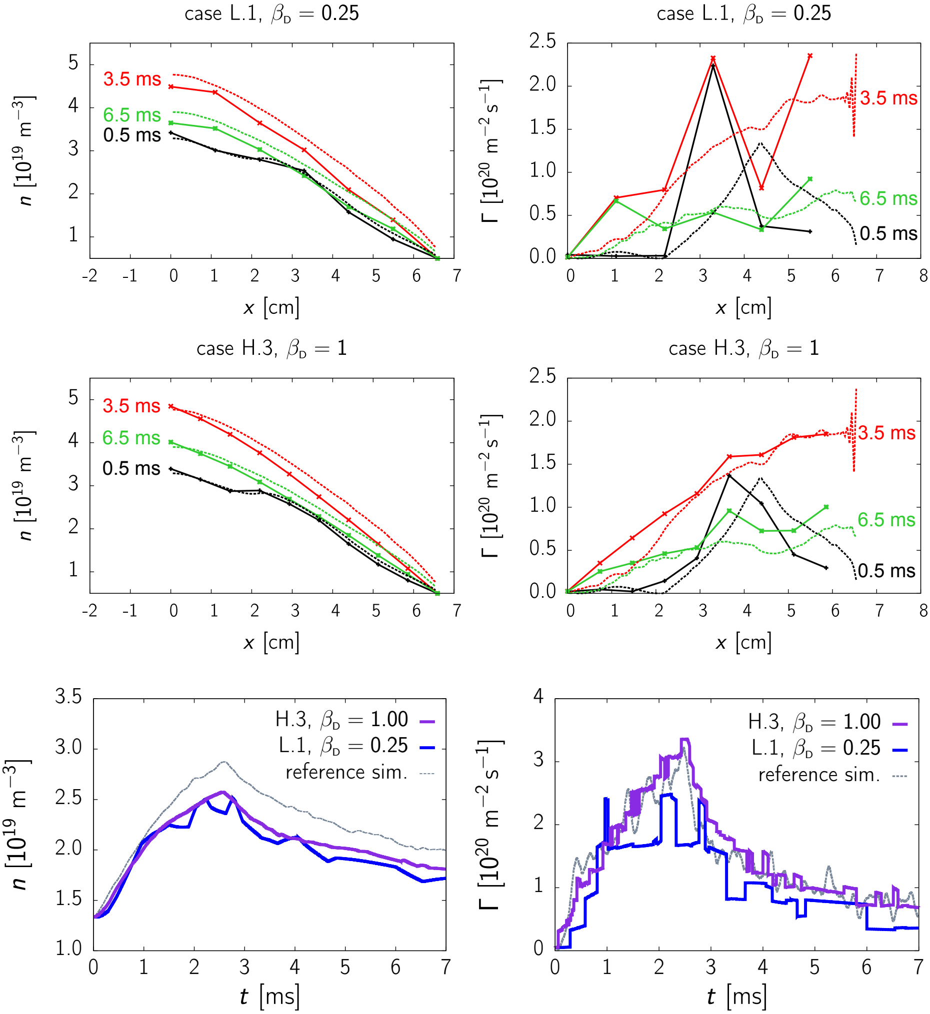

Figure 7.10.: Comparison of the coupled code simulations with the reference simulations. **First and second row:** Radial profiles of the densities n_0 (left column) and the fluxes Γ_0 (right column) of the coupled code simulations L.1, $\beta_D = 0.25$, and H.3, $\beta_D = 1$ (continuous lines with points) and the profiles of $\langle n \rangle$ and $\langle \Gamma \rangle$ of the reference simulation (dashed lines). **Third row:** Time traces of the densities n_0 and the fluxes Γ_0 at position $x = 4.4$ cm and the time traces of the reference simulation.

of Γ_0 and $\langle \Gamma \rangle$ at the radial position $x = 4.4$ cm, shown in fig. 7.10, third row, right.

Whereas for H.3, $\beta_{\mathrm{D}} = 1$, fluctuations of Γ_0 around the reference value (gray line) are small, the flux of the case L.1, $\beta_{\mathrm{D}} = 0.25$, generally underestimates the results of the reference simulation.

This first analysis with the naked eye should be complemented by a closer look at the errors $\eta(n)$ and $\eta(\Gamma)$, shown in fig. 7.11. The differentiation regarding the time intervals, source on, source off, and the entire simulated time, is chosen since the evolution time $\tau_{\mathrm{D}}(\alpha_0) \approx 1$ ms of the macroscale profile while the source is on is about three times as long as for the time interval where the source is switched off ($\tau_{\mathrm{D}}(\alpha_0) \sim 3$ ms), as it can be observed in the time traces of $\langle n \rangle$ and $\langle \Gamma \rangle$ shown in fig. 7.10, third row. This influences how pronounced the scale separation between the mesoscale and macroscale dynamics is and therefore can be expected to have an effect on the errors $\eta(n)$ and $\eta(\Gamma)$.
For $\eta(n)$, fig. 7.11, left column, three trends can be identified. Firstly, $\eta(n)$ is lower while the source is switched on than while it is switched off. This can be accounted for by the offset of the densities n_0 and $\langle n \rangle$ for times $t \gtrsim 1$ ms. However, the difference regarding $\eta(n)$ for both phases is with 3 to 4 percentage points rather small. Secondly, the error for the entire simulated time slightly decreases for decreasing values of the limit parameters d_1 and d_2, i.e. increasing case number. This means that by decreasing Δt_{up} (decreasing d_1) and forcing the coupled code system into a rather concurrent procedure (decreasing d_2), the agreement between n_0 and $\langle n \rangle$ is improved. Thirdly, for the L cases $\eta(n)$ shows the tendency to decrease the higher β_{D}, i.e. the higher the diffusive part of the macroscale transport model. However, the overall agreement of n_0 with $\langle n \rangle$ is rather good for all simulations, the error $\eta(n)$ being in the range between 4 and 6.5%.

Significantly larger errors and a larger error variation between the different cases are found for the flux, see fig. 7.11, right column. Here, the values of $\eta(\Gamma)$ for the entire simulated time vary between $\eta(\Gamma) \approx 18.9\%$ (H.3, $\beta_{\mathrm{D}} = 1$) which is comparable to the errors $\eta_{\mathrm{st}} \approx 14\%$ found for the comparison of fluxes in the statistically stationary state (see paragraph 7.2), and $\eta(\Gamma) \approx 40.7\%$ (H.1, $\beta_{\mathrm{D}} = 0.25$).
The first trend that was mentioned above for $\eta(n)$ – better agreement between n_0 and $\langle n \rangle$ while the source is on – cannot be found for $\eta(\Gamma)$. It is rather the other way around, with smaller $\eta(\Gamma)$ for the time interval with the source switched off. This corresponds to the theoretical considerations that the coupled code system produces more accurate results the more disparate the dynamics of the mesoscale and the macroscale are. Assuming that the typical evolution times on the mesoscale are the same for both time intervals the scale separation is more pronounced while the source is switched off.
The other two trends that can be deduced for $\eta(n)$ – decreasing error with decreasing limit parameters d_1 and d_2 and increasing number of N_x^{1D}, and decreasing error with increasing β_{D} – are even more pronounced for $\eta(\Gamma)$. The latter is especially visible for the case H.3 where $\eta(\Gamma)$ for the entire simulated time increases from 18.9% to 34.8%

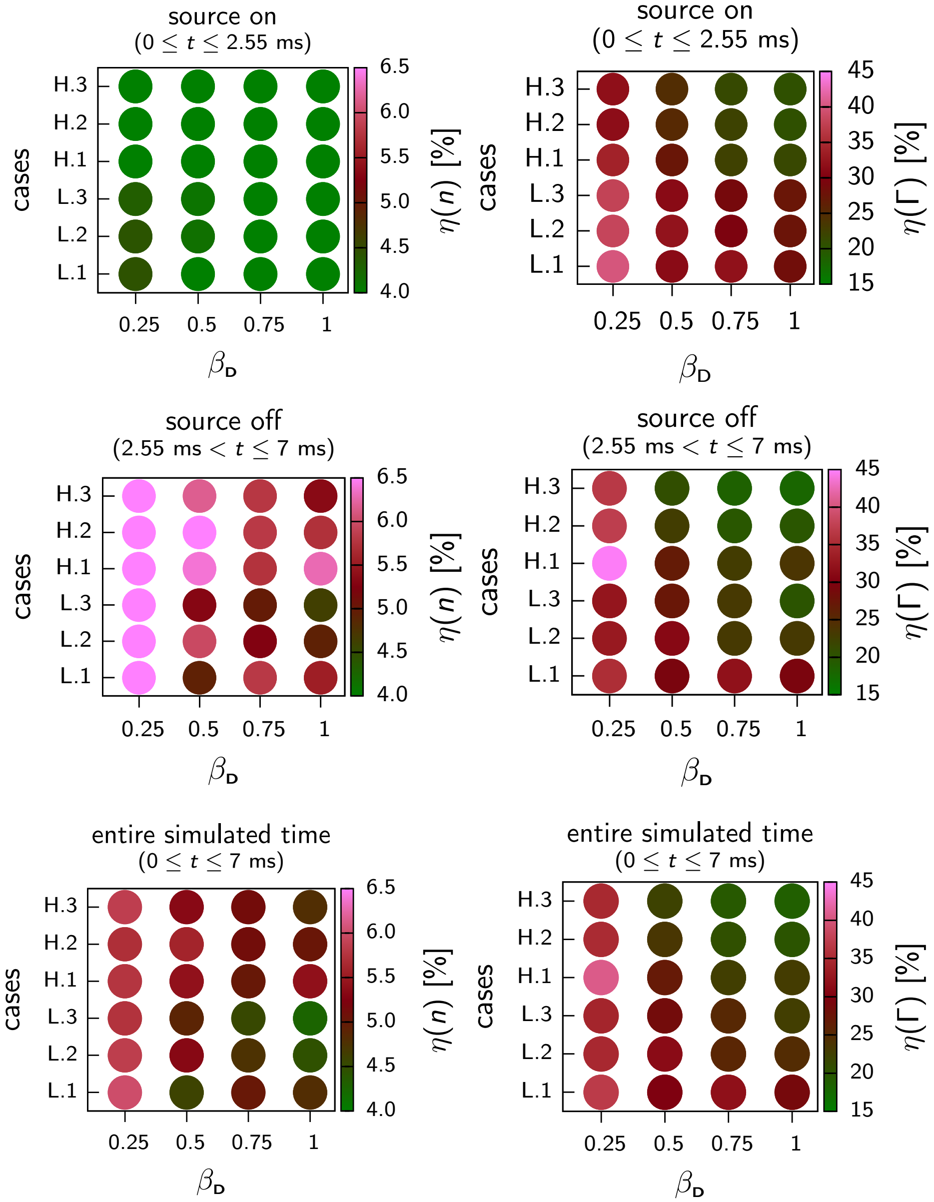

Figure 7.11.: Errors $\eta(n)$ (**left column**) and $\eta(\Gamma)$ (**right column**) for the time interval with the source switched off (first row, 0 ms $\leq t \leq$ 2.55 ms), and switched off (second row, 2.55 ms $< t \leq t_{\mathrm{sim}} =$ 7 ms), and for both intervals together (third row, 0 ms $\leq t \leq$ 7 ms).

while β_{D} decreases from 1 to 0.25, i.e. the macroscale transport model becomes more diffusive. Lowering the limit parameters d_1 and d_2 and increasing $N_x^{1\mathrm{D}}$, i.e. moving upwards in y direction in the single plots, also shows the clear tendency to decrease the $\eta(\Gamma)$. Take for instance the cases with $\beta_{\mathrm{D}} = 1$ and the entire simulated time where $\eta(\Gamma)$ decreases from 28.9% (L.1) to 18.9% (H.3). In comparison, the associated $\eta(n)$ changes only slightly, the maximum $\eta(n)$ being 5.4% (H.1) and the minimum 4.3% (H.3). The only outlier regarding this trend for $\eta(\Gamma)$ is the case H.1, $\beta_{\mathrm{D}} = 0.25$, where for the interval with the source off $\eta(\Gamma) = 44.7\%$.

The rather good agreement between n_0 and $\langle n\rangle$ ($\eta(n)$ around 5%) for all cases and all β_{D} while at the same time $\eta(\Gamma)$ varies from $\eta(\Gamma) = 18.9\%$ to $\eta(\Gamma) = 40.7\%$ has two explanations. The first one is that temporal fluctuations of Γ_0 around an average value close to the reference value $\langle\Gamma\rangle$ lead to a high error $\eta(\Gamma)$. However, the frequency of these fluctuations is so high that only their time average affects the density evolution. This time average is close to the correct time average. The second reason is that the divergence term $\partial_x\Gamma_0$, appearing in the macroscale evolution equation (7.3), which might be underestimated by the coupled code system at one spatial position is compensated by an overestimated divergence term at a neighboring cell and vice versa.

For the highest occurring velocities shown in fig. 7.12, $v_c \approx 7\ \mathrm{m\,s^{-1}}$, and a characteristic length λ_{D} of one centimeter, a characteristic transport time $\tau(v_c)$ can be determined by $\tau(v_c) = \lambda_{\mathrm{D}}/v_c \approx 1.4$ ms. On the other hand, the time intervals where v_c reaches these high values ($t \approx 3$ ms) have a length of below 0.1 ms, thus are an order of magnitude smaller than $\tau(v_c)$. Therefore, they are too short for the high convective v_c to transport a significant amount of particles over typical spatial scales of the system which are of the order of 1 cm. This consideration also holds if one considers an average $v_c \approx 3$ m s^{-1} which yields for $\tau_{\mathrm{D}}(v_c) \approx 3$ ms, still being one order of magnitude larger than the interval length of the fluctuations which is around 0.3 ms. This difference regarding the transport times and a significantly smaller interval length of the fluctuations of v_c (and also Γ_0) are responsible for the effect that a large flux error $\eta(\Gamma)$ is not accompanied by a large error $\eta(n)$.

The second reason mentioned above can be elucidated by having a look at the divergence of the flux, $\partial_x\Gamma_0$, which acts like a source term in the density continuity equation (7.3). This term mediates the effect of the averaged mesoscale flux on the macroscale profile evolution. One notes, looking at fig. 7.12, bottom, that even though $\partial_x\Gamma_0$ (see the dashed violet lines) might vary notably from the reference value at certain radial positions and instances (the reference being here given by the thick blue line of case H.3, $\beta_{\mathrm{D}} = 1$, having the minimal flux error $\eta(\Gamma)$) its spatial and temporal average does not: both the thick violet line and the thick blue line almost coincide, especially for $t < 4$ ms.

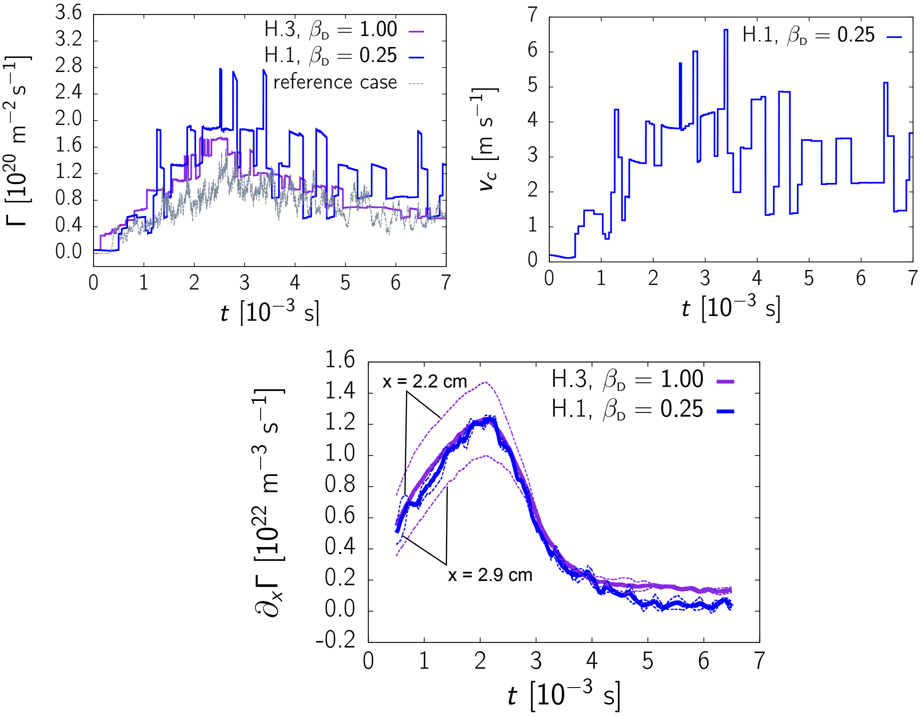

Figure 7.12.: **Left:** Time traces of the fluxes Γ_0 for two different coupled code simulations (blue and violet), and the reference flux $\langle\Gamma\rangle$ of the non-local simulation (gray) at position $x = 2.9$ cm. **Right:** Time trace of v_c of H.1, $\beta_D = 0.25$. **Bottom:** Time averaged time traces of $\partial_x\Gamma$, corresponding to the simulations shown in the upper left plot. The thick lines correspond to the average over both spatial positions $x = 2.2$ cm and $x = 2.9$ cm, for which the time traces are given by the dotted lines. The averaging time was 10^{-3} s.

7.3.3. Performance of the procedure to check for the average mesoscale flux

Before further analyzing the transport modeling, the performance of the coupling procedure regarding the determination of the averaged mesoscale fluxes $\langle\widetilde{\Gamma}\rangle$ is evaluated. Once it has been decided by the coupling procedure that a new set of transport coefficients has to be determined for the 1D code (fig. 7.2, (S)), there are four different possibilities of how $\langle\widetilde{\Gamma}\rangle^{i,l}$ for global iteration i and 1D code cell l is determined. The choice of these options and the percentage they constitute regarding the total number of fluxes that have to be determined for the entire simulated time are as follows. The values below refer to the average over all cases and values β_D since their variations for the different multiscale simulations is rather low which is reflected by the small errors of the values:

- gradient $\partial_x n_0^{i,l}$ above the maximum value ($\partial_x n_0 > \partial_x n_{\max}$), minimal flux used (fig. 7.2, (A)):
  29.8% ± 5.8%,
- gradient $\partial_x n_0^{i,l}$ comparable to previous simulation ($r_2 < d_2$), flux re-used (fig. 7.2, (C)):
  67.3% ± 6.6%,
- local ATTEMPT simulation started:
  2.8% ± 1.7%, subdivided into:
  - statistical stationarity reached (fig. 7.4, (X)):
    2.0% ± 1.2%.
  - statistical stationarity not reached (maximum number $N_k^{\max}$ of internal ATTEMPT iterations reached), flux determined with data from $k_{\max}\delta t_{\mathrm{run}}/3$ to $k_{\max}\delta t_{\mathrm{run}}$ (fig. 7.4, (XIII)):
    0.8% ± 0.6%,

The largest amount of fluxes, 67.3%, is determined by re-using a previously determined value of $\langle\widetilde{\Gamma}\rangle$ from a simulation with a comparable input gradient $\partial_x n_0$; the second largest amount, 29.8%, by using the predetermined minimal flux for input gradients $\partial_x n_0 > \partial_x n_{\max}$. Interestingly, these percentages are almost constant for the different cases and values of β_{D} as it is reflected by the relatively small errors of 6.6% and 5.8%, respectively. One might expect that the relative percentage of cases where a previously determined flux is re-used decreases the lower d_2 which corresponds to a higher case number. This effect is apparently compensated by the fact that the number of pairs $(\partial_x n_0, \langle\widetilde{\Gamma}\rangle)$ that can be used for comparison at (B) in fig. 7.2 also increases for higher case numbers.

It is noticeable that the percentage of local ATTEMPT simulations being started is relatively low. Of these runs, roughly one third (around 29.8%, or 0.8% in total) are stopped because the maximum number of internal ATTEMPT iterations $N_k^{\max}$ is reached and the criteria for statistical stationarity and/or sufficient data for averaging $\langle\widetilde{\Gamma}\rangle$ have not been met yet. It is obviously desirable to reduce this percentage: for the respective runs $\langle\widetilde{\Gamma}\rangle$ might deviate from the statistically stationary flux associated with the input value of $\partial_x n_0^{i,l}$. A reduction of this percentage can probably be achieved by increasing the maximum number $N_k^{\max}$ of internal ATTEMPT iterations. However, this also increases the average runtime $t_c(\widetilde{n})$ of the local ATTEMPT simulations and therefore reduces the time savings of the coupled code system. A better way of improving the performance might therefore be the reassessment of the choice of the parameters a_2, a_3, and a_t which are used in the procedure to check for the averaged mesoscale flux which eventually determine when the averaged mesoscale flux is calculated (compare fig. 7.4).

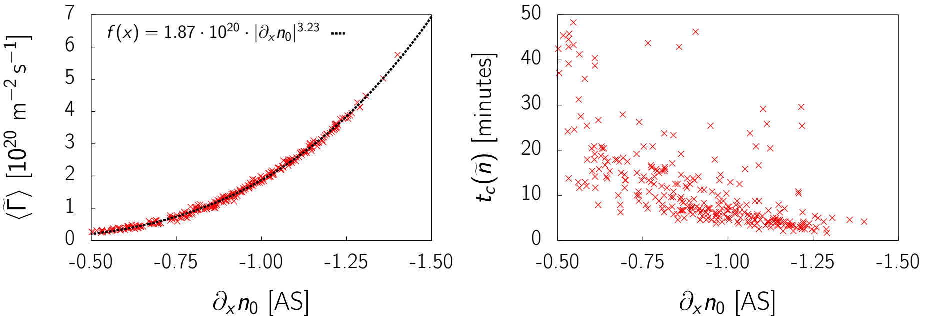

Figure 7.13.: **Left:** Relation between the input gradient $\partial_x n_0$ of the local ATTEMPT simulations and the averaged flux $\langle\widetilde{\Gamma}\rangle$ of the statistically stationary state with the fitted function $f(x)$ given by the black dotted line. **Right:** Relation between the input gradient $\partial_x n_0$ of the local ATTEMPT simulations and the runtime $t_c(\widetilde{n})$ of the simulation on one processor.

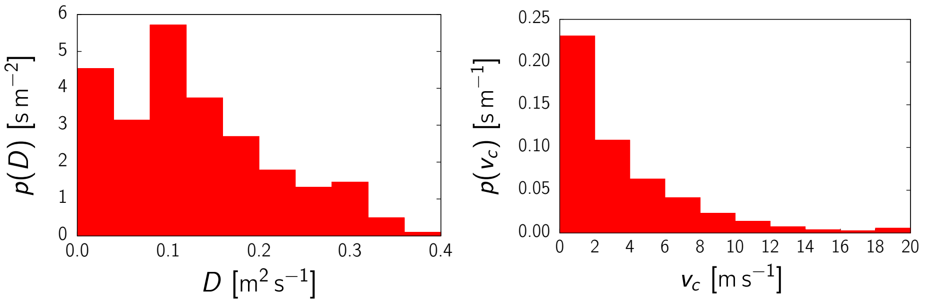

Figure 7.14.: Histogram of D (**left**) and v_c (**right**), compiled with the data from runs H.X with X = 1,2,3 and $\beta_{\mathrm{D}} = 1$ for D and $\beta_{\mathrm{D}} = 0.25$ for v_c, respectively.

To complement the performance analysis it is important to check if the procedure to determine the averaged mesoscale flux $\langle\widetilde{\Gamma}\rangle$ for a given input gradient $\partial_x n_0$ produces consistent results. This means that for slightly varying gradients $\partial_x n_0$ a somewhat similar averaged mesoscale flux is to be expected. In fig. 7.13, left, the flux $\langle\widetilde{\Gamma}\rangle$ is plotted against the input gradient $\partial_x n_0$, using the data from all cases and values of β_{D}. The minimal spreading of the values around the fitted function $f(\partial_x n_0) = 1.87 \cdot 10^{20} \cdot |\partial_x n_0|^{3.23}$ illustrates that the procedure to determine the averaged mesoscale flux works properly. Note that also the data of runs where the maximum number $N_k^{\max}$ of internal ATTEMPT iterations was reached is included in fig. 7.13, left. It fits to the results of the local ATTEMPT runs which were finished

before $N_k^{\max}$ was reached, confirming that the estimate for the averaged mesoscale flux, obtained by averaging over two thirds of the time trace of $\bar{\Gamma}(t)$, is rather good (see fig. 7.4, (XIII)).
Two additional conclusions can be drawn from the data shown in fig. 7.13, left: Firstly, the relation between $\langle\widetilde{\Gamma}\rangle$ and $\partial_x n_0$ is not linear but approximately cubic with an exponent of 3.23. This means that even though the diffusive macroscale model leads to a greater accuracy of the coupled code results than a rather convective one, the averaged mesoscale flux as given by the employed local drift fluid model is not diffusive. In future studies it would be interesting to investigate in how far the exponent of $|\partial_x n_0|$ depends on the other input parameters of the local mesoscale model, such as the electron temperature or the background density, which are kept constant here.
Secondly, the vanishing gradient of the function $\langle\widetilde{\Gamma}\rangle(\partial_x n_0)$ around $\partial_x n_0 \approx -0.6$ justifies the use of a constant minimal flux for all input gradients $\partial_x n_0$ which are larger than $\partial_x n_{\max}$. Thus, introduction of an appropriate $\partial_x n_{\max}$ means additional time savings while having minimal losses in accuracy. The value of $\partial_x n_0^{\max} = -0.5$ chosen for the coupled code simulations here seems adequate.

The relation between $\partial_x n_0$ and the runtime $t_c(\tilde{n})$ of the local ATTEMPT simulation is shown in fig. 7.13, right. Even though the relation between the two quantities is not as clear as for $\partial_x n_0$ and $\langle\widetilde{\Gamma}\rangle$ one can find the tendency that the time $t_c(\tilde{n})$ increases as the gradient $\partial_x n_0$ increases. For large $\partial_x n_0$ the characteristic time $\tau_{\mathrm{D}}(\bar{\Gamma})$ can become significantly longer than for smaller $\partial_x n_0$. This is also illustrated by the contrasting time traces of $\bar{\Gamma}$ shown in fig. 7.3, top left and bottom right. Larger temporal structures, as reflected by the trace shown in fig. 7.3, top left, result in longer averaging times δt_{av} and therefore longer runtimes $t_c(\tilde{n})$. While the flattening of the function $\langle\widetilde{\Gamma}\rangle(\partial_x n_0)$ towards larger gradients $\partial_x n_0$ allows for using an appropriate minimal flux without sacrificing the overall accuracy, one can especially avoid the ATTEMPT simulations which have the longest runtimes by this procedure, i.e. make the coupled code system more efficient.

Next, the transport as determined by the local mesoscale simulations is discussed. To give an overview over the transport coefficients used, histograms of the diffusion coefficient D for the case H.3, $\beta_{\mathrm{D}} = 1$, and for the convective velocity v_c for H.3, $\beta_{\mathrm{D}} = 0.25$, are shown in fig. 7.14. The typical D is around 0.15 $\mathrm{m}^2\ \mathrm{s}^{-1}$ and of the same magnitude as for comparable studies [41, 25]. Note that the convective velocities v_c are significantly smaller than the accessible values of v_{Ex} (compare the PDF of v_{Ex} in fig. 7.7), resulting from the fact that only the *averaged* transport is modeled by v_c.

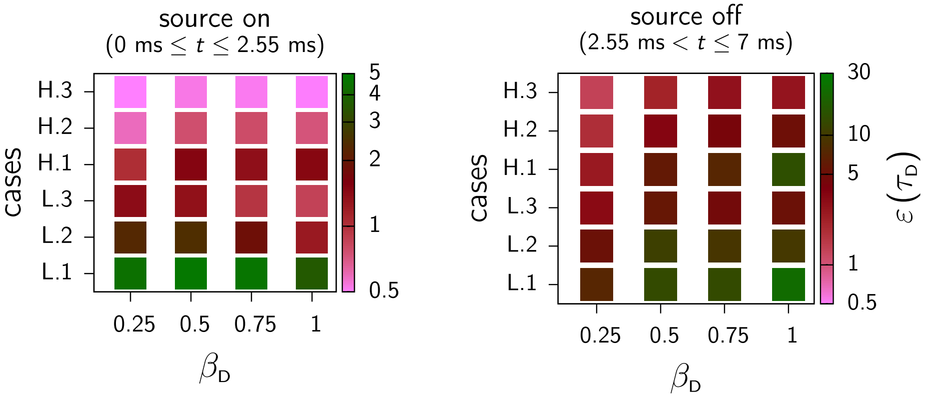

Figure 7.15.: Ratio $\varepsilon(\tau_{\mathrm{D}}) = \tau_{\mathrm{D}}(\alpha_0)/\delta t_{\mathrm{st}}$ for the two time intervals with the source switched on (**left**) and the source switched off (**right**). The time $\langle\tau_{\mathrm{f}}\rangle_{\mathrm{ms}} = 3.51 \cdot 10^{-5}\ s$ is valid for all cases.

7.3.4. Time savings of the coupled code system

In a first step, the potential time savings of the system can be evaluated by analyzing the quantity $\varepsilon(\tau_{\mathrm{D}})$ [37],

$$\varepsilon(\tau_{\mathrm{D}}) \equiv \frac{\tau_{\mathrm{D}}(\alpha_0)}{\delta t_{\mathrm{st}}} , \tag{7.30}$$

which is given by the ratio of the characteristic time $\tau_{\mathrm{D}}(\alpha_0)$ of the macroscale profile evolution and the time δt_{st} the local mesoscale system needs to reach the statistically stationary state. Note that $\varepsilon(\tau_{\mathrm{D}})$ is a parameter determined by the underlying physics of the system. In contrast, the speedup factor $\varepsilon(t_c)$ which was introduced in paragraph 2.3 (compare eq. (2.74)) is a technical parameter, associated to a specific realization of a coupled code system. It is analyzed further down. If $\varepsilon(\tau_{\mathrm{D}})$ is smaller than one, usually also a speedup factor $\varepsilon(t_c)$ smaller than one can be achieved, meaning that the coupled code system will result in time savings as compared to simulations of the full system.

To obtain $\varepsilon(\tau_{\mathrm{D}})$ for the different multiscale simulations two approximations are made: $\tau_{\mathrm{D}}(\alpha_0)$ is approximated by the updating time Δt_{up} used in the 1D code, and δt_{st} is approximated by τ_{f}, the estimate of the correlation time which was introduced in paragraph 7.1.4 to check for the flux $\langle\widetilde{\Gamma}\rangle$. Therefore

$$\varepsilon(\tau_{\mathrm{D}}) \approx \frac{\langle\Delta t_{\mathrm{up}}\rangle_t}{\langle\tau_{\mathrm{f}}\rangle_{\mathrm{ms}}} , \tag{7.31}$$

where the average over the time $\langle ... \rangle_t$ corresponds to the interval of interest, either that with the source switched on or that with the source switched off. The average $\langle ... \rangle_{\mathrm{ms}}$ corresponds to the average over all multiscale simulations. Here, it is not distinguished between the time interval of interest like for $\langle \Delta t_{\mathrm{up}} \rangle_t$ because of the re-use of previously determined fluxes: if τ_{f} were to be determined for each interval separately this re-using (i.e. the sequential part of the coupling model) would have to be stopped. Hence, $\tau_{\mathrm{f}} = 3.5 \cdot 10^{-5} \pm 1.7 \cdot 10^{-5}$ s for all coupled code simulations and time intervals.

In fig. (7.15), $\varepsilon(\tau_{\mathrm{D}})$ is shown separately both for the time interval with the source being switched on (left) and off (right). Note that by increasing the case number, e.g. going from L.1 over L.2 to L.3, Δt_{up} and therefore also $\varepsilon(\tau_{\mathrm{D}})$ is effectively reduced. This is due to the decrease of the limit parameter d_1 which accordingly decreases from 0.25 over 0.1 to 0.05. Eventually, this variation of $\varepsilon(\tau_{\mathrm{D}})$ can be related to the question which level of change of the macroscale profiles corresponds best to the characteristic time of the dynamics: $d_1 = 25$, 10 or 5%. This also relates to the fact that even though at the beginning of this paragraph it was stated that $\varepsilon(\tau_{\mathrm{D}})$ is a purely *physical* quantity which should not be influenced by technical parameters like Δt_{up} or β_{D}, the one finds that the contrary is the case. Ultimately this is due to the approximations made in eq. (7.31).
As fig. (7.15) illustrates, the equilibration time δt_{st} is smaller than $\tau_{\mathrm{D}}(\alpha_0)$ for almost all cases, values of β_{D} and the two time intervals, meaning that $\varepsilon(\tau_{\mathrm{D}})$ is larger than one except for the cases cases H.2 and H.3 while the source is switched on. However, $\varepsilon(\tau_{\mathrm{D}})$ is significantly larger for the time interval with the source switched off, reaching values of $\varepsilon(\tau_{\mathrm{D}})$ of up to 25. For the interval with the source switched on, the maximum $\varepsilon(\tau_{\mathrm{D}})$ is around 5. This coincides with the observation that also the macroscale evolution of $\langle n \rangle$ and $\langle \Gamma \rangle$ of the non-local ATTEMPT simulation takes place on a larger time scale while the source is switched off than while the source is switched on. Increasing the number of macroscale cells (i.e. the transition from L to H and from $N_x^{1\mathrm{D}} = 6$ to $N_x^{1\mathrm{D}} = 9$) leads to a decrease of $\varepsilon(\tau_{\mathrm{D}})$. This can be explained by the fact that the more cells are taken into account on the macroscale, the more possibilities there are for the deviation r_1 to exceed the limit parameter d_1.

The investigation of this set of multiscale cases is concluded by an analysis of the time savings of the multiscale simulations compared to the reference simulation. Consider the speedup factor $\varepsilon(t_c)$ which is given by eq. (2.74) and approximated here by neglecting the runtime $t_c(n_0)$ of the macroscale part:

$$\varepsilon(t_c) \approx \frac{t_c(n)}{t_c(\tilde{n})} . \tag{7.32}$$

Here, $t_c(n)$ is the computational time needed by the reference non-local ATTEMPT simulation to determine the evolution of $\langle n \rangle$, and $t_c(\tilde{n})$ is the corresponding computational time of the mesoscale part of the multiscale simulation. Both times refer to

the same interval of simulated time t_{sim} and are understood as the computing time on one processor. The quantity $\varepsilon(t_c)$ can be read as 'the coupled code simulation is $\varepsilon(t_c)$ times faster than the non-local simulation'. In contrast to $\varepsilon(\tau_{\mathrm{D}})$, $\varepsilon(t_c)$ takes into account both the equilibration time δt_{st} and the averaging time δt_{av}.
While $t_c(n)$ is easily accessible from the non-local ATTEMPT simulation, an exact value of $t_c(\tilde{n})$ is not yet available from the coupled code simulations. This is due to the fact that up to now the set of local ATTEMPT simulations is carried out in sequential order once it is decided that the transport coefficients in the 1D code have to be updated. Obviously, the time savings of the coupled code system can be increased if the local ATTEMPT simulations for different 1D code cells are distributed to different groups of processors and done in parallel. This feature is to be included in the next version of the coupled code script. However, to estimate the potential time savings of the coupled code system taking into account this distribution of local ATTEMPT simulations the quantity $t_c(\tilde{n})$ is approximated by

$$t_c(\tilde{n}) \;=\; \frac{r_{\mathrm{A}}\langle t_c(\tilde{n})\rangle_{\mathrm{ms}}}{\langle \Delta t_{\mathrm{up}}\rangle_t} \quad \text{with} \quad r_{\mathrm{A}} \;=\; \frac{\begin{array}{c}\text{number of global iterations}\\ \text{where at least for one}\\ \text{1D code cell a local ATTEMPT}\\ \text{simulation is carried out}\end{array}}{\text{total number of global iterations}}\;. \tag{7.33}$$

The components of $t_c(\tilde{n})$ are to be understood as follows. The average runtime of one local ATTEMPT simulation is given by $\langle t_c(\tilde{n})\rangle_{\mathrm{ms}}$. It is averaged over all multiscale simulation and is multiplied by the factor r_{A} to obtain the average runtime of one local ATTEMPT code *per global iteration*: recall that for some global iterations no local ATTEMPT simulations are started since previously determined values of $\langle\widetilde{\Gamma}\rangle$ are used, for instance. The factor r_{A} depends on the coupling input parameters and varies between 0.056 for the case H.1, $\beta_{\mathrm{D}} = 0.25$, and 0.299 for L.3, $\beta_{\mathrm{D}} = 0.5$, with an average for all coupled code simulations of $\langle r_{\mathrm{A}}\rangle_{\mathrm{ms}} = 0.174 \pm 0.073$.
The simulated time in the 1D code per global iteration, on the other hand, is given by the updating time $\langle\Delta t_{\mathrm{up}}\rangle_t$ where the time average refers either to the interval with the source switched on or off or to the entire simulated time. Thus, on average, one can simulate a time span of length $\langle\Delta t_{\mathrm{up}}\rangle_t$ in the 1D code by letting the coupled code system run for a time $r_{\mathrm{A}}\langle t_c(\tilde{n})\rangle_{\mathrm{ms}}$ on a computer. Therefore, the 'unit' of $t_c(\tilde{n})$ is computational time per simulated time.

As it was stated in paragraph 2.3, the time savings of the coupled code system are potentially larger the more disparate the scales of the mesoscale and macroscale dynamics are. This is confirmed by the values of $\varepsilon(t_c)$ which are shown in fig. 7.16, left column. While for the time interval with the source switched on, the maximum $\varepsilon(t_c)$ is 1.78 (L.1, $\beta_{\mathrm{D}} = 0.75$), the value for the interval with the source switched off is $\varepsilon(t_c) = 5.12$, the overall maximum value being $\varepsilon(t_c) = 8.42$ (H.1, $\beta_{\mathrm{D}} = 1$). The difference of $\varepsilon(t_c)$ between the two time intervals is only due to changes in $\langle\Delta t_{\mathrm{up}}\rangle_t$ which is about four times smaller while the source is switched on than while it is

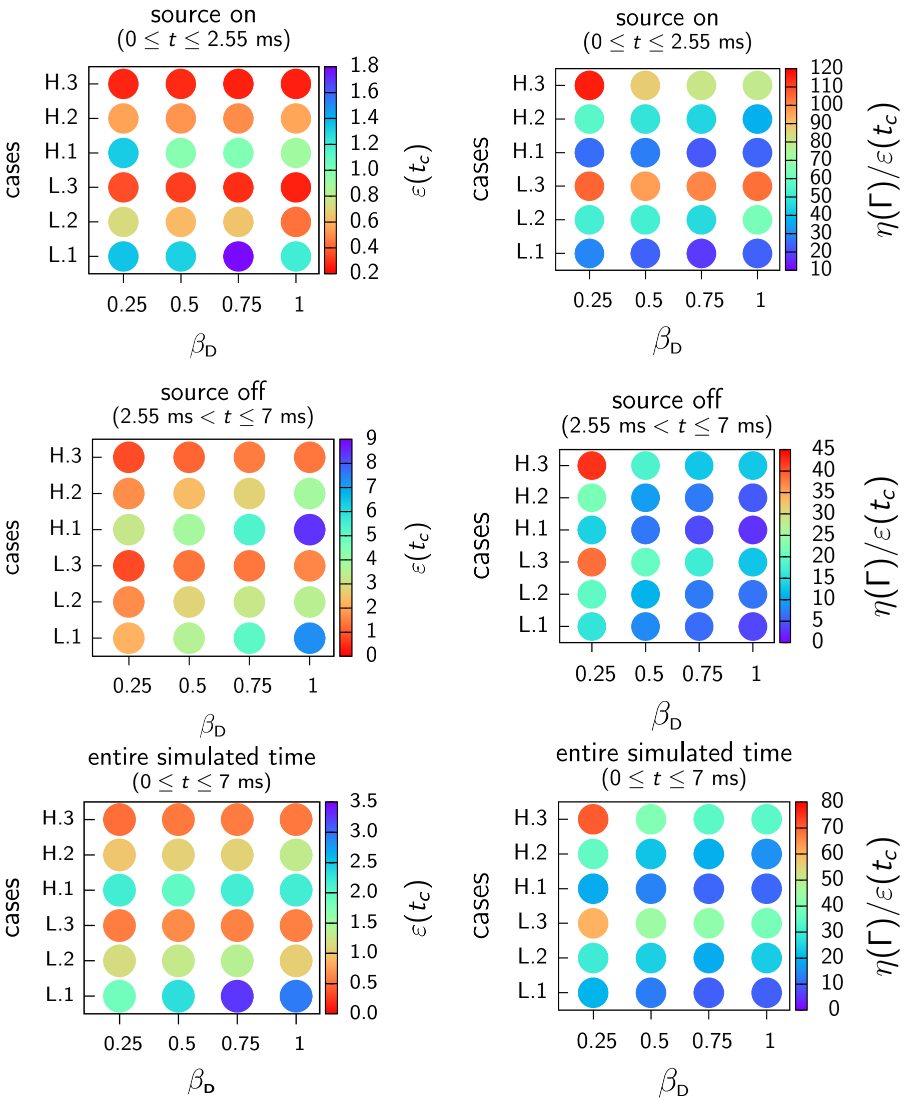

Figure 7.16.: Speedup factor $\varepsilon(t_c)$ (**left column**) and ratio $\eta(\Gamma)/\varepsilon(t_c)$ (**right column**) for the time interval with the source switched off (first row, 0 ms $\leq t \leq$ 2.55 ms) and switched off (second row, 2.55 ms $< t \leq t_{\text{sim}} =$ 7 ms) and for both intervals together (third row, 0 ms $\leq t \leq$ 7 ms).

switched off. The minimal value for the entire simulated time is found for case L.1,

$\beta_{\rm D} = 0.75$, with $\varepsilon(t_c) = 3.26$, meaning that the coupled code simulation is more than three times faster than the reference non-local ATTEMPT simulation.
As one would expect from theoretical considerations the time savings augment the larger the limit parameters d_1 (less frequent updates of transport coefficients) and d_2 (less strict restrictions regarding the re-use previously determined values of $\langle\widetilde{\Gamma}\rangle$). The factor by which $\varepsilon(t_c)$ increases from case L/H.2 to L/H.1 and from L/H.3 to L/H.1 (while keeping $\beta_{\rm D}$ constant) is between 1.3 to 2.8 for the entire simulated time. Increasing the number of macroscale cells from $N_x^{\rm 1D} = 6$ to $N_x^{\rm 1D} = 9$ affects $\varepsilon(t_c)$ little except for the cases L/H.1, with a mostly diffusive macroscale transport model ($\beta_{\rm D} = 1$ and $\beta_{\rm D} = 0.75$), where $\varepsilon(t_c)$ becomes smaller the larger $N_x^{\rm 1D}$.

It was stated above that the radial extent of the simulation domain is chosen rather small with $x_{\rm sim} = 6.5$ cm, while the characteristic length of the profile of $\langle n\rangle$ in radial direction is about one centimeter. Making the transition to an edge region of the order of $x_{\rm sim} \approx 30$ cm, which is realistic for future tokamak devices such as ITER, and assuming that the characteristic lengths scale correspondingly ($\lambda_{\rm D}(\alpha_0) \approx 5$ cm), it would still suffice to consider a radial resolution of the order of $N_x^{\rm 1D} \approx 6$ in the 1D code of the coupled code system, increasing only the step width Δx. Therefore, the computational time of the multiscale simulation would be of the same order as for the cases considered here. If the computational time of the non-local simulation increases linearly with the radial extent $x_{\rm sim}$, keeping the same resolution in all directions, it can be assumed to be about five times higher than the value of $t_c(n)$ used here. Thus, the maximum speedup factor $\varepsilon(t_c)$ would be around a factor 15 (instead of 3) for the whole time interval and about a factor 40 while the source is off[2].

Employing a multiscale model and a coupled code system is, to some extent, a balancing act between accuracy of the results and the possible time savings. To give an insight into how good this balance is realized here, the ratio $\eta(\Gamma)/\varepsilon(t_c)$ is presented in fig. 7.16, right column. Obviously, inaccurate results cannot be compensated by fast simulations, but a comparison between the different cases provides information about how efficient the coupled code system works with different sets of coupling input parameters. The focus here is rather on relative than on absolute values of $\eta(\Gamma)/\varepsilon(t_c)$. The smaller $\eta(\Gamma)/\varepsilon(t_c)$, the better the performance of the coupled code system.
The coupled code system shows the best performance, i.e. lowest values of $\eta(\Gamma)/\varepsilon(t_c) \approx 5$, for the time interval with the source switched off. While the flux error $\eta(\Gamma)$ is only slightly smaller for this interval than for the interval with the source switched on, the potential time savings, expressed by $\varepsilon(t_c)$, are significantly larger. The general tendency that the time savings $\varepsilon(t_c)$ decrease with the case number is not compensated by a decreasing error $\eta(\Gamma)$, leading to larger values of $\eta(\Gamma)/\varepsilon(t_c)$ when

---

[2] In this calculation it is assumed that the CPU time of both the non-local and local ATTEMPT simulation per second of simulated time are equal, i.e. that the calculations of both codes are equally costly.

moving upwards in y direction. The cases L.3 and H.3 with low limit parameters and a mostly convective macroscale transport model strike the eye with the highest value of $\eta(\Gamma)/\varepsilon(t_c)$, lacking accuracy and time savings, while the lowest values of $\eta(\Gamma)/\varepsilon(t_c)$, corresponding to the best performance, are found for L.1 and H.1 with $\beta_{\text{D}} = 0.75, 1$. Hence, a stepwise diffusive macroscale transport model is suited best for the model problem considered. The 'strictness' of the coupling procedure, determined by the parameters d_1 and d_2, has to be kept at a rather low level to ensure sufficient time savings.

7.3.5. Additional studies

To complement the multiscale simulations analyzed in the previous paragraph, four additional coupled code simulations have been carried out. They are based on the case L.1, $\beta_{\text{D}} = 1$, and use the same simulation domain, resolution, and input parameters (see tables 7.4 and 7.5) except for those that are listed in table 7.6.

The coupled code simulation L.1.01 and L.1.02 are employed to investigate how the coupled code system performs if poloidal mode numbers with $m < 54$ are taken into account in the mesoscale simulations. For L.1.01, the minimal m is 27, for L.1.02 it is 12 (plus the mode number $m = 0$, which is present in all cases). The cell width δy_s in the local ATTEMPT code is approximately kept constant so that the number of cells N_y^{A} in y direction is increased from 256 to 512 (L.1.01) and 1024 (L.1.02) cells to cover the entire toroidal domain with less flux tubes, $N_{\text{f}} = 9$ and $N_{\text{f}} = 4$, respectively. The reference non-local ATTEMPT simulations to determine the errors $\eta(n)$ and $\eta(\Gamma)$ are carried out with corresponding N_{f} and N_y^{A}.
The results for $\eta(n)$, $\eta(\Gamma)$, and $\varepsilon(t_c)$ are listed in table 7.6. Both $\eta(n)$ and $\eta(\Gamma)$ decrease the smaller N_{f}. Especially eye-catching is the reduction of $\eta(\Gamma)$ from 28.93% for $N_{\text{f}} = 18$ to 19.51% for $N_{\text{f}} = 4$. These results show that the coupling is also successful for simulations including dynamics with smaller poloidal mode numbers, i.e. larger structures in poloidal direction.
The simulations L.1.03 and L.1.04 focus on a technical detail regarding the check for the averaged flux $\langle\widetilde{\Gamma}\rangle$, see fig. 7.4: here, once it is determined that enough data for averaging is available (fig. 7.4, (VII)), the parameter a_3 determines the 'acceptable' deviation between the two fluxes $\langle\widetilde{\Gamma}\rangle_1$ and $\langle\widetilde{\Gamma}\rangle_2$, being part of the final check if the statistically stationary state has been reached (fig. 7.4, (VII)). The value a_3 was kept constant at 0.15 in the coupled code simulations above and is reduced to 0.1 and 0.05, respectively, to check on its influence on the errors $\eta(n)$ and $\eta(\Gamma)$, and the time savings.
The values listed in table 7.6 show that diminishing a_3 neither changes $\eta(n)$ nor $\eta(\Gamma)$ significantly. The same is true for the speedup factor $\varepsilon(t_c)$ which slightly increases. This seems to be counterintuitive: one would rather expect $\varepsilon(t_c)$ to decrease with decreasing a_3 since the restrictions for the check for $\langle\widetilde{\Gamma}\rangle$ become stricter the lower a_3. However, the average percentage of local ATTEMPT runs reaching the maximum

case	β_D	N_f	N_y^A	a_3	$\eta(n)$	$\eta(\Gamma)$	$\varepsilon(t_c)$
L.1	1	18	256	0.15	4.80%	28.93%	2.94 (5.95)
L.1.01	1	9	512	0.15	4.57%	26.29%	4.57
L.1.02	1	4	1024	0.15	4.52%	19.51%	6.39
L.1.03	1	18	256	0.10	4.89%	28.53%	3.46
L.1.04	1	18	256	0.05	4.78%	27.77%	3.79

Table 7.6.: Parameters of the additional coupled code simulations. The data for the previously discussed case L.1 is shown here again for the sake of completeness. Note that for both L.1.01 and L.1.02 the average runtime of the local ATTEMPT simulations $t_c(\tilde{n})$ used for determining $\varepsilon(t_c)$ is calculated only with the data form the corresponding simulations, while the value used for determining $\varepsilon(t_c)$ of L.1 is the average over all multiscale simulations to obtain a more meaningful reference value, compare eq. (7.33). The value given in brackets in table 7.6, first line, is that obtained by using only the data of the case L.1 to determine $\varepsilon(t_c)$.

internal iteration N_k^max increases from 0.9%, $a_3 = 0.15$, to 1.1% for $a_3 = 0.1$ and to 1.7% for $a_3 = 0.05$. Thus, by decreasing a_3 one should also consider decreasing N_k^max so that the local ATTEMPT simulations can run sufficiently long to find the statistically stationary state.

7.3.6. Summary and discussion of results

The results of the 1D coupled code simulation and its comparison with the benchmark are summarized below.

- The time evolution of the flux surface averaged radial density profile as given by a reference simulation with the non-local ATTEMPT code can be reproduced satisfactorily with an error $\eta(n)$ regarding the density between 4 to 6.5% and an error $\eta(\Gamma)$ regarding the radial particle flux between 19 to 41%. A reduction of the limit parameters d_1 and d_2 increases the accuracy of the results, especially regarding the error of the particle flux. A decrease of d_1 leads to a decrease of the updating time for renewing the transport coefficients in the macroscale 1D code. Reduction of d_2 increases the concurrent part of the multiscale model. The errors $\eta(n)$ and $\eta(\Gamma)$ can be further reduced by increasing the number of cells N_x^1D of the 1D code, being related to decreasing the updating length Δx_up, and increasing the diffusive part β_D of the macroscale transport model. The effect of a variation of d_1, d_2 and N_x^1D on the errors follows theoretical considerations.

- The discrepancy between the relatively large variation of $\eta(\Gamma)$ and the rather small effect on $\eta(n)$ has two possible explanations: Firstly, the flux Γ_0 in the 1D code fluctuates around an average value $\langle\Gamma_0\rangle_t$ close to the reference value $\langle\Gamma\rangle$. This means that while $\eta(\Gamma)$ increases due to the fluctuations, the particle transport due to an overestimated or underestimated flux is limited: the typical transport time that can be associated to the transport coefficients stemming from the local mesoscale simulations is much longer than the time during which these transport coefficients remain unchanged in the 1D code. One finds that an disproportionately high or low flux can only change the profile significantly if it persists for a long enough time. Secondly, while the divergence $\partial_x\Gamma_0$ of the flux may vary significantly for different radial positions the spatial average of $\partial_x n_0$ of the order of two 1D code cells does not. This kind of a self-controlling effect also keeps the density profile n_0 from deviating strongly from the reference profile $\langle n\rangle$.

- The choice of a purely diffusive macroscale transport model ($\beta_{\mathrm{D}} = 1$) leads to significantly lower errors $\eta(\Gamma)$ than an increasingly convective $\mathcal{M}$. However, the averaged flux $\langle\widetilde{\Gamma}\rangle$ does not show a diffusive behavior with $\langle\widetilde{\Gamma}\rangle \propto |\partial_x n_0|$, but rather a proportionality of $\langle\widetilde{\Gamma}\rangle \propto |\partial_x n_0|^{3.23}$. The order of magnitude found for D in the cases with $\beta_{\mathrm{D}} = 1$ coincides with the results of previous studies [41, 25]. The shape of the graph of $\langle\widetilde{\Gamma}\rangle(\partial_x n_0)$ justifies the use of a minimal flux if the input gradient $\partial_x n_0$ exceeds a maximum value $\partial_x n_{\max}$ since in the region of large $\partial_x n_0$ (small absolute values of $\partial_x n_0$) the sensitivity of $\langle\widetilde{\Gamma}\rangle$ on $\partial_x n_0$ is relatively low.

- The larger the ratio $\varepsilon(\tau_{\mathrm{D}})$ of the characteristic time $\tau_{\mathrm{D}}(\alpha_0)$ of the macroscale dynamics and the equilibration time δt_{st}, the larger is the potential for time savings of the coupled code system as compared to the reference non-local ATTEMPT simulation. This is reflected by the estimated values for the speedup factor $\varepsilon(t_c)$ which are given by the ratio of the computational time of the non-local simulation and the coupled code simulation. For the interval with the source switched on the maximum $\varepsilon(t_c)$ equals approximately 1.8 while for the interval with the source switched off the maximum $\varepsilon(t_c)$ is 8.4, the maximum of $\varepsilon(t_c)$ for the overall case being 2.8. Making the transition to an edge region of about 30 cm radial extent and assuming that the typical radial macroscale lengths are around 5 cm, i.e. considering a large tokamak device like ITER, this means time savings of the order of a factor 15 (for the entire time interval) or 40 (for the time interval with the source switched off).

- The procedure used to determine the statistically stationary state and the respective averaged mesoscale flux $\langle\widetilde{\Gamma}\rangle$ works properly and leads to a consistent relation between $\langle\widetilde{\Gamma}\rangle$ and the input gradient $\partial_x n_0$. However, for about one third of the cases where a local ATTEMPT simulation is started, the maximum number $N_k^{\max}$ of internal ATTEMPT iterations is reached for this specific problem. At the same time, the runs with largest input gradient $\partial_x n_0 \approx -0.5$ can be related to the longest runtimes $t_c(\tilde{n})$ of the local ATTEMPT simulations.

To circumvent this issue, there are basically two possibilities: Firstly, to increase $N_k^{\max}$ which will increase the accuracy of the simulations but diminish the time savings. Secondly, to lower the maximum gradient $\partial_x n_{\max}$ further, in the present case from -0.5 to -0.75, for instance. By doing this the number of local ATTEMPT simulations with rather long runtimes can be reduced and the time savings increased while not affecting the accuracy significantly.

- The overall performance of the different coupled code simulations among each other can be compared by evaluating the ratio $\eta(\Gamma)/\varepsilon(t_c)$. The cases L.3 and H.3 with a mainly convective macroscale transport model, $\beta_{\text{D}} = 0.25$, and low limit parameters d_1 and d_2, can be highlighted as rather inefficient (regarding the time savings) and inaccurate (regarding the comparison with the reference non-local simulation) while the cases L.1 and H.1 with $\beta_{\text{D}} = 1$ exhibit the smallest values of $\eta(\Gamma)/\varepsilon(t_c)$. The latter multiscale simulation corresponds to an error of $\eta(\Gamma) \approx 23$ and a speedup of about a factor 2 (potentially 10 for a larger edge area of $x_{\text{sim}} \approx 30$ cm).

From these results a number of conclusions can be drawn regarding the design of an efficient two-dimensional coupled code system, as it is investigated in chapter 8. There, the large scale code B2 evolves the macroscale profiles of n_0, $u_{\|0}$, T_{0i}, and T_{0e}, while for previously determined radial regions local ATTEMPT simulations are started. This means that the averaged mesoscale terms as well as the transport coefficients have a radial *and* a poloidal dependence. It is assumed here that the times δt_{st} and δt_{av} will be approximately the same as for the one-dimensional problem, assuming that the statistically stationary state at one radial and poloidal position is reached at the same time when the whole system reaches the statistically stationary state.

The following points should be highlighted regarding a two-dimensional coupled code system:

- To evaluate the agreement between coupled code simulation and the reference results several quantities should be compared. As it was shown above the flux error $\eta(\Gamma)$ is better suited for the evaluation of the simulations than the error $\eta(n)$ of the density due to disparate time scales for the typical transport times and the fluctuations of the fluxes. Note that while the macroscale transport model $\mathcal{M}$ did not influence $\eta(n)$ greatly this might change when it comes to statistically stationary problems.

- For a good agreement of the coupled code results with experimental measurements and/or global mesoscale simulations, the choice of the damping term

$\gamma(\tilde{n})$ and, consequently, that of the dissipation coefficients $s_{\parallel}(\tilde{\alpha})$ and $s_{\perp}(\tilde{\alpha})$ has to be assessed. Part of this analysis should be a comparison of the local mesoscale simulations with experimental results. A sensitivity study regarding these parameters should be carried out to determine the magnitude of influence they have on the simulation results.

- The coupling procedure analyzed in this chapter uses a dynamic determination of Δt_{up} so that Δt_{up} is chosen corresponding to the macroscale dynamics. This procedure is advantageous regarding the time savings and the accuracy of the coupled code simulations and should therefore be kept. However, moving to two-dimensional simulations, the number of input parameters for the local mesoscale code increases: not only the gradient $\partial_x n_0$ may then be used as an input parameter but also the density n_0, the temperatures T_{0i} and T_{0e}, etc.. Therefore, one can expect that Δt_{up} decreases since there are both more spatial positions as well as more quantities for which the deviation r_1 may exceed the limit parameter d_1 (compare fig. 7.2, (L)). To prevent that local mesoscale simulations are started too often without the results changing significantly, the sensitivity of the local mesoscale system on the macroscale input parameters should be evaluated. The results can then also be used to determine adequate limit parameters d_2 for the re-use of previously determined mesoscale results, see fig. 7.2, (B). In the 1D coupled code simulations in 67.3% of the cases previously determined fluxes could be re-used, identifying this sequential part of the coupled code system as crucial to increase time savings significantly.

- The time savings can be additionally improved if the adequate limits for the macroscale input parameters and a minimal flux are set, like it was done here with $\partial_x n_{\text{max}}$. By this procedure it can be decided in which cases a drift fluid simulation will provide significantly larger transport than that determined by the artificial dissipation.

Even though actual simulations are needed to answer the question regarding the potential time savings of a two-dimensional coupled code system it is most likely that the lower limits for the characteristic times and lengths of the macroscale dynamics have to be of the order of milliseconds and centimeters if the coupled code system should be faster than a non-local ATTEMPT simulation. In this regime, the speedup factor $\varepsilon(t_c)$ can potentially be of the order of ten. However, if one moves to significantly longer macroscale profile lengths ($\approx$ 5 cm) and a typical evolution time of the order of $\varepsilon(t_c) \approx \tau_{\text{D}}(\alpha_0) \approx 10$ ms, a speedup factor $\varepsilon(t_c)$ of the order of 100 might become achievable.

8. Simulations with the B2-ATTEMPT coupled code system

The one-dimensional coupled code system discussed in the previous chapter 7 is extended for the realization of the specific multiscale model outlined in chapter 5 in form of the B2-ATTEMPT coupled code system. The extension basically consists of replacing the one-dimensional code of the 1D coupled code system by the B2 large scale code [28, 29, 4]. Instead of evolving only the macroscale density n_0 it also determines the profiles of the parallel ion velocity $u_{0\|}$, and the ion and electron temperatures T_{0i} and T_{0e}. The local version of the ATTEMPT code is again employed for the local mesoscale simulations. The coupled code procedure into which these two codes are embedded is basically the same as the procedure used for the one-dimensional cases of chapter 7, with slight modifications to adjust it to the requirements of the two-dimensional configuration.

The main objective of the B2-ATTEMPT system is to provide a coupled code system in which the arbitrary particle transport coefficients used in B2 are replaced by profiles of radially and poloidally varying transport coefficients which are based on a local drift fluid model. These coefficients should provide radial particle fluxes which are of the order of magnitude as those found experimentally as well as a poloidal dependence which accounts for the ballooning character of transport, i.e. increased transport on the low field side of the tokamak device, e.g. see [106].

This chapter is structured as follows. In paragraph 8.1, the straightforward derivation of the B2 model from the large scale model for the plasma edge of chapter 3 is outlined. The 2D coupled code system is presented in paragraph 8.2. In paragraph 8.3, the results of the 2D coupled code system are compared to simulations by D. Gray [17] and associated experimental results, the focus being on the coupling regarding the radial particle flux and statistically stationary cases. The use of different macroscale transport models and the effect of a poloidal dependence of transport coefficients are discussed in paragraphs 8.3.1 and 8.3.2, respectively. The results of this chapter are summarized in paragraph 8.3.3.

8.1. Multiscale model of the B2-ATTEMPT system

The B2 model for a toroidal coordinate system is derived from the macroscale part of the specific multiscale model of chapter 5, consisting of eqs. (5.1) to (5.4).
For the derivation the assumptions of the self-contained large scale edge model of paragraphs 3.3.1 and 3.3.2 are used, adding the assumption that the perpendicular anomalous transport is dominated by the transport in radial direction so that its diamagnetic component within the flux surfaces can be neglected. This means that

$$\boldsymbol{\nabla} \cdot \langle \widetilde{n} \widetilde{\boldsymbol{u}} \rangle \;=\; \boldsymbol{\nabla} \cdot \langle \widetilde{n} \widetilde{\boldsymbol{u}}_x \rangle \;=\; \nabla_x^{\mathrm{D}} \langle \widetilde{\Gamma} \rangle \qquad \text{with} \qquad \nabla_i^{\mathrm{D}} \;\equiv\; \frac{1}{\sqrt{g}} \frac{\partial}{\partial u^i} \frac{\sqrt{g}}{h_i} \;, \tag{8.1}$$

where $\sqrt{g}$ is the Jacobian determinant of the coordinate system used and the h_i are the metric coefficients. If the coordinate system is orthogonal like it is the case for the toroidal coordinate system employed here ∇_i^{D} is related to the divergence of a vector $\boldsymbol{a}$ by

$$\boldsymbol{\nabla} \cdot \boldsymbol{a} \;=\; \sum_i \frac{1}{\sqrt{g}} \frac{\partial}{\partial u^i} \left(\frac{\sqrt{g}}{h_i} \, a_i \right) \;=\; \sum_i \nabla_i^{\mathrm{D}} a_i \;. \tag{8.2}$$

For the terms of the form $\langle \widetilde{u} \cdot \boldsymbol{\nabla} \widetilde{u}_{\|} \rangle$ which appear in the macroscale part of the specific multiscale model one has

$$\left\langle \widetilde{u} \cdot \boldsymbol{\nabla} \widetilde{u}_{\|} \right\rangle \;=\; -\boldsymbol{\nabla} \cdot \left(D_{\perp} \boldsymbol{\nabla}_x u_{\|0} \right) \;. \tag{8.3}$$

Note also that an adjusted version of eq. (3.52) holds:

$$\eta_{ax} \;=\; m_a n_{a0} D_{\perp} \;, \qquad \kappa_{ax} \;=\; n_{a0} D_{\perp} \;, \tag{8.4}$$

where the index a refers to the particle species. Even though relation (8.4) is to be implemented in future to relate the anomalous transport coefficients η_{ax} and κ_{ax} to $D_{\perp}$, η_{ax} and κ_{ax} are currently arbitrary input parameters chosen by the modeler. Nevertheless, in the derivation below relation (8.4) is used to replace the terms $m_a n_{a0} D_{\perp}$ and $n_{a0} D_{\perp}$. It is also assumed that the radial direction of the toroidal coordinate system is always normal to the flux surfaces and that the poloidal direction always lies within the flux surfaces. This is true for circular (regarding a poloidal cut) and concentrically nested flux surfaces centered within the tokamak vessel, the configuration which is assumed here.

With the assumptions outlined above the **ion particle balance** (5.1) for B2 becomes:

$$\boxed{\frac{\partial n_0}{\partial t} \;+\; \nabla_x^{\mathrm{D}} \langle \widetilde{\Gamma} \rangle \;+\; \nabla_\theta^{\mathrm{D}} \left(n_0 u_{\|0} \frac{B_\theta}{B} \right) \;=\; S_{0in}^{ic} \;.} \tag{8.5}$$

Due to the assumption of toroidal symmetry and $\boldsymbol{u}_0 = \boldsymbol{u}_{\|0}$ the poloidal and toroidal velocity components are determined by $u_{\|0}$:

$$u_{0\theta} \;=\; \frac{B_\theta}{B}\, u_{\|0}\ , \qquad u_{0\varphi} \;=\; \frac{B_\varphi}{B}\, u_{\|0}\ . \tag{8.6}$$

The **total parallel momentum balance** of B2 is derived from eq. (5.2) and yields:

$$\boxed{\begin{aligned} &\frac{\partial}{\partial t}\Big(m_i n_0 u_{\|0}\Big) \;+\; \nabla_x^{\mathrm{D}}\Big(m_i u_{\|0}\langle\widetilde{\Gamma}\rangle - \eta_{ix}\nabla_x u_{\|0}\Big) \;+\; \nabla_\theta^{\mathrm{D}}\left(m_i n_0 u_{\|0}^2\frac{B_\theta}{B} - \eta_{i\theta}\nabla_\theta u_{\|0}\right) \\ &\qquad = \;-\frac{B_\theta}{B}\nabla_\theta(p_{0i}+p_{0e}) \;+\; S_{0\|imV}\ , \qquad (8.7) \end{aligned}}$$

where the approximation

$$\Big[\boldsymbol{\nabla}\cdot\boldsymbol{\Pi}_{0i}\Big]_{\|} \;=\; -\nabla_\theta^{\mathrm{D}}\Big(\eta_{i\theta}\nabla_\theta u_{\|0}\Big) \tag{8.8}$$

was used. The ion energy balance of B2 is derived from eq. (5.3) and gives:

$$\boxed{\begin{aligned} &\frac{\partial}{\partial t}\left(\frac{3}{2}n_0T_{0i} + \frac{1}{2}m_in_0u_{\|0}^2\right) \\ &\qquad +\; \nabla_x^{\mathrm{D}}\left(\frac{3}{2}T_{0i}\langle\widetilde{\Gamma}\rangle \;+\; \frac{1}{2}m_iu_{\|0}^2\langle\widetilde{\Gamma}\rangle \;-\; \frac{3}{2}\kappa_{ix}\nabla_xT_{0i} \;-\; \frac{1}{2}\eta_{ix}\nabla_xu_{\|0}^2\right) \\ &\qquad +\; \nabla_\theta^{\mathrm{D}}\left(\frac{5}{2}n_0T_{0i}u_{\|0}\frac{B_\theta}{B} \;+\; \frac{1}{2}m_in_0u_{\|0}^3\frac{B_\theta}{B} \;-\; \kappa_{i\theta}\nabla_\theta T_{0i} \;-\; \frac{1}{2}\eta_{i\theta}\nabla_\theta u_{\|0}^2\right) \\ &\qquad =\; -u_{\|0}\frac{B_\theta}{B}\nabla_\theta\Big(n_0T_{0e}\Big) \;-\; u_x^*\nabla_x(n_0T_{0e}) \;+\; Q_{0i} \;+\; S_{0iE}^{ic}\ . \qquad (8.9) \end{aligned}}$$

For the electron energy balance of B2, basing on eq. (5.4), one finds:

$$\boxed{\begin{aligned} &\frac{\partial}{\partial t}\left(\frac{3}{2}\,n_0T_{0i}\right) + \nabla_x^{\mathrm{D}}\left(\frac{3}{2}\,T_{0e}\langle\widetilde{\Gamma}\rangle - \frac{3}{2}\,\kappa_{ex}\nabla_xT_{0e}\right) + \nabla_\theta^{\mathrm{D}}\left(\frac{5}{2}\,n_0T_{0e}u_{\|0}\frac{B_\theta}{B} - \kappa_{e\theta}\nabla_\theta T_{0e}\right) \\ &\qquad =\; u_{\|0}\frac{B_\theta}{B}\nabla_\theta\Big(n_0T_{0e}\Big) \;+\; u_x^*\nabla_x(n_0T_{0e}) \;+\; Q_{0e} \;+\; S_{0Ee}^{ic}\ . \qquad (8.10) \end{aligned}}$$

The basic input parameters of the B2 model are the ion viscosities η_{ix}, $\eta_{i\theta}$, the ion and electron thermal conductivities κ_{ix}, $\kappa_{i\theta}$, κ_{ex}, $\kappa_{e\theta}$, and the source terms S^{ic}_{0in}, $S_{\|0imV}$, S^{ic}_{0iE}, and S^{ic}_{0Ee}. A couple of terms has been neglected in the derivation for simplification: The term $2m_in_0u^*_x\nabla_xu_{\|0}$ on the rhs of the momentum balance (8.7), the terms $\eta_{ix}(\nabla_xu_{\|0})^2$, $3n_0u^*_x\nabla_xT_{0i}$, and $m_in_0u^*_x\nabla_xu^2_{\|0}$ on the rhs of the ion energy balance (8.9), and the term $3n_0u^*_x\nabla_xT_{0e}$ on the rhs of the electron energy balance (compare the corresponding balances (3.55), (3.56), and (3.57) of the self-contained large scale model which still contain these terms). The term $u^*_x\nabla_x(n_0T_{0e})$, appearing on the rhs of the ion and electron energy balances (8.9) and (8.10), respectively, with alternating sign, is added to account for a radial pressure gradient. Eqs. (8.5), (8.7), (8.9), and (8.10) are solved by the finite-volume spatial discretization outlined by Patankar in [107] on a non-uniform staggered mesh, using a fully implicit discretization in time.

For the mesoscale part, the local version of the ATTEMPT code is used, given by eqs. (7.12) to (7.15), as it was the case for the one-dimensional coupled code system of chapter 7.

8.2. Outline of the 2D coupling procedure

The coupling procedure for the B2-ATTEMPT coupled code system is similar to the procedure used for the 1D coupled code simulations of chapter 7. An explanatory flowchart is shown in fig. 8.1. The most significant changes compared to the 1D coupled code simulations are as follows, the major letters in brackets referring to fig. 8.1:

- On the macroscale, only stationary solutions are considered: $\partial\alpha_0/\partial t = 0$.
- The coupling procedure is fully concurrent, i.e. no previously determined fluxes are re-used. This feature is to be included in the next version of the 2D coupled code system.
- Not only the macroscale density gradient ∂_xn_0 but also the macroscale density n_0, the macroscale electron temperature T_{0e}, and the minor radius a are used as input parameters for the local ATTEMPT runs (B).
- From the local ATTEMPT simulations, a *poloidally dependent* profile of macroscale transport coefficients is determined (F).
- A relaxation factor α_r to relax the macroscale transport coefficients is used (C).
- The coupled code simulation is finished when two consecutive profiles of transport coefficients differ from each other on average less than an arbitrary limit parameter e_1 set by the modeler (L), here $e_1 = 0.05$.

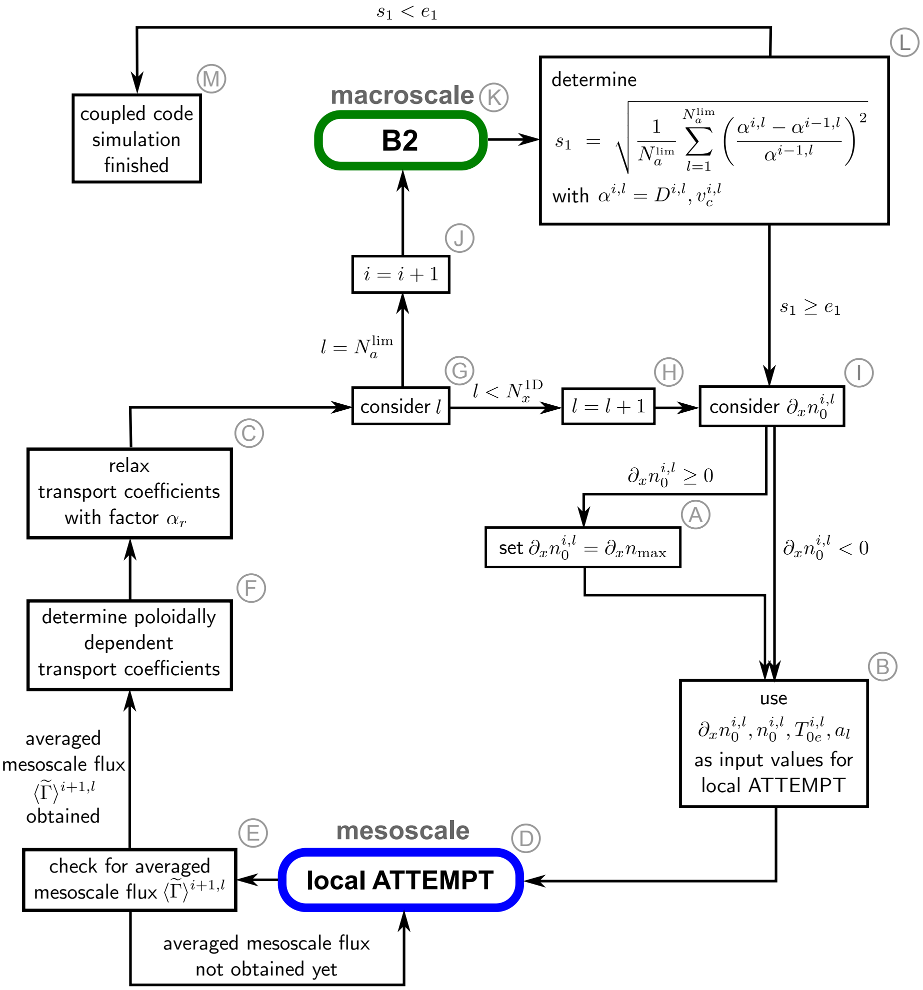

Figure 8.1.: Sketch of a coupled code simulation for the B2-ATTEMPT coupled code system. See paragraph 8.2 for an explanation of the parameters and procedures.

The check for the averaged mesoscale flux $\langle\widetilde{\Gamma}\rangle$ at (E) is the same that is used for the one-dimensional coupled code simulations (see paragraph 7.1.4 for the explanation of the procedure). For each global iteration i the B2 code runs for a large number of time steps, which are here to be understood as iterative steps, until the residua for the separate equations are negligible. The macroscale transport model used to represent the averaged mesoscale terms $\langle \tilde{n}\tilde{u}_x \rangle$ in the B2 code is a combination of a diffusive and convective model:

$$\langle \widetilde{\Gamma} \rangle \; = \; n_0 v_c \; - \; D\partial_x n_0 \; , \tag{8.11}$$

with the transport coefficients being determined by

$$v_c^i(x,\theta) \; = \; \alpha_r \, (1-\beta_\mathrm{D}) \frac{\langle \widetilde{\Gamma} \rangle^{i,l}(\theta)}{n_0^{i-1,l}} \; + \; (1-\alpha_r) \, v_c^{i-1}(x,\theta) \; , \tag{8.12}$$

$$D^i(x,\theta) \; = \; -\alpha_r \, \beta_\mathrm{D} \, \frac{\langle \widetilde{\Gamma} \rangle^{i,l}(\theta)}{\partial_x n_0^{i-1,l}} \; + \; (1-\alpha_r) \, D^{i-1}(x,\theta) \; . \tag{8.13}$$

The index l refers to the radial zone of the B2 simulation domain for which the local ATTEMPT simulation was carried out (see below). For each given radial coordinate x the corresponding radial zone l can be unambiguously determined. The parameter β_D determines the diffusive part of the flux while the remaining part is represented by the convective velocity v_c. The relaxation factor α_r chosen for the simulations presented below is 0.3.

The determination of the averaged mesoscale flux $\langle \widetilde{\Gamma} \rangle^{i,l}$ and the corresponding transport coefficients of the macroscale transport model is sketched in fig. 8.2 and carried out as follows. Before starting the coupled code simulation, the B2 simulation domain is poloidally divided into N_θ^c zones of extent $\delta\theta_\mathrm{av}$ and radially divided into N_x^c equidistant zones of extent δx_av which are referred to by the index l. Of the latter N_x^c zones N_x^lim are situated in the edge region of closed magnetic flux surfaces for which local ATTEMPT simulations are started. For the remaining radial zones within the SOL the poloidal profile of macroscale transport coefficients of the radial zone closest to the SOL for which local ATTEMPT simulations are carried out is used.

For each of the N_x^lim radial zones in the region of closed flux surfaces a separate local ATTEMPT simulation is started which can be associated with the differently colored rings in fig. 8.2. The input parameters $\langle n_0 \rangle_{x,\mathrm{fs}}$, $\langle \partial_x n_0 \rangle_{x,\mathrm{fs}}$, $\langle T_{0\mathrm{e}} \rangle_{x,\mathrm{fs}}$, and $\langle a_0 \rangle_{x,\mathrm{fs}}$ are the averages of n_0, $\partial_x n_0$, T_{0e}, and a_0 over all flux surfaces within the respective radial zone of the B2 simulation domain. Once the local ATTEMPT simulation has reached its statistically stationary state – which is determined via the time trace of $\bar{\Gamma}(t)$ as for the 1D coupled code cases – the profile of the poloidally dependent averaged flux $\langle \widetilde{\Gamma} \rangle^{i,l}(\theta)$ is determined. For this purpose first a radial average of the flux from the local ATTEMPT simulation is carried out. Then for each of the N_θ^c poloidal zones N_ip^A equidistant interpolation points are chosen in poloidal direction over which the flux is again averaged. The toroidal angle φ is kept fixed for calculating these averages. The final profile of $\langle \widetilde{\Gamma} \rangle^{i,l}(\theta)$ is used to determine the transport coefficients $v_c(x,\theta)$ and $D(x,\theta)$ (see eq. (8.12) and (8.13)) for the specific radial zone of the B2 simulation domain. The procedure is subsequently carried out for all remaining

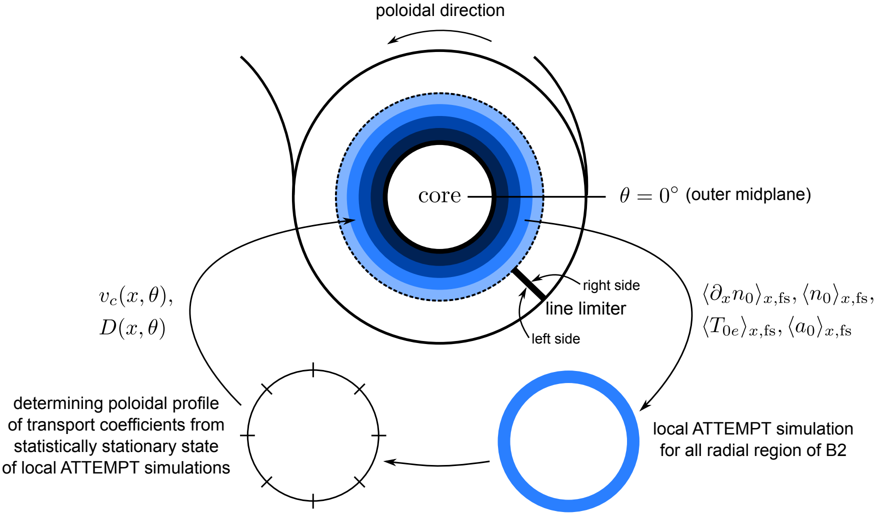

Figure 8.2.: Sketch of a coupling loop of the B2-ATTEMPT coupled code system.

radial zones until the complete profiles of $v_c(x,\theta)$ and $D(x,\theta)$ are handed back to B2.

8.3. Results of the 2D coupled code system

The results of the 2D coupled code system are compared here to experimental measurements and former modeling results with the B2-EIRENE code [14] provided by D. Gray [17] for the tokamak TEXTOR [108] (see fig. B.2). The advantage of the study presented in [17] is that the anomalous particle transport coefficients v_c and D were chosen so that the resulting profiles of plasma quantities of the B2-EIRENE simulations coincided with the measured radial profiles at the outer midplane ($\theta = 0^\circ$). With the simulated profiles and the employed transport coefficients at hand one can reconstruct the respective radial particle fluxes and the effective diffusion coefficient which can then be compared to the results of the B2-ATTEMPT simulations. Hence, it can be evaluated if the latter coupled code system self-consistently provides transport coefficients of the order of those being used to fit simulated profiles to experimental data.

The focus of the comparison presented here is on the cases 3, 4, and 5 shown in [17] (see fig. B.2). For each of these cases three coupled code simulations with different

coupling parameters		**mesoscale local ATTEMPT**		**macroscale B2**	
R_0	1.75 m	N_s^{A}	16	N_x^{B2}	32
B_0	2.25 T	N_x^{A}	64	N_θ^{B2}	48
q_0	3	N_y^{A}	256	Δx_s	3.125 mm
$\hat{s}$	2	N_{f}	9	$\Delta\theta_s$	7.5°
m_i	2 u	δt_s	$1.63 \cdot 10^{-8}$ s		
N_x^{lim}	4	δx_s	$1\,\rho_s$		
N_x^c	8	δy_s	$0.71\,\rho_s$		
N_θ^c	12	$L_\perp$	5 cm		
δx_{av}	1.25 cm	N_k^{max}	10		
$\delta\theta_{\mathrm{av}}$	30°	$N_t^{\mathrm{A,ii}}$	5 000		
x_{sim}	10 cm	δt_{run}	$8.15 \cdot 10^{-5}$ s		
e_1		a_1	0.5		
		a_2	1/7		
		a_3	0.15		
		a_t	1/40		

Table 8.1.: Parameters of the B2-ATTEMPT coupled code cases.

case	n_0^{in} [10^{19} m^{-3}]	T_{0i}^{in}, T_{0e}^{in} [eV]	D [m^2 s^{-1}]	v_c [m s^{-1}]	N_i $\beta_{\mathrm{D}}=1$	N_i $\beta_{\mathrm{D}}=0.75$	N_i $\beta_{\mathrm{D}}=0.5$
3	1.8	130	0.69	-6.9	5	9	9
4	1.0	130	0.9	0.0	4	8	8
5	3.8	75	1.51	-7.6	6	11	11

Table 8.2.: Values n_0^{in}, T_{0i}^{in}, and T_{0e}^{in} for Dirichlet boundary conditions at the inner radial boundary of the B2 domain for the B2-ATTEMPT simulations, transport coefficients D, v_c as used by D. Gray for the B2-EIRENE simulations to fit the experimental measurements [17], and global iterations N_i of the B2-ATTEMPT system until the convergence criteria of the coupled code system are met.

macroscale transport models were carried out, employing values of 1, 0.75, and 0.5 for β_{D}. The boundary conditions of the B2 code of the coupled code system were chosen as similar as possible to those being employed for the B2-EIRENE simulations outlined in [17]. Not all the necessary data is given in [17] for this purpose; in those cases, the boundary conditions were chosen with respect to the simulation results shown in [17].

At the inner simulation boundary in radial direction a constant electron density and ion and electron temperatures are assumed, with the exact values given in table

8.2, being reconstructed from [17]. At the outer radial boundary decay lengths $\lambda_n = \lambda_{T_i} = \lambda_{T_e} = 2$ cm for the radial profiles of the density and the temperatures are set. The parallel velocity $u_{\|0}$ is set to zero at the inner radial boundary; at the outer radial boundary $m_i n_0 u_x^* u_{\|0} = 0$ has to be fulfilled. The coefficients for the anomalous heat conduction are the same for both electrons and ions, $\kappa_{ix} = \kappa_{ex}$.
In the edge region with closed flux surfaces periodic boundary conditions are used in poloidal direction. At the surfaces of the line limiter at $\theta = 315°$ within the SOL sheath boundary conditions were prescribed. These are as follows:

$$\frac{\partial n_0}{\partial \theta} = 0 , \tag{8.14}$$

$$u_{\|0} = c_s = \sqrt{\frac{T_{0i} + T_{0e}}{m_i}} , \tag{8.15}$$

$$q_{i\theta} = \delta_i n_0 u_{0\theta} T_{0i} + \frac{m_i n_0 u_{\|0}^2 u_{0\theta}}{2} , \tag{8.16}$$

$$q_{e\theta} = (\delta_e + 3.1) n_0 u_{0\theta} T_{0e} , \tag{8.17}$$

with $\delta_i = 2.5$, $\delta_e = 1.7$, and $q_{i\theta}$ and $q_{e\theta}$ being the ion and electron heat fluxes in poloidal direction, respectively. The minimal neutral particle model of B2 is employed [29], meaning that the particle influx is sent back into the main plasma with a recycling rate of 65% and up to a poloidal extent of 90° away from the limiter plates.

The two main differences of the B2-ATTEMPT from the B2-EIRENE simulations are (apart from using the ATTEMPT code in the former system to determine the radial particle transport coefficients): the simplified shape of the toroidal limiter which is taken to be a line limiter in B2-ATTEMPT system but has a mushroom-like poloidal cross section in the B2-EIRENE simulations (compare fig. B.1)), and the simplified neutral model of B2-ATTEMPT which is replaced by EIRENE calculations in the B2-EIRENE system. The influence of these alterations on the simulation results is discussed below.

The simulation results of the B2-ATTEMPT system for case 3, $\beta_{\mathrm{D}} = 1$, are exemplarily shown in fig. 8.3. The Mach number M_a, shown in the right column, top, is given by the parallel velocity, divided by the local speed of sound, $M_a(x, \theta) = u_{\|0}(x, \theta)/c_s(x, \theta)$. The profiles of n_0, T_{0i}, and T_{0e} show only a marginal poloidal dependence (except for T_{0i} which drops at the limiter surfaces around $\theta = 315°$ for $x \approx 46$ cm). This means that the assumption of constant values of $\partial_x n_0$, n_0, and T_{0e} on the flux surfaces which is made for the local ATTEMPT simulations is reasonable. This is not the case for the poloidal and radial fluxes $\Gamma_{\theta 0}$ and Γ_{x0}. Both are larger in the poloidal region at the LFS from $\theta = 315°$ to 135°, seen in counterclockwise direction, than in the region at the HFS from $\theta = 135°$ to $\theta = 315°$. The respective profile of D, shown in fig. 8.5, right column, top, shows a similar dependence, with the highest

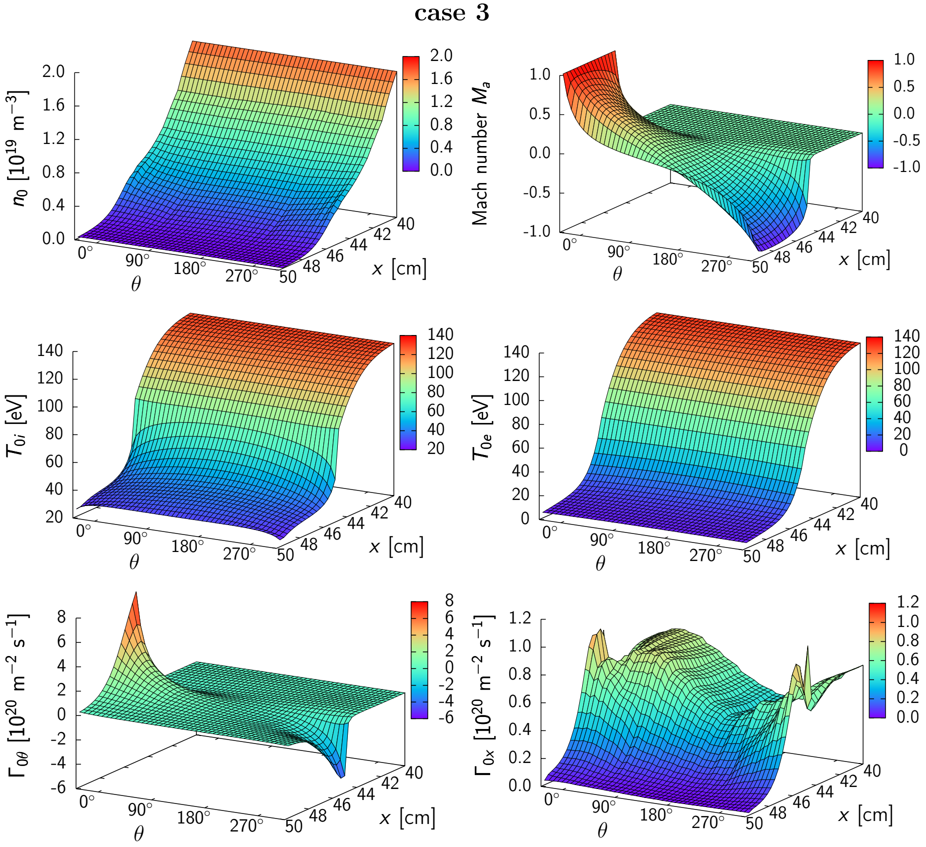

Figure 8.3.: Plasma profiles of the B2-ATTEMPT simulations for case 3 with $\beta_{\mathrm{D}} = 1$.

values of D at the LFS around $\theta \approx 0°$ and thus an increased radial flux. However, the poloidal asymmetry of Γ_{0x} and $\Gamma_{0\theta}$ regarding the limiter position is also visible if poloidally homogeneous transport coefficients are used in the B2 simulations. It can be explained by the fact that the region from $\theta = 315°$ to $\theta = 135°$ corresponds to a larger volume than the region from $\theta = 135°$ to $\theta = 315°$ since it is situated at the outer side of the torus. This means that effectively more particles are accelerated towards the target plates at the LFS due to the existing pressure drop in front of the limiter than at the HFS. This increased poloidal flux $\Gamma_{0\theta}$ at the LFS subsequently leads to an increased radial flux Γ_{0x} which ensures that the resulting pressure (and density) profile is homogeneous in poloidal direction.

To compare the results of the B2-ATTEMPT system with the B2-EIRENE simulations

case 3

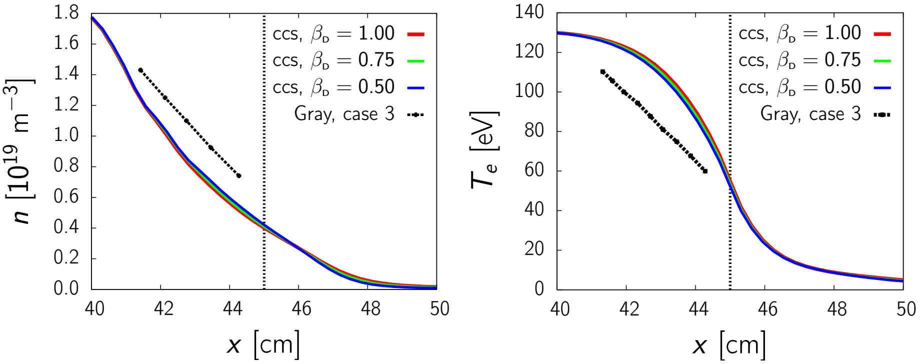

case 4

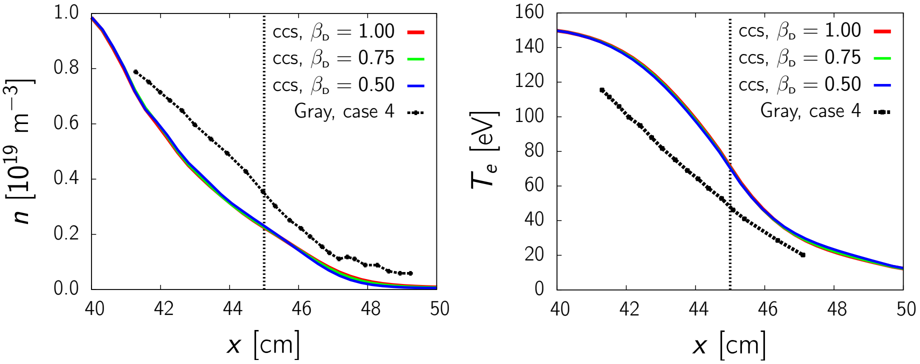

case 5

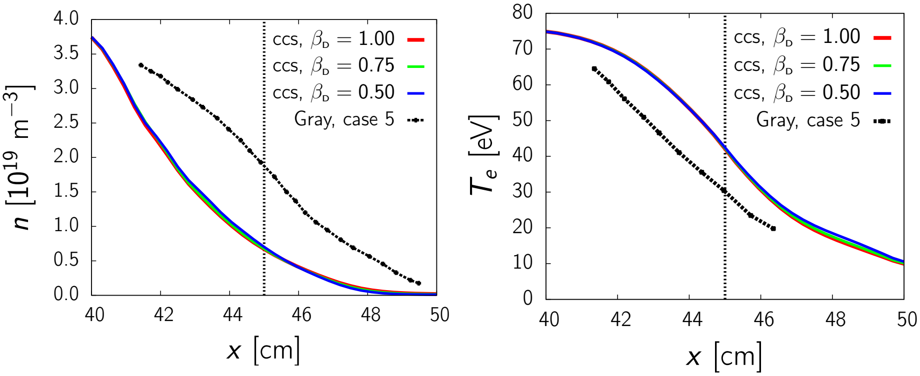

Figure 8.4.: Profiles of the density (**left column**) and the electron temperature (**right column**) from the B2-ATTEMPT simulations (ccs) and the B2-EIRENE simulations from the paper by D. Gray [17].

the radial profiles of n_0 and T_{0e} for the outer midplane ($\theta = 0°$) are shown in fig. 8.4. The black, dotted lines refer to the B2-EIRENE profiles that were obtained by D. Gray by adjusting the spatially constant transport coefficients D and v_c in B2 so that the simulated profiles coincided with the experimentally measured profiles.
For cases 3 and 4, the values of n_0 and T_{0e} predicted by the B2-ATTEMPT coupled code system are somewhat lower than those given by the B2-EIRENE simulations with minimum values around 60 to 80% of the B2-EIRENE predictions. For case 5 the density drops to values of around 40% of the B2-EIRENE simulations. The main qualitative difference between the B2-ATTEMPT and B2-EIRENE simulations is that in the latter the profiles of n_0 and T_{0e} are roughly linear in radial direction within the region of closed flux surfaces while the B2-ATTEMPT simulations show a slight trend towards an exponential decay. This can be explained by the simplified line limiter model used in the B2-ATTEMPT simulations which leads to zero reflection of particles in radial direction (compare fig. 8.2). In [17] the limiter has a component facing the plasma also in radial direction (compare fig. B.1) which results in reflection of particles into the edge region of closed flux surfaces and thus an increase of density there. An associated effect can be observed for T_{0e} which, in the B2-ATTEMPT simulations, is higher in the region of closed flux surfaces than predicted by the B2-EIRENE simulations. In the latter simulations the neutral particles which are reflected from the plasma facing surface of the limiter in radial direction can be re-ionized in the region of closed flux surfaces and therefore may lead to an energy loss and a subsequent temperature decrease.

In fig. 8.5, left column, the diffusion coefficient D of the B2-ATTEMPT simulations with $\beta_{\mathrm{D}} = 1$ is shown (continuous, red lines), together with the effective diffusion coefficients from the B2-EIRENE simulations (black, dotted lines). The latter profiles were reconstructed from the profiles of n_0 of the B2-EIRENE simulations (see fig. B.2) and the transport coefficients D and v_c employed in these simulations (see table 8.2). While for case 5 the diffusion coefficient determined by B2-ATTEMPT is up to 80% smaller than the B2-EIRENE effective D, this deviation is reduced for the cases 3 and 4: here, the deviation is only around 10 to 30%. In cases 3 and 5, the trend of an increasing effective diffusion coefficient when moving radially outwards can also be found in the B2-ATTEMPT simulations.

For a better evaluation of B2-ATTEMPT results regarding D one can compare them with the predictions of radial transport from the classical and neoclassical transport theory. For the former one can estimate D as [64]

$$D_{\mathrm{cls}} \sim \frac{\rho_s^2}{\tau_i} , \tag{8.18}$$

where τ_i is the ion-ion collision time as given by eq. (3.4b). With edge conditions as for the cases 3 and 4 ($T_{0i} \approx 80$ eV, $n_0 \approx 1 \cdot 10^{19}$ m^{-3}) one can estimate the ion Larmor radius with $\rho_s \approx 0.5$ mm and the ion collision time with $\tau_i \approx 0.1$ ms. One

case 3

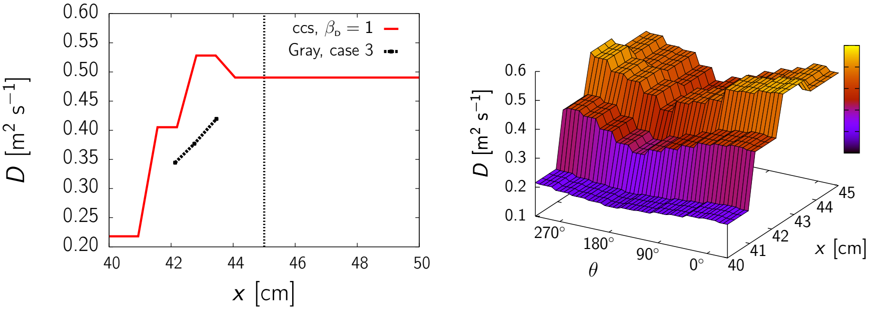

case 4

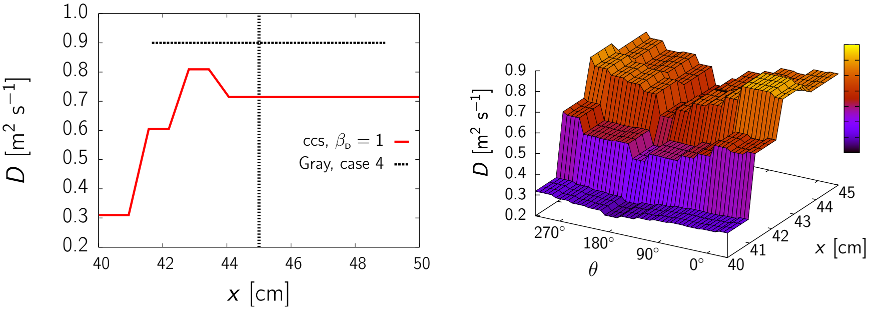

case 5

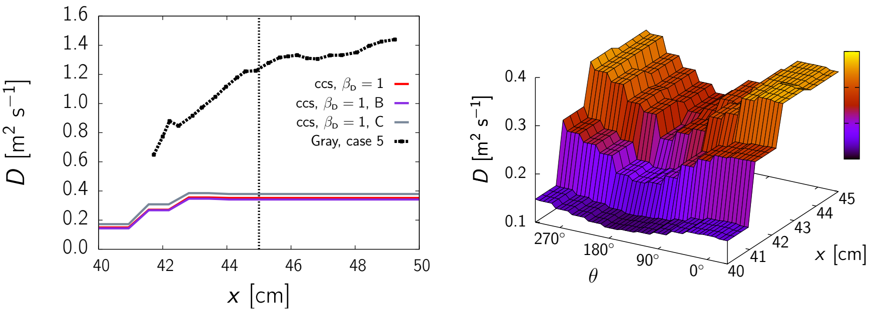

Figure 8.5.: Left column: Final profiles of the diffusion coefficient from the B2-ATTEMPT simulations (ccs) and the effective diffusion coefficient from B2-EIRENE simulations of the paper by D. Gray [17]. The latter values have been reconstructed from fig. B.2 by calculating the radial flux, employing the given transport coefficients D and v_c, and then determining the radially heterogeneous diffusion coefficient (which is shown in the plots) via division by the radial density gradient. **Right column:** Final profiles of the diffusion coefficients D of the B2-ATTEMPT simulations with $\beta_D = 1$. The color coding refers to the value on the z axis.

obtains

$$D_{\mathrm{cls}} \;\approx\; 0.0025 \text{ m}^2 \text{ s}^{-1} \; . \tag{8.19}$$

For a neoclassical estimate of D one has [64]:

$$D_{\mathrm{neo}} \;\sim\; (q^2+1)\frac{\rho_s^2}{\tau_i} \;\approx\; 0.025 \text{ m}^2 \text{ s}^{-1} \; . \tag{8.20}$$

D_{neo} and D_{cls} underestimate the radial particle diffusion coefficient by one and two orders of magnitude, respectively. Typical D found by the B2-ATTEMPT simulations and those used in the B2-EIRENE simulations are of the order of 0.5 m^2 s^{-1}. This means that the B2-ATTEMPT systems provides adequate values of D for the radial particle transport while at the same time also the input values of n_0, $\partial_x n_0$ and $T_{0\mathrm{e}}$ are close to experimentally found profiles.

To check for possible reasons for the comparably strong deviation of the diffusion coefficient by the B2-ATTEMPT system for case 5 from the effective diffusion coefficient of the B2-EIRENE simulations two additional simulations have been carried out. For case 5B the ATTEMPT domain in toroidal direction was increased to $N_y^{\mathrm{A}} = 512$ cells instead of 256 (keeping the cell width constant) so that only $N_{\mathrm{f}} = 4$ flux tubes were needed to cover the whole torus instead of 9 flux tubes. Regarding the local ATTEMPT simulations this means the inclusion of drift fluid dynamics with lower poloidal mode numbers down to $m = 12$, whereas for the previous case with $N_{\mathrm{f}} = 9$ the lower limit was $m = 27$. For case 5C the perpendicular dissipation coefficients $s_\perp(\alpha)$ (see eq. (7.20)) as well as the damping term γ_0 of the constant part of $\widetilde{n}$ (see eq. (7.21)) were reduced by a factor of two.
As one can see by the violet (case 5B) and gray (case 5C) profiles in fig. 8.5, left column, bottom, both variations of the input parameters do not affect strongly the resulting profile of D. Hence, the lower diffusion coefficient associated to the B2-ATTEMPT simulation most likely has a different reason than the limitation of the poloidal mode numbers regarding the local mesoscale simulations or too large dissipation and damping coefficients. One possibility is that inclusion of the temperature dynamics in the mesoscale simulation could lead to an additional particle flux (e.g. due to convective energy transport) and thus to an increase in the particle diffusion coefficient. Also, effects of a radial electric field on the macroscale have not been included yet. However, there is also the possibility that the density measurements for case 5 in [17] might be erroneous: the Greenwald density limit [50], an upper operational density limit above which disruptions become more frequent, is $5.3 \cdot 10^{19}$ m^{-3} for this TEXTOR experiment. The maximum density measured in the edge at $x = 33$ cm is already around $5 \cdot 10^{19}$ m^{-3} (compare fig. B.2) so that a further density increase towards the core region (which usually is observed) becomes almost impossible without exceeding the Greenwald limit.

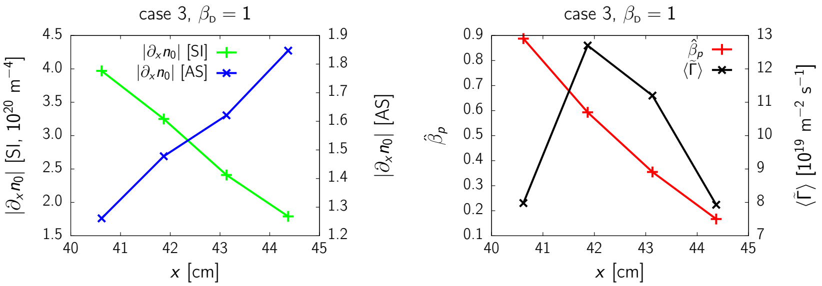

Figure 8.6.: Left: Absolute value of the radial density gradient in SI units $|\partial_x n_0|$ [SI] and in the ATTEMPT scaling $|\partial_x n_0|$ [AS]. **Right:** Corresponding scaled plasma beta $\hat{\beta}_p$ and averaged mesoscale flux $\langle\widetilde{\Gamma}\rangle$. The data is obtained from the local ATTEMPT simulations for case 3, $\beta_\mathrm{D} = 1$, last iteration of the coupled simulation.

Next, the characteristics of the transport coefficients as determined with the local ATTEMPT data are analyzed. For this purpose the final profiles of the diffusion coefficients are shown in fig. 8.5, right column, for the cases 3, 4, and 5 with $\beta_\mathrm{D} = 1$. All profiles reflect the poloidal dependence of the averaged mesoscale flux with the lowest flux (and lowest D) at the HFS ($\theta = 180°$) and the highest flux at the LFS ($\theta = 0°$), the region of 'bad curvature'. The variation of D with the poloidal angle θ is largest for case 5 where D varies by a factor two between the HFS and the LFS for radial positions $x \approx 42$ cm. The poloidal variation of D is considerably smaller negligible near the inner simulation boundary ($x \approx 40.5$ cm).
Besides the poloidal variation $D(x, \theta)$ shows the tendency to increase in radial direction outwards before slightly dropping in the radial domain of closed flux surfaces closest to the SOL around $x = 44$ cm. This trend is explained below for the exemplary case 3. Moving in radial direction outwards the scaled gradient $\partial_x n_0$ [AS] increases: even though the physical gradient $\partial_x n_0$ [SI] decreases, as it can be seen from the green graph in fig. 8.6, left, the density n_0 decreases as well (compare fig. 8.4, left column, top), effectively leading to an increase of the gradient $\partial_x n_0$ [AS] in the ATTEMPT scaling, given by $\partial_x n_0 = L_\perp[\partial_x n_0]^{\mathrm{SI}}/n_0$ (see fig. 8.6, left, blue graph). This increases the drive for the drift fluid dynamics.
However, when moving in radial direction outwards one finds that there is an opposing trend leading to a reduction of the drive of the drift fluid dynamics: the temperature decreases, resulting in a diminished plasma pressure and therefore a decreasing plasma beta β_p. This is reflected by the scaled plasma beta $\hat{\beta}_p$, depicted in fig. 8.6, right, red graph, which is defined as $\hat{\beta}_p \equiv (q_0 R_0/L_\perp)^2 \beta_p$. A decreasing $\hat{\beta}_p$ means that the confinement of the plasma by the external magnetic field increases and transport in radial direction is diminished. Moving in radial direction outwards this effect outbalances the increase of $\partial_x n_0$ [AS] around $x = 44$ cm, leading to decrease in the

averaged mesoscale flux, see fig. 8.6, right, black graph, and subsequently a decreasing diffusion coefficient. It is also stronger than the effect of a radially decreasing value of $|\partial_x n_0|$ [SI] which would normally increase D (since $D = \Gamma_{0x}/|\partial_x n_0|$).

8.3.1. Assessment of different macroscale transport models

For each of the three cases from [17] B2-ATTEMPT simulations with three different macroscale transport models were carried out. The transport models are specified by the value of β_D which indicates the part of the averaged mesoscale flux which is represented by a diffusive model while the remaining part is modeled via a convective velocity v_c. Comparing the resulting profiles of these simulations assesses the influence the choice of the macroscale transport model might have on the simulation results. In the stationary state the macroscale flux Γ_{0x} should match the values of the averaged mesoscale fluxes $\langle\widetilde{\Gamma}\rangle$ and should not differ for different macroscale transport models as it can be illustrated by the following reasoning. For the stationary case it holds:

$$\begin{aligned}
\Gamma_{0x}^i &= (1-\beta_\mathrm{D})\Big[\alpha_r v_c^i + (1-\alpha_r)v_c^{i-1}\Big]n_0^i \;-\; \beta_\mathrm{D}\Big[\alpha_r D^i + (1-\alpha_r)D^{i-1}\Big]\partial_x n_0^i \\
&\approx (1-\beta_\mathrm{D})v_c^i n_0^i \;-\; \beta_\mathrm{D} D^i n_0^i \\
&= (1-\beta_\mathrm{D})\frac{\langle\widetilde{\Gamma}\rangle(\langle\boldsymbol{\alpha}_0^{i-1}\rangle_{x,\mathrm{fs}})}{n_0^{i-1}}\,n_0^i \;+\; \beta_\mathrm{D}\frac{\langle\widetilde{\Gamma}\rangle(\langle\boldsymbol{\alpha}_0^{i-1}\rangle_{x,\mathrm{fs}})}{\partial_x n_0^{i-1}}\,\partial_x n_0^i \\
&\approx \langle\widetilde{\Gamma}\rangle(\langle\boldsymbol{\alpha}_0^{i}\rangle_{x,\mathrm{fs}})\ .
\end{aligned} \tag{8.21}$$

The vector $\langle\boldsymbol{\alpha}_0^i\rangle_{x,\mathrm{fs}}$ refers to the macroscale input values for the local mesoscale simulation for global iteration i, such as $\langle n_0\rangle_{x,\mathrm{fs}}$, $\langle\partial_x n_0\rangle_{x,\mathrm{fs}}$, etc.. In the step from the first to the second line it has been used that the transport coefficients from iteration $i-1$ and i are approximately identical due to the convergence criterion of the coupled code system. In the step from the third to the fourth line it has been assumed that the profiles of n_0 and $\partial_x n_0$ of iterations $i-1$ and i are approximately the same since for both B2 simulations similar macroscale transport coefficients v_c and D were used. Eq. (8.21) therefore states that in the case of convergence of the coupled code system the flux $\Gamma_0(x,\theta)$ of the final global iteration corresponds to the averaged mesoscale flux given by the local mesoscale model independently from the employed macroscale transport model.

In fig. (8.7) the variation $\eta(\alpha)$ between the simulations with $\beta_\mathrm{D} = 0.75$ and $\beta_\mathrm{D} = 0.5$, compared to the simulation with $\beta_\mathrm{D} = 1$ for $\alpha = n_0$, $u_{\|0}$, T_{0i}, T_{0e}, $\Gamma_{0\theta}$, and Γ_{0x} is shown. The value of $\eta(\alpha)$ is defined as

$$\eta(\alpha) \;\equiv\; 100\cdot\left\langle\frac{|\alpha_0(\beta_\mathrm{D}\!=\!X) - \alpha_0(\beta_\mathrm{D}\!=\!1)|}{\max\Big\{\langle|\alpha_0(\beta_\mathrm{D}\!=\!1)|\rangle_{r_\mathrm{sim}},\alpha_0(\beta_\mathrm{D}\!=\!1)\Big\}}\right\rangle_{r_\mathrm{sim}}, \tag{8.22}$$

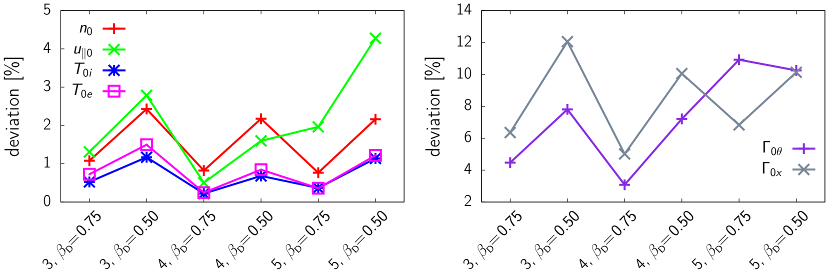

Figure 8.7.: Averaged variation of the plasma quantities of the B2-ATTEMPT simulations with $\beta_D = 0.75$ and $\beta_D = 0.5$ from the B2-ATTEMPT simulation with $\beta_D = 1$ for the cases 3, 4, and 5.

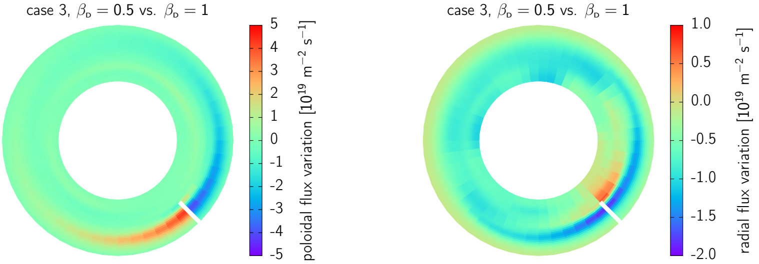

Figure 8.8.: Absolute variation of the poloidal (left) and radial flux (right) of the simulation with $\beta_D = 0.5$ from the simulation with $\beta_D = 1$ for case 3.

where X is either 0.75 or 0.5 and the average $\langle ... \rangle_{r_{\text{sim}}}$ refers to the average over the whole B2 simulation domain of the final global iteration. For n_0, $u_{\|0}$, T_{0i}, and T_{0e}, the average variation is below 5% for all cases, showing a tendency to slightly increase the smaller β_D. A higher average deviation is found for the radial and the poloidal flux, shown in fig. (8.7), right. Here, $\eta(\Gamma_{0x})$ reaches values of up to 12% for case 3, $\beta_D = 0.5$.

To examine this variation of the fluxes regarding its spatial dependency the absolute deviation $\alpha_0(\beta_D{=}0.5) - \alpha_0(\beta_D{=}1)$ of the poloidal and radial fluxes of the simulation with $\beta_D = 0.5$ from the simulation with $\beta_D = 1$ is plotted in fig. 8.8. For $\Gamma_{0\theta}$, fig. 8.8, left, the flux onto the limiter is higher for the simulation with $\beta_D = 0.5$[1], reaching an absolute deviation of up $5 \cdot 10^{19}$ m^{-2} s^{-1}. Compared to the typical total magnitudes of the poloidal flux, the maximum value of $\Gamma_{0\theta}$ being around $80 \cdot 10^{19}$ m^{-2} s^{-1} for

---

[1] Note that the flux $\Gamma_{0\theta}$ onto the limiter changes its sign, depending on which side is looked at.

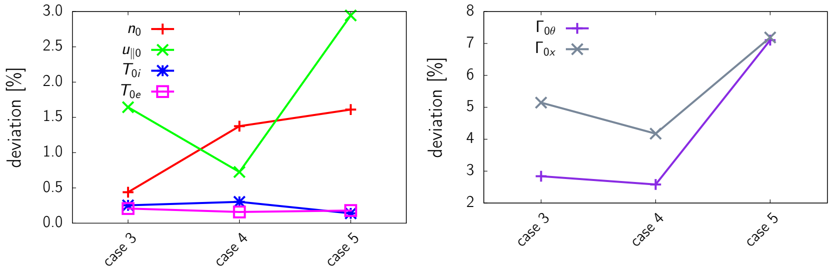

Figure 8.9.: Averaged variation of the results of the B2-ATTEMPT simulations with poloidally varying diffusion coefficient $D = D(x,\theta)$ from the results of the simulations with poloidally homogeneous $D = D(x)$ for cases 3, 4, and 5 with $\beta_\mathrm{D} = 1$.

the right side of the limiter and $40 \cdot 10^{19}$ m^{-2} s^{-1} for its left side, this is a rather small variation.

While the poloidal flux to the limiter increases for $\beta_\mathrm{D} = 0.5$ the radial flux changes significantly only for the flux surfaces close to $x \approx 0.46$ cm: Γ_{0x} decreases here as compared to the simulation with $\beta_\mathrm{D} = 1$, with maximum values of the variations of around $1.5 \cdot 10^{19}$ m^{-2} s^{-1}. A typical reference value for the simulation with $\beta_\mathrm{D} = 1$ is $\Gamma_{0x} = 6 \cdot 10^{19}$ m^{-2} s^{-1} (compare fig. 8.3, right column, third row). Even though the relative variation of Γ_{0x} is larger than that of $\Gamma_{0\theta}$, it is not large enough to alter the plasma profiles resulting from simulations with different β_D significantly.

8.3.2. Poloidal variation of transport coefficients

To conclude this analysis of the two-dimensional coupled code simulations it is investigated in how far the poloidal dependence of the diffusion coefficient $D = D(x,\theta)$ influences the macroscale plasma profile. The focus is on the simulations with a purely diffusive macroscale transport model ($\beta_\mathrm{D} = 1$). For the purpose of comparison, B2-ATTEMPT coupled code simulations were carried out where the poloidal dependence of D has been neglected. $D^i(x)$ is then given by

$$D(x) \;=\; D(x_i) \;=\; -\alpha_r\, \beta_\mathrm{D}\, \frac{\langle\widetilde{\Gamma}\rangle^{i,l}}{\partial_x n_0^{i-1,l}} \;+\; (1-\alpha_r)\, D^{i-1}(x)\;, \tag{8.23}$$

where the average used for $\langle\widetilde{\Gamma}\rangle^{i,l}$ includes the average over the whole mesoscale simulation domain (as for the one-dimensional coupled code cases of chapter 7).

case 3

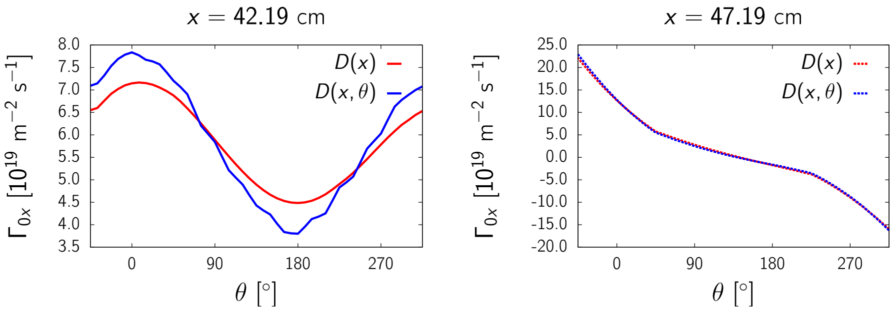

case 4

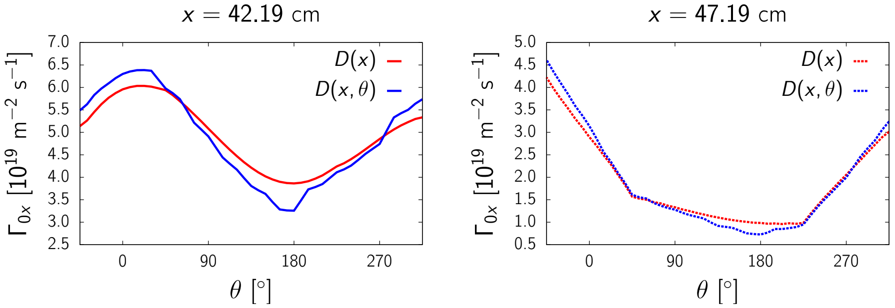

case 5

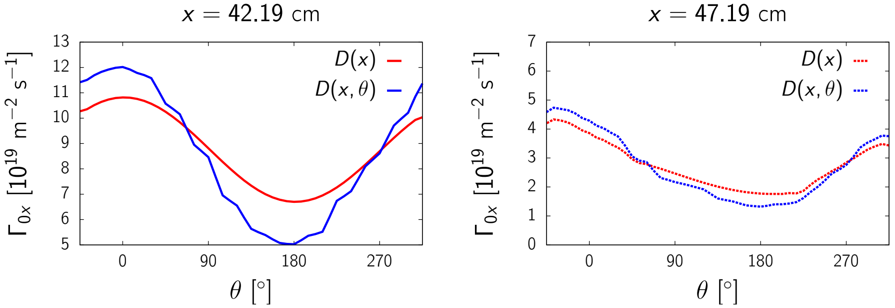

Figure 8.10.: Poloidal profiles of the radial flux of the B2-ATTEMPT simulations at two radial positions (left column: $x = 42.19$ cm, right column: $x = 47.19$ cm) for cases 3, 4 and 5 with $\beta_{\mathrm{D}} = 1$. The red graphs correspond to the simulation where $D = D(x)$ is poloidally homogeneous while for the blue graph, the poloidal variation of $D = D(x, \theta)$ was taken into account.

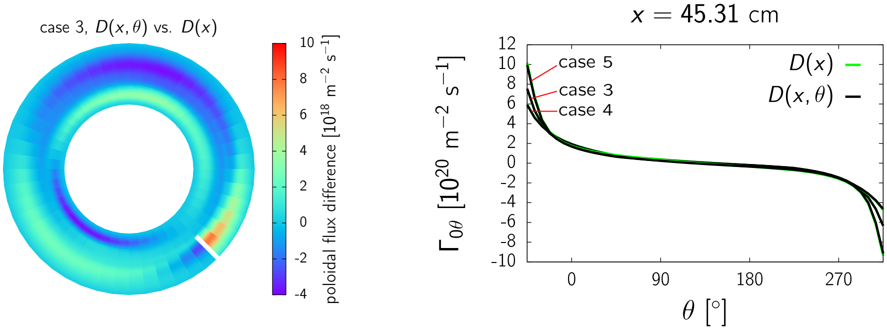

Figure 8.11.: Left: Poloidal flux from the simulation with poloidally dependent $D(x,\theta)$ minus the poloidal flux from the simulation with poloidally constant $D(x)$. **Right:** Poloidal profiles of the poloidal flux of the B2-ATTEMPT simulations for radial positions $x = 45.31$ cm for cases 3, 4 and 5 with $\beta_\mathrm{D} = 1$. The green graphs correspond to the simulation where $D = D(x)$ is poloidally homogeneous while for the black graph, the poloidal variation of $D = D(x,\theta)$ was taken into account.

The averaged variation $\eta(\alpha)$ of the simulations with $D = D(x,\theta)$ from the simulations with $D = D(x)$ for the whole macroscale simulation domain is shown in fig. 8.9, $\eta(\alpha)$ being calculated as given by eq. (8.22), only that not β_D is varied but the form of D. The variation between the two models for D regarding n_0, $u_{0\|}$, T_{0i}, and T_{0e} is below 3% for all cases. Only for the poloidal and radial flux, $\eta(\Gamma_{0x})$ and $\eta(\Gamma_{0\theta})$ reach values of about 7% for case 5. Here, the poloidal variation of D is most pronounced, $D(x,\theta)$ varying up to a factor of two for a constant radial coordinate (compare fig. 8.5 for the profiles of $D(x,\theta)$).

Poloidal profiles of the radial flux Γ_{0x} for two radial positions are shown in fig. 8.10. While the plots in the left column ($x = 42.19$ cm) are from the region of closed flux surfaces, those in the right column ($x = 47.19$ cm) are from the SOL, the limiter plates being situated at the left border (right side of the limiter) and right border (left side of the limiter) of the plot. As one can see Γ_{0x} shows a stronger poloidal dependence where the poloidal dependency of radial transport is included, leading to an increased radial flux at the LFS ($\theta = 0°$, the region of bad curvature) and a diminished flux at the HFS ($\theta = 180°$), the variation being around 10 to 30% for $x = 42.19$ cm. It corresponds to experimental findings of the ballooning character of transport at the tokamak Tore Supra [106]. The variation of Γ_{0x} with θ is less pronounced in the SOL, with a typical variation around 10%.

The fact why the additional ballooning of the radial flux (that appears when taking into account the poloidally dependent diffusion coefficients) does not influence significantly the profiles of the plasma parameters can be explained by modified poloidal fluxes. In fig. 8.11, left, the poloidal flux from the simulation with poloidally dependent $D(x,\theta)$ minus the poloidal flux from the simulation with poloidally constant $D(x)$ is shown. In the region of closed flux surfaces the poloidal flux towards the HFS is increased (positive difference from $\theta \approx 315°$ to $\theta \approx 180°$ – additional flux in counterclockwise direction, negative difference from $\theta \approx 180°$ to $\theta \approx 315°$ – additional flux in counterclockwise direction). This balances the diminished radial flux at the HFS (see fig. 8.10, top, left) via transport from the LFS which sees increased radial flux. The magnitude of the flux difference in radial and poloidal direction coincides: while the additional radial flux is around $5 \cdot 10^{18}$ m^{-2} s^{-1} at its maximum this is also the order of magnitude of the change in the poloidal flux. Note also that in the region of open flux surfaces the poloidal flux towards the limiter is slightly increased for poloidally varying $D(x,\theta)$. However, this variation is negligible as it is illustrated by fig. 8.11 where the poloidal profiles of the poloidal flux $\Gamma_{0\theta}$ for the radial position $x = 45.31$ cm (in the SOL, right behind the limiter which extends up to $x = 45$ cm) for the cases 3, 4, and 5 is shown.

8.3.3. Summary and conclusions

In this paragraph, the results of the two-dimensional coupled code simulations with B2-ATTEMPT are summarized.

- Using the B2-ATTEMPT coupled code system to model the plasma edge for the simulation of experiments at the tokamak TEXTOR leads to multiscale simulations which converge after about ten global iterations under the given criteria (variation of the transport coefficient profiles between two global iterations lower than prescribed limit). Resulting plasma profiles of the density n_0 and the electron temperature T_{0e} are comparable to experimental measurements. The coupled code system accounts for the effects of varying particle density gradient drive, collisionality, plasma beta, and minor radius on the local drift fluid dynamics, resulting in a poloidally and radially inhomogeneous averaged mesoscale flux and macroscale transport coefficients.

- Comparisons of B2-ATTEMPT simulations with B2-EIRENE simulations performed by D. Gray [17] for TEXTOR experiments show that the diffusion coefficients obtained by the local mesoscale simulations of ATTEMPT are of the same order of magnitude as the effective diffusion coefficients used by D. Gray to match experimental measurements. Also, profiles of the density and electron temperature from B2-ATTEMPT simulations are similar to those experimentally measured, the main differences being accounted for by a reduced neutral model and a simplified limiter shape employed in the B2-ATTEMPT simulations. For the cases 3 and 4 presented in [17] the diffusion coefficient varies around 10 to 30% from the effective diffusion coefficients determined with the data provided by the B2-EIRENE simulations of D. Gray at the outer midplane. In contrast, estimates of radial diffusion by classical or neoclassical transport theory underestimate the transport by at least one order of magnitude. For case 5 the significant deviations of the B2-ATTEMPT simulations from the B2-EIRENE simulations and the extremely high density values close to the Greenwald density limit given in [17] suggest that the corresponding measurements presented in [17] might be erroneous.

- In addition to the model of poloidally homogeneous transport coefficients used in [17] the B2-ATTEMPT simulations provide a poloidal dependence of transport coefficients which is in agreement with the ballooning of particle flux found in experiments [106]. For the cases considered, the variation of the radial flux in poloidal direction as compared to B2-ATTEMPT simulations where no poloidal dependence of the flux was assumed, is around 10 to 30%. The variation of the respective profiles of $n_0, u_{\|0}, T_{0i}$, and T_{0e} due to this poloidal dependence is rather low, showing maximum deviations around 3%. This is due to balancing processes via poloidal fluxes which ensure homogeneous profiles within one flux surface.

- Employing different macroscale transport models in the B2 code of the B2-ATTEMPT coupled code system, changing the division of the averaged radial mesoscale flux into convective and diffusive parts, results in only small variation in the profiles of $n_0, u_{\|0}, T_{0i}$, and T_{0e}, the total averaged variation being below 5%. This result is in agreement with theoretical considerations stating that in the stationary case the macroscale transport model should not influence the plasma profiles obtained on the macroscale. For the radial and poloidal fluxes Γ_{0x} and $\Gamma_{0\theta}$ the variation for different macroscale transport profiles is slightly larger, however only resulting in a slight increase of the total particle flux to the limiter plates of locally around 10%.

9. Conclusions and Outlook

In this chapter, the results of chapters 2 to 8 are summarized and an outlook regarding future investigations is given.

- **Generic multiscale model for a fluid:** Based on the hypothesis of a scale separation and employing the Reynolds decomposition with the respective averaging operator, the generic fluid balances for particle, momentum, and energy can be used for the formulation of a multiscale model. The model formulated here consists of a mesoscale part and a macroscale part and belongs to the class of heterogeneous multiscale models. The scale separation means that the typical times $\tau_{\mathrm{D}}(\widetilde{\alpha})$ and lengths $\lambda_{\mathrm{D}}(\widetilde{\alpha})$ of processes on the mesoscale are significantly smaller than the corresponding quantities $\tau_{\mathrm{D}}(\alpha_0)$ and $\lambda_{\mathrm{D}}(\alpha_0)$ of the characteristic macroscale processes. The resulting balance equations for the macroscale evolution are characterized by averaged mesoscale terms, describing the averaged advection of the mesoscale density, velocity, or temperature, respectively, by the mesoscale velocity. In the mesoscale balances these terms are present as well with opposite sign to filter out any macroscale evolution from the mesoscale and thus ensure a clear and enduring scale separation. The macroscale quantities and their gradients enter the mesoscale balances as constant parameters.

  The objective of a **coupled code system** is to solve the multiscale fluid equations numerically. Its efficiency, represented by the savings of computational resources compared to solving the full equations (including the mesoscale and macroscale evolution), increases the more pronounced the scale separation is. Macroscale transport models used in the macroscale part of the multiscale approach aim at expressing the averaged mesoscale terms in form of macroscale variables and transport coefficients which are determined with the mesoscale data.

- **Large scale description of the plasma edge:** The properties of a tokamak device and the Braginskii closure are used to specify the fluid of interest of this thesis as a collisional, magnetized plasma. The large scale model for the plasma edge, based on the macroscale part of the generic multiscale model and the assumptions of the B2 model, is characterized by a differentiation between the dynamics parallel and perpendicular to the magnetic field. It accounts for the evolution of the density, parallel ion momentum, and ion and electron temperature on the scale of a tokamak device (typical times around one second, typical lengths of the order of centimeters or above). For the self-contained version of the large scale model, the averaged mesoscale terms are replaced by a diffusive macroscale transport model with arbitrary transport coefficients which is motivated by results of passive scalar system.

- **Drift fluid models for the plasma edge:** The perpendicular dynamics which are treated in an approximate way in the large scale model are accounted for in detail by the drift fluid models presented in chapter 4. The E×B drift and the diamagnetic drift are taken as dominant perpendicular velocities. The corresponding drift fluid equations evolve the density, the ion and electron momentum, the electric potential, and the perturbations of the equilibrium magnetic field. The drift fluid models cover processes down to scales of $\tau_{\mathrm{D}}(\widetilde{\alpha}) \approx 10^{-6}$ s and $\lambda_{\mathrm{D}}(\widetilde{\alpha}) \approx \rho_s$. Its global version describes the evolution of the system on both the mesoscale and macroscale. The associated local drift fluid model which is obtained from the mesoscale part of the generic fluid model under the assumptions of the global drift fluid model and a scale separation describes only the mesoscale evolution of the system, taking the macroscale quantities as constants.

- **Specific multiscale model:** The specific multiscale model for the plasma edge consists of the large scale model for the macroscale evolution of profiles and the local drift fluid model for the mesoscale dynamics. The latter model is simplified in so far as the temperature dynamics on the mesoscale are neglected.

- **Investigation of the relation between mesoscale and macroscale dynamics by means of a passive scalar system:** The passive scalar system investigated in chapter 6 is governed by the advection of a passive quantity by a velocity field with arbitrary correlation length $\lambda_c(\boldsymbol{v})$, correlation time $\tau_c(\boldsymbol{v})$, and root mean square velocity v_{RMS}. Earlier studies for small Kubo numbers $K \ll 1$ have shown that the macroscale behavior of the system is diffusive. The corresponding diffusion coefficient is determined by the statistical characteristics of the velocity field, $D(K \ll 1) = v_{\mathrm{RMS}}^2 \tau_c(\boldsymbol{v})$, while on the mesoscale the system dynamics is convective. In the present work it is shown by numerical experiments that also in the regime of large Kubo numbers $K \gg 1$ (as believed to be relevant for magnetic fusion edge plasmas) the macroscale transport remains diffusive. This extends the applicability of the diffusion hypothesis that is employed for the derivation of the self-contained large scale model. D is given by a power law, $D(K \gg 1) = 0.35 \cdot v_{\mathrm{RMS}}^{0.74} [\lambda_c(\boldsymbol{v})]^{1.20} / [\tau_c(\boldsymbol{v})]^{0.26}$. The dependence of D on v_{RMS} with an exponent of 0.74 is consistent with theoretical considerations regarding percolation theory, the motion of particles or fluid parcels through porous media.

- **Coupled code system:** A combined concurrent-sequential coupling procedure is developed for the one-dimensional coupled code system. In this context, an algorithm for the determination of the statistically stationary state and the corresponding averaging intervals for the non-local simulations is presented, which is a well-known problem in the field of time series analysis. The algorithm serves the specific needs of the coupling procedure employed here, including a quick assessment of both the equilibration time δt_{st} and the characteristic evolution time $\tau_{\mathrm{D}}(\alpha)$ of the quantity of interest as well as a decision-making process to determine the adequate length for averaging of the time trace considered. Simulations with the 1D coupled code system proof that the procedure works efficiently and consistently.

- **One-dimensional benchmark case:** The results of the coupled code simulations for a one-dimensional transient test problem which are performed here for the first time for a *time-dependent* evolution of profiles in the tokamak plasma edge show satisfactory agreement with the reference simulation, carried out with the non-local version of the drift fluid code ATTEMPT. The test problem consists of determining the evolution of the flux surface averaged density and radial flux in the edge region in radial direction. Typical deviation of the coupled code results regarding the reference simulation are between 4 and 6.5% for the density and 19 and 41% for the radial particle flux. Further adjustment of the damping term $\gamma(\tilde{n})$ employed in the local drift fluid equations might reduce this uncertainties.

  The time savings achievable with the coupled code system depend on the typical time scale of the macroscale dynamics. For typical macroscale evolution times of one millisecond the coupled code system is about as fast as the reference simulation. For macroscale evolution times of the order of ten milliseconds the time savings of the coupled code system are around a factor ten while the uncertainties for density and flux are around 6 and 22%, respectively. Time savings potentially increase up to a factor of 50 for a fusion edge plasma region with a radial extent of 30 cm and typical radial profile lengths around 5 cm while preserving the same level of agreement with the fully resolved reference simulations.

  The level of agreement of the density varies little regarding different coupling input parameters and the choice of the macroscale transport model. In contrast, the level of agreement of the radial particle flux shows a comparably strong variation. This observation can be accounted for by two effects: Firstly, fluctuations of the radial flux around an adequate average value increase the flux error but have little effect on the density since the transport time associated with the fluctuating macroscale transport coefficients is shorter than the typical time of the fluctuations. Secondly, the divergence of the flux $\boldsymbol{\nabla} \cdot \boldsymbol{\Gamma}_{0x}$, which acts like a source term in the macroscale density continuity equation, exhibits self-correcting mechanism: an underestimated divergence at one point in the macroscale simulation domain is compensated by an overestimated divergence at a neighboring point and vice versa.

- **Two-dimensional B2-ATTEMPT coupled code simulations:** The realization of the specific multiscale model within the B2-ATTEMPT coupled code system leads to self consistent solutions for two-dimensional plasma profiles in the edge region of a tokamak. The local drift fluid simulations take into account the radial background gradient, the collisionality, and the plasma beta as determined by the macroscale solution as well as the corresponding minor radius. They provide a poloidally and radially varying profile of the averaged mesoscale flux which is translated into radial transport coefficients employed in the macroscale simulations. The resulting profiles account for the ballooning character of transport in a torus, leading to increased transport coefficients at the low field side up to a factor two larger than those on the high field side. Representing the averaged mesoscale flux by macroscale transport coefficients with different diffusive and convective parts leads to negligible variation of the macroscale profiles of density, parallel ion velocity and ion and energy temperatures. This confirms theoretical considerations stating that the choice of the macroscale transport model should not influence the profiles of the converged stationary macroscale state.

  B2-ATTEMPT simulations are compared to B2-EIRENE simulations where spatially homogeneous transport coefficients were used to adjust the simulation results to experimentally measured radial profiles on the outer midplane. The diffusion coefficients determined by the B2-ATTEMPT system are of the order of 0.3 to 0.9 m^2 s^{-1} and are of the same magnitude as the effective diffusion coefficients that can be determined from the B2-EIRENE simulations. The same is true for the radial profiles of the density and the electron temperature at the outer midplane. This shows that a coupled drift fluid transport model self-consistently determines a level of radial particle transport being of the correct order of magnitude, quite distinct from the 10 to 100 times smaller radial transport estimates found from neoclassical and classical collision plasma transport theory.

There are various possibilities for extending the work presented in this thesis. A major step would be the inclusion of the temperature dynamics in the local mesoscale model and the associated extension of the coupled code system. The existing B2-EIRENE simulations could then be used to evaluate in how far the corresponding transport coefficient coincide with experimental findings. In this context it would also be advantageous to use the EIRENE code in the B2-ATTEMPT system as an improved neutral particle model.

Making the ATTEMPT code applicable to different shapes of poloidal cuts of flux surfaces, e.g. including the more typical vertically elongated (‘D-shaped’) poloidal flux surfaces, allows for using it also to investigate transport properties at larger tokamak devices such as JET and ITER with more detailed magnetic field and machine designs. Regarding the coupling script it is foreseen to allow the B2-ATTEMPT system to re-use previously determined transport coefficients, i.e. adding a sequential ('learning') part to the coupling procedure as it was already implemented in the prototypical 1D coupled code system studies.

Additionally, two further questions remain to be addressed in future. Firstly, in how far non-local transport effects can be included in the present multiscale model [109] and secondly, in how far two-dimensional transient events can can be reproduced. For this purpose it has to be assured that the macroscale part which, in current applications to fusion edge plasmas, is typically operated in a stationary mode only, delivers reliable time-dependent simulations. The concepts of the present thesis then have to be extended towards the area of unsteady Reynolds-averaged simulations (URANS).

A. Sampling the velocity field for the passive scalar system

To sample the potential $\phi(\boldsymbol{r}, t)$ from which the velocity field $\boldsymbol{v}(\boldsymbol{r}, t)$ for the passive scalar simulations is derived (see paragraph 6.2.2), the stochastic Langevin equation

$$\tau \frac{\partial \phi}{\partial t} \;=\; -\phi \;+\; \varepsilon\, Q[-\lambda^2 \nabla^2] \zeta \; . \tag{A.1}$$

has to be solved. The solution of eq. (A.1) is outlined below.

For periodic boundary conditions, Q, ζ, and ϕ are expanded into a Fourier series with

$$\begin{aligned} \phi &= \sum_{m,n} \phi_{m,n} e^{imk_x x + ink_y y} \; , \\ Q &= \sum_{m,n} Q_{m,n} e^{imk_x x + ink_y y}, \qquad \zeta \;=\; \sum_{m,n} \zeta_{m,n} e^{imk_x x + ink_y y} \; . \end{aligned} \tag{A.2}$$

The extent of the simulation domain being defined by x_{sim} and y_{sim}, one has for the wavenumbers k_x and k_y

$$k_x \;=\; \frac{2\pi}{x_{\mathrm{sim}}} \; , \qquad k_x \;=\; \frac{2\pi}{y_{\mathrm{sim}}} \; . \tag{A.3}$$

The Fourier components $\phi_{m,n}$ have to fulfill the equation

$$\tau \frac{\partial \phi_{m,n}}{\partial t} \;=\; -\phi_{m,n} \;+\; \varepsilon\, Q_{m,n} \zeta_{m,n} \; . \tag{A.4}$$

The solution of this Ornstein-Uhlenbeck process for $\phi_{m,n}$ is

$$\phi_{m,n}(t + t_l) \;=\; \phi_{m,n}(t) \exp\left(-\frac{t_l}{\tau} \right) \;+\; \omega_{m,n}(t_l, \tau) \; , \tag{A.5}$$

where

$$\omega_{m,n} \;\equiv\; \frac{\varepsilon}{\tau} \int\limits_{t}^{t+t_l} \exp\left(-\frac{t + t_l - t'}{\tau} \right) Q_{m,n}\, \zeta_{m,n}\; dt' \tag{A.6}$$

is a Gaussian random number with zero mean and variance σ_ω^2 [110],

$$\sigma_\omega^2 \;=\; \Big\langle |\omega_{m,n}|^2 \Big\rangle_e \;=\; \frac{\varepsilon^2 Q_{m,n}^2}{2\tau}\left[1 - \exp\left(-\,\frac{2t_l}{\tau}\right)\right] \;. \tag{A.7}$$

One can then rewrite $\omega_{m,n}$ as

$$\omega_{m,n}(t_l,\tau) \;=\; \frac{\varepsilon Q_{m,n}}{\sqrt{2\tau}}\sqrt{1 - \exp\left(-\,\frac{2t_l}{\tau}\right)}\;\alpha_{m,n} \;, \tag{A.8}$$

the $\alpha_{m,n}$ being anti-correlated Gaussian random numbers with zero mean. They fulfill

$$\Big\langle \alpha_{m,n}(t)\,\alpha_{l,k}(t)\Big\rangle_e \;=\; \delta_{m,-l}\,\delta_{n,-k} \;. \tag{A.9}$$

The stationary probability density $p(\phi_{m,n})$ is Gaussian with zero mean and variance $\sigma_{m,n}^2$. For the potential $\phi(x,y,t+t_l)$ one obtains

$$\phi(x,y,t+t_l) \;=\; \sum_{m,n}\Big[\phi_{m,n}(t)e^{-t_l/\tau} \;+\; \omega_{m,n}(t_l,\tau)\Big]e^{imk_x x + ink_y y} \;. \tag{A.10}$$

Next, the correlation time $\tau_c(\phi)$ and length $\lambda_c(\phi)$ shall be related to the corresponding quantities of the velocity field, $\tau_c(\boldsymbol{v})$ and $\lambda_c(\boldsymbol{v})$, respectively, to be able to determine D^* via eq. (6.29b). For the former quantities one has

$$\tau_c(\phi) \;=\; \int_0^\infty \langle\rho_\phi\rangle_{x,y}(0,0,t_l)\;dt_l \;, \qquad \lambda_c(\phi) \;=\; \int_0^\infty \langle\rho_\phi\rangle_{x,y}(x_l,y_l,0)\;dr_l \;, \tag{A.11}$$

where $r_l^2 = x_l^2 + y_l^2$. The spatially averaged autocorrelation function $\langle\rho_\phi\rangle_{x,y}(x_l,y_l,t_l)$ for lags x_l, y_l, and t_l is

$$\langle\rho_\phi\rangle_{x,y}(x_l,y_l,t_l) \;=\; \frac{\langle\gamma_\phi\rangle_{x,y}(x_l,y_l,t_l)}{\langle\sigma_\phi^2\rangle_{x,y}} \;, \tag{A.12}$$

with γ_ϕ being the autocovariance of ϕ and $\langle\sigma_\phi^2\rangle_{x,y}$ being its variance. It holds that $\langle\sigma_\phi^2\rangle_{x,y} = \langle\gamma_\phi(0,0,0)\rangle_{x,y}$. For the spatial average of the autocovariance γ_ϕ one has

$$\begin{aligned}\langle\gamma_\phi\rangle_{x,y}(x_l,y_l,t_l) \;&=\; \Big\langle \phi(x+x_l,y+y_l,t+t_l)\,\phi^*(x,y,t)\Big\rangle_{e,x,y}\\ &=\; \sum_{m,n,m',n'}\Big\langle\phi_{m,n}(t+l_t)\,\phi^*_{m',n'}(t)\Big\rangle_e\Big\langle e^{i(m-m')k_x x + i(n-n')k_y y}\;e^{imk_x x_l + ink_y y_l}\Big\rangle_{x,y}\\ &=\; e^{-l_t/\tau}\sum_{m,n}\sigma_{m,n}^2 e^{imk_x x_l + ink_y y_l}\end{aligned} \tag{A.13}$$

with

$$\sigma_{m,n}^2 \;=\; \Big\langle |\phi_{m,n}(t)|^2 \Big\rangle \;=\; \frac{\varepsilon^2 Q_{m,n}^2}{2\tau} \;. \tag{A.14}$$

For the operator $Q[-\lambda^2\nabla^2]$ different choices are possible [98]. Here, it takes the form

$$Q_{m,n} \;=\; \exp\Big[-\lambda^2(m^2k_x^2 + n^2k_y^2)\Big] \;. \tag{A.15}$$

Hence, $\langle\gamma_\phi\rangle_{x,y}(x_l, y_l, t_l)$ can be approximated by

$$\begin{aligned}
\langle\gamma_\phi\rangle_{x,y}(x', y', t') \;&=\; e^{-t_l/\tau}\frac{\epsilon^2}{2\tau}\sum_{m,n} e^{-2\lambda^2(m^2k_x^2+n^2k_y^2)}\, e^{imk_xx_l+ink_yy_l} \\
&\approx\; e^{-t_l/\tau}\frac{\epsilon^2}{2\tau}\int\limits_{-\infty}^{\infty}\int\limits_{-\infty}^{\infty} e^{-2\lambda^2(m^2k_x^2+n^2k_y^2)}\, e^{imk_xx_l+ink_yy_l}\; dm\; dn \\
&=\; \frac{\pi\varepsilon^2}{4\tau k_xk_y\lambda^2}\exp\left[-\frac{t_l}{\tau} - \frac{r_l^2}{8\lambda^2}\right] \;.
\end{aligned} \tag{A.16}$$

By converting the sum in the first line of eq. (A.16) into an integral the periodicity in spatial direction is lost. Therefore, this approximation holds only for $\lambda \ll x_{\text{sim}}, y_{\text{sim}}$ and $r_l < x_{\text{sim}}/2, y_{\text{sim}}/2$. For the correlation time $\tau_c(\phi)$ and correlation length $\lambda_c(\phi)$ one then has, according to eqs. (A.11a), (A.11b), and (A.12):

$$\tau_c(\phi) \;=\; \tau \;, \qquad \lambda_c(\phi) \;=\; \sqrt{2\pi}\lambda \;. \tag{A.17}$$

With the definition (6.32) of the velocity components the corresponding averaged covariances of v_x and v_y can be calculated:

$$\langle\gamma_{v_x}\rangle_{x,y}(x', y', t') \;\approx\; \frac{\varepsilon^2}{2\tau}\frac{\pi}{32k_xk_y\lambda^6}\Big[4\lambda^2 - (x')^2\Big]\exp\left[-\frac{t'}{\tau} - \frac{(r')^2}{8\lambda^2}\right] \;, \tag{A.18}$$

$$\langle\gamma_{v_y}\rangle_{x,y}(x', y', t') \;\approx\; \frac{\varepsilon^2}{2\tau}\frac{\pi}{32k_xk_y\lambda^6}\Big[4\lambda^2 - (y')^2\Big]\exp\left[-\frac{t'}{\tau} - \frac{(r')^2}{8\lambda^2}\right] \;, \tag{A.19}$$

$$\langle\gamma_{v_xv_y}\rangle_{x,y}(x', y', t') \;\approx\; -\frac{\varepsilon^2}{2\tau}\frac{\pi}{32k_xk_y\lambda^6}\; x'\, y' \exp\left[-\frac{t'}{\tau} - \frac{(r')^2}{8\lambda^2}\right] \;. \tag{A.20}$$

The associated correlation time $\tau_c(\boldsymbol{v})$ and length $\lambda_c(\boldsymbol{v})$ of the velocity are

$$\tau_c(\boldsymbol{v}) \;=\; \tau \;=\; \tau_c(\phi) \;, \qquad \lambda_c(\boldsymbol{v}) \;=\; \sqrt{\frac{\pi}{2}}\lambda \;=\; \frac{\lambda_c(\phi)}{2} \;. \tag{A.21}$$

The last input parameter of interest is the root mean square velocity v_{RMS} which yields:

$$v_{\mathrm{RMS}} \;=\; \sqrt{\langle \boldsymbol{v}^2 \rangle_e} \;=\; \sqrt{\left\langle v_x^2 + v_y^2 \right\rangle_e} \;=\; \frac{\sqrt{\pi}\varepsilon}{\sqrt{8\tau k_x k_y}\lambda^2}\ , \tag{A.22}$$

i.e. v_{RMS} is proportional to the amplitude ε of the Gaussian white noise. For the two-dimensional problem D is determined by

$$D \;=\; \frac{1}{2} v_{\mathrm{RMS}}^2 \tau_c(\boldsymbol{v}) \;=\; \frac{\pi \varepsilon^2 x_{\mathrm{sim}} y_{\mathrm{sim}}}{256 \lambda_c^4(\boldsymbol{v})}\ . \tag{A.23}$$

B. Reference figures of B2-EIRENE simulations

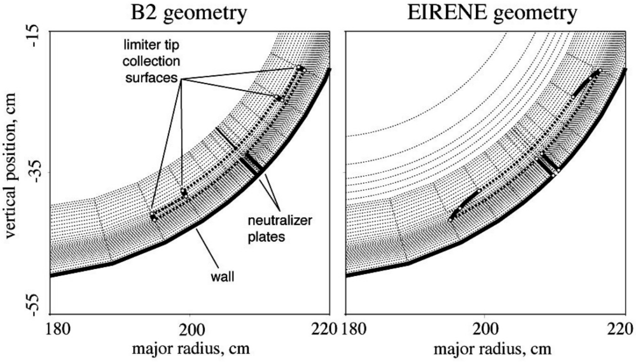

Figure B.1.: Shape of the toroidal limiter in the B2-EIRENE simulations of [17]. Plots taken from [17].

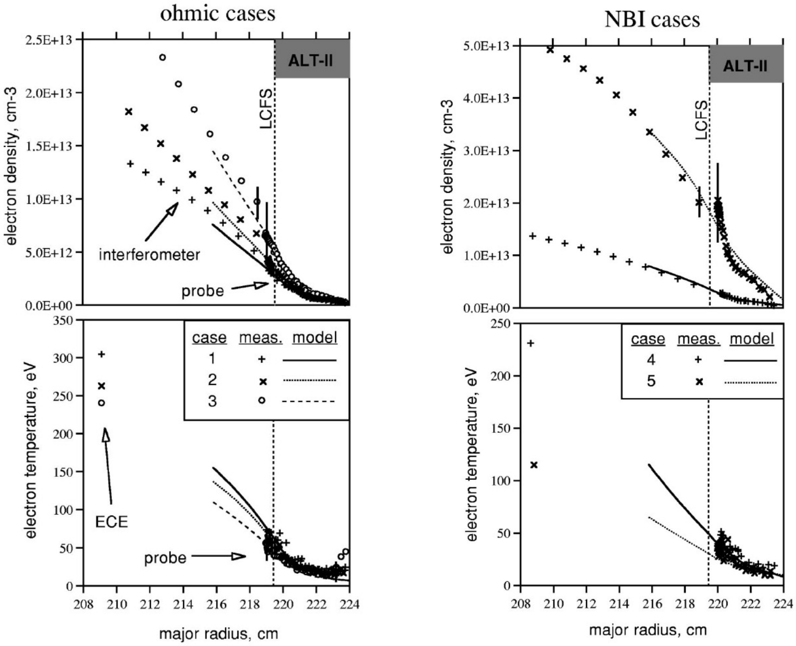

Figure B.2.: Radial electron density and electron temperature profiles in TEXTOR at the outer midplane as measured and simulated by the B2-EIRENE code. Plots taken from [17].

Bibliography

[1] Born, M. and Oppenheimer, R. Zur Quantentheorie der Molekeln. *Annalen der Physik*, **20** (1927), 458–484.

[2] Pope, S. B. Turbulent flows. Cambridge University Press (2000).

[3] Reiter, D. EIRENE - A Monte Carlo linear transport solver.
URL `http://www.eirene.de`

[4] Reiter, D.; Baelmans, M. and Boerner, P. The EIRENE and B2-EIRENE codes. *Fusion Science and Technology*, **47** (2005), 2, 172.

[5] Jenko, F. et al. Electron temperature gradient driven turbulence. *Physics of Plasmas*, **7** (2000), 5, 1904. doi:10.1063/1.874014.

[6] Candy, J. and Waltz, R. An Eulerian gyrokinetic-Maxwell solver. *Journal of Computational Physics*, **186** (2003), 2, 545–581. doi:10.1016/S0021-9991(03)00079-2.

[7] Grandgirard, V. et al. Global full-f gyrokinetic simulations of plasma turbulence. *Plasma Physics and Controlled Fusion*, **49** (2007), 12B, B173–B182. doi:10.1088/0741-3335/49/12B/S16.

[8] Sarazin, Y. and Ghendrih, P. Intermittent particle transport in two-dimensional edge turbulence. *Phys. Plasmas*, **5** (1998), 12, 4214–4228.

[9] Scott, B. D. The nonlinear drift wave instability and its role in tokamak edge turbulence. *New Journal of Physics*, **4** (2002), 52.1–52.30.

[10] Naulin, V. Electromagnetic transport components and sheared flows in drift-Alfven turbulence. *Physics of Plasmas*, **10** (2003), 10, 4016. doi:10.1063/1.1605951.

[11] Reiser, D. Impact of large island perturbations on turbulent blob transport in tokamaks. *Physics of Plasmas*, **14** (2007), 8, 082314. doi:10.1063/1.2771133.

[12] Tamain, P. et al. TOKAM-3D: A 3D fluid code for transport and turbulence in the edge plasma of Tokamaks. *Journal of Computational Physics*, **229** (2010), 2, 361–378. doi:10.1016/j.jcp.2009.09.031.

[13] Rognlien, T. D. et al. Two-dimensional electric fields and drifts near the magnetic separatrix in divertor tokamaks. *Physics of Plasmas*, **6** (1999), 5, 1851. doi:10.1063/1.873488.

[14] Reiter, D. Progress in two-dimensional plasma edge modelling. *Journal of Nuclear Materials*, **198** (1992), 80–89.

[15] Bufferand, H. et al. Applications of SOLEDGE-2D code to complex SOL configurations and analysis of Mach probe measurements. *Journal of Nuclear Materials*, **415** (2010), 1, 589–592. doi:10.1016/j.jnucmat.2010.11.037.

[16] Feng, Y. et al. A 3D Monte Carlo code for plasma transport in island divertors. *Journal of Nuclear Materials*, **241-243** (1997), 930–934. doi:10.1016/S0022-3115(97)80168-7.

[17] Gray, D. S. et al. Self-consistent plasma-neutral modeling in tokamak plasmas with a large-area toroidal belt limiter. *Physics of Plasmas*, **6** (1999), 7, 2816. doi:10.1063/1.873239.

[18] Schumacher, U. Fusionsforschung. Wissenschaftliche Buchgesellschaft Darmstadt (1993).

[19] Shaing, K. C. Neoclassical quasilinear transport theory of fluctuations in toroidal plasmas. *Physics of Fluids*, **31** (1988), 8, 2249. doi:10.1063/1.866626.

[20] Balescu, R. Is Onsager symmetry relevant in the transport equations for magnetically confined plasmas? *Physics of Fluids B: Plasma Physics*, **3** (1991), 3, 564. doi:10.1063/1.859855.

[21] Ross, D. W. On standard forms for transport equations and quasilinear fluxes. *Plasma Physics and Controlled Fusion*, **34** (1992), 2.

[22] Candy, J. et al. Tokamak profile prediction using direct gyrokinetic and neoclassical simulation. *Physics of Plasmas*, **16** (2009), 6, 060704. doi:10.1063/1.3167820.

[23] Barnes, M. et al. Direct multiscale coupling of a transport code to gyrokinetic turbulence codes. *Physics of Plasmas*, **17** (2010), 5, 056109. doi:10.1063/1.3323082.

[24] Rognlien, T. D. et al. Simulation of plasma fluxes to material surfaces with self-consistent edge turbulence and transport for tokamaks. *Journal of Nuclear Materials*, **337-339** (2005), 327–331. doi:10.1016/j.jnucmat.2004.10.023.

[25] Nishimura, Y. et al. Effects of resistive drift wave turbulence on tokamak edge transport. *Contributions to Plasma Physics*, **44** (2004), 194–199. doi:10.1002/ctpp.200410027.

[26] Cercignani, C. The Boltzmann Equation and Its Applications. Springer-Verlag (1988).

[27] Braginskii, S. I. Transport processes in a plasma. *Reviews of Plasma Physics*, **1** (1965), 205.

[28] Braams, B. Computational studies in tokamak equilibrium and transport. Ph.D. thesis, Rijksuniversiteit Utrecht (1986).

[29] Baelmans, M. Code improvements and applications of a two-dimensional edge plasma model for toroidal fusion devices. Ph.D. thesis, Katholieke Universiteit Leuven (1993).

[30] Scott, B. Low frequency fluid drift turbulence in magnetized plasmas. IPP Report IPP 5/92 (2001).

[31] Lipscombe, T. C.; Frenkel, A. L. and ter Haar, D. On the convection of a passive scalar by a turbulent Gaussian velocity field. *Journal of Statistical Physics*, **63** (1991), 1-2, 305–313. doi:10.1007/BF01026606.

[32] Careta, A. and Sancho, J. M. Diffusion of passive scalars under stochastic convection. *Physics of Fluids*, **6** (1993), 1, 349–355.

[33] Careta, A. et al. Effective diffusion in a stochastic velocity field. *Journal of Statistical Physics*, **71** (1993), 235–242.

[34] Neubauer, O. et al. Design features of the tokamak TEXTOR. *Fusion Science and Technology*, **47** (2005), 76–86.

[35] Miyamoto, K. Plasma physics for nuclear fusion. MIT Press (1980).

[36] The New Encyclopaedia Britannica, volume 4. Encyclopaedia Britannica, Inc. (2007).

[37] E, W. Principles of Multiscale Modeling. Cambridge University Press (2011).

[38] Medeiros Kremer, G. An introduction to the Boltzmann equation and transport processes in gases. Springer-Verlag (2010).

[39] D'haeseleer, W. et al. Flux coordinates and magnetic field structure. Springer-Verlag (1991).

[40] Steinhauer, M. O. Computational Multiscale Modeling of Fluids and Solids. Springer-Verlag Berlin Heidelberg (2007).

[41] Nishimura, Y.; Coster, D. and Scott, B. Characterization of electrostatic turbulent fluxes in tokamak edge plasmas. *Phys. Plasmas*, **11** (2004), 115. doi:10.1063/1.1631811.

[42] Hartung, J.; Elpelt, B. and Klösener, K.-H. Statistik. R. Oldenbourg Verlag (1999).

[43] E, W. and Engquist, B. Multiscale Modeling and Computation. *Notices of the American Mathematical Society*, **50** (2003), 9, 1062–1070.

[44] Engquist, B. et al. Heterogeneous Multiscale Methods: A Review. *Communications in Computational Physics*, **2** (2007), 3, 367–450.

[45] Brockwell, P. J. and Davis, R. A. Introduction to time series and forecasting. Springer-Verlag (2002).

[46] Brandt, A. Multi-level adaptive solutions to boundary-value problems. *Mathematics of Computation*, **31** (1977), 138, 333–390.

[47] Kevrekidis, I. G. et al. Equation-free, coarse-grained multiscale computation: enabling microscopic simulators to perform system-level analysis. *Comm. Math. Sci.*, **1** (2003), 4, 715–762.

[48] Einstein, A. Über die von der molekularkinetischen Theorie der Wärme geforderte Bewegung von in ruhenden Flüssigkeiten suspendierten Teilchen. *Annalen der Physik*, **322** (1905), 8, 549–560.

[49] Lucas, K. and Roosen, P., editors. Emergence, analysis and evolution of structures. Springer-Verlag (2010). doi:10.1007/978-3-642-00870-2.

[50] Wesson, J. Tokamaks. Oxford: Clarendon Press (2004).

[51] Kadomtsev, B. Tokamak plasma: a complex physical system. Institute of Physics Publishing, Bristol and Philadelphia (1992).

[52] Freidberg, J. Plasma Physics and Fusion Energy. Cambridge University Press (2007).

[53] ITER - the way to new energy.
URL `http://www.iter.org`

[54] EFDA - JET: photo gallery.
URL `http://www.efda.org/multimedia/graphics/`

[55] Müller, S. et al. Source formulation for electron-impact ionization for fluid plasma simulations. *Plasma Physics and Controlled Fusion*, **51** (2009), 10, 105014. doi:10.1088/0741-3335/51/10/105014.

[56] Kobayashi, M. et al. 3D edge transport analysis of ITER start-up configuration for limiter power load assessment. *Nuclear Fusion*, **47** (2007), 2, 61–73. doi:10.1088/0029-5515/47/2/001.

[57] Schmitz, O. et al. The influence of three-dimensional stochastic magnetic boundaries on plasma edge transport and the resulting plasma wall interaction. *Journal of Nuclear Materials*, **415** (2011), 1, 886–893. doi:10.1016/j.jnucmat.2011.01.136.

[58] Hasegawa, A. and Wakatani, M. Plasma Edge Turbulence. *Physical Review Letters*, **50** (1983), 9, 682–686.

[59] Scott, B. Three-dimensional computation of drift Alfvén turbulence. *Plasma Physics and Controlled Fusion*, **39** (1997), 1635–1668.

[60] Chen, F. Introduction to plasma physics and controlled fusion. Plenum Press (1984).

[61] Jackson, J. D. Electrodynamics. John Wiley & Sons (1998).

[62] Chang, Z. and Callen, J. D. Generalized gyroviscous force and its effect on the momentum balance equation. *Physics of Fluids B: Plasma Physics*, **4** (1992), 1766.

[63] Tsai, S.-t. Thermal Conductivity and Low Frequency Waves in Collisional Plasmas. *Physics of Fluids*, **13** (1970), 8, 2108.

[64] Haberscheidt, T. Turbulenter Plasmatransport im ergodisierten Magnetfeld. Ph.D. thesis, Ruhr-Universität Bochum (2006).

[65] Garcia, O. E. et al. Turbulence and intermittent transport at the boundary of magnetized plasmas. *Physics of Plasmas*, **12** (2005), 062309. doi:10.1063/1.1925617.

[66] Reiser, D. et al. A plasma source driven predator-prey like mechanism as a potential cause of spiraling intermittencies in linear plasma devices. *Physics of Plasmas*, **21** (2014), 3, 032302. doi:10.1063/1.4867492.

[67] Havlíčková, E. et al. The effect of plasma fluctuations on parallel transport parameters in the SOL. *Journal of Nuclear Materials*, **415** (2011), 1, S471–S474. doi:10.1016/j.jnucmat.2010.09.050.

[68] Pigarov, A. Y.; Krasheninnikov, S. I. and Rognlien, T. D. New approach in two-dimensional fluid modeling of edge plasma transport with high intermittency due to blobs and edge localized modes. *Physics of Plasmas*, **18** (2011), 9, 092503. doi:10.1063/1.3626841.

[69] Pigarov, A. Y.; Krasheninnikov, S. I. and Rognlien, T. D. Time-dependent 2-D modeling of edge plasma transport with high intermittency due to blobs. *Physics of Plasmas*, **19** (2012), 7, 072516. doi:10.1063/1.4739464.

[70] Scott, B. The character of transport caused by ExB drift turbulence. *Physics of Plasmas*, **10** (2003), 4, 963. doi:10.1063/1.1545100.

[71] Press, W. H. et al. Numerical Recipes. Cambridge University Press, third edit edition (2007).

[72] Barnes, M. Trinity: A Unified Treatment of Turbulence, Transport, and Heating in Magnetized Plasmas. Ph.D. thesis, University of Maryland (2008).

[73] Kotschenreuther, M.; Rewoldt, G. and Tang, W. M. Comparison of initial value and eigenvalue codes for kinetic toroidal plasma instabilities. *Computer Physics Communications*, **88** (1995), 128–140.

[74] Belli, E. a. and Candy, J. Kinetic calculation of neoclassical transport including self-consistent electron and impurity dynamics. *Plasma Physics and Controlled Fusion*, **50** (2008), 9, 095010. doi:10.1088/0741-3335/50/9/095010.

[75] Nishimura, Y. et al. Coupling of perpendicular transport in turbulence and divertor codes. *Contributions to Plasma Physics*, **42** (2002), 2–4.

[76] Braams, B. J. Radiative divertor modelling for ITER and TPX. *Contributions to Plasma Physics*, **36** (1996), 276–281.

[77] Rozhansky, V. A. et al. Simulation of tokamak edge plasma including self-consistent electric fields. *Nuclear Fusion*, **41** (2001), 387.

[78] Scott, B. D. Self-sustained collisional drift-wave turbulence in a sheared magnetic field. *Physical Review Letters*, **65** (1990), 26, 3289–3292.

[79] Scott, B. D. The mechanism of self-sustainment in collisional drift wave turbulence. *Physics of Fluids B: Plasma Physics*, **4** (1992), 8, 2468. doi:10.1063/1.860215.

[80] Rognlien, T. D. et al. Self-consistent simulation of turbulence and transport in tokamak edge plasmas. *Contributions to Plasma Physics*, **44** (2004), 13, 188–193. doi:10.1002/ctpp.200410026.

[81] Shestakov, A. et al. Self-consistent modeling of turbulence and transport. *Journal of Computational Physics*, **185** (2003), 2, 399–426. doi:10.1016/S0021-9991(02)00063-3.

[82] Xu, X. Q. et al. Low-to-high confinement transition simulations in divertor geometry. *Physics of Plasmas*, **7** (2000), 5, 1951. doi:10.1063/1.874044.

[83] Reuss, J. and Misguich, J. Low-frequency percolation scaling for particle diffusion in electrostatic turbulence. *Physical Review E*, **54** (1996), 2, 1857–1869.

[84] van Kampen, N. Stochastic processes in physics and chemistry. North-Holland Publishing Company (1981).

[85] Gardiner, C. W. Handbook of stochastic methods. Springer-Verlag Berlin Heidelberg (1983).

[86] Cussler, E. L. Diffusion – Mass Transfer in Fluid Systems. Cambridge University Press, third edit edition (2009).

[87] Dill, K. A. and Bromberg, S. Molecular driving forces: statistical thermodynamics in chemistry and biology. Garland Science (2003).

[88] Fick, A. Über Diffusion. *Annalen der Physik*, **170** (1855), 1, 59–86.

[89] Kull, H.-J. Plasmaphysik - Skriptum zur Forlesung im WS 2006/2007 (2007). URL `http://llp.ilt.fhg.de/skripten/pp06/pp_profile.pdf`

[90] Naulin, V. Turbulent transport and the plasma edge. *Journal of Nuclear Materials*, **363-365** (2007), 24–31. doi:10.1016/j.jnucmat.2006.12.058.

[91] Ghendrih, P. et al. Thermodynamical and microscopic properties of turbulent transport in the edge plasma. *Journal of Physics: Conference Series*, **401** (2012), 012007. doi:10.1088/1742-6596/401/1/012007.

[92] Bakunin, O. G. Turbulence and diffusion. Springer-Verlag Berlin Heidelberg (2008).

[93] Kubo, R. Stochastic Liouville Equations. *Journal of Mathematical Physics*, **4** (1963), 2, 174. doi:10.1063/1.1703941.

[94] Castiglione, P. Diffusion coefficients as function of Kubo number in random fields. *Journal of Physics A: Mathematical and General*, **1975** (2000).

[95] Hauff, T. and Jenko, F. Turbulent ExB advection of charged test particles with large gyroradii. *Physics of Plasmas*, **13** (2006), 10. doi:10.1063/1.2360173.

[96] Hauff, T. and Jenko, F. ExB advection of trace ions in tokamak microturbulence. *Physics of Plasmas*, **14** (2007), 9, 1–11. doi:10.1063/1.2768025.

[97] Toro, E. F. Riemann Solvers and Numerical Methods for Fluid Dynamics. Springer-Verlag Berlin Heidelberg, third edit edition (2009).

[98] Careta, A.; Sagués, F. and Sancho, J. M. Stochastic generation of homogeneous isotropic turbulence with well-defined spectra. *Physical Review E*, **48** (1993), 3.

[99] Gnuplot – a portable command-line driven graphing utility.
URL `http://www.gnuplot.info`

[100] Levenberg, K. A method for the solution of certain non-linear problems in least sqares. *Quart. Appl. Math.*, **2** (1944), 164–168.

[101] Kosuga, Y. et al. Progress on theoretical issues in modelling turbulent transport. *Nuclear Fusion*, **53** (2013), 4, 043008. doi:10.1088/0029-5515/53/4/043008.

[102] Gruzinov, A. V.; Isichenko, M. B. and Kalda, Y. L. Two-dimensional turbulent diffusion. *Sov. Phys. JETP*, **70** (1990), 263.

[103] Fortran programming language.
URL `http://www.fortran.com/`

[104] Python programming language.
URL `https://www.python.org/`

[105] Van Bellegem, S. Adaptive methods for modelling, estimating and forecasting locally stationary processes. Ph.D. thesis, Unversité Catholique de Louvain (2003).

[106] Fedorczak, N. et al. Electrostatic transport in L-mode scrape-off layer plasmas in the Tore Supra tokamak. I. Particle balance. *Physics of Plasmas*, **19** (2012), 7, 072313. doi:10.1063/1.4739058.

[107] Patankar, S. V. Numerical Heat Transfer and Fluid Flow. Taylor & Francis Inc. (1980).

[108] Wolf, G. H. TEXTOR: Research programme on plasma wall interaction. *J. Nucl. Mat.*, **123 & 123** (1984), 1124–1135.

[109] Dif-Pradalier, G. et al. On the validity of the local diffusive paradigm in turbulent plasma transport. *Physical Review E*, **82** (2010), 2, 025401. doi:10.1103/PhysRevE.82.025401.

[110] Bao, J.-D.; Li, R.-W. and Wu, W. Numerical simulations of generalized Langevin equations with deeply asymptotic parameters. *Journal of Computational Physics*, **197** (2004), 1, 241–252. doi:10.1016/j.jcp.2003.11.025.

Acknowledgements

First and foremost I would like to thank my supervisor, Dr. Dirk Reiser. I have profited enormously from his imminent help to the many questions and problems emerging during the work on my thesis. His thorough approach to (theoretical) physics impressed me greatly. I also very much enjoyed our off-topic conversations regarding movies, music, and many more things.

I am sincerely grateful for the support of my thesis adviser at Forschungszentrum Jülich, Prof. Dr. Detlev Reiter. He made this thesis possible and was always at hand when I needed help. I especially enjoyed the tolerant and open atmosphere in his group.

I am also very grateful to my supervisor Prof. Dr. Hans-Jörg Kull at the Institute for Theoretical Physics A at the RWTH-Aachen University. He facilitated the work within this collaborative project between Forschungszentrum Jülich and the RWTH-Aachen.

I would like to thank Dr. Philippe Ghendrih, Dr. Patrick Tamain, and Dr. Yannick Marandet from IRFM – CEA Cadarache and Aix Marseille University, respectively, for a very fruitful time in the South of France, the many helpful discussions, and their interest in my work.

I am thankful for the many colleagues that made the work during my PhD a pleasure (most of the time) – not only with their help on-topic questions but also with the great number of off-topic conversations and activities. To name all would take to long but I would like to thank especially Christian Salmagne, Sören Möller, Niels Gierse, Michael Rack, André Hoffmann, and Paul Zakalek, the guys from Forschungszentrum Jülich, and also David Moulton, Claudia Norscini, Unkyu Lee, Aakanksha Saxena, Olivier Fabbris, and François Orain who I met during my time in France.

Of course I owe a lot to my family who supported me in numerous material and immaterial ways. Thank you very much!

Pero más que nada quiero agradecerte a tí, Midori, por venir a Alemania, tu apoyo indispensable, tu paciencia enorme, tu humor encantador y muchas cosas más! Muchísimas gracias!

Band / Volume 295
Hydration and dehydration at the tropical tropopause
C. Schiller (2015), 72 pp
ISBN: 978-3-95806-101-9

Band / Volume 296
Influence of Impurities on the Fuel Retention in Fusion Reactors
M. Reinhart (2015), 140 pp
ISBN: 978-3-95806-105-7

Band / Volume 297
The role of abiotic processes in the formation and degradation of gaseous nitrogen compounds in the soil
J. Heil (2015), XIV, 106 pp
ISBN: 978-3-95806-106-4

Band / Volume 298
12th Carolus Magnus Summer School on Plasma and Fusion Energy Physics
edited by Kristel Crombé (2015), 468 pp
ISBN: 978-3-95806-107-1

Band / Volume 299
Optical near-field investigations of photonic structures for application in silicon-based thin-film solar cells
A. M. Ermes (2015), vi, 157 pp
ISBN: 978-3-95806-108-8

Band / Volume 300
Strom- und Gasmarktdesign zur Versorgung des deutschen Straßenverkehrs mit Wasserstoff
M. Robinius (2015), VI, 255 pp
ISBN: 978-3-95806-110-1

Band / Volume 301
Alterung von Vakuum-plasmagespritzten MCrAlY-Schutzschichten und ihre Wechselwirkung mit Nickel- und Cobalt-basierten γ/γ’-Superlegierungen
P. J. Terberger (2015), IX, 149 pp
ISBN: 978-3-95806-113-2

Band / Volume 302
Verbundvorhaben ELFA Effiziente Luftfahrzeuge
Brennstoffzellensysteme zur Energieerzeugung BREZEN –
Teilprojekt: Kerosinaufbereitung
R. Peters, J. Meißner, J. Pasel, R. C. Samsun, D. Stolten
(2016), viii, 84 pp
ISBN: 978-3-95806-114-9

Band / Volume 303
Cavity-Ringdown-Spektroskopie zur Untersuchung der Rolle höherer Stickoxide für den nächtlichen Schadstoffabbau in der unteren Atmosphäre
S. Schrade (2016), II, 118 pp
ISBN: 978-3-95806-116-3

Band / Volume 304
Thermo-mechanical Properties of Mixed Ionic-Electronic Conducting Membranes for Gas Separation
V. K. Stournari (2016), 167 pp
ISBN: 978-3-95806-117-0

Band / Volume 305
Untersuchungen zu suspensionsplasmagespritzten Wärmedämmschichtsystemen
N. Schlegel (2016), X, 136 pp
ISBN: 978-3-95806-118-7

Band / Volume 306
Laser processing for the integrated series connection of thin-film silicon solar cells
B. Turan (2016), XII, 190 pp
ISBN: 978-3-95806-119-4

Band / Volume 307
Development and Application of a Multiscale Model for the Magnetic Fusion Edge Plasma Region
F. Hasenbeck (2016), 188 pp
ISBN: 978-3-95806-120-0

Weitere ***Schriften des Verlags im Forschungszentrum Jülich*** unter
http://wwwzb1.fz-juelich.de/verlagextern1/index.asp

Energie & Umwelt /
Energy & Environment
Band / Volume 307
ISBN 978-3-95806-120-0

JÜLICH
FORSCHUNGSZENTRUM